Transition Regime Collisions in Aerosols

A DISSERTATION
SUBMITTED TO THE FACULTY OF
UNIVERSITY OF MINNESOTA
BY

Ranganathan Gopalakrishnan

IN PARTIAL FULFILLMENT OF THE REQUIREMENTS
FOR THE DEGREE OF
DOCTOR OF PHILOSOPHY

Professor Christopher J. Hogan Jr.
Professor Peter H. McMurry

August 2013

Acknowledgements

None of this would have been possible sans the support and guidance of my advisers Professors Chris Hogan and Peter McMurry. They have helped this kid from India get an education, that was enlightening, humbling and inspirational. Chris has been a great mentor. I am forever in debt to his meticulous planning, exemplary vision and more importantly the faith he placed on my abilities during moments when I did not believe in myself. Peter has been a great father figure, happy to take me under his wings and help discover my scientific interests.

My "PhD bro" Derek Obereitt is a walking personal aerosol encyclopedia. He has been a part of the pivotal moments of my grad school experience. His enthusiasm and perfectionism is infectious. My other PhD bro Thaseem Thajudeen is not just a great coworker but also a great friend, always taking care of people when they need it the most. I also thank my first teacher in the lab Jacob Scheckmann who helped to get my feet wet! Special thanks to my co-authors Hui Ouyang, Mark Meredith and Carlos Larriba. Thanks are due to all past and present McMurry and Hogan group members, "Gradfather" John, ME department folks who have been helpful and supportive in innumerable ways.

Parts of this work were carried out in the Characterization Facility, University of Minnesota, which receives partial support from NSF through the MRSEC program. Thanks to Dr. Robert Hafner and Dr. Jason Myers of Charfac UMN for their guidance in carrying out electron microscopy. Computational resources for simulations were provided by the Minnesota Supercomputing Institute. Financial support from the following sources is gratefully acknowledged: Center for Filtration Research, CBET-1133285, GOALI: Fundamental Studies of Nanoparticle-Protein Binding – instrumentation, CHE-1011810, Studies of Nanometer Scale Metal Cluster Dissociation in the Gas Phase, NSF BES-0646507, Lung Deposition of Highly Agglomerated Nanoparticles, ME Departmental Fellowship, several ME Departmental Teaching Assistantships and the University of Minnesota Doctoral Dissertation Fellowship.

Five years in Minneapolis have blessed me with a truckload of friends who made the journey light. In no specific order, Praggy, Roba, Coma, Savio, Aswin, Raja, Dabade, Durbha, Ben, Madhava, Thavil, Pulkit, Vijay, Nikhil, Kumaraswamy, Sumathi, Kicha, Twiggs, Mamunuru, Claudie and many others – miss y'all.

கற்பனை என்றாலும் கற்சிலை என்றாலும் கந்தனே உனை மறவேன்!

To Anu and Gopal

Abstract

In most natural and engineered aerosol systems, particles fall in the "transition regime", intermediate to the free molecular and continuum ranges. Furthermore, while theories for transport properties of spherical particles in the free molecular and continuum ranges have been available for decades, theories that are applicable to particles of arbitrary shape are lacking. This thesis addresses the transport of neutral and charged molecules (ions) as well as coagulation with particles of arbitrary shape and size. Computational and experimental studies are performed to develop and validate models of collisional mass transfer onto aerosol particles. A broad overview of the thesis is presented in Chapter 1. Using dimensional analysis and Brownian Dynamics trajectory calculations, the collisions between spherical and nonspherical particles are analyzed in Chapters 2 & 3. This approach is extended to include the effect of Coulombic potential interactions in Chapter 4, along with a critical assessment of existing theories. Further, the unipolar charging of arbirary shaped aerosol particles is studied in Chapter 5. Different from previous chapters, an approach to directly calculate the steady state charge distribution of particles exposed to arbitrary bipolar ion populations is developed in Chapter 6. Experiments are conducted with spherical and cylindrical particles to better understand momentum transfer (Chapter 7) and bipolar charging (Chapter 8) in the transition regime. Finally, conclusions derived from this research and future directions are discussed in Chapter 9.

Table of Contents

List of Tables

List of Figures

Chapter 1: Introduction

1.1. Collisions in Gas-phase systems

The motion of suspended entities (such as solid/liquid particles, macromolecules or ions) in a bath of background gas molecules, due to their thermal energy (diffusion) leads to inadvertent collisions and ensuing physical and/or chemical transformations. The nature of the mass transfer processes depends on the nature of the collision partners. The collision between a vapor molecule and a particle (condensation) or between two finite sized particles (coagulation) can lead to growth of particles (fig. 1.1a). In addition, collision between gas phase ions and particles can lead to modification of the charges carried by particles (fig 1.1b). The rate of such processes is directly dependent on the surface flux of species *j* to the surface of species *i* (fig. 1.1c). Among all the factors that influence such transport, in this thesis, the effects of thermal diffusion (Brownian motion) and electrostatic interactions are considered, in the absence of external flow or force fields.

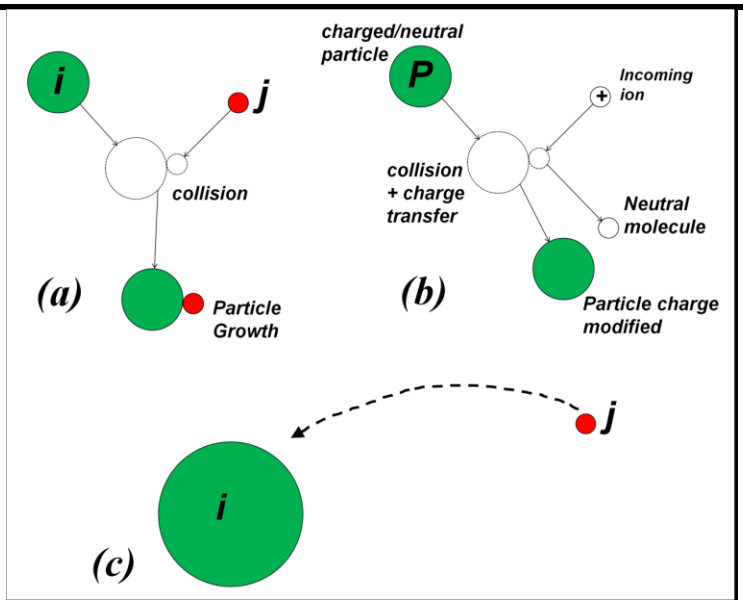

Figure 1.1: (a) Collisional growth of particles by condensation/coagulation. (b) Modification of charge of particles by collision with gas phase ions (c) Transport of species *j* to the surface of species *i*.

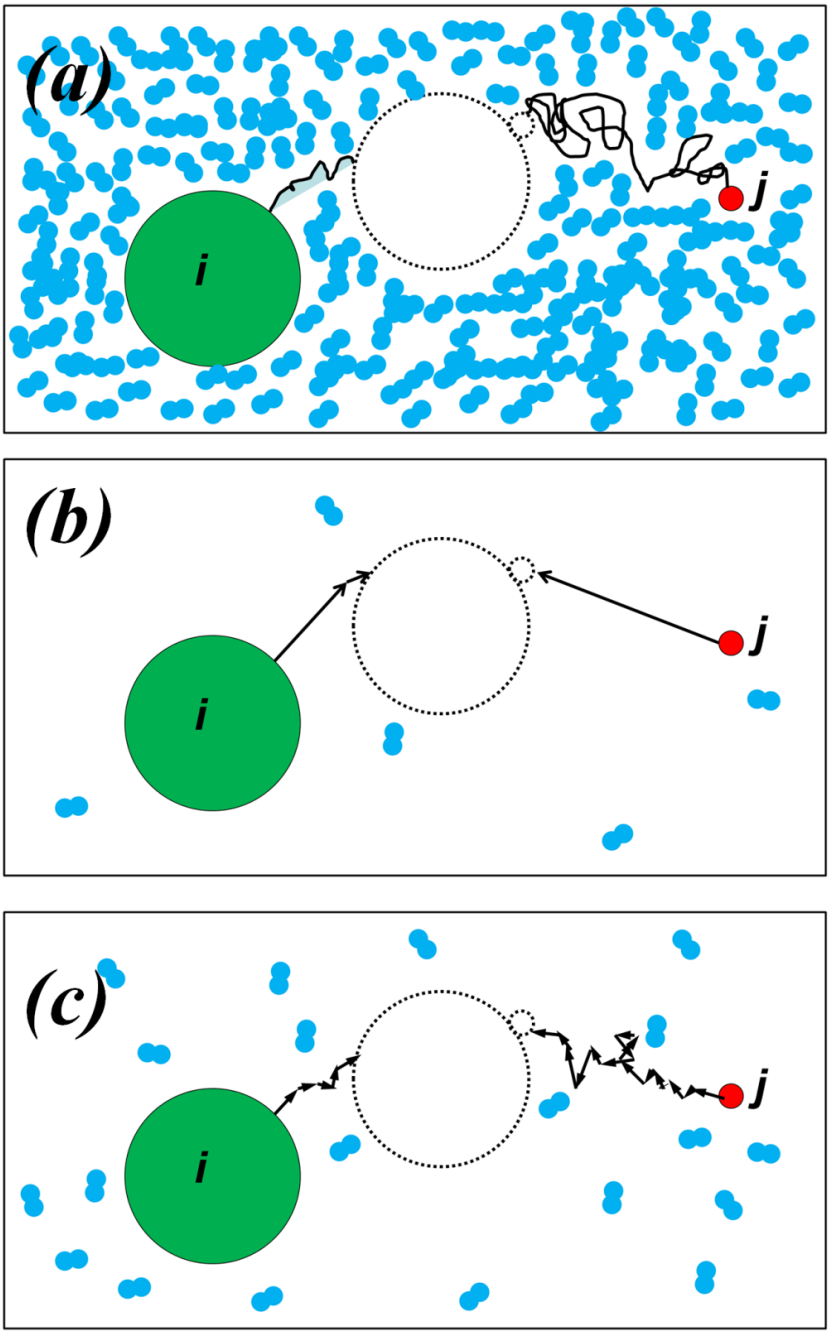

Figure 1.2: (a) Schematic illustrating the diffusion dominated trajectories of suspended entities in a high pressure system such as a colloid (b) Inertia dominated trajectories of suspended entities in a rarefied systems (c) Transition regime nature of motion of entities in an aerosol system. *i* and *j* represent suspended entities, while the blue objects represent gas molecules.

The trajectory of suspended entities and thereby the nature of species transport is strongly influenced by the collisions they undergo with background gas molecules. The frequency of such collisions is dependent directly on the pressure of the background gas. Particles suspended in high pressure systems (usually colloids), exhibit undergo highly diffusive motion (fig. 1.2a) characterized by random trajectories that are far from straight line motion. If on the other hand, the same particles are immersed in a low pressure gas (such as in outer space), the collisions are near straightlines because of sparse interactions (fig. 1.2b) with gas molecules that deviate their path. Aerosol systems, by virtue of their atmospheric pressure and temperature in most circumstances, lead to entity motion that is intermediate in nature to the low pressure and high pressure gas environments. In this "transition" regime of aerosol particle motion, both diffusivity and inertia of the particles contribute significantly in determining the trajectories (fig. 1.2c), which is parameterized by a diffusive Knudsen number Kn_D defined as the ratio of a *mean persistence path* of the colliding entities to a suitable measure of their size. It can be readily seen that the mean persistence is a length scale describing a collisional *interaction* between two entities, rather than than entities themselves and is distinct from the conventional definition of gas mean free path (which is based on gas molecule motion entirely). While a formal definition of Kn_D will be introduced in forthcoming chapters, the continuum limit (colloidal systems for eg.) is represented by the limit of $Kn_D \rightarrow 0$ and the free molecular limit (rarefied systems, macromolecules, etc.) is described by $Kn_D \rightarrow \infty$. The finite Kn_D regime which in terms of particle size represents the 5 – 2000 nm range at atmospheric pressure, represents the domain where most aerosol systems are operated (fig 1.3).

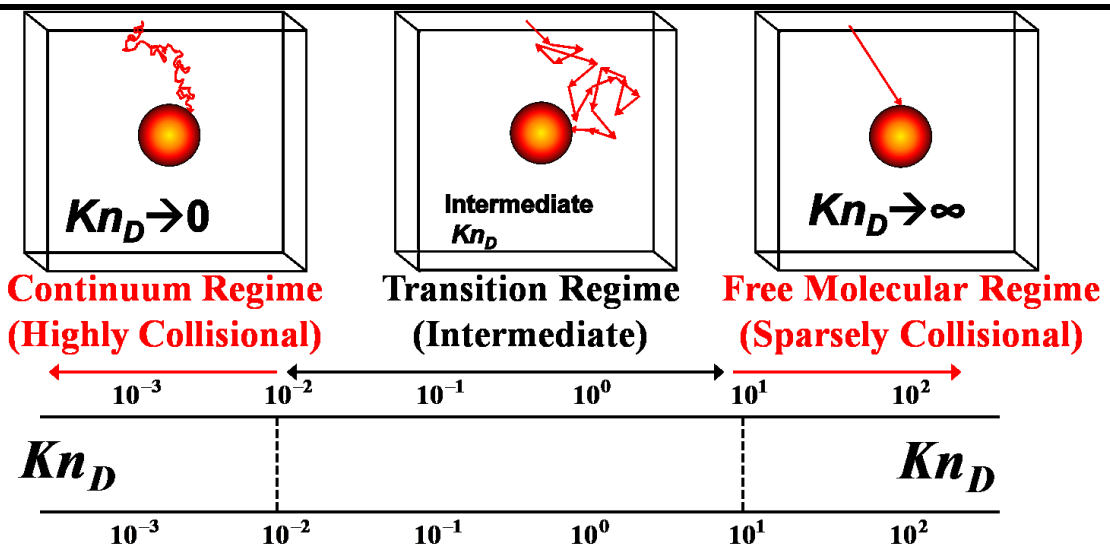

Figure 1.3: Collisional Transport regimes parameterize by the diffusive Knudsen number Kn_D.

Focussing on the transition regime of aerosol particle motion, the key objectives of this thesis include:

1) To take a fresh look at transition regime motion, that is completely described neither by continuum field approaches nor free molecular kinetic approaches, and to develop accurate models for the same.

2) While the analysis of collisions in which the colliding entities are spherical or point shaped has many applications, it is necessary to understand the effect of shape. Nonspherical particles posses unique quirks that make their analysis interesting and useful for technological applications.

3) Accurate accounting of potential interactions between colliding entities, complicated by the effect of particle shape, is required to develop accurate models for particle charging.

While there is interest in understanding collision/transport limited mass transfer pertaining to sub-micrometer aerosol particles, particle charging which involves

significant interplay of long range and short range potentials between colliding entities is of great importance. The reminder of this introduction discusses the problem of charging in detail and sets up the rest of the thesis for development of charging models and experiments conducted to verify the same. Situations in which such interactions are negligible are also widespread and important. For example, the condensation of vapor onto spherical particles leading to growth in size is important in the context of atmospheric particle growth and cloud formation. The interest in novel shaped nanomaterials needs a clear understanding of growth by coagulation, wherein precursor particles can quickly deviate from the shape of a sphere as they agglomerate with other particles. To build collision models applicable to charging, a bottom approach is undertaken with considerable effort dedicated to understanding transition regime collisions in the absence of potentials as well.

Diffusion charging of aerosol particles is a fundamental problem in aerosol science. Aerosol particle dynamics in the atmosphere and in synthesis reactors such as flames and plasmas are affected by electric charge which can enhance (Huang *et al.*, 1991; Ravi & Girshick, 2009) or diminish (Kortshagen & Bhandarkar, 1999) the rate of growth of particles. From the vantage point of electrical mobility measurements (Knutson & Whitby, 1975b), size-dependent particle charged fractions are needed to obtain number distributions (Alofs & Balakumar, 1982; Hagen & Alofs, 1983; Hogan *et al.*, 2009). Commonly, aerosol particles flow through a charger prior to mobility measurement which allows them to interact with ions and to attain a certain charge state. The key to inversion of mobility measurements depends on knowing the charge fraction of particles leaving the charger as exactly as possible (Hoppel & Frick, 1990; Stolzenburg & McMurry, 2008).

Aerosol particle charging is a combined effect of the transport of ions to the surface of the particle and a charge transfer reaction between the two entities. For particles above 0.5 nm in size, the charge transfer reaction can be considered to be independent of chemical interactions (Premnath *et al.*, 2011) and observed to take place

with near certainty and the charging kinetics depend solely on the physical transport of ions to the particle surface. The surface flux of ions onto the particle is determined by the combined effect of advection of ions by a carrier gas flow; electro-kinetic motion induced by the presence of an external electric field as well as long range potential interactions between particles and ions; and finally due to Brownian diffusion of the ions. (In practical aerosol chargers, the concentration of ions of the order of 10^{13} per cubic meter and gas molecule concentrations are of the order of 10^{25} per cubic meter. It is safe to assume that, in the analysis of charging dynamics ion-ion interactions are very improbable and the space charge effect in such instances can be neglected in the analysis of ion transport to particle surfaces) In the case of nanometer sized aerosol particle systems at atmospheric pressure, the effect of advection of ions, unless carrier gas flows at speeds comparable to the speed of sound or higher are employed, is negligible due to the small length scales associated with the particles. Ion diffusion is the dominant mechanism in the atmosphere and in chargers designed for aerosol particles that do not rely on an external electric field (Romay *et al.*, 1991; Adachi *et al.*, 1992; Wiedensohler *et al.*, 1994; Chen & Pui, 1999; Hernandez-Sierra *et al.*, 2003; Qi *et al.*, 2007). Thus, diffusion charging has received considerable attention and has been the subject of numerous investigations from the perspective of aerosol systems (Bricard, 1962; Fuchs, 1963; Brock, 1966; Gentry, 1972; Marlow & Brock, 1975a; Lushnikov & Kulmala, 2004b; Gopalakrishnan & Hogan, 2012) and also by researchers in the field of plasma science (Gentry & Brock, 1967; Goree, 1994; Lushnikov & Kulmala, 2004a, 2005; Khrapak *et al.*, 2006; Gatti & Kortshagen, 2008; Khrapak & Morfill, 2009).

1.2. Diffusion Charging of Spherical Aerosol Particles

The vast amount of literature accumulated on the topic is evidence to both the importance and the complexity of diffusion charging. Aerosol systems, by virtue of their typical size ranges, fall in the transition regime of mass transfer (Gopalakrishnan & Hogan, 2012) between the continuum (Gunn, 1955; Keefe, 1959; Pollak & Metnieks, 1962; Lawless, 1996) and free molecular regimes (Mott-Smith & Langmuir, 1926; Allen,

1992). This presents a complexity in handling the motion of ions as they exhibit both bulk as well as individual behavior. The limiting sphere model pioneered by Bricard (1962) and by Fuchs (1963) and later derived independently by D'yachkov and coworkers (D'yachkov *et al.*, 2007), and other similar approaches (Gentry, 1972; Lushnikov & Kulmala, 2004b), deal with this intermediate nature of ion motion by dividing the space around the particle into two zones – far away from the particle, the ion moves diffusively and in close proximity (within a certain distance from the center of the particle, known as the limiting sphere), the ion moves in deterministic trajectories without any intermediate collisions, driven purely by electrostatic force and the kinetic energy with which it entered the limiting sphere. The continuum flux of ions to the surface of the limiting sphere is matched to the free molecular flux at the limiting sphere surface and the resulting equation is solved for the flux of ions onto the particle surface. It was later realized that, the ions do not strictly undergo free molecular motion within the limiting sphere and that they undergo finite number of collisions with gas molecules or other ions and this can drastically alter their rate of transport to the particle surface. In order to address this situation, corrections were made to the limiting sphere model to account for ion recombination reactions (Hoppel & Frick, 1986). First order corrections were made to the theory, thus making it more closer to being exact but it is understood that higher order corrections can be added (Gatti & Kortshagen, 2008), and in principle up to infinite order. It has also been pointed out that, the limiting sphere theories make some questionable assumptions about the thermodynamic equilibrium of the ions that are initiated on the surface of the limiting sphere (Gopalakrishnan & Hogan, 2012).

Many experimental studies have been conducted to test the theories of diffusion charging in both bipolar and unipolar ion environments. The charge fraction of particles of a given size can be obtained from bipolar charging experiments and can be compared with theoretical predictions by solving population balance equations (see for example Adachi et al. (1985)) with knowledge about the mass and mobility values of the ions produced from atmospheric air via ionization (Kilpatrick, 1971; Mohnen, 1977; Steiner & Reischl, 2012), commonly by the radiation generated by radioactive sources such as Po-210, Am-241, Kr-85 or Ni-63. The fraction of uncharged (see for example Pui et al.

(1988)), the mean charged acquired by the particles of a given size (see for example Liu and Pui (1977)), can be obtained from unipolar charging experiments and can be compared with theoretical predictions with knowledge about the ion mass and mobility values as well as the parameter characterizing the exposure of the particles to the ions, known as $N_{ion}t$ product for a given charger, N_{ion} being the ion concentration in the charger and t is the residence time of the particles in the charger.

Measurements made in the size range of 100 nm or more (Nolan & Kennan, 1949; Pollak & Metnieks, 1962; Liu & Pui, 1974, 1977; Kojima, 1978) agree well with the predictions of the Boltzmann charge distribution derived for diffusion charging in the continuum regime (Gunn, 1955; Keefe, 1959; Gentry & Brock, 1967; Lawless, 1996). Measurements in the size range of 5-100 nm (Hussin *et al.*, 1983; Reischl *et al.*, 1983; Wiedensohler *et al.*, 1986) show substantial deviation from the Boltzmann charge distribution agree better with the limiting sphere model (Fuchs, 1963). Later works by Wiedensohler and coworkers, Reischl and coworkers (Wiedensohler & Fissan, 1988, 1990, 1991; Reischl *et al.*, 1996) note that the measured charge distributions are increasingly deviant from the limiting sphere theory predictions in gases other than air (high purity argon and nitrogen), at elevated temperatures and at particles sizes less than about 20 nm. Also, the key parameters in obtaining charge fraction predictions from theory (i.e.) the mass and electrical mobility values of the ions are taken from previously published data (Wellisch, 1909; Kilpatrick, 1971; Mohnen, 1977) or obtained by fitting experimentally inferred ion-particle combination coefficients and corresponding theoretical predictions. Thus, it can be argued that experiments in which the ion properties were not independently measured cannot rigorously test charging theories. It has been noted that the uncertainty in the ion properties can lead to incorrect inferences about the ability of the theory to correctly explain experimentally observed charge fractions (Wiedensohler & Fissan, 1991; Reischl, et al., 1996). Another aspect of ion mass and mobility determination is that, the measured distributions are quite complex (Steiner & Reischl, 2012) and the effect of the same on the measured charge fractions is yet to be investigated, as it is not available at this point.

Further, charging measurements made in dusty plasmas reveal that at high values of ion mean persistence path to particle diameter ratios, where the charging process is expected to be near free molecular rather than being near continuum, substantial differences are seen between charging theories (Khrapak, et al., 2006; D'yachkov, et al., 2007; Gatti & Kortshagen, 2008) and experiment (Khrapak *et al.*, 2005). In summary, it can be understood that the analysis of diffusion charging is still an open problem, given the dearth of exactness that persists in the theories after decades since the first attempts were made and the need for design of experiments that will push the theory in areas where it is likely to have made questionable assumptions.

1.3. Effect of Particle Morphology on Diffusion Charging of Aerosol Particles

Advances in the synthesis and usage of novel shaped nanomaterials have generated interest in developing methods to produce them efficiently in aerosol reactors in a clean and scalable pathway (Pratsinis, 1998; Spicer *et al.*, 1998; Swihart, 2003; Mangolini *et al.*, 2005; Pratsinis, 2010). Particles of diverse shapes such as fractal aggregates, carbon nanotubes and fibers, fullerenes are increasingly used in consumer products as well as specialized applications in the field of aerospace engineering, defense and space travel (http://www.nanotechproject.org). Electrical mobility measurement methods such as Scanning Mobility Particle Spectrometry (Wang & Flagan, 1990) and Ion-Mobility Spectrometry (Makela *et al.*, 1996; Kulkarni & Wang, 2006; Olfert *et al.*, 2008) are increasingly used for online diagnostics of aerosol reactors (Unrau *et al.*, 2007a). The charge distribution of the particles as they enter the mobility classifier is needed to solve for the mobility distribution from a finite set of measured signal intensity (particle counts or electrometer current) as a function of applied classifier voltage (Knutson & Whitby, 1975a, 1975b; Stolzenburg & McMurry, 2008). Thus, there is growing interest to understand the diffusion charging characteristics of non-spherical particles. A few

theoretical approaches (Laframboise & Chang, 1977; Wen *et al.*, 1984a; Mayya, 1990a; Han *et al.*, 1991; Han & Gentry, 1993; Filippov, 1994) and computational studies (Cheng & Yeh, 1981; Han & Gentry, 1994; Biskos *et al.*, 2004) have been undertaken. The theoretical approaches undertaken so far cater to only special shapes (spheroids, cylinders and linear aggregates) and do not offer themselves for extension to all conceivable shapes easily. Also, many of them are applicable only in the continuum limit and there is a need for a viable theory in the transition regime where most charging processes take place.

Measurements on soot agglomerates (Maricq, 2008) show that the soot agglomerates acquire 10% more charges than mobility equivalent spheres in the range of 50 nm and acquire 15% less charges than mobility equivalent spheres in the range of 400 nm as the soot particles become more compact and closer to a sphere (approaching fractal dimension of 3). Rogak and Flagan (1992a) have measured the neutral fractions in soot agglomerates to be 5% lower than mobility equivalent spheres in the range of 100-800 nm. Measurements done using single walled carbon Nanotubes of mobility diameters in the range of 100-1000 nm (Kulkarni *et al.*, 2009) show that the measured neutral fraction is 30-53% lower than that of mobility equivalent spheres. This translates as higher fractions of singly, doubly and other charge states for the particle population. These measurements clearly show that particle morphology has a significant effect on charging that is not accurately explained by existing theories (Keefe, 1959; Fuchs, 1963; Laframboise & Chang, 1977; Wen, et al., 1984a). It should also be noted that, the uncertainty in ion properties that is found in the experiments done with spheres, holds true with these measurements also. Measurements of unipolar charging made with fractal aggregates (Yu *et al.*, 1987; Ntziachristos *et al.*, 2004; Oh *et al.*, 2004; Biskos *et al.*, 2005; Jung & Kittelson, 2005) show that more open structured particles acquire more charges on average than spheres of the same mobility diameter. These measurements cannot be interpreted directly using a theory derived for spheroidal or cylindrical particles and thus call for a more inclusive approach to modeling that can handle complex aggregates as well.

1.4. Topics of this dissertation

In Chapter 2, using scaling analysis and a Brownian Dynamics calculation procedure to obtain a transition regime collision kernel expression is described and the results of the same are compared with the predictions of existing approaches in the literature. From this comparison, it is seen that the approach presented here produced results that are consistent with other approaches and is simple to use. In subsequent chapters, the approach is extended to include complexities in particle shape and interaction potentials. Chapter 3 deals with hard sphere collisions between a point mass (for e.g. a vapor molecule) and an arbitrary shaped particle. Test geometries consisting of point contacting spheres are used to demonstrate that the expression derived in Chapter 2 is accurate in this case as well by identifying two critical length scales – one each in the continuum and free molecular regimes.

The effect of long range potentials is investigated in Chapter 4, wherein Coulombic interactions between a point mass (for e.g. an ion) and a spherical particle is considered. The assumptions behind flux matching theories are re-visited by comparing collision kernels calculated using Brownian Dynamics simulations. Along those lines, in Chapter 5, long range repulsive interactions between point masses and a particle of arbitrary shape are studied and it is shown that a closed form solution for the unipolar charging of aerosol particles can be derived. To tackle the problem of bipolar diffusion charging, due to the issues discussed in detail in Chapter 6, an approach to calculate the steady state charge distribution of particles without directly solving population balance equations using collision kernels is developed. This method is used to understand the effect of shape and material (dielectric) on the charging characteristics of particles. In addition, the method is also capable of handling arbitrary ion mass-mobility distributions, whose effect is also investigated.

A secondary, yet important study to verify a transition regime drag law for non-spherical particles published by Zhang et al. (2012) is undertaken so as to facilitate characterization of nonspherical particles using the DMA. For this purpose, the electrical

mobility of moderate to high aspect ratio cylindrical nanoparticles are measured and compared to theoretical predictions (Chapter 7). To provide at least limited experimental validation of the approaches proposed in this thesis, bipolar diffusion charging experiments are conducted, again using spherical and cylindrical particles. The experimentally observed charge distributions are compared to the predictions of the BD approach developed in Chapter 6, as described in Chapter 8. Finally, the conclusions and recommendations for future work are discussed in Chapter 9. Each chapter begins with an overview of the entire chapter in a few sentences, followed by an introduction to the topic comprising of a review of the literature and a concise lay of the reminder of the chapter. Theoretical/Experimental methods are subsequently presented followed by a detailed discussion of the results obtained. The conclusions drawn from each study are summarized at the end of each chapter. Instances where parts of the text and figures were published in peer reviewed journals are noted as foot notes.

Chapter 2: Transition Regime Collision Kernel determination using Mean First Passage Time Calculations[1]

In this chapter, a transition regime collision kernel for hard spheres interactions between sphere-sphere and sphere-point mass is derived. The validity of the calculation technique is assessed by inter-comparison with other methods from the literature. Collision kernel calculations in subsequent chapters are built on the methods developed here.

2.1. Introduction

The growth and modification of particles in the gas-phase by thermally driven collisions between particles (coagulation), particles and molecular clusters, particles and vapor molecules (condensation/surface growth), particles and gas phase ions (diffusion charging) play critical roles in a number of aerosol processes, including new particle formation in the atmosphere (Kuang *et al.*, 2009a) and nanomaterials synthesis (Gurav *et al.*, 1993; Swihart, 2003). The behavior of these systems is largely governed by the collision rate, R (the number of collisions per unit time per unit volume of aerosol), the calculation of which is simplified by the fact that particles, clusters, ions and vapor molecules are typically found at low volume fractions in the gas-phase. Under such dilute conditions, collisions can be modeled as two-body interactions wherein thermal motion drives collisions (Narsimhan & Ruckenstein, 1985; Friedlander, 2000), and the collision rate is given as:

$$R = \beta n_i n_j \tag{1}$$

where n_i is the number concentration of particles of type i (of a specific size), n_j is concentration of particles/clusters/ions/vapor molecules of type j, and β is the collision kernel/collision rate coefficient for collisions between type i and type j entities.

[1] Aspects of the results described in this chapter (including some text and figures) have been published in Gopalakrishnan & Hogan (2011)

Accurate calculation of collision rates thus requires accurate calculation of β. When the radius of at least one object is large relative to the mean persistence distance of the colliding entities (Rader, 1985), the continuum approximation is satisfied and Smoluchowski's β applies (Chandrasekhar, 1943; Given *et al.*, 1997), which is given as:

$$\beta = 4\pi\left(\frac{kT}{f_i} + \frac{kT}{f_j}\right)\left(a_i + a_j\right) \tag{2}$$

for collisions between entities of type i and type j, where, f_i and f_j are the friction factors of type i and type j entities, respectively, with $f_i = kT/D_i$, D_i is the diffusion coefficient defined appropriately for the entity i, a_i and a_j are the radii of type i and type j entities, respectively, k is Boltzmann's constant (1.38×10^{-23} J K^{-1}), and T is the temperature of the colliding entities and background gas. Conversely, for moving hard-spheres with radii which are small relative to the mean persistence distance, the free molecular approximation applies, and from kinetic theory the collision kernel is given as (Vincenti & Kruger, 1975):

$$\beta = \left(a_i + a_j\right)^2\left(\frac{8\pi kT}{\mu_{ij}}\right)^{1/2} \tag{3}$$

with $\mu_{ij} = m_i m_j/(m_i+m_j)$ (the reduced mass), where m_i and m_j are the masses of entities i and j, respectively. While both equations (2) and (3) apply exactly in the continuum and free molecular limits, respectively, aerosol particles in atmospheric pressure environments typically have radii ranging from tens to hundreds of nanometers. In this 'transition regime' (Brock, 1966; Sitarski & Nowakowski, 1979) the continuum and free molecular collision models break down. Two types of transition regime collisions have generally been examined: those between aerosol particles and low mass vapor molecules, and collisions between two aerosol particles. In the former, the vapor molecule to gas molecule mass ratio, Z, is often taken as zero (Li & Davis, 1996), and the motion of the particle relative to the vapor molecule is neglected. Conversely, in the latter, the motion of both particles is considered, and Z is considered large ($Z \rightarrow \infty$). In examining $Z \rightarrow 0$ collisions, Fuchs (1934, 1959, 1964) first proposed the "limiting sphere model", in which distant from the particle, a vapor molecule/cluster moves diffusively (as in a continuum) but when the distance between the vapor molecule/cluster and particle is less than a

critical value Δ_F, it moves ballistically (as in a vacuum). Although this approach results in an analytical expression for β, Δ_F remains as a free parameter, which precludes β calculation without additional information. As an alternative, Fuchs & Sutugin (1970) later interpolated Sahni's (1966) solution to the Boltzmann equation for neutron absorption by a black body, giving an expression for β for all ratios of the colliding entities' persistence distance to particle radius. Collision kernel expressions for particle collisions with small entities have also been proposed by Loyalka (1973, 1982), Seaver (1984), and Sitarski & Nowakowski (1979). Experimental measurements (Davis & Ray, 1978; Ray *et al.*, 1979; Li & Davis, 1996) (of evaporation, the reverse process) show reasonable agreement with these expressions in the transition regime, with particularly good agreement with the Fuchs-Sutugin expression; thus, it is the most widely used expression to describe particle-vapor molecule collisions (Kuang, et al., 2009a). Similarly, Fuchs (1964) has used physical arguments to develop an expression for β for collisions between particles in the $Z \rightarrow \infty$ limit, with several other researchers likewise developing expressions for the particle-particle collision kernel (Sitarski & Seinfeld, 1977; Dahneke, 1983; Sahni, 1983; Veshchunov, 2010). Fuchs's particle-particle collision expression remains the most widely used for β calculation in this instance as well, based upon reasonable agreement with experimental measurements (Chatterjee *et al.*, 1975; Wagner & Kerker, 1977; Shon *et al.*, 1980; Szymanski *et al.*, 1989; Kim *et al.*, 2003).

With few exceptions (Chernyak, 1995; Gutsch *et al.*, 1995; Heine & Pratsinis, 2007; Azarov & Veshchunov, 2010; Veshchunov, 2010), there has been little recent focus on better understanding both $Z \rightarrow 0$ and $Z \rightarrow \infty$ thermally driven collision processes. Nonetheless, there are several reasons for further examination of the transition regime collision kernel. First, collision kernel expressions have been sparingly compared to results of Brownian dynamics simulations (Trzeciak *et al.*, 2004; Madler *et al.*, 2006; Heine & Pratsinis, 2007), and when comparison has been performed (Nowakowski & Sitarski, 1981; Narsimhan & Ruckenstein, 1985), it has been limited to collisions between identical sized particles, or led to poor agreement with the unambiguous free

molecular and continuum limiting expressions (Gutsch, et al., 1995). With recent advances in computational capabilities, Brownian dynamics simulations can accurately predict thermally driven particle-particle collision rates (the $Z \rightarrow \infty$ limit); hence they should be able to provide a means for more detailed examination of collision kernel expressions than is possible with currently available experimental approaches. Second, various authors have used different definitions for the mean persistence distance of the colliding entities (Jeans, 1954; Dahneke, 1983; Adachi, et al., 1985; Rader, 1985; Sceats, 1989; Gatti & Kortshagen, 2008), and hence different definitions of the dimensionless parameter (i.e. the ratio of the persistence distance to the collision radius) used to determine whether a collision is continuum, free molecular, or transition regime process. We refer to this parameter as Kn_D, the diffusive Knudsen number (Loyalka, 1976; Dahneke, 1983; Rogak & Flagan, 1992b), which must approach 0 in the continuum limit and approach ∞ in the free molecular limit. The lack of consensus on an appropriate definition of Kn_D has complicated comparisons between different collision rate expressions (Rader, 1985), and therefore comparisons of available collision kernel expressions are sparsely performed. Finally, in examining collision processes, vapor molecule condensation has been examined in a distinctly different manner than has particle-particle coagulation. As noted above, the theoretical basis for this is clear; while aerosol particles are significantly more massive than gas molecules ($Z>>1$), this need not be the case for vapor molecules. However, while the most commonly used collision kernel expression in condensation (the Fuchs-Sutugin kernel) derives from a Boltzmann equation solution in the limit of $Z = 0$, condensing vapor molecules or molecular clusters are often significantly more massive than the surrounding background gas (Li & Davis, 1996), and for these species, the $Z \rightarrow \infty$ collision kernel would be preferred. A single collision kernel should be able to describe both thermally driven condensation and coagulation in the dilute limit as $Z \rightarrow \infty$, as the motion of all entities can be described in a similar manner. Furthermore, the extent to which Z influences the collision kernel can be better understood by comparing kernels inferred with the assumption $Z = 0$ to those inferred as $Z \rightarrow \infty$.

Motivated by these issues, first, an expression for the collision kernel in the $Z \rightarrow \infty$ limit, which converges to the correct continuum and free molecular expressions and, with an appropriate definition of Kn_D, can correctly predict collision kernels in the transition regime is developed. For this purpose mean first passage time calculations (Klein, 1952; Narsimhan & Ruckenstein, 1985), with the assumptions that the colliding entities are dilute in concentration and that the motion of colliding entities is accurately described by Langevin dynamics (Chandrasekhar, 1943; Sitarski & Seinfeld, 1977; Ermak & Buckholz, 1980; Madler, et al., 2006; Isella & Drossinos, 2010) are used. Further it is shown that transition regime collision kernel is best represented in a non-dimensionalized form which can be predicted with Buckingham Π theorem (Buckingham, 1914, 1915). The second goal of this study is to compare the mean first passage time derived collision kernel expression to previously developed $Z \rightarrow 0$ and $Z \rightarrow \infty$ expressions. In doing so, it is shown that all examined collision kernel expressions can also be written in this non-dimensionalized form, and that are all in good agreement with the results of first passage calculations, regardless of whether they were derived for low mass vapor molecule condensation, coagulation, or using Fuchs' limiting sphere approach.

2.2. Mean First Passage Time Calculations

2.2.1. Motion in the Transition Regime

To utilize mean first passage time calculations to determine the collision kernel, an appropriate model of the motion of colliding entities is necessary. This model is first described, followed by a description of the mean first passage time calculation procedure. We assume that for a dilute, hard sphere, $Z \rightarrow \infty$ entity surrounded by a homogenous bath gas under isothermal conditions, motion is well described by a Langevin equation (Chandrasekhar, 1943), given as:

$$m_i \frac{d\vec{v}_i}{dt} = -f_i \vec{v}_i + \vec{X}(t) \tag{4a}$$

where $\vec{v}$ is the velocity vector of the diffusing entity, and $\vec{X}(t)$ is the "effective diffusion force", which is a time varying, Gaussian distributed vector with the following properties:

$$\left\langle \vec{X}(t) \right\rangle = 0 \qquad \left\langle \vec{X}(t)\vec{X}(t') \right\rangle = 6 f_i kT\delta(t-t') \tag{4b}$$

Use of the Langevin equation restricts the presented analysis to situations where the time required for entities to collide is significantly longer than the characteristic time of motion, thus allowing separation of the drag force and the fluctuating diffusion force acting on moving entities in the force balance equation. Fortunately, most realistic aerosol systems are sufficiently dilute in concentration for this criterion to hold valid. Solutions to (4) were developed by Ermak and Buckholtz (Ermak & Buckholz, 1980), with which the velocity vector, $\vec{v}$, and position vector, $\vec{x}$, at any time $t+\Delta t$ can be predicted, provided that the velocity and position are known at the previous time, t, and that moving entity has a known mass and diffusion coefficient/friction factor. For hard sphere entities this solution can be expressed by the equations:

$$\vec{v}_i(t+\Delta t) = \vec{v}_i(t)\exp\left(-\frac{f_i}{m_i}\Delta t\right) + \vec{B}_1 \tag{5a}$$

$$\vec{x}_i(t+\Delta t) = \vec{x}_i(t) + \frac{m_i}{f_i}\left(\vec{v}_i(t+\Delta t) + \vec{v}_i(t)\right)\left(\frac{1-\exp\left(-\frac{f_i}{m_i}\Delta t\right)}{1+\exp\left(-\frac{f_i}{m_i}\Delta t\right)}\right) + \vec{B}_2 \tag{5b}$$

$$\left\langle \vec{B}_1{}^2 \right\rangle = \left(\frac{3kT}{m_i}\right)\left(1-\exp\left(-2\frac{f_i}{m_i}\Delta t\right)\right) \tag{5c}$$

$$\left\langle \vec{B}_2{}^2 \right\rangle = \left(\frac{6kTm_i}{f_i{}^2}\right)\left(\frac{f_i}{m_i}\Delta t - 2\left(\frac{1-\exp\left(-\frac{f_i}{m_i}\Delta t\right)}{1+\exp\left(-\frac{f_i}{m_i}\Delta t\right)}\right)\right) \tag{5c, contd.}$$

where $\vec{B}_1$ and $\vec{B}_2$ are Gaussian distributed random vectors with zero means and variances defined by (5c).

2.2.2. Simulation Procedure

A number of previous studies have used the Langevin equation to examine transition regime collisions (Nowakowski & Sitarski, 1981; Gutsch, et al., 1995; Trzeciak, et al., 2004; Heine & Pratsinis, 2007; Isella & Drossinos, 2010). For our calculations, we build upon the methods of Narshiman & Ruckenstein (Narsimhan & Ruckenstein, 1985), who were the first to note that in examining dilute systems, only the motion of two colliding entities need be considered, as opposed to a large multi-entity computational domain. The calculations described in this chapter are later extended to include complexities in particle shape and interaction potentials. In aerosol systems at thermal equilibrium, a large number of aerosol particles and vapor molecules are dispersed within a background gas. Assuming that initially there are no concentration gradients of particles or vapor molecules within this medium, the collision and subsequent sticking of two entities reduces the local particle/vapor molecule concentration, such that the probability of a collision occurring within the same region of space is reduced as compared to regions where a collision has not occurred. In a sufficiently dilute system, prior to any further collisions, aerosol particles and vapor molecules will again redisperse themselves via thermal motion such that no concentration gradients exist within the medium, hence the probability of collision is spatially uniform at all times. The simplification to monitor the motion of only two bodies applies only in this instance. Combined with the prior restriction arising from use of the Langevin equation, the calculations and theoretical expressions developed in this thesis thus only apply when the characteristic time of particle/vapor molecule motion is faster than the characteristic time for particle mixing, which in turn must be faster than the time for collision. Again, with the exception of highly concentrated aerosol systems (Heine & Pratsinis, 2007), this assumption is reasonable for most systems studied experimentally. We also note that the assumption of homogenously distributed particles and vapor molecules differs from the assumption traditionally made in analyzing continuum regime collisions, i.e. that concentration gradients of particles and vapor molecules exist at

steady state, driving the flux of particles and vapor molecules to a collector particle surface (Chandrasekhar, 1943; Friedlander, 2000). However, as shown by Veschunov (2010), in the continuum limit, analysis via the steady-state flux approach (the diffusion regime) and of dilute, homogenously distributed systems (the kinetic regime) lead to matching functional forms of the continuum regime collision kernel. For this reason, mean first passage time calculations and related Brownian Dynamics algorithms can and have been successfully employed to determine diffusion-limited reaction rates in the continuum regime (Klein, 1952; Northrup *et al.*, 1984; Northrup *et al.*, 1986; Douglas *et al.*, 1994; Given, et al., 1997), and are employed here for rate determination in the continuum, transition, and free molecular regimes.

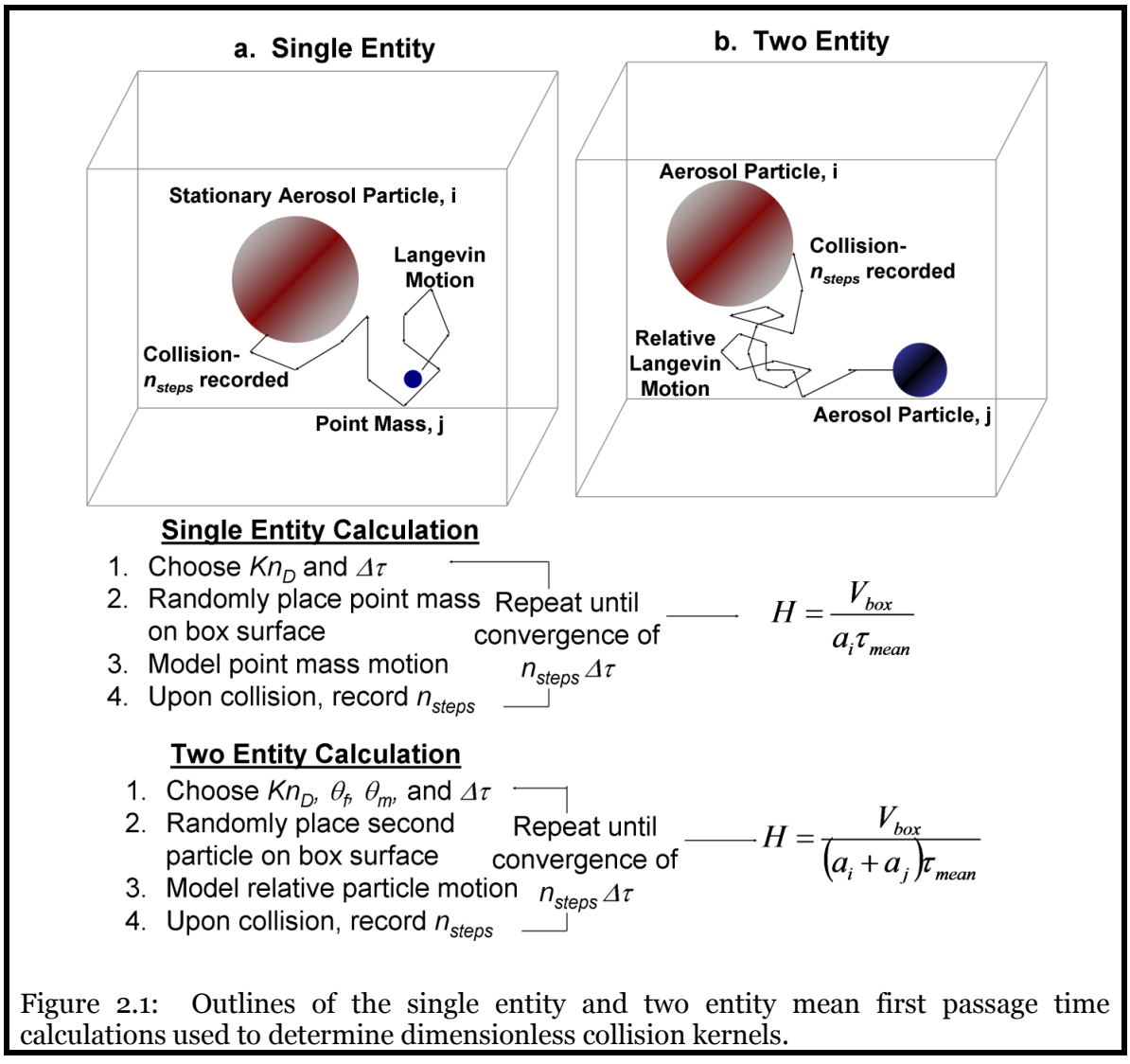

Figure 2.1: Outlines of the single entity and two entity mean first passage time calculations used to determine dimensionless collision kernels.

Two types of mean first passage time calculations are performed in this work. First, collisions in which one entity is considerably less massive and faster than the other are examined, which represent collisions between a heavy vapor molecule or molecular cluster and a particle. In this case the radius, mass, and friction factor of the particle are >> than that of the vapor molecule/cluster; thus particle motion is negligible, and moving vapor molecule/cluster may be treated as a point mass (assuming densities are identical for both entities). Figure 2.1a shows a simple depiction of this mean first passage time calculation, which we henceforth refer to as the single entity calculation. A spherical particle of radius a_i is placed in the center of a square box with a side length of $50a_i$ and periodic boundary conditions. A single moving point mass of zero radius but non-zero f_j and m_j is also placed at a random location on the surface of the box, and a given a random velocity sampled from a Maxwell-Boltzmann distribution (Vincenti & Kruger, 1975) (at the specified temperature). To move the point mass in the simulation domain, we first non-dimensionalize equations (5a-c) by defining $\Delta\tau = (f_j/m_j)\Delta t$, $\vec{v}^* = \left(m_j / f_j\right)\left(\vec{v}/a_i\right)$, and $\vec{x}^* = \vec{x}/a_i$, where i denotes the immobile particle and j denotes the moving point mass, which gives:

$$\vec{v}_j^{\,*}(\tau+\Delta\tau) = \vec{v}_j^{\,*}(\tau)\exp(-\Delta\tau) + \vec{A}_1 \tag{6a}$$

$$\vec{x}_j^{\,*}(\tau+\Delta\tau) = \vec{x}_j^{\,*}(\tau) + \left(\vec{v}_j^{\,*}(\tau+\Delta\tau) + \vec{v}_j^{\,*}(\tau)\right)\left(\frac{1-\exp(-\Delta\tau)}{1+\exp(-\Delta\tau)}\right) + \vec{A}_2 \tag{6b}$$

$$\left\langle \vec{A}_1{}^2 \right\rangle = 3Kn_D^2\left(1-\exp(-2\Delta\tau)\right) \tag{6c}$$

$$\left\langle \vec{A}_2{}^2 \right\rangle = 6Kn_D^2\left(\Delta\tau - 2\left(\frac{1-\exp(-\Delta\tau)}{1+\exp(-\Delta\tau)}\right)\right) \tag{6c, contd.}$$

$\vec{A}_1$ and $\vec{A}_2$ are dimensionless vectors, which, like $\vec{B}_1$ and $\vec{B}_2$, are Gaussian distributed random vectors with zero means and variances defined by (6c). Through this non-dimensionalization we also find that $Kn_D = (kTm_j)^{1/2}/(f_j a_i)$, which we propose to be a simple and appropriate form for Kn_D in the limit where one entity moves significantly faster than its collision partner. It is apparent from (6a-6c) that calculated trajectories are dependent on the parameters Kn_D and $\Delta\tau$. We are only interested in results where $\Delta\tau \to 0$,

i.e. a sufficiently small time step is needed to ensure correct simulation results. The criteria $\Delta\tau \leq 0.005 Kn_D^{-2}$ is found sufficient to mitigate any influence of time step in all simulations. With $\Delta\tau$ selected for a given Kn_D, equations (6a-6c) are used to monitor the motion of the point mass until it collides with the particle. Upon collision, the number of timesteps required for collision, n_{steps} is recorded. A new point mass is subsequently placed randomly on the surface of the simulation box, at which time the collision simulation is repeated. After N collisions are simulated, the dimensionless mean first passage time τ_{mean} is calculated as:

$$\tau_{mean} = \frac{1}{N}\sum_{i=1}^{N} n_{steps}\Delta\tau \tag{7a}$$

from which the dimensionless collision rate, H, is calculated as:

$$H = \frac{V_{box}}{a_i^3 \tau_{mean}} \tag{7b}$$

where V_{box}/a_i^3 is the normalized size of the simulation box (50^3). We note that for convergence of the mean first passage time to the correct value, a sufficiently large simulation domain must be used. Furthermore, with a sufficiently large simulation domain and periodic boundary conditions, equivalent results are found regardless of whether the point mass is initiated within the domain volume or on the domain surface (see calculation results in the supplementary information). For each selected Kn_D, successive collisions are monitored, and after each collision, τ_{mean} is calculated. Each simulation is stopped once the standard deviation on τ_{mean} is less than 1% of its average value over the past 200 collisions. This generally leads to each τ_{mean} calculation requiring simulation of 500-1200 collisions. For H determination, each calculation is, in turn, repeated 10 times. In total, 5,000 – 12,000 collisions per calculated value are used, with a relative standard deviation of ~3-5% and 12-24 hours of computation time required per value reported.

The second set of mean first passage time calculations mimics particle-particle collisions, (Figure 2.1b), in which the motion of both colliding entities is monitored. As two equations of motion are needed, we refer to this calculation as the two entity

calculation. Equations are again solved in a dimensionless fashion, with $\Delta\tau = (f_{ij}/\mu_{ij})\Delta t$, $\vec{v}_{i,j}^{\,*} = \left(\mu_{ij} / f_{ij}\right)\left(\vec{v}_{i,j}/\left[a_i + a_j\right]\right)$, and $\vec{x}_{i,j}^{\,*} = \vec{x}_{i,j}/\left(a_i + a_j\right)$, where $f_{ij} = f_i\, f_j/(f_i+f_j)$ is the reduced friction factor. This normalization gives the following two solutions for the motions of particles type *i* and type *j*:

$$\vec{v}_i^{\,*}(\tau+\Delta\tau) = \vec{v}_i^{\,*}(\tau)\exp\left(-\frac{\theta_m}{\theta_f}\Delta\tau\right) + \vec{D}_{1,i} \tag{8a}$$

$$\vec{x}_i^{\,*}(\tau+\Delta\tau) = \vec{x}_j^{\,*}(\tau) + \frac{\theta_f}{\theta_m}\left(\vec{v}_i^{\,*}(\tau+\Delta\tau) + \vec{v}_i^{\,*}(\tau)\right)\left(\frac{1-\exp\left(-\frac{\theta_m}{\theta_f}\Delta\tau\right)}{1+\exp\left(-\frac{\theta_m}{\theta_f}\Delta\tau\right)}\right) + \vec{D}_{2,i} \tag{8b}$$

$$\left\langle \vec{D}_{1,i}{}^2 \right\rangle = 3\theta_m Kn_D^2\left(1-\exp\left(-2\frac{\theta_m}{\theta_f}\Delta\tau\right)\right) \tag{8c}$$

$$\left\langle \vec{D}_{2,i}{}^2 \right\rangle = 6\frac{Kn_D^2\theta_f^2}{\theta_m}\left(\frac{\theta_m}{\theta_f}\Delta\tau - 2\left(\frac{1-\exp\left(-\frac{\theta_m}{\theta_f}\Delta\tau\right)}{1+\exp\left(-\frac{\theta_m}{\theta_f}\Delta\tau\right)}\right)\right) \tag{8c, contd.}$$

$$\vec{v}_j^{\,*}(\tau+\Delta\tau) = \vec{v}_j^{\,*}(\tau)\exp\left(-\frac{(1-\theta_m)}{(1-\theta_f)}\Delta\tau\right) + \vec{D}_{1,j} \tag{8d}$$

$$\vec{x}_j^{\,*}(\tau+\Delta\tau) = \vec{x}_j^{\,*}(\tau) + \frac{1-\theta_f}{1-\theta_m}\left(\vec{v}_j^{\,*}(\tau+\Delta\tau) + \vec{v}_j^{\,*}(\tau)\right)\left(\frac{1-\exp\left(-\frac{(1-\theta_m)}{(1-\theta_f)}\Delta\tau\right)}{1+\exp\left(-\frac{(1-\theta_m)}{(1-\theta_f)}\Delta\tau\right)}\right) + \vec{D}_{2,j} \tag{8e}$$

$$\left\langle \vec{D}_{1,j}{}^2 \right\rangle = 3(1-\theta_m)Kn_D^2\left(1-\exp\left(-2\frac{(1-\theta_m)}{(1-\theta_f)}\Delta\tau\right)\right) \tag{8f}$$

$$\left\langle \vec{D}_{2,j}{}^2 \right\rangle = 6\frac{Kn_D^2(1-\theta_f)^2}{(1-\theta_m)}\left(\frac{(1-\theta_m)}{(1-\theta_f)}\Delta\tau - 2\left(\frac{1-\exp\left(-\frac{(1-\theta_m)}{(1-\theta_f)}\Delta\tau\right)}{1+\exp\left(-\frac{(1-\theta_m)}{(1-\theta_f)}\Delta\tau\right)}\right)\right) \tag{8f, contd.}$$

where $Kn_D = \frac{\sqrt{kT\mu_{ij}}}{f_{ij}\left(a_i + a_j\right)}$ is the diffusive Knudsen number for the two entity calculation, $\theta_m = m_j/(m_i+m_j)$ and $\theta_f = f_j/(f_i+f_j)$. In two entity calculations, equations (8a-f) are used to monitor the motion of both particles, with the motion of particle *i* superimposed onto particle *j* such that particle *i* remains stationary in the simulation domain (though all equations are used in simulations without simplification). To initialize each simulation, particle *i* is placed at the center of the simulation domain, while particle *j* is placed at a random location on the domain surface. A specific set of values of Kn_D, θ_m, and θ_f is used for each simulation. As with single entity calculations, $\Delta\tau \leq 0.005Kn_D^{-2}$, while the side length of the simulation box size is $L_1(a_i+a_j)$, where L_1 ranges from 10 to 40, with smaller values of L_1 generally used at higher Kn_D. After N trials the dimensionless collision rate is calculated as:

$$H = \frac{V_{box}}{\left(a_i + a_j\right)^3 \tau_{mean}} \tag{9}$$

Identical convergence criteria are used for two entity calculations as are for single entity calculations, again with 500-1200 collisions necessary for each τ_{mean} calculation and 10 τ_{mean} calculations used for each reported value.

2.3. Results and Discussion

2.3.1. Non-Dimensionalized Collision Kernels

Non-dimensionalization of the Ermak & Buckholtz solution suggests that the dimensionless collision kernel, H, is dependent upon Kn_D for the single entity system and upon Kn_D, θ_m, and θ_f for the two entity system. With dimensional analysis we can gain further insight into the correct functional form for the transition regime collision kernel. From equations (2) and (3), it is apparent that the collision kernel when a single entity of negligible radius is moving depends upon the thermal energy, kT, the moving entity

friction factor, f_j, the stationary particle radius, a_i, and the moving entity mass, m_j (note $f_i \rightarrow \infty$, $a_j \rightarrow 0$, and $m_i \rightarrow \infty$ in the single entity limit). These 5 variables form two dimensionless groups, which can be used to fully describe transition regime collisions: H, and Kn_D (as defined for single entity collisions), which are the non-dimensionalizations of β and kT, respectively. The traditional normalization of β/β_c (Fuchs, 1964; Loyalka, 1976; Narsimhan & Ruckenstein, 1985; Veshchunov, 2010) can also follow from dimensional analysis, where β_c is the continuum collision kernel (equation 2) and the second dimensionless number is again Kn_D, but in this system it is the nondimensionalization of m_j. A final approach to scale the collision process is to normalize β by β_{FM}, the free molecular collision rate (equation 3), leading to Kn_D as a nondimensionalization of the friction factor. Here, we elect to use H for the dimensionless collision kernel as opposed to β/β_c or β/β_{FM} as nondimensionalization of the Langevin equations allows for H to be directly determined from mean first passage time calculations, and in both the continuum and free molecular regime, thermal energy drives collisions; hence, β and kT are the most appropriate non-repeating variables in describing the collision process. H can be expressed in terms of the aforementioned variables as:

$$H = \frac{\beta m_j}{f_j a_i^3} \tag{10}$$

By comparing to equations (2) and (3), the following, simple, limiting expressions for H are obtained:

$$H = 4\pi Kn_D^2 \quad \text{as} \quad Kn_D \rightarrow 0 \tag{11a}$$

$$H = \sqrt{8\pi} Kn_D \text{ as} \quad Kn_D \rightarrow \infty \tag{11b}$$

For collision processes with two moving entities, from equations (2) and (3) β is found to be a function of kT, f_i, f_j, m_i, m_j, a_i, and a_j. The description of a system of 8 variables should require 5 dimensionless groups. However, in equations (2) and (3), the following groupings are found: f_i and f_j as f_{ij}, m_i and m_j as μ_{ij}, and a_i and a_j as a_i+a_j. This again reduces the system to 5 variables, which can be described by H and Kn_D, where H is redefined as:

$$H = \frac{\beta \mu_{ij}}{f_{ij}\left(a_i + a_j\right)^3} \tag{12}$$

Kn_D is also redefined with μ_{ij} and f_{ij} substituted for m_j and f_j (as noted in the previous section). The reduction to two dimensionless groups would at first seem at odds with the non-dimensionalization performed for two entity mean first passage time calculations, which leads to H dependent upon Kn_D, θ_m, and θ_f. However, the definitions of type i and type j entities are arbitrary, i.e. $H(Kn_D, \theta_m, \theta_f) = H(Kn_D, 1-\theta_m, 1-\theta_f) = H(Kn_D, \theta_m, 1-\theta_f) = H(Kn_D, 1-\theta_m, \theta_f)$ for $0 < \theta_m < 1$ and $0 < \theta_f < 1$, which suggests (but by no means proves) that H depends upon neither θ_m nor θ_f, although they are still inputs for mean first passage time calculations. As $Kn_D \rightarrow 0$ and $Kn_D \rightarrow \infty$, H for two moving entities is again described by the limiting equations (11a) and (11b), respectively; thus, single moving entity and two moving entities are described by the same collision kernel in the continuum and free molecular limits.

2.3.2. Mean First Passage Time Results

Mean first passage time simulations are performed at varying Kn_D for single entities and at varying Kn_D, θ_m, and θ_f for two moving entities. Calculated H values are shown at varying Kn_D for single and two entity systems in Figures 2.2a and 2.2b respectively. Also shown in both figures are the low and high Knudsen number limiting expressions for H (equations 11a and 11b, dashed gray lines). Tables of results from mean first passage time calculations are given in the supplementary information. In performing two-entity calculations, we have used only θ_m and θ_f values which are realistic for collisions between entities of similar density in the continuum, transition, and free molecular regimes. This leads to a correlation between the examined θ_m and θ_f values, and although this places a restriction on the presented results, in realistic systems dominated by collision growth in which the motion of both colliding entities is important, the colliding entities typically have a similar density (i.e. collisions between a massive small particle and much less massive larger particle are rare). From both figures it is

apparent that (1) H is a single valued function of Kn_D for both types of collisions, and (2) at low and high Knudsen numbers, both shown data sets converge to the appropriate $Kn_D \rightarrow 0$ and $Kn_D \rightarrow \infty$ limits, respectively.

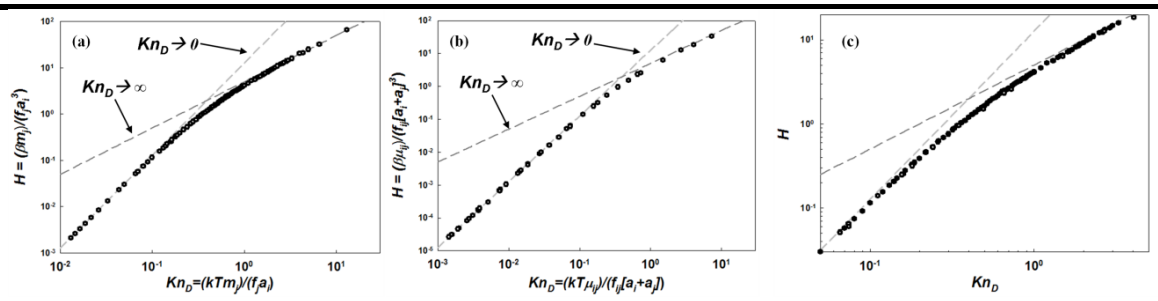

Figure 2.2: The nondimensionalized collision rate, H, for single entity (**a.**) and two entity (**b.**) mean first passage simulations as a function of Kn_D. Gray lines denote the expected limits as $Kn_D \rightarrow 0$ and $Kn_D \rightarrow \infty$. (**c.**) A zoomed in plot of $H(Kn_D)$ in the region $0.05 < Kn_D < 5$. Closed symbols- single entity mean first passage time calculations. Open symbols- two entity mean first passage time calculations.

Figure 2.2c shows a zoomed in plot about the Knudsen number range from 0.05 to 5, with results from both single entity (closed circles) and two entity (open circles) calculations. Although several calculated two entity results are slightly (~3%) lower than single entity results near $Kn_D \approx 1$, the two sets of results collapse to a single curve remarkably well. Overall, these results support predictions made from dimensional analysis, namely, there is a single curve, $H(Kn_D)$, to describe collisions between dilute concentration, transition regime entities in the $Z \rightarrow \infty$ limit.

Table 2.1: A summary of previous developed collision kernels for transition regime condensation and coagulation, expressed in the form $H(Kn_D)$.

Expression	Z restriction	Non-dimensionalized Form
Fuchs-Sutugin (1970)	Z→0	$\boldsymbol{H = \frac{12.566Kn_D^2 + 23.625Kn_D^3}{1 + 3.590Kn_D + 4.712Kn_D^2}}$
Loyalka (1973)	Z→0	$\boldsymbol{H = \frac{12.566Kn_D^2 + 23.695Kn_D^3}{1 + 3.323Kn_D + 4.727Kn_D^2}}$
Fuchs (1964)*	Z→∞	$\boldsymbol{H = \frac{12.566Kn_D^2}{\frac{1}{1 + g'(Kn_D)} + 2.507Kn_D}}$
Dahneke (1983)	Z→∞	$\boldsymbol{H = \frac{12.566Kn_D^2 + 15.749Kn_D^3}{1 + 2.506Kn_D + 3.142Kn_D^2}}$
Veschunov (2010)	Z→∞	$\boldsymbol{H = \frac{12.566Kn_D^2 + 672.83Kn_D^3 + 625.33Kn_D^4}{1 + 51.173Kn_D + 134.59Kn_D^2 + 124.77Kn_D^3}}$
Fuchs (1963)**	Flu Matching	$\boldsymbol{H = \frac{5.013Kn_D}{1 + 0.399j'(Kn_D)}}$
First Paggage Regression (this study)	Z→∞	$\boldsymbol{H = \frac{12.566Kn_D^2 + 25.836Kn_D^3 + 56.204Kn_D^4}{1 + 3.502Kn_D + 7.211Kn_D^2 + 11.211Kn_D^3}}$

* $\boldsymbol{g'(Kn_D) = \frac{4}{3Kn_D} + Kn_D + \frac{Kn_D^2}{6} - \left(\frac{16}{9Kn_D^2} + \frac{4}{3} + \frac{Kn_D^2}{3} + \frac{Kn_D^4}{36}\right)^{\frac{1}{2}}}$

** $\boldsymbol{j'(Kn_D) = \frac{Kn_D}{1.766}\left[\frac{(1+1.329Kn_D)^5}{5} - \frac{(1+1.766Kn_D^2)(1+1.329Kn_D)^3}{3} + \frac{2(1+1.766Kn_D^2)^{5/2}}{15}\right]}$

2.3.3. Comparison to Existing Kernels

Earlier studies of transition regime collisions via Langevin simulations suffered from high statistical variability in the obtained results or made use of a limited number of calculated values (Nowakowski & Sitarski, 1981; Narsimhan & Ruckenstein, 1985; Gutsch, et al., 1995). Due to the small timesteps used in calculations as well as the strict convergence criteria employed, the results obtained in this study do not suffer from the same degree statistical variability as prior work (though some random variations in results from Brownian Dynamics are inevitable). The following collision kernels from the literature, used numerously in investigations of collision governed systems are

compared with the results of mean first passage time calculations: (a) the Fuchs-Sutugin (Fuchs & Sutugin, 1970) expression for the condensation collision kernel in the limit $Z = 0$, (b) Loyalka's condensation collision kernel in the limit $Z = 0$ (Loyalka, 1973), (c) Fuchs's expression (Fuchs, 1964) for the coagulation kernel for which $Z \rightarrow \infty$, (d) Dahneke's expression for the coagulation collision kernel (Dahneke, 1983) with $Z \rightarrow \infty$, (e) the recently developed collision kernel from Veschunov (2010) with $Z \rightarrow \infty$, and (f), the hard-sphere limit of the collision kernel from Fuchs's diffusion charging theory (Fuchs, 1963), which utilizes the limiting sphere concept. For appropriate comparison, each of these expressions is recast in terms of H and Kn_D, shown in Table 2.1. The Fuchs-Sutugin expression (a.), Loyalka's expression (b.), and Dahneke's expression (d.) all fit the general form of:

$$H = \frac{4\pi Kn_D^2 + \sqrt{8\pi} C_1 Kn_D^3}{1 + C_2 Kn_D + C_1 Kn_D^2} \tag{13}$$

where C_1 and C_2 are "tuning" constants for the calculation of the collision rate in the transition regime. Fuchs' coagulation theory and diffusion charging theory similarly contain these tuning constants, embedded into the polynomials $g'(Kn_D)$ and $j'(Kn_D)$, respectively. Figures 3a-e show the quantity $(H_{express}-H_{sim})/H_{sim}$ x 100% as a function of Kn_D for the aforementioned collision kernels, where $H_{express}$ is the dimensionless collision kernel determined from the expression in question, and H_{sim} is the dimensionless collision kernel from mean first passage time calculations. Similarly, H values from each expression are plotted in Figure 2.4 as functions of Kn_D in range $0.3 < Kn_D < 2.5$. Any disagreement between $H_{express}$ and H_{sim} values at low ($Kn_D < 0.01$) and high ($Kn_D > 5$) is a result of statistical variation in calculations, as all expressions for H are set to converge to the appropriate continuum and free molecular limits. As seen in Figure 2.3a-f, there is excellent agreement between existing expressions and meaning first passage time calculations in these limits, with most values falling within +/- 5% of each other. At intermediate Kn_D, good agreement is also found between simulation results (both for single entity and two entity systems) with almost all simulation results within 10% of those predicted by the examined collision kernels. The best agreement is found with the Veschunov coagulation kernel and the Dahneke coagulation kernel, both of which apply

in the $Z \rightarrow \infty$ limit. Successively worse (but still within 10% excluding a single anomalous mean first passage time calculation value) agreement is found with Fuchs' diffusion charging theory kernel, the Loyalka condensation kernel, the Fuchs-Sutugin condensation kernel, and the Fuchs coagulation kernel.

In addition to this comparison, mean first passage time calculations are used to construct a nondimensionalized collision kernel which may be used to predict particle-particle collision rates, and based on the good agreement with the Fuchs-Sutugin and Loyalka curves, also particle-vapor molecule collision rate with reasonable accuracy. Following Veschunov (2010), a four parameter fit of the form is proposed:

$$H = \frac{4\pi Kn_D^2 + C_1 Kn_D^3 + \sqrt{8\pi} C_2 Kn_D^4}{1 + C_3 Kn_D + C_4 Kn_D^2 + C_2 Kn_D^3} \tag{14}$$

which must converge to (11a) and (11b) at high and low Knudsen numbers, respectively, and where C_1, C_2, C_3, and C_4 are tuning constants which describe the transition regime. Nonlinear least squares regression of mean first passage time calculations in the region $0.05 < Kn_D < 2.0$ (the transition regime) gives C_1 =25.836, C_2 = 11.211, C_3 = 3.502, and C_4 = 7.211. Figure 2.3g shows the calculated $(H_{express}-H_{sim})/H_{sim}$ *x 100%* value for this regression equation for all mean first passage time calculations and the resulting equation is plotted in Figure 2.4 with all other expressions. With the exception of several apparent outlier data points, regression calculated H values are within 5% of mean first passage time H values.

Overall, through comparison of mean first passage time calculations to existing collision kernel expressions, it is found that all examined expressions, regardless of the limits imposed during their derivation, are within several percent of mean first passage derived values and of one another across the entire diffusive Knudsen number range. Although the comparisons made by Veschunov (2010) anticipate this agreement, that mean first passage time calculations give rise to a similar collision kernel expression as do other approaches further suggests that a single collision kernel expression can be used to describe collision processes at all Z (both condensation and coagulation) across the

entire Kn_D range, with an accuracy suitable for examination of almost all dilute aerosol systems.

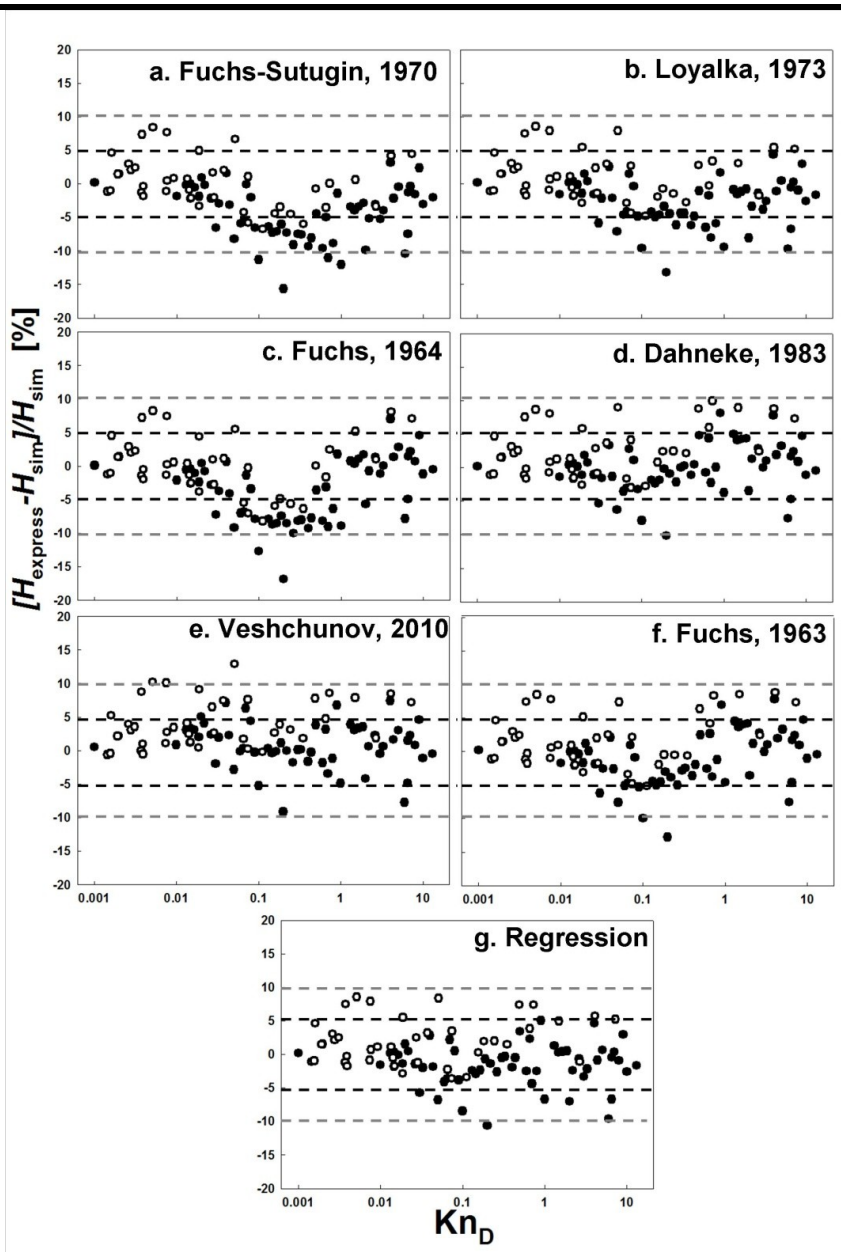

Figure 2.3: Percent deviation of previously developed expressions for the collision kernel as a function of Kn_D. (a.) Fuchs-Sutugin condensation kernel, (b.) Loyalka's condensation kernel, (c.) Fuchs's coagulation kernel, (d.) Dahneke's coagulation kernel, (e.) Veschunov's coagulation kernel, (f.) the hard sphere limit of Fuchs collision kernel, and (g.) the regression equation (14). Closed symbols- single entity mean first passage time calculations. Open symbols- two entity mean first passage time calculations. Black guide lines are marked at +/- 5% deviation, and gray guidelines are marked at +/-10% deviation.

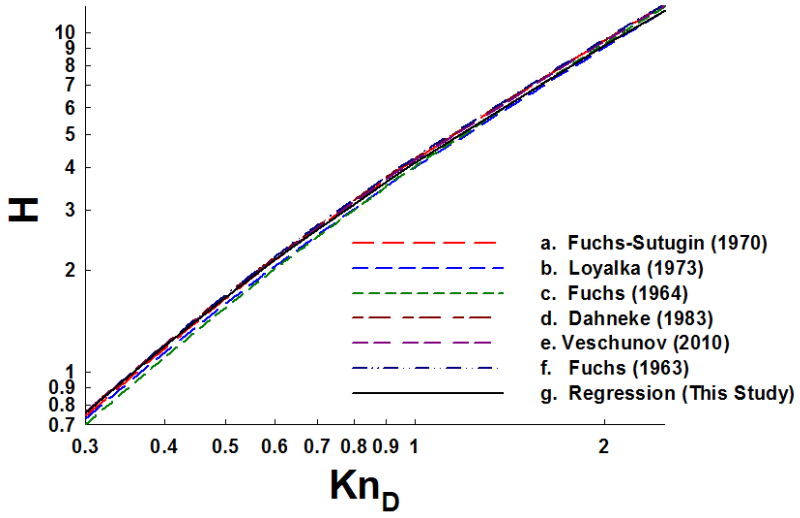

Figure 2.4: Comparison of 6 selected transition regime collision kernels (2 derived for condensation, 3 for coagulation, and the limiting sphere model) to the collision kernel based on regression analysis of mean first passage time calculations.

2.4. Conclusions

The derivation of a transition regime collision kernel based on Mean first passage time calculations coupled with dimensional analysis was described in this chapter. Based upon this work, the following conclusions are derived:

- For hard-sphere, dilute entities whose motion can be described by the Langevin equation, the dimensionless collision kernel, H, can be determined solely as a function of the diffusive Knudsen number, Kn_D. Both H and Kn_D can be derived from non-dimensionalization of the Langevin-based first passage time calculations, as well as by use of traditional dimensional analysis.
- A number of existing expressions for the collision kernel also collapse into the dimensionless functional form $H(Kn_D)$, and are compared to mean first passage time results. The good agreement between all examined kernels and our calculations strongly suggests that a single dimensionless collision kernel can be used to reliably infer both condensation and coagulation rates. Along these lines,

a four parameter fit is developed from first passage time calculations for the collision kernel.

- The determined collision kernel applies rigorously only to hard-sphere, $Z \rightarrow \infty$ entities in the dilute limit, whose friction factors (diffusion coefficients) do not vary spatially. It is also important to note the determined function $H(Kn_D)$ is not influenced by the functional form of the friction factor (e.g. it may be inferred from the Stokes-Millikan equation (Larriba *et al.*, 2011) or from Chapman-Enskog based diffusion coefficients), though friction factors must be known in order to determine β at a given H.
- While our findings indeed suggest that the influence of Z on the dimensionless collision kernel is small, the approach utilized here is vastly simpler than Boltzmann equation based approaches, and results in an approximation to the true form of $H(Kn_D)$. More exact analysis, however, particularly of low mass vapor molecule-particle collisions under non-isothermal conditions are still required to fully describe transition regime collisions.

Chapter 3: Vapor Condensation onto Arbitrary Shaped Aerosol Particles[2]

By defining the diffusive Knudsen number in terms of the Smoluchowski Radius, a continuum length scale descriptor and the Orientation Averaged Projected Area, a free molecular size parameter, it is shown here that the collision kernel derived in Chapter 2 is valid for particles of arbitrary shape in the presence of hard sphere interactions.

3.1. Introduction

An important group of reactions in both natural and engineered gaseous systems are those involving aerosol nanoparticles and vapor molecules or molecular clusters (Friedlander, 2000). Engineered nanoparticles form and grow via their collisions with vapor molecules (Gurav, et al., 1993; Swihart, 2003) and subsequent surface reaction. These particles can in turn be used to catalyze the reaction of vapor phase species (Biswas & Wu, 1998; Lee *et al.*, 2001, 2004), or as sorbents to capture and irreversibly bind toxic vapor molecules (Biswas & Zachariah, 1997; Biswas & Wu, 1998; Lee *et al.*, 2005). There is therefore, a clear need to study such reactions. Particle-vapor molecule reactions are often collision rate limited, and to determine the reaction rate it is sufficient to calculate the collision rate between particles and vapor molecules (Porstendorfer *et al.*, 1979b).

Quite often, however, transition regime aerosol particles, such as those generated in combustion sources, are highly non-spherical, morphologically complex entities (Rogak *et al.*, 1991; Rogak & Flagan, 1992b; Cai *et al.*, 1995; Koylu *et al.*, 1995; Biswas & Zachariah, 1997; Huang *et al.*, 1998; Tandon & Rosner, 1999; Filippov *et al.*, 2000; Sorensen, 2011). Despite prior investigation into condensation onto non-spherical

[2] Aspects of the results described in this chapter (including some text and figures) have been published in Gopalakrishnan et al. (2011)

particles in the continuum and near-continuum regimes (Loyalka & Griffin, 1993; Griffin & Loyalka, 1994), there is, at present, no general theory which describes collision limited reactions between vapor molecules and such non-spherical particles in the transition regime. Not only is this an unresolved issue of fundamental importance in the study of aerosols, but also given the prevalence of combustion generated particles in a number of systems, a collision kernel which describes non-spherical particle-vapor molecule collisions in the transition regime with reasonable accuracy is of considerable interest. In this chapter, the transition regime expression developed for spherical particles in Chapter 2 is extended to vapor molecule collisions with aerosol particles of arbitrary shape. The determination of the collision kernel in the continuum and free molecular regimes from the vapor molecule properties and appropriate geometric descriptors of particles in these two regimes is first described followed by details of calculation procedure at any appropriately defined Kn_D. In total, the approach described here allows for determination of the dimensionless collision kernel, H, as a single valued function of Kn_D which is valid for arbitrarily shaped particles.

3.2. Theoretical Approach

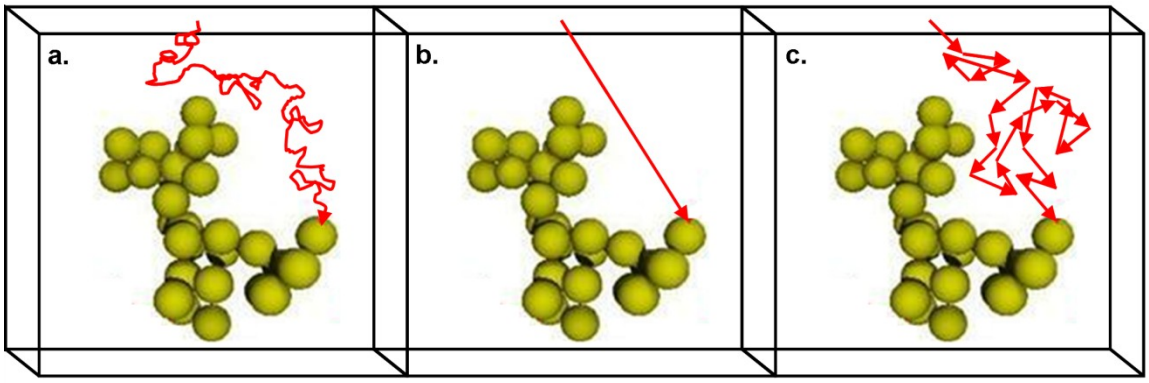

Figure 3.1: Representation of (a.) wholly diffusive vapor molecule collisions with a particle in the continuum regime, (b.) wholly ballistic vapor molecule collisions with a particle in the free molecular regime, and (c.) transition regime collisions, where drag, diffusion, and inertial forces all play a significant role.

3.2.1. The Continuum Collision Kernel

The collision process between vapor molecules and non-spherical particles in the continuum regime is represented schematically in Figure 3.1a. Considering only hard sphere potentials, the vapor molecules (approximated as point masses) migrate diffusively towards the much larger and near-motionless aerosol particles, and because of numerous collisions with gas molecules prior to collision with particles, vapor molecules have negligible inertia. Under these conditions, the collision kernel for vapor molecules/clusters of a given "friction factor" (f_v, defined as ratio of the thermal energy, kT to the vapor molecule diffusion coefficient) with spherical particles of radius a_p can be determined as:

$$\beta = 4\pi \frac{kT}{f_v} a_p \qquad (2a)$$

In defining a friction factor for the diffusing vapor molecule, it is assumed that the vapor molecule mass is significantly greater than that of the background gas molecules. (This assumption is examined more carefully later.) Equation (2a) can be adapted to particles of arbitrary shape by defining an effective radius, R_s, subsequently referred to here as the Smoluchowski radius (as Smoluchowski pioneered the analysis of continuum regime

collisions (Chandrasekhar, 1943)). The collision kernel between vapor molecules and particles of arbitrary shape is thus given as:

$$\beta = 4\pi \frac{kT}{f_v} R_s \tag{2b}$$

Prior analysis (Douglas, et al., 1994; Zhou *et al.*, 1994; Given, et al., 1997) of continuum transport shows very clearly that although the Smoluchowski radius cannot be determined analytically for most shapes, it is a clear geometric descriptor of an arbitrarily shaped particle, i.e. given a clearly defined particle geometry, a particle's Smoluchowski radius can be determined without foreknowledge of the properties of the colliding point mass. To this end, Brownian dynamics algorithms have been developed to determine the orientationally averaged Smoluchowski radii of arbitrarily shaped particles, which, in turn, clearly define their collision kernels for collisions with point mass vapor molecules in the continuum regime. A modified version of these algorithms is utilized here for calculation of Smoluchowski radii for particles of various geometries, with a brief summary of the algorithm given elsewhere (Gopalakrishnan, et al., 2011). A much more complete description of this algorithm is also found elsewhere (Northrup, et al., 1984; Rubinstein & Torquato, 1988; Kim & Torquato, 1991; Torquato & Avellaneda, 1991; Douglas, et al., 1994; Zhou, et al., 1994; Zhou, 1995; Potter *et al.*, 1996).

3.2.2. The Free Molecular Collision Kernel

For vapor molecules with large persistence distances relative to the effective size of the particle, the vapor molecules move ballistically (Figure 3.1b), with their motion appropriately described by free molecular mechanics. From kinetic theory, the collision kernel between a stationary, arbitrarily shaped hard-sphere aerosol particle and a point mass vapor molecule is given as (Vincenti & Kruger, 1975):

$$\beta = \sqrt{\frac{8kT}{\pi m_v}} PA \tag{3}$$

where m_v is the vapor molecule mass, and PA is the orientationally averaged projected area of the aerosol particle. As in the continuum regime, calculation of the collision

kernel in the free molecular regime for specified vapor molecule properties becomes a matter of appropriately quantifying the particle geometry, in this case through calculation of the orientationally averaged projected area. The algorithm to compute PA is also described in detail in (Gopalakrishnan, et al., 2011).

3.2.3. The Transition Regime Collision Kernel-Scaling Analysis

As discussed in Chapter 1, between the continuum and free molecular limits, vapor molecule motion depends upon both thermally driven diffusion and inertia (Figure 3.1c). This leads to neither purely diffusive nor deterministic trajectories, and complicates analysis of the collision process.

For non-spherical particles, the collision kernel in the transition regime, similar to spherical particles, is dependent upon kT, m_v, and f_v, but rather than a single radius a_p, the particle has a continuum size, quantified by R_s, and a free molecular size, quantified by PA. Dimensional analysis suggests that 3 dimensionless groups are needed to describe the interrelationships of these 6 parameters. Nonetheless, we attempt to collapse this system again to an $H(Kn_D)$ functional form, where H is redefined as:

$$H = \frac{\beta m_v}{f_v L_H^3} \tag{5a}$$

and $$Kn_D = \frac{\sqrt{kTm_v}}{f_v L_{Kn}} \tag{5b}$$

Here, L_H and L_{Kn} are yet undetermined length scales, but it is required they must be defined such that dimensionally, equations (2b) and (3) hold valid, as do the dimensionless limiting expressions (equations 11a & b from Chapter 1 repeated here):

$$H = 4\pi Kn_D^2 \quad \text{as} \quad Kn_D \rightarrow 0 \tag{6a}$$

$$H = \sqrt{8\pi} Kn_D \text{ as} \quad Kn_D \rightarrow \infty \tag{6b}$$

Using these restrictions, L_H and L_{Kn} are found to be:

$$L_H = \left(\left(\frac{PA}{\pi} \right)^2 \frac{1}{R_s} \right)^{1/3} \tag{7a}$$

$$L_{Kn} = \frac{PA}{\pi R_s} \tag{7b}$$

With L_H and L_{Kn} defined, the $H(Kn_D)$ curve must approach the continuum limit at low Kn_D and the free molecular limit at high Kn_D, irrespective of particle shape. We thus hypothesize that with appropriately defined H and Kn_D for arbitrarily shaped particles, the expression (equation 14 from Chapter 1 reproduced here) will apply, correctly describing particle-vapor collisions across the entire Kn_D range:

$$H = \frac{4\pi Kn_D^2 + C_1 Kn_D^3 + \sqrt{8\pi} C_2 Kn_D^4}{1 + C_3 Kn_D + C_4 Kn_D^2 + C_2 Kn_D^3} \tag{8}$$

3.3. The Transition Regime Collision Kernel- Mean Hitting Time Calculations

As described in Chapter 1, the $H(Kn_D)$ function can be determined via mean first passage time calculations using the Langevin equation of motion for entities whose masses are significantly greater than the background gas molecule mass. To determine if the previously developed $H(Kn_D)$ relationship does indeed hold valid for collisions with arbitrarily shaped particles, mean first passage time calculations are also performed here. For such calculations, a particle of known geometry, and therefore known R_s, PA, L_H, and L_{Kn} is placed in the center of cubic domain of volume V_{box}, where the side length of the domain is much longer than the maximum length scale of the particle. Next, a point mass of known properties is placed at a random location on the surface of the periodic simulation domain. The point mass is given an initial velocity vector sampled from the Maxwell-Boltzmann distribution (Vincenti & Kruger, 1975) and a force balance, described by the Langevin equation, is then applied to the point mass, where the point mass inertia (mass x acceleration), effective drag force (product of the friction factor and velocity), and diffusive motion (a stochastic force parameter) are each considered. The equations of motion presented in chapter 1 are used to advance the position, $\vec{x}$, and

velocity, $\vec{v}$, over time. As before simulations are performed nondimensionally, $\vec{x}^* = \vec{x}/\gamma$, $\vec{v}^* = (m_v/f_v)\,\vec{v}/\gamma$, $\tau = (f_v/m_v)\,t$, and $V^*_{box} = V_{box}/\gamma^3$, where $\vec{x}^*$ is the dimensionless position vector for the gas molecule, $\vec{v}^*$ is the dimensionless velocity vector for the gas molecule, t is time (dimensional), and τ is the dimensionless time. The parameter γ is characteristic length scale for the non-spherical particle of interest, the choice of which is arbitrary (e.g. the radius of the primary particles of the aggregate ensembles examined in this study). For brevity, the equations are not repeated here. Eventually, the point mass will collide with the particle, and the number of time steps required for collision, n_i is recorded. A new point mass is subsequently placed on the domain surface, and its trajectory until collision is also monitored. After N collision events are monitored, the dimensionless mean first passage time, τ_{mean}, is used to calculated as the dimensionless collision kernel H:

$$H = \frac{V^*_{box}}{\tau_{mean}}\left(\frac{\gamma}{L_H}\right)^3 \tag{9}$$

Dimensionless collision kernels are determined for selected nonspherical particles (described subsequently) as functions of Kn_D. Each mean first passage time calculation is performed with various simulation domain dimensions (V^*_{box}) and dimensionless timesteps, until a sufficiently large simulation domain and sufficiently small timestep are found (where the inferred H depends neither on domain dimensions or timestep). For all simulations, a dimensionless timestep of $0.005\left(\frac{\gamma}{L_H Kn_D}\right)^2$ is found satisfactory for convergence to timestep independent results.

3.4. Results and Discussion

3.4.1. Non-spherical Particle Geometries

A number of non-spherical particle geometries are examined to test the validity of equation (8): spheres, dimers, linear chains composed of 3, 5, 10, and 20 point contacting spheres, cubes (Hwang & Mascagni, 2004), and randomly generated fractal-like structures (Filippov, et al., 2000) with pre-exponential factors of 1.3 and 1.5, fractal dimensions of 1.78 and 2.5, and 5-20 primary particles. Fractal like structures are generated using the sequential algorithm described in detail by Filippov et al. (2000). Although structure factor calculations show that this algorithm cannot produce well described fractal particles with more than ~100 primary spheres, we utilize this algorithm here for fractal aggregates with 20 or fewer primary particles only. Moreover, equation (8) should be valid for particles of any shape, provided that R_s and PA are appropriately evaluated. For each test shape, R_s and PA are calculated as described in the prior sections, and R_s, PA, L_H, and L_{Kn}, for each examined shape are listed in Table 3.1. A digital representation of each shape is also shown in the table. In total these 13 shapes cover a $PA/\pi R_s^2$ range from 0.509 to 1.0, which spans a range covered by a wide variety of non-spherical particles.

Table 3.1: Summary of the R_S, PA, L_H, and L_{Kn} for the spherical and non-spherical particles examined via mean first passage time calculations.

Particle#	Type	Image	PA^y	R_s^y	L_H	L_{Kn}
1	Sphere		3.142	1.000	1.260	1.000
2	Doublet- Two contacting spheres Linear chain.	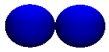	5.800	1.392	1.384	1.326
3	Trimer- Three contacting spheres Linear chain.	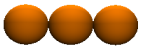	8.460	1.718	1.463	1.567
4	Pentamer- Five contacting spheres Linear chain.	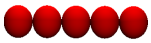	13.778	2.319	1.558	1.892
5	Decamer- Ten contacting spheres Linear chain.	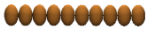	27.072	3.594	1.686	2.398
6	Icosamer- Twenty contacting spheres Linear chain.		53.660	5.793	1.807	2.948
7	*N=5 D_f=1.78 K_f=1.30*		13.283	2.193	1.568	1.928
8	*N=10 D_f=1.78 K_f=1.30*	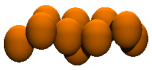	24.725	3.033	1.731	2.595
9	*N=20 D_f=1.78 K_f=1.30*	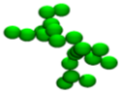	47.117	4.357	1.902	3.442
10	*N=5 D_f=2.50 K_f=1.50*		12.092	1.975	1.574	1.949
11	*N=10 D_f=2.50 K_f=1.50*	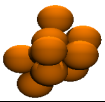	21.104	2.586	1.732	2.598
12	*N=20 D_f=2.50 K_f=1.50*	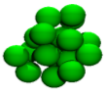	37.246	3.437	1.904	3.450
13	Cube*		1.500	0.663	1.129	0.720

y – Calculated with a primary sphere radius of 1 (arbitrary units).
*** - For a cube of unit side (arbitrary units)**

3.4.2. Mean First Passage Time Derived Collision Kernels

For each non-spherical particle, mean first passage time calculations were performed by varying Kn_D as described in the prior section. The determined dimensionless collision kernels are shown in Figure 3.2a for all performed calculations, and focused in the range $0.05 < Kn_D < 5$ (the transition regime) in Figure 3.2b. Also shown is the predicted curve developed previously from single spherical entity and two spherical entity mean first passage time calculations (equation (8)). By definition, in the low and high Kn_D limits, first passage time calculations and the regression equation agree well with one another as well as with the correct continuum and free molecular limiting expressions. Agreement between non-spherical particle first passage derived collision kernels and regression equation collision kernel is also excellent in the transition regime, with the maximum difference of 7.4% attributable to the statistical nature of first passage time calculations (with differences closer to ±1-2% more commonly found). These results show, unambiguously, that for collisions between a point mass and a non-spherical object in a low mass background gas, there is a universal expression $H(Kn_D)$, which, with proper definitions of H and Kn_D, successfully describes collision processes in the continuum, free molecular, and transition regimes. We strongly caution, however, that, as mentioned earlier, these results strictly apply only in the limit where the ratio of the moving object's mass to the background gas mass, Z, approaches infinity, thus allowing a friction factor (drag force) for the moving object to be defined and the motion of the moving vapor molecule to be monitored via the Langevin equation. Therefore, theoretically, the determined collision kernel expression applies only for the collision of a large non-spherical particle with a much smaller aerosol particle (coagulation), a molecular cluster, or a high mass vapor molecule. While at first glance this appears to limit the applicability of calculated results, we can compare $Z \rightarrow \infty$ dimensionless collision kernel calculations to expressions derived in the $Z \rightarrow 0$ limit to better understand the influence of Z on the collision process. Again, beginning with dimensional analysis, the

collision kernel between a non-spherical particle and a low mass vapor molecule depends upon R_s, PA, kT, m_v, and kT/D_v, which we may consider again to be f_v, a pseudo-friction factor for a low mass vapor molecule. This is essentially the same non-dimensionalization which was performed in the high mass limit, and leads to the dimensionless groups H and Kn_D, with H and Kn_D again defined by 5a and 5b, respectively. For a spherical collector, Sahni (Sahni, 1966) has determined the rate of neutron absorption when the collector is surrounded by a background gas at variable pressure. Fuchs and Sutugin (Fuchs & Sutugin, 1970; Friedlander, 2000) subsequently developed a regression equation for this $Z \rightarrow 0$ situation, which, in terms of H and Kn_D defined here, is given as:

$$H = \frac{4\pi Kn_D^2 + \sqrt{8\pi} G_1 Kn_D^3}{1 + G_2 Kn_D + G_1 Kn_D^2} \tag{10}$$

where $G_1 = 4.712$ and $G_2 = 3.590$. The hypothesis that $H(Kn_D)$ is a particle shape-independent, universal curve for the description of the transition regime collision kernel does not depend on the assumption of high mass colliding entities; thus, the information concerning the influence of Z on the collision process can be gained by comparing mean first passage time calculation results to the $Z \rightarrow 0$ regression equation. This comparison is shown in Figure 3.3a across the entire Kn_D range and in Figure 3.3b in the $0.05 < Kn_D < 5$ range. Unlike the comparison to the $Z \rightarrow \infty$ regression equation, a systemic deviation from the Fuchs-Sutugin collision kernel is apparent in Figure 3b. Nonetheless, this deviation is only ~7% at its greatest extent, and stays bounded below 5% for most of the Kn_D range. While collision kernel Z dependencies are certainly of fundamental interest, knowledge of the collision kernel across all Kn_D to within several percent is most often satisfactory for present analysis techniques which invoke the transition regime collision kernel (e.g. solutions to the general dynamic equation (Kuang *et al.*, 2009b)). It is therefore concluded that mean first passage time derived collision kernels may be used to predict collision rates for arbitrarily shaped particles with vapor molecules of any mass, with reasonable accuracy.

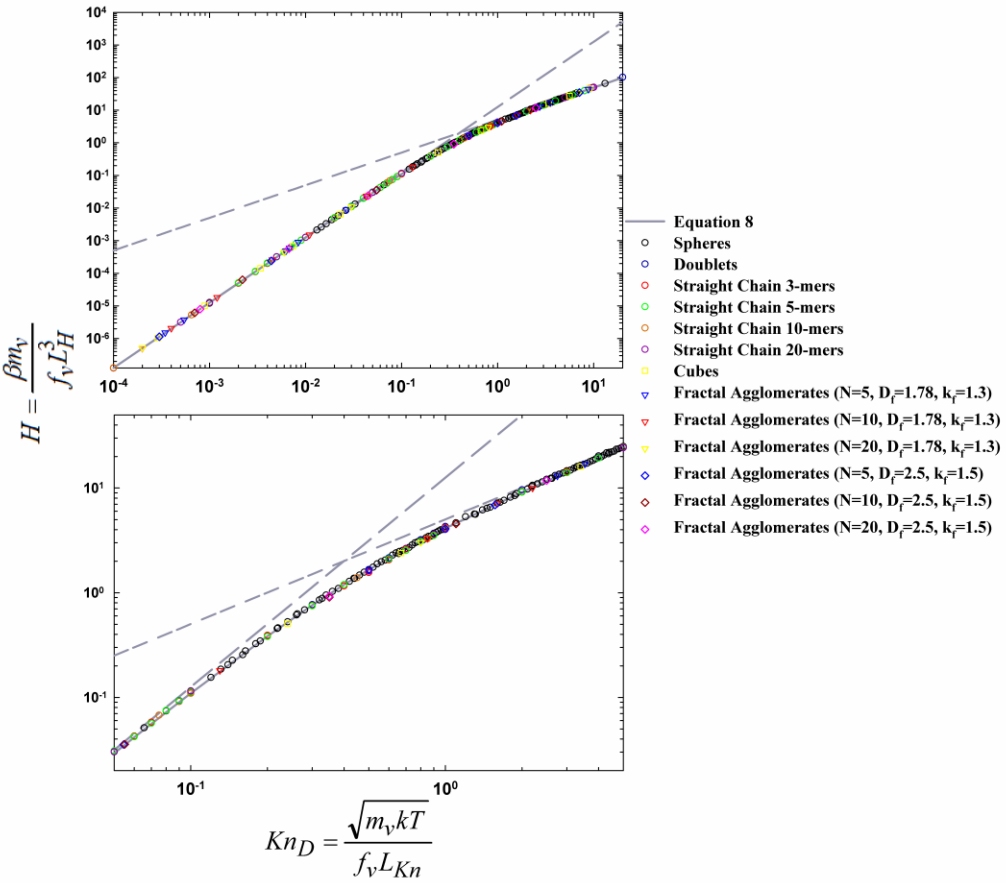

Figure 3.2: (a.) The dimensionless collision kernel, H, as a function of the diffusive Knudsen number as predicted by equation 8 and as determined for selected shapes from mean first passage time simulations. (b.) A zoomed in view of the $H(Kn_D)$ results for the range $0.05 < Kn_D < 5$.

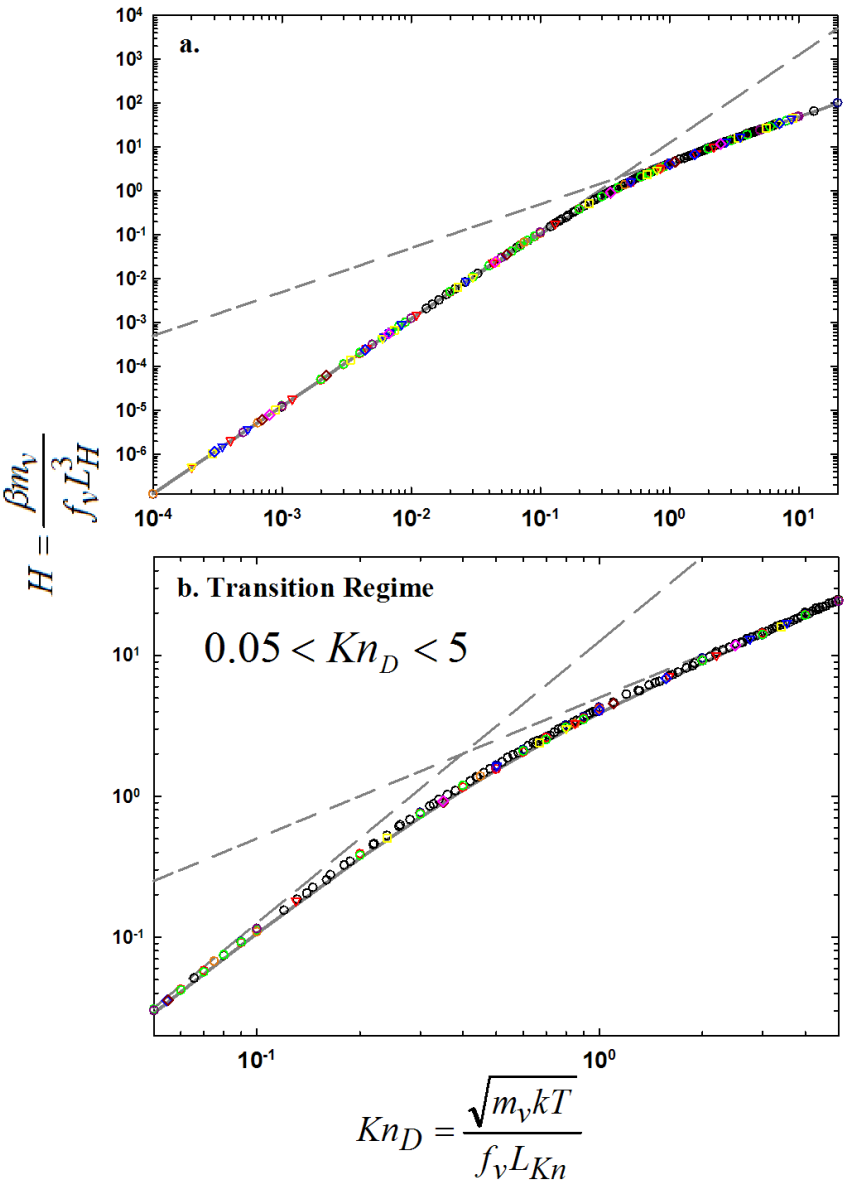

Figure 3.3: (a.) The dimensionless collision kernel, H, as a function of the diffusive Knudsen number as predicted by the Fuchs-Sutugin (1970) regression (solid gray line) for low mass vapor molecules and as determined for selected shapes from mean first passage time simulations. (b.) A zoomed in view of the $H(Kn_D)$ results for the range $0.05 < Kn_D < 5$. The color legend for mean first passage time calculations in shown in Figure 3.2.

3.5. Conclusions

Collisions between arbitrarily shaped aerosol particles and point masses (used to approximate vapor molecules) were examined via dimensional analysis and mean first passage time calculations. From this work, we can conclude the following:

- The rate of vapor molecule/molecule cluster/small spherical particle collision with a larger, non-spherical particle is directly proportional to the particle's Smoluchowski radius in the continuum regime and its orientationally averaged projected area in the free molecular regime, if thermal motion is the sole driving force for collisions. These two parameters may be calculated with knowledge of the non-spherical particle's geometry alone.
- In the transition regime, the collision rate also depends upon R_S and PA, and no additional geometric descriptor is necessary to determine the collision rate at any diffusive Knudsen number.
- Mean first passage time simulations confirm that the previously developed functional form for $H(Kn_D)$ for spheres applies to arbitrarily shaped particles. However, these simulations only apply in the limit of low mass gas molecules relative to vapor molecules ($Z \rightarrow \infty$). This is a reasonable assumption for a wide class of vapor molecules encountered in aerosol systems. Although collision kernel Z dependencies have not yet been clearly elucidated, these dependencies are expected to be small, given the good agreement between mean first passage time collision kernels and the regression equation of Fuchs and Sutugin (1970) developed for neutron deposition on a spherical collector (Sahni, 1966) (a $Z \rightarrow 0$ example).
- Mean first passage time calculation coupled with dimensional analysis, as applied here, is a simple yet powerful means to examine mass transfer rate Knudsen number dependencies. The investigation of particle ion-collisions important in the context of aerosol particle charging is described in Chapters 4 – 6.

Chapter 4: Coulombic Interactions in the Transition Regime[3]

Long range potential interactions between a sphere and a point mass ion are considered here. Calculated collision kernel values are compared with two prominent approaches from the literature. The concept of a Capture Radius is introduced as the appropriate length scale to describe attractive long range potential interactions. A regression expression suitable for collision kernel calculation in the near continuum regime is presented.

4.1. Introduction

Gas phase collisions of charged particles with ions as well as with other charged particles play an important role in governing the behavior of aerosols (Fuchs, 1963; Marlow & Brock, 1975b; Porstendorfer, et al., 1979b; Adachi, et al., 1985; Huang *et al.*, 1990; Jiang *et al.*, 2007; Michael *et al.*, 2011; Premnath, et al., 2011) and dusty plasmas (Goree, 1992, 1994; Matsoukas *et al.*, 1996; Matsoukas & Russell, 1997; Kortshagen & Bhandarkar, 1999; Khrapak, et al., 2006; Khrapak & Morfill, 2009; Ravi & Girshick, 2009; Chaudhuri *et al.*, 2010) as well, with particle charge distributions in these systems dependent on the rates at which these collisions occur. Determination of the collision kernel, and thereby the collision rate as discussed before, of charged entities is essential in characterizing the properties and behavior of aerosol and dusty plasma particles. The collision kernel β (introduced in previous chapters) is determined by the physics governing the collision process determined by both the thermal energy of the ions and the potential energy between particles and ions. For collisions involving at least one entity which is large in size relative to the collision persistence distance (the average straight line distance an entity in the gas phase travels due to thermal motion (Dahneke, 1983; Gopalakrishnan & Hogan, 2011)), continuum approximations are valid and the influence

[3] Aspects of the results described in this chapter (including some text and figures) have been published in Gopalakrishnan & Hogan (2012)

of both the thermal energy and the potential energy can be accounted by evaluating the collision kernel as the product of the Smoluchowki hard-sphere collision kernel (Chandrasekhar, 1943) and an enhancement factor, determined by the variation in potential energy with distance between colliding entities (Fuchs, 1964; Northrup, et al., 1984; Friedlander, 2000). Conversely, when both entities are extremely small relative to the collision persistence distance, free molecular mechanics best describe collisions. Under these circumstances as well, the collision kernel can be expressed as the product of the hard sphere collision kernel and a potential energy-determined enhancement factor (different than the continuum enhancement factor) (Marlow, 1980a). More specifically, for free molecular colliding entities interacting via a monotonic potential function which is finite at contact (e.g. the Coulomb potential), the collision kernel can be evaluated using orbital motion limited (OML) theory (Allen, 1992), while more involved analysis is required for singular contact potentials (Marlow, 1980a, 1980b; Lushnikov & Kulmala, 2005; Ouyang *et al.*, 2012).

In the transition regime, the sizes of the colliding entities are neither substantially larger nor substantially smaller than the persistence distance and both continuum and free molecular approaches fail to correctly predict collision kernels accurately. The first and most prevalently used method to determine collision kernels in this intermediate range is the flux matching theory, also proposed by Fuchs (1934; 1963; 1964), primarily for the analysis of aerosol systems. In flux matching, when the colliding entities are far from one another, their motion is described by continuum mechanics (inertialess motion with diffusion), while, when the radial distance between the entities is less than a critical "limiting sphere radius" (Natanson, 1960b; Wright, 1960), motion is modeled using free molecular mechanics (ballistic motion). On the surface of the limiting sphere (centered on one of the colliding partners), the flux of incoming entities from the outer continuum is equated with their flux into the inner free molecular region, which allows for calculation of the collision kernel.

Several researchers have applied the flux matching theory to transition regime collisions in the presence of both thermal energy and potential energy (Marlow, 1980a; Hoppel & Frick, 1986; Lushnikov & Kulmala, 2004b). Most examinations along these lines focus on collisions between particles and ions, in which the combined Coulomb-image potential is considered (Adachi, et al., 1985), or between oppositely charged particles, considering the simple Coulomb potential (Maisels *et al.*, 2002). As with hard-sphere collisions, predictions from alternative approaches to examine particle-ion interactions (Huang & Seinfeld, 1990; Biskos, et al., 2004) and the results of experimental studies of charged entity collisions in aerosols (Kirsch & Zagnitko, 1981; Adachi, et al., 1985; Pui, et al., 1988; Romay & Pui, 1992; Maisels, et al., 2002; Biskos, et al., 2005) are in good agreement with flux matching predictions. Because of its success in these instances, flux matching theory is widely accepted in aerosol science as an appropriate method for the calculation of transition regime collision rates. Moreover, quantitative size distribution measurements of submicrometer and nanometer sized particles (via electrical mobility based instruments), which are crucial in atmospheric sciences, currently depend upon flux-matching predictions of particle-ion collision kernels (Wiedensohler, 1988), further amplifying the importance of correct collision kernel calculation.

Unlike the study of aerosols, in the study of dusty plasmas, flux-matching has only recently been used to describe collisions between ions and charged particles (referred to in most works in dusty plasmas as grains). Apparently unaware of the precedent of Fuchs (1963) and the subsequent efforts of others (Bricard, 1962; Marlow, 1980a; Adachi, et al., 1985; Hoppel & Frick, 1986; Lushnikov & Kulmala, 2004b), to determine the collision rate between ions and dusty plasma grains, D'yachkov et al. (2007) redeveloped flux-matching theory for collisions in the presence of thermal energy and potential interactions, only differing from the original theory slightly in that they: (1) assumed a slightly different limiting sphere radius, (2) considered the Coulomb potential between colliding entities as opposed to a Coulomb-image potential, and (3) considered entities crossing the limiting-sphere to be moving with a Maxwell-Boltzmann velocity

distribution, as opposed to Fuchs's assumption that all entities travel at the mean thermal speed. Contrary to the conclusions found in examinations of aerosols, Gatti and Kortshagen (2008) report that flux-matching predictions of the steady-state charge level of plasma grains consistently overpredict the negative charge on plasma grains, which in turn implies that flux matching theory underpredicts the ion-charged particle collision kernel when they carry unlike charges. As a simple alternative, they have proposed an analytical model in which a linear combination of continuum, free molecular, and transition regime collisions (i.e. three body trapping (Hoppel & Frick, 1986), not considered in the standard flux matching approach) are accounted for. This model, however, fails to recover the correct collision kernel for hard-spheres, and in its derivation the influence of thermal energy in the continuum regime was omitted.

In addition to the evidence provided by Gatti and Kortshagen, a closer examination of reported measurements (Kirsch & Zagnitko, 1981; Adachi, et al., 1985; Pui, et al., 1988; Romay & Pui, 1992; Biskos, et al., 2005) of charged particle-ion collisions in aerosol systems reveals that although most prior works conclude that the flux matching predictions agree well with measurements, it would be more appropriate to conclude that the predictions of flux matching theory "can be fit" to experimental data. Essential to calculating the collision kernel is a priori knowledge of the mass and friction factor (inverse mobility or thermal energy/diffusion coefficient) of both colliding entities. In the case of aerosol particle-ion collisions, there are distributions of ions mass and friction factor (Marlow, 1978), and these ion properties have not thus far been measured directly; rather, for a set of experimental data, a single ion mass and friction factor have been inferred from simple correlations and used for comparison to theoretical predictions (Adachi, et al., 1985; Pui, et al., 1988). Further, the good agreement of experimental measurements as well as alternative theoretical predictions (Huang & Seinfeld, 1990) with flux matching predictions in aerosols is generally found only when the ratio of the potential energy between colliding entities to the thermal energy (Ψ_E) is less than unity. In dusty plasmas, where disagreement is found, Ψ_E is often in the 2-4 range (Khrapak & Morfill, 2009). Therefore, while flux-matching permits calculation of the transition

regime collision kernel reliably when $\Psi_E = 0$, its validity for collisions in the presence of potential interactions is in question.

In this chapter the extension of mean first passage time calculations to examine collisions between spherical entities suspended in a light background gas (relative to the masses of the spheres), which are interacting with one another via a Coulombic potential is described. The results of such calculations are compared to the predictions of flux matching theory (D'yachkov, et al., 2007) and to a modified form of the analytical expression of Gatti and Kortshagen (2008). It is then shown that flux matching theory does not correctly predict collision kernels for sufficiently large Ψ_E, and that collisions in the transition regime can be subdivided into three regimes: (1) the near-hard sphere regime, (2) the potential-enhanced, near continuum regime, and (3) the potential-enhanced near free molecular regime. Simple closed-form expressions for evaluating the collision kernel are given for the former two regimes.

4.2. Theoretical Framework for Transition Regime Collisions

4.2.1. Dimensional Analysis

In chapter 2, the collision kernel describing collisions between point masses and spherical particles in the absence of potentials was described. We now consider collisions in the presence of both thermal energy and Coulombic potential energy, and similarly attempt to develop appropriate independent and dependent dimensionless ratios to describe the collision kernel in the transition regime under such conditions. In the continuum limit, the collision kernel in presence of potential interactions is expressed as (Chandrasekhar, 1943; Fuchs, 1963):

$$\beta_{ij} = 4\pi \frac{kT}{f_{ij}} \left(a_i + a_j\right) \eta_c \tag{1a}$$

where η_c is the continuum limit enhancement factor, which, for the Coulombic potential, is expressed as (Friedlander, 2000):

$$\eta_c = \frac{\psi_E}{1 - \exp(-\psi_E)} \tag{1b}$$

Similarly, in the free molecular limit, the collision kernel, when modified to account for potential energy, is expressed as (Mott-Smith & Langmuir, 1926; Allen, 1992):

$$\beta_{ij} = \left(\frac{8\pi kT}{m_{ij}}\right)^{1/2} (a_i + a_j)^2 \eta_{FM} \tag{1c}$$

where the free molecular limit enhancement factor, η_{FM}, is given as (Allen, 1992):

$$\eta_{FM} = 1 + \psi_E \tag{1d}$$

for attractive Coulombic interactions and as (Matsoukas, 1997):

$$\eta_{FM} = \exp(\psi_E) \tag{1e}$$

for repulsive Coulombic interactions. The potential energy to thermal energy ratio for the Coulombic potential, Ψ_E, is expressed as:

$$\psi_E = \frac{-z_i z_j e^2}{4\pi\varepsilon_0 (a_i + a_j) kT} \tag{1f}$$

where z_i and z_j are the integer charge levels of entities i and j, respectively, ε_0 is the permittivity of the background gas, and e is the unit charge. As Ψ_E is positive for collisions between attracting entities and negative for collisions between repelling entities, η_c and η_{FM} are greater than 1.0 for attractive collisions, and less than 1.0 for repulsive collisions.

Unlike the collision kernel in the presence of thermal energy alone, non-dimensionalization of the collision kernel in the presence of both thermal and potential energy requires that the dimensionless collision kernel be expressed as a function of two independent dimensionless variables. The first of the independent variables is Ψ_E. To arrive at the remaining dimensionless ratios (H and Kn_D), we require that dimensionally, equations (1a) and (1c) hold valid in their corresponding limits, and dimensionlessly the following limits hold, as before:

$$H = 4\pi \mathrm{Kn}_\mathrm{D}^2 \qquad \text{as} \qquad \mathrm{Kn}_\mathrm{D} \to 0 \tag{2a}$$

$$H = (8\pi)^{1/2} \mathrm{Kn}_\mathrm{D} \qquad \text{as} \qquad \mathrm{Kn}_\mathrm{D} \to \infty \tag{2b}$$

These conditions lead to H expressed by the equation:

$$H = \frac{\beta_{ij} m_{ij} \eta_C}{f_{ij} \left(a_i + a_j\right)^3 \eta_{FM}^2} \tag{3a}$$

and $\mathrm{Kn_D}$ expressed by the equation:

$$\mathrm{Kn_D} = \frac{\left(kTm_{ij}\right)^{1/2} \eta_C}{f_{ij} \left(a_i + a_j\right) \eta_{FM}} \tag{3b}$$

In the transition regime, a number of methods (Fuchs, 1934, 1964; Fuchs & Sutugin, 1970; Loyalka, 1973; Dahneke, 1983; Veshchunov, 2010; Gopalakrishnan & Hogan, 2011; Gopalakrishnan, et al., 2011), including the flux-matching approach, lead to prediction of the $H(\mathrm{Kn_D})$ relationship, with all $H(\mathrm{Kn_D})$ predictions within 5% of one another across the entire $\mathrm{Kn_D}$ range. The hard sphere transition regime collision kernel $H(\mathrm{Kn_D})$ is repeated from chapters 2 and 3:

$$H = \frac{4\pi \mathrm{Kn_D^2} + C_1 \mathrm{Kn_D^3} + (8\pi)^{1/2} C_2 \mathrm{Kn_D^4}}{1 + C_3 \mathrm{Kn_D} + C_4 \mathrm{Kn_D^2} + C_2 \mathrm{Kn_D^3}} \tag{4}$$

where C_1 =25.836, C_2 = 11.211, C_3 = 3.502, and C_4 = 7.211.

4.2.2. Mean First Passage Time Calculations

With the above dimensional analysis, the inference of H at specified values of $\mathrm{Kn_D}$ and Ψ_E is performed assuming that the relative motion between the colliding entities can be described by monitoring the trajectory of a point mass with mass m_{ij} and friction factor f_{ij} within a simulation domain of prescribed dimensions until it collides with a stationary spherical entity of radius a_i+a_j. As before, motion of the point mass within the domain is described by a single Langevin equation implicitly assuming (in addition to the assumed negligible mass of the background gas): 1) the ratios $\theta_m = m_i/(m_i+m_j)$ and $\theta_f = f_i/(f_i+f_j)$ must be equivalent, as is the case for two equal sized particles of the same material, or for an ion-particle collision wherein the particle is significantly larger and more massive than the ion. Between these two limiting cases, for spherical particles of similar density, θ_m and θ_f are in close proximity, to the point where the errors brought about by their assumed equality are small (Gopalakrishnan & Hogan, 2011). 2) The

process under examination occurs on a time scale for which the drag force and stochastic diffusive force, which both arise from collisions with the bath gas molecules, may be treated as distinguishable quantities. This assumption is also reasonable for entities in dilute gas-phase systems. Following the non-dimensionalization developed in Chapter 1, the solution of the Langevin equation for the point mass, including Coulombic force can be written non-dimensionally as:

$$\vec{v}^{*}(\tau+\Delta\tau)=\vec{v}^{*}(\tau)\exp(-\Delta\tau)-\psi_E \mathrm{Kn}_\mathrm{D}^2\frac{\eta_{FM}^2}{\eta_C^2}(1-\exp(-\Delta\tau))\frac{\hat{r}}{r^{*2}}+\vec{A}_1 \tag{5a}$$

$$\vec{x}^{*}(\tau+\Delta\tau)=\vec{x}^{*}(\tau)+\left(\vec{v}^{*}(\tau+\Delta\tau)+\vec{v}^{*}(\tau)+2\psi_E \mathrm{Kn}_\mathrm{D}^2\frac{\eta_{FM}^2}{\eta_C^2}\frac{\hat{r}}{r^{*2}}\right)\left(\frac{1-\exp(-\Delta\tau)}{1+\exp(-\Delta\tau)}\right)-\psi_E \mathrm{Kn}_\mathrm{D}^2\frac{\eta_{FM}^2}{\eta_C^2}\frac{\hat{r}}{r^{*2}}\Delta\tau+\vec{A}_2 \tag{5b}$$

where τ is the nondimensionalized time ($\tau = (f_{ij}/m_{ij})t$) and $\Delta\tau$ is small change in τ, thus $\vec{v}^{*}(\tau+\Delta\tau)$, $\vec{x}^{*}(\tau+\Delta\tau)$, $\vec{v}^{*}(\tau)$, and $\vec{x}^{*}(\tau)$ denote the point mass dimensionless velocities and positions at dimensionless times τ and $\tau+\Delta\tau$,respectively. The vector $\hat{r}$ and the scalar r^* denote a unit vector in radial direction and the dimensionless distance of the point mass from the origin in the simulation domain, respectively. Finally, $\vec{A}_1$ and $\vec{A}_2$ are both Gaussian distributed random vectors with zero mean and variances given in equations (5c) and (5d), respectively:

$$\left\langle \vec{A}_1{}^2 \right\rangle = 3\mathrm{Kn}_\mathrm{D}^2\frac{\eta_{FM}^2}{\eta_C^2}(1-\exp(-2\Delta\tau)) \tag{5c}$$

$$\left\langle \vec{A}_2{}^2 \right\rangle = 6\mathrm{Kn}_\mathrm{D}^2\frac{\eta_{FM}^2}{\eta_C^2}\left(\Delta\tau-2\left(\frac{1-\exp(-\Delta\tau)}{1+\exp(-\Delta\tau)}\right)\right) \tag{5d}$$

A cubical simulation domain is used with periodic boundary conditions employed on the domain surface. Calculations are performed with prescribed Kn_D, Ψ_E, $\Delta\tau$, and dimensionless box side length, s (all dimensions are normalized by a_i+a_j), with no other inputs required. At the start of each calculation, the point mass is placed at a random location on the box surface, with a velocity sampled from equation (5c), while the

stationary particle is placed in the center of the domain. The motion of the point mass is monitored with equations (5a-5d) until it collides with the fixed central sphere, at which point the dimensionless time required for collision τ_i is recorded, a new point mass is placed on the domain surface, and calculation of the collision time is again repeated. After N collisions have been monitored, the mean first passage time, τ_{mean} is calculated as:

$$\tau_{mean} = \frac{\sum_{i=1}^{N} \tau_i}{N} \tag{6}$$

For each set of Kn_D, Ψ_E, $\Delta\tau$, and s values, a value of N in the range 500-1500 is chosen, such that the relative standard deviation of τ_{mean} is less than 1% over the most recent 200 collisions. The dimensionless collision kernel is subsequently determined from τ_{mean} as:

$$H = \frac{s^3 \eta_C}{\tau_{mean} \eta_{FM}^2} \tag{7}$$

Equation (7) follows directly from the definition of H in equation (3a), as well as the definitions of the dimensionless parameters s and τ_{mean}. Although $\Delta\tau$ and s are inputs for each calculation, we are interested in results where the mean first passage time is insensitive to both $\Delta\tau$ and s, i.e. as $\Delta\tau \to 0$ and $s \to \infty$. The criteria $\Delta\tau = 0.005 Kn_D^{-2}$ when $|\psi_E| < 1$ and $\Delta\tau = 0.005 Kn_D^{-2} \Psi_E^{-1}$ when $|\psi_E| \geq 1$ are found satisfactory to mitigate the influence of timestep on calculation results. To mitigate the effects of domain size, dimensionless side lengths ranging from 50-200 are used, increasing with increasing Ψ_E such that at the domain surface, the influence of the electrostatic force on the change in point mass velocity and position is substantially less than the influence of diffusion ($\vec{A}_2$ and $\vec{A}_1$) for the prescribed $\Delta\tau$. While the aforementioned values are found appropriate for mean first passage time calculations, smaller timesteps and larger domain side lengths are also used to ensure that results are insensitive to both these values, and to further ensure convergence, calculations of H for a given Kn_D and Ψ_E are repeated 10 times, with reported values as the average of these 10 calculations. H values are thus determined for attractive collisions with Ψ_E = 0.01 to 30 (at 300 K this corresponds to singly charged

particles with a_i+a_j ranging from 5.56 μm down to 1.85 nm) and for repulsive collisions with Ψ_E = -0.01 to -3. Finally, as extremely small timesteps are required to probe situations of large Kn_D and Ψ_E, computations are limited to Kn_D values below 30 for most Ψ_E.

The inferred H values apply for entities which are sufficiently dilute such that the time for collision is much less than the mixing time for the system, and concentration gradients do not develop as a result of collisions. While this condition is in conflict with the original theory of Smoluchowski in the analysis of thermally driven collisions (Chandrasekhar, 1943), Veshchunov (2010, 2011) has shown that the dilute limit assumption leads to similar results as does the Smoluchowski approach, at least in the case of hard sphere collisions in three dimensions. Described in the results and discussion section, by the convergence of mean first passage time inferred collision kernels to the appropriate continuum and free molecular limits, we show that this holds true in the presence of potential interactions between colliding entities as well.

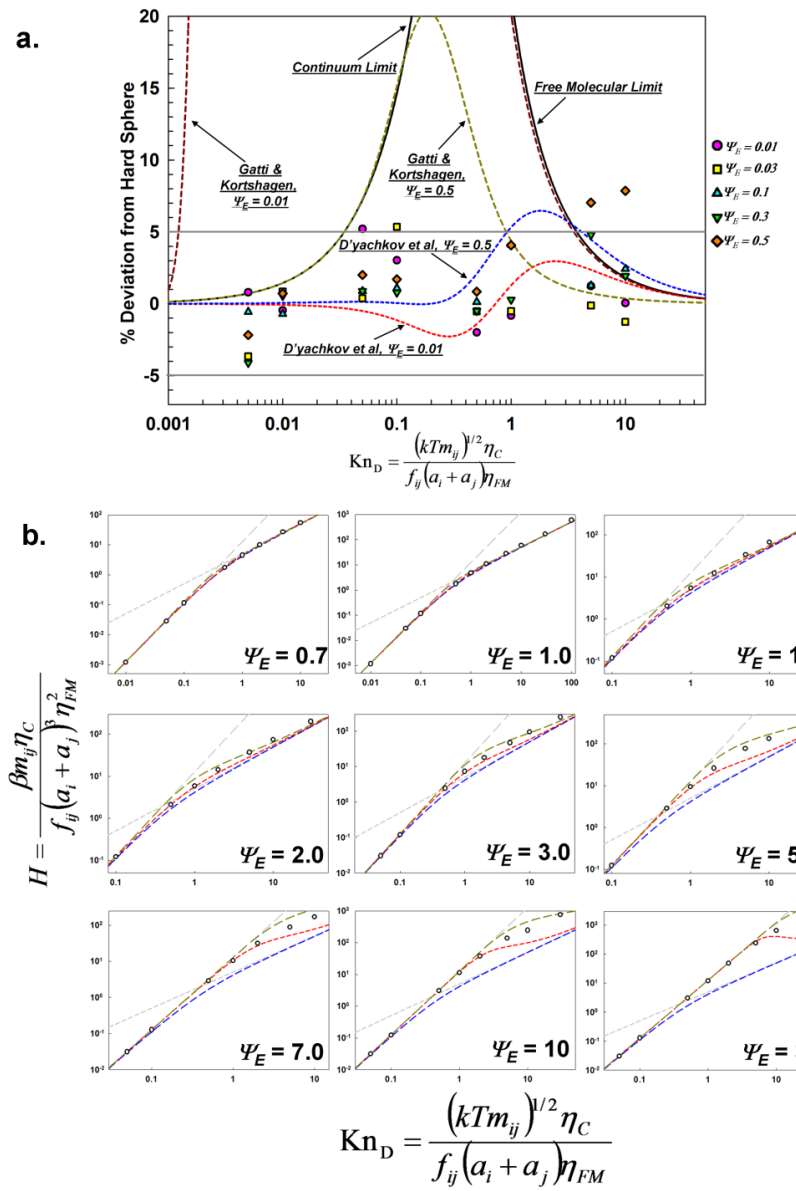

Figure 4.1 (a.) Results of mean first passage time calculations for attractive collisions in the Ψ_E = 0.01 to 0.5 range, represented by the percent deviation of calculation inferred H values from the expected hard sphere curve (equation 4). Also shown are the predictions from D'yachkov et al (2007) and Gatti and Kortshagen (2008). (b.) $H(\mathrm{Kn_D})$ curves from mean first passage time calculations for attractive collisions in the Ψ_E = 0.7 to 30 range. Also plotted are the predictions from D'yachkov et al (2007) (red curve), Gatti and Kortshagen (2008) (gold curve), and the previously developed hard sphere curve (equation 4). Dashed gray lines denote the continuum (long dash) and free molecular (short dash) expected $H(\mathrm{Kn_D})$ curves.

4.3. Mean First Passage Time Results and Interpretation

4.3.1. Influence of Kn_D and Ψ_E

Attractive potential calculation results are shown as functions of Kn_D for $0.01 \leq \Psi_E \leq 0.5$ in figure 4.1a and for $0.7 \leq \Psi_E \leq 30$ in figure 4.1b, respectively. Results are represented in terms of the percent deviation between the calculation and the expected $H(Kn_D)$ for hard sphere collisions (equation 4) in figure 4.1a, while in figure 1b $H(Kn_D)$ curves at fixed Ψ_E are shown directly. For further comparison, also shown in both figures are the continuum and free molecular limiting curves (equations 2a and 2b), the $H(Kn_D, \Psi_E)$ taken from the flux matching theory put forth by D'yachkov et al (2007), which, when the Coulomb potential is considered, only differs from the predictions of Fuchs's original theory (Fuchs, 1963) by several percent across the entire Kn_D range, and is expressed as:

$$H = 4\pi \mathrm{Kn}_\mathrm{D}^2 \left(F\left(\mathrm{Kn}_\mathrm{D}, \psi_E\right)\right)^{-1} \tag{8a}$$

$$F\left(\mathrm{Kn}_\mathrm{D}, \psi_E\right) = \frac{(2\pi)^{1/2}\mathrm{Kn}_\mathrm{D}\eta_{FM}\exp\left(\dfrac{-\psi_E}{1+\dfrac{\eta_{FM}}{\eta_C}\mathrm{Kn}_\mathrm{D}}\right)}{\left(1+\dfrac{\eta_{FM}}{\eta_C}\mathrm{Kn}_\mathrm{D}\right)^2 - \dfrac{\eta_{FM}}{\eta_C}\mathrm{Kn}_\mathrm{D}\left(2+\dfrac{\eta_{FM}}{\eta_C}\mathrm{Kn}_\mathrm{D}\right)\exp\left(\dfrac{-\psi_E}{\left(1+\dfrac{\eta_{FM}}{\eta_C}\mathrm{Kn}_\mathrm{D}\right)\left(2+\dfrac{\eta_{FM}}{\eta_C}\mathrm{Kn}_\mathrm{D}\right)}\right)} + \frac{1-\exp\left(\dfrac{-\psi_E}{1+\dfrac{\eta_{FM}}{\eta_C}\mathrm{Kn}_\mathrm{D}}\right)}{1-\exp\left(-\psi_E\right)} \tag{8b}$$

and finally the proposed equation of Gatti and Kortshagen (2008), expressed as:

$$H = 4\pi \mathrm{Kn}_\mathrm{D}^2\left(1-\left(1+\frac{\pi^{1/2}\alpha\eta_C\psi_E}{2\eta_{FM}\mathrm{Kn}_\mathrm{D}}\right)\exp\left(\frac{-\pi^{1/2}\alpha\eta_C\psi_E}{2\eta_{FM}\mathrm{Kn}_\mathrm{D}}\right)\right) + (8\pi)^{1/2}\mathrm{Kn}_\mathrm{D}\left(1+\frac{2\pi^{1/2}\alpha^3\psi_E^3\eta_C}{9\eta_{FM}\mathrm{Kn}_\mathrm{D}}\right)\exp\left(\frac{-\pi^{1/2}\alpha\eta_C\psi_E}{2\eta_{FM}\mathrm{Kn}_\mathrm{D}}\right) \tag{9}$$

In equations (8) and (9), η_{FM} and η_C are defined in equations (1b) and (1d), respectively, and $\alpha = 1.22$. Although equation (9) is adapted from Gatti and Kortshagen, it has been reformulated following their approach such that as $Kn_D \rightarrow 0$, the expression approaches the expected value of $4\pi Kn_D^2$; in the original work the influence of thermal energy on the collision process in the continuum regime was neglected. As noted in the introduction section, the Gatti and Kortshagen proposed $H(Kn_D, \Psi_E)$ curve results from the assumption that the collision rate can be calculated as a linear combination of the collision rate for entities moving via continuum transport, the collision rate for entities moving via free molecular transport, and the collision rate for entities where a single gas molecule collision occurs prior to the charged entity collision. For this reason, Gatti and Kortshagen proposed curve is referred to as linear combination theory, while the curve from D'yachkov et al. (2007) as flux matching theory in the reminder of the chapter.

Focusing first on $H(Kn_D)$ curves for $\Psi_E \leq 0.5$, with the exception of calculations at high Kn_D (5-10) with $\Psi_E = 0.5$, all calculated H values are within 6% of the expected $H(Kn_D)$ values determined for hard spheres. Variations of +/- 6% are well within the bounds of expected statistical variation for mean first passage time calculations, and it is thus concluded that for attractive Coulombic potentials with $\Psi_E \leq 0.5$, $H(Kn_D)$ may be calculated using equation (4), with the definitions of H and Kn_D adjusted (equations (3a) and (3b)) for convergence to the correct low Kn_D and high Kn_D limiting expressions. Flux matching theory predictions of $H(Kn_D)$ are also within +/- 6% of both the hard sphere curve and calculated values, in line with prior comparisons made to limiting sphere theory in this Ψ_E range (Porstendorfer, et al., 1979b; Kirsch & Zagnitko, 1981; Adachi, et al., 1985; Pui, et al., 1988). Conversely, even with the aforementioned corrections made, the $H(Kn_D, \Psi_E)$ curve from linear combination theory is in sharp contrast with our calculations and limiting sphere predictions, suggesting it is not appropriate for collision rate calculations in these circumstances.

For Ψ_E in the 0.7 to 30 range, clear deviations of $H(Kn_D)$ from the hard sphere curve are evident. As Ψ_E increases, the Kn_D value at which $H(Kn_D)$ departs from the

continuum curve also increases greatly. For example, the continuum limit H value ($4\pi Kn_D^2$) at $Kn_D = 2$ is 5.5 times larger than the calculated $H(Kn_D)$ at $\Psi_E = 0$, while for $\Psi_E = 30$ at this Kn_D the continuum limit prediction differs from the calculated value by less than 5%. Similarly, the Kn_D value at which $H(Kn_D)$ approaches the free molecular limit also increases drastically with Ψ_E, with differences between the free molecular curve and $H(Kn_D)$ persisting beyond $Kn_D = 30$ at $\Psi_E = 1$. These two influences combined lead to a shift in the Kn_D range corresponding to the transition regime (where neither limiting expression applies). Along with this shift, unlike the hard sphere curve, in the presence of potential energy $H(Kn_D)$ is not bounded below both the predicted continuum and free molecular limits; a collision rate faster the free molecular limit prediction is achievable. The shift in the transition regime Kn_D range with increasing Ψ_E is expected from both flux matching and linear combination theories. Neither of these approaches, however, appears to correctly predict the dimensionless collision kernel in the transition regime. Flux matching theory consistently underestimates the collision kernel outside the continuum regime at large Ψ_E, in line with conclusions of comparisons of flux matching predictions to experimental examined collision rates in the Ψ_E = 2-4 range (Gatti & Kortshagen, 2008). The agreement between mean first passage time calculations and linear combination theory improves in the $\Psi_E > 0.7$ range and is quite reasonable for $\Psi_E = 1-3$, the range for which it was originally developed. Nonetheless, linear combination theory leads to a consistent overestimation of $H(Kn_D)$ in the transition regime across all Ψ_E.

4.3.2. Limitations of Flux Matching Theory

It is clear from mean first passage time calculations that although flux match theory appears to correctly predict the collision kernel for repulsive potentials as well as attractive potentials with low values of Ψ_E, both flux matching and linear combination theory fail to predict the collision kernel in the transition regime at large positive Ψ_E.

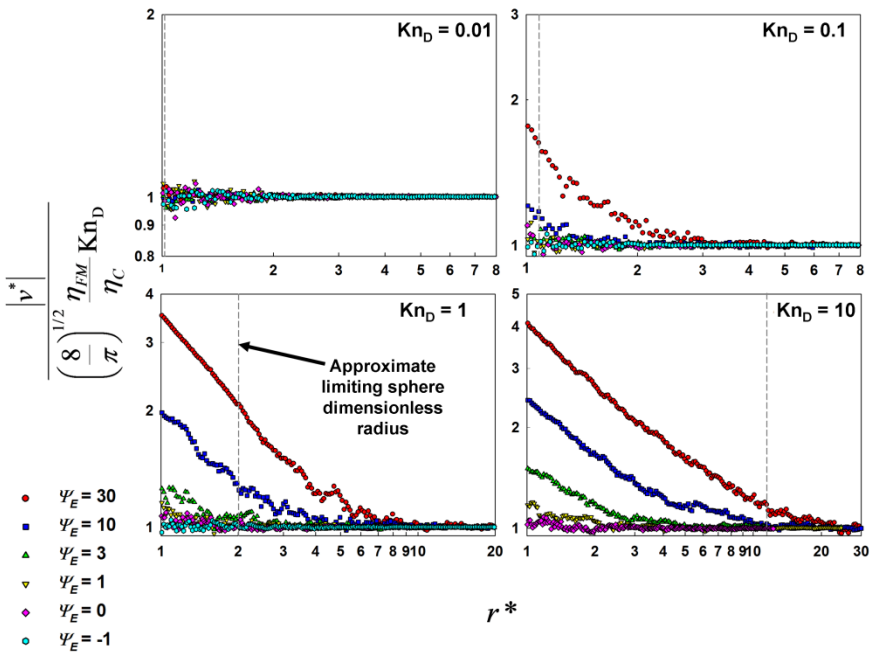

Figure 4.2: Normalized mean speeds of point masses in mean first passage time calculations for selected Kn_D and Ψ_E as functions of the dimensionless radial coordinate. Dashed gray lines in each graph denote the approximate dimensionless location of the limiting sphere in flux matching theory, where incoming point masses are typically assumed to have the mean thermal speed or follow a Maxwell-Boltzmann distribution.

The flux matching theory is compared to mean first passage time calculations in terms of the process by which calculations are carried out in each approach. In both, the collision rate/kernel is inferred via examination of the collision of a point mass with an absorbing sphere. In all incarnations of flux matching theory (Bricard, 1962; Fuchs, 1963; Marlow, 1980a; Hoppel & Frick, 1986; Lushnikov & Kulmala, 2004b; D'yachkov, et al., 2007), the flow rate/current of point masses to the surface of a limiting sphere, which has a dimensionless radius (Natanson, 1960b; Wright, 1960; Marlow, 1980a) of approximately $1+(\eta_{FM}/\eta_C)Kn_D$ and surrounds an immobile sphere of unit radius, is first calculated. The point masses move to the limiting sphere via continuum transport; thus, a modified form of Fick's law is used in evaluating the point mass flow rate (Fuchs, 1964). The fraction of point masses that enter the limiting sphere and subsequently collide with the central sphere is next calculated. This ultimately enables the collision kernel calculation as the product of the point mass flow rate and the fraction of point masses that

collide with the central sphere, divided by the number concentration of point masses. In determining the fraction of point masses which collide with the central sphere, free molecular trajectory calculations are typically carried out, and to initialize these calculations, the point masses are assumed to have either the mean thermal speed (Fuchs, 1963) or follow a Maxwell-Boltzmann distribution (D'yachkov, et al., 2007). On the contrary, with large Ψ_E, point masses are exposed to a strong attractive force, and flux matching theory may fail if the resulting increase in speed beyond the mean thermal speed is not correctly accounted for. Mean first passage time calculations do account for this change in speed by construction, and Figure 4.2 shows the average point mass speed (dimensionless) as a function of dimensionless radial coordinate in the calculation domain for selected $\mathrm{Kn_D}$ and Ψ_E, from our calculations. In the dimensionless system employed, the dimensionless mean thermal speed, v_{th}^*, is given as:

$$v_{th}^* = \left(\frac{8}{\pi}\right)^{1/2} \frac{\eta_{FM}}{\eta_C} \mathrm{Kn_D} \tag{10}$$

Therefore, in Figure 4.2, a value of 1.0 denotes that the point mass mean speed is equal to the mean thermal speed. Also noted on the graphs in Figure 4.2 are the approximate limiting sphere radii for each $\mathrm{Kn_D}$ (which varies slightly with Ψ_E). As expected for $\Psi_E = 0$, at all $\mathrm{Kn_D}$, the average speed of the point mass in calculations is equal to the mean thermal speed. This also appears to hold approximately true for $\Psi_E = \pm 1$. However, for $\Psi_E = 3, 10,$ and 30 with $\mathrm{Kn_D} \geq 0.1$, as the point mass approaches the central sphere, the average speed of the point mass increases. Larger increases in speed are evident at higher $\mathrm{Kn_D}$, such that the point mass speed can be several multiples of the mean thermal speed close to the sphere surface. In addition, for these high Ψ_E cases, at the surface of a constructed limiting sphere (with dimensionless radial coordinates noted by dashed gray vertical lines in each graph), the point mass speed is larger than the thermal speed, with the maximum speed increase at the limiting sphere surface found for $\mathrm{Kn_D} = 1$.

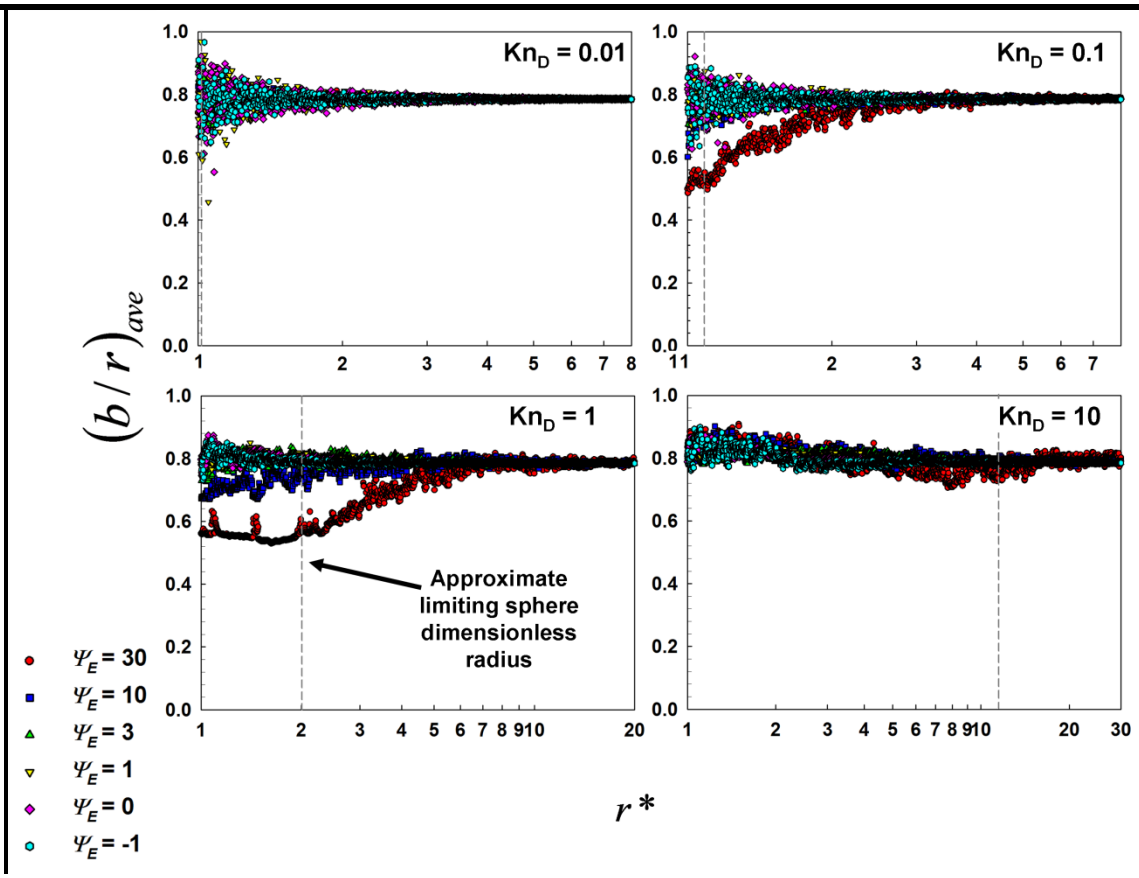

Figure 4.3: Mean nondimensionalized impact parameters in mean first passage time calculations for selected Kn_D and Ψ_E as functions of the dimensionless radial coordinate. Dashed gray lines in each graph denote the approximate dimensionless location of the limiting sphere in flux matching theory, where incoming point masses are typically assumed to have uniformly distributed impact parameters (mean value 0.78).

Coupled with an initial speed distribution in flux matching theory calculations is the initial distribution of point masses on the limiting sphere surface, i.e. the distribution of point mass impact parameters (Fuchs, 1963; Li & Wang, 2003). At any point in space, the ratio of the impact parameter for a point mass to its radial coordinate, b/r, can be calculated as the sine of the angle formed between the point masses velocity vector and position vector. For uniformly distributed impact parameters, which would be expected in the absence of potential interactions and which are assumed on the limiting sphere surface in flux matching theory, the average value of b/r, $(b/r)_{ave}$, is $\pi/4$ (0.7854). However, associated with the change in speed, at high Ψ_E, $(b/r)_{ave}$ is expected to decrease, with the direction of the point mass velocity vectors biased towards the center

of the collecting sphere. As with changes in speed, the change in impact factor distribution due to potential energy is accounted for in mean first passage time calculations, with $(b/r)_{ave}$ as a function of the dimensionless radial position in calculations displayed in Figure 4.3. Under most conditions, $(b/r)_{ave}$ fluctuates about its expected hard sphere value, with the fluctuations attributable to the statistical nature of mean first passage time calculations. However, at intermediate Kn_D (*0.1-1.0*) and large Ψ_E, a decrease in $(b/r)_{ave}$ is indeed evident, further demonstrating that flux matching theory makes use of inappropriate boundary conditions on the constructed limiting sphere surface.

Although certain (Kn_D , Ψ_E) pairs are readily found for which flux matching theory fails to account for the correct speed and impact parameter distributions on the limiting sphere surface, it nonetheless gives rise to a near identical collision kernel to mean first passage time calculations under many of these conditions. For example, at $Kn_D = 1$ and $\Psi_E = 10$, where the point mass speed is well above the mean thermal speed and the impact parameter distribution is skewed towards the collecting sphere center, the collision kernels predicted by both approaches differ by only 5%. In such instances, it is readily observed that (1) the predicted collision kernel is in good agreement with continuum predictions, and (2) in flux matching theory calculations all point masses entering the limiting sphere are collected, hence little to no error is introduced by the incorrect boundary conditions. It thus appears that it is only for sufficiently high Kn_D (outside the continuum regime) and high Ψ_E (e.g. $\Psi_E = 30$) where the inappropriate boundary conditions have consequences in collision kernel calculation. Conversely, there are a number of (Kn_D , Ψ_E) pairs for which the mean first passage time determined point mass speeds and impact parameters are near identical to expected values for hard spheres, and yet flux matching theory predicts a much lower collision kernel value than is found in mean first passage time calculations (e.g. 61.4% different at $Kn_D = 10$, $\Psi_E = 3$). While not evident from speed or impact parameter calculations, the low collision kernel values in these instances, which are for $\Psi_E \geq 0.5$ and outside the continuum limit, arise because of the failure of flux matching theory to account for point mass-gas molecule collisions

occurring close to the collecting sphere surface and inducing collision with the central sphere. Such collisions may result in a reduced speed for the charge carrying point mass, such that the point mass can be captured by the central collecting sphere. This type of occurrence, termed three-body trapping (Hoppel & Frick, 1986) or a charge-exchange collision (Gatti & Kortshagen, 2008), can become the dominant mechanism by which collisions occur at high Kn_D and Ψ_E. By use of the Langevin equation to describe point mass motion, three body trapping is considered in mean first passage time calculations. It is also accounted for in linear combination theory; however, based on mean first passage time results (and our presumption that these calculations correctly lead to determination of the collision kernel to +/-5%), it appears that outside the $\Psi_E = 0.1 - 2.0$ range the increase in collision rate due to three body trapping is overestimated with this approach. Aware that three body trapping is not considered in the original derivation of flux matching theory, Hoppel and Frick (1986) attempted to modify Fuchs's approach specifically for particle-ion collisions by noting that a calculation of the collision rate between a particle and a point mass ion for positive Ψ_E should converge to the positive ion-negative ion recombination rate when the particle is of similar size to the ions themselves. Requiring an experimentally-determined ion recombination rate as an input, they incorporated Natanson's method (Natanson, 1960a) to determine the rate of three body trapping based collisions into Fuchs's original approach. While this model perhaps allows for more reasonable approximation of the collision kernel than the original flux matching theory, there are several possible issues with utilizing Hoppel and Frick's approach. First, it requires a "tuning constant" input from experiments and is therefore not a complete theory for describing collisions. Second, while the ion recombination rate may be inferred from experiments correctly, collisions between two ions may be subject to different potentials than the ion-particle potential, and further the molecular structures of ions may have a strong influence on the collision rate between oppositely charged ions (i.e. while modeling particles as spheres be may acceptable, it is often inaccurate to model ions as spheres in ion-ion collisions) (Amadon & Marlow, 1991a, 1991b; Girshick *et al.*, 2009). When the influences of ion structure and the ion-ion potential interaction are considered, there is no reason to expect that the particle-ion collision kernel function

should collapse to the ion-ion collision kernel at large Kn_D. Finally, as is customary in flux matching theory, Hoppel and Frick's approach does not address the issues of incorrect speed and impact parameter distributions, which become important in conjunction with three body trapping.

4.3.3. Coulombic Capture Radii

Overall, based on mean first passage time calculations, it is seen that neither any existing incarnation of flux matching theory nor linear combination theory satisfactorily describes collisions in the gas phase in the presence of attractive Coulombic energy across a wide range of Kn_D and Ψ_E. Moreover, in the instances where flux matching theory does agree with calculations, the hard sphere inferred $H(Kn_D)$ expression with adjusted definitions of H and Kn_D for the Coulombic potential is also in excellent agreement with calculations. The modified hard sphere $H(Kn_D)$ curve which is based on scaling analysis and is simpler to apply can be used for collision kernel calculation under these conditions, and additionally mean first passage time results are fit to an appropriate functional form for $H(Kn_D, \Psi_E)$ in the $\Psi_E \geq 0.5$ range suitable for collision kernel determination under a wide range of conditions.

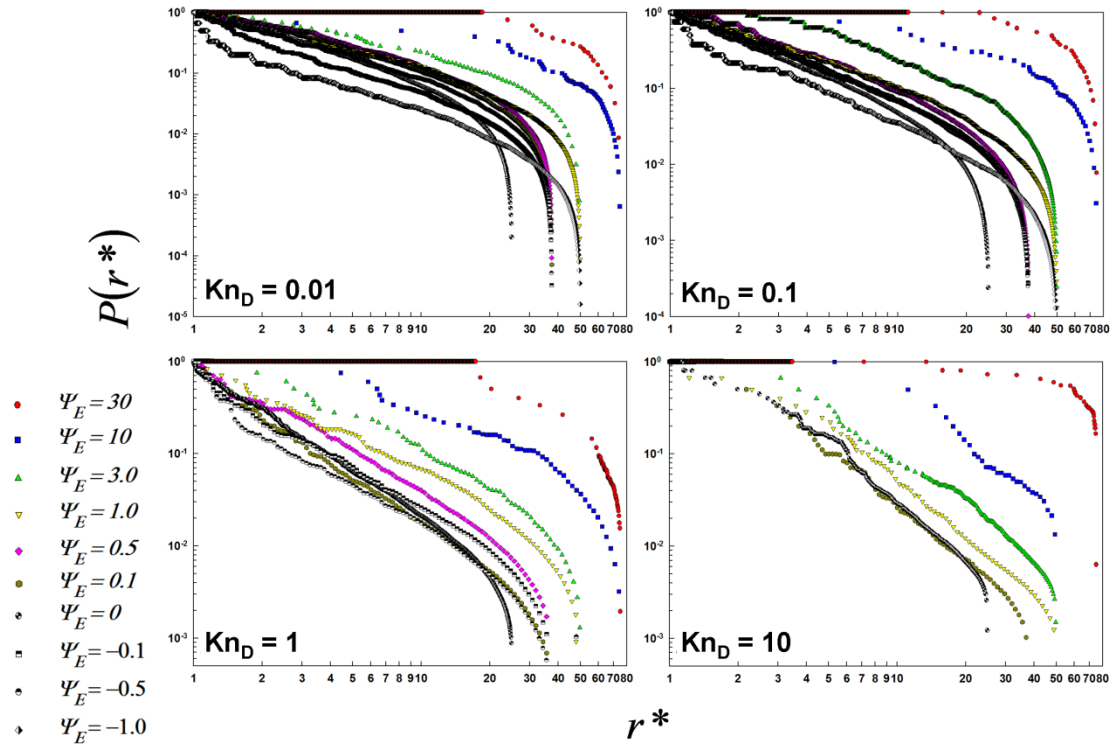

Figure 4.4: *P(r*)*, the probability that an incoming point mass will collide with the central sphere, as a function of the dimensionless radial coordinate, as determined from mean first passage time calculations at selected Kn_D and Ψ_E.

Although the results of mean first passage calculations are typically in poor agreement with linear combination theory predictions, there are some important features to this theory which can be used in the analysis of mean first passage time calculations. Central to linear combination theory development is the definition of a capture radius, i.e. the radial distance at with the thermal energy is equal to the potential energy, such that for a monotonic attractive potential, a point mass is highly likely to collide with the absorbing sphere upon arriving at the capture radius. For the Coulomb potential, the capture radius, R_C, is defined as:

$$R_C = \max\left[a_i + a_j, \frac{2}{3}\psi_E\left(a_i + a_j\right)\right] \tag{11}$$

and with $\Psi_E > 1.5$, the capture radius is larger than the absorbing sphere radius. The influence of a capture radius at high Ψ_E can be observed in mean first passage time

calculations. Figure 4.4 shows the probability, $P(r^*)$, that a point mass at a given dimensionless radial distance from the domain origin will collide with the central absorbing sphere for selected Kn_D and Ψ_E. Calculation for these curves proceeds as follows: for each value of r^*, it is determined whether a point mass, having reached a dimensionless distance r^* from the domain center, will collide with the central sphere rather than return to the domain boundary. If the point mass reaches the absorbing sphere, then a *collision* is counted for all r^* up to s, as point masses are initiated at least a distance s from the domain center. However, if a point mass returns to the domain surface, a *miss* is counted for all values of r^* ranging from s down to the minimum r^* value the point mass reached. $P(r^*)$ is then calculated as *collisions / (misses + collisions)* for each r^*. While this calculation approach leads to inaccuracies (underestimation) for r^* close to s, $P(r^*)$ near s is close to zero and otherwise the probability that a point mass will collide with the central sphere is accurately determined for all other r^*. For $\Psi_E < 1.5$ and including repulsive potentials, $P(r^*)$ curves are similar to one another, with little shift in $P(r^*)$ curves even when comparing those with positive and negative Ψ_E. Conversely, for the examined cases with $\Psi_E = 3$, 10, and 30 at all examined Kn_D, $P(r^*)$ curves are clearly shifted, such that at the dimensionless capture radius ($2\Psi_E/3$), probability of collision is typically ≥ 0.80.

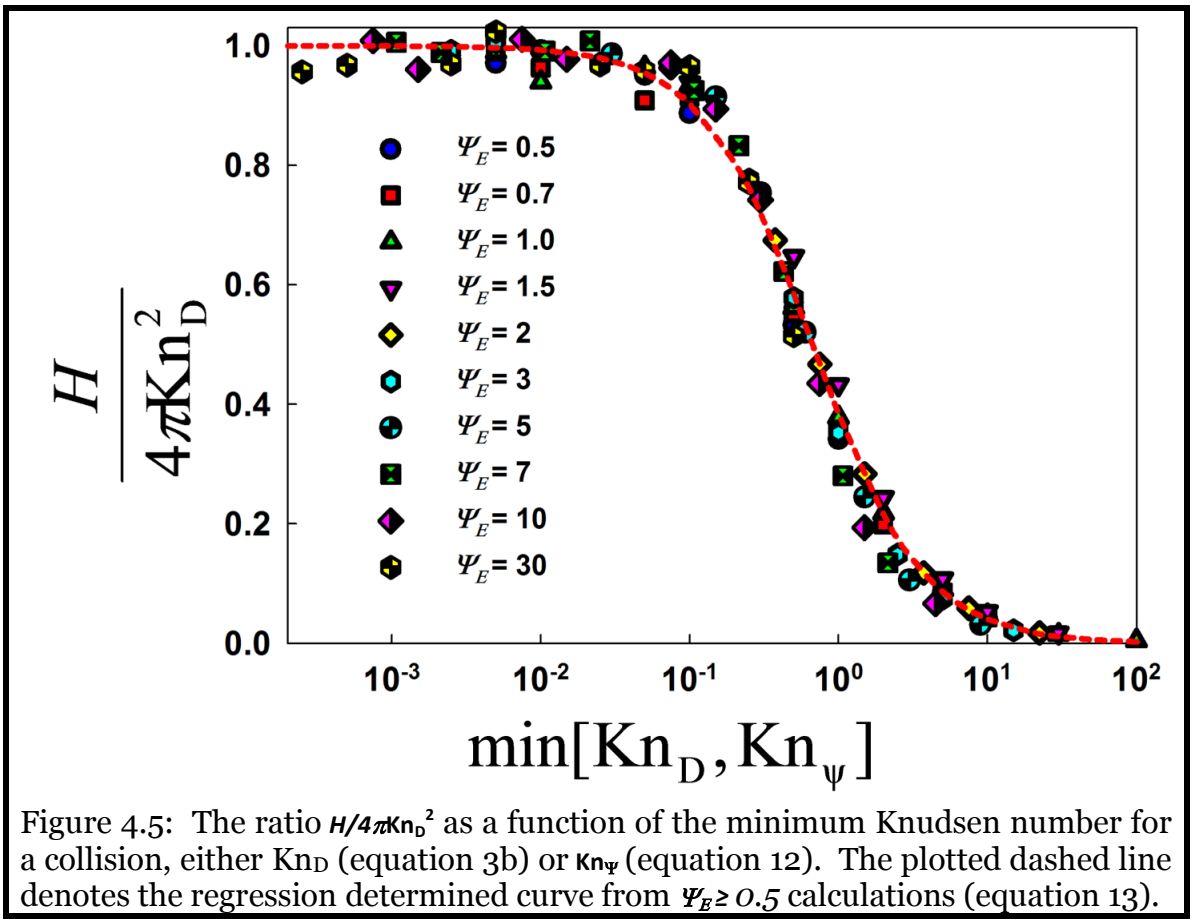

Figure 4.5: The ratio $H/4\pi Kn_D^2$ as a function of the minimum Knudsen number for a collision, either Kn_D (equation 3b) or Kn_Ψ (equation 12). The plotted dashed line denotes the regression determined curve from $\Psi_E \geq 0.5$ calculations (equation 13).

Gatti and Kortshagen (2008) show that when the Knudsen number is defined using the capture radius as the normalizing length scale in lieu of the sum of colliding entity radii, the shift in Knudsen number range for which the collision kernel approaches its expected continuum value is not apparent, implying that the collision radius is the correct normalizing length for the Knudsen number. Lushnikov and Kumala (2004b) also propose that the Knudsen number for charged entity collisions at large Ψ_E should be defined based upon Coulombic length scale, as opposed to colliding entity radii. Moreover, the physics of the collision process suggests that an appropriately defined capture radius is the correct normalizing length scale for collisions in the presence of potential energy; at the surface of the collision radius, the capture probability is close to 1.0, and similarly the probability of avoiding collision is close to 0. Therefore, if transport to the capture radius surface (at which point collision occurs) can be described solely as a continuum regime process, then it follows that the entire collision process can

be described by continuum transport relations. Only under circumstances where colliding entities can move in close proximity to one another on time scales where (1) motion is not described by continuum transport and (2) a collision can be avoided, will the collision kernel deviate from the expected continuum value. Given these arguments and the suggestions of prior work, we define the potential Knudsen number, Kn_Ψ as:

$$Kn_\psi = \frac{3\left(kTm_{ij}\right)^{1/2}\eta_C}{2f_{ij}\psi_E\left(a_i + a_j\right)\eta_{FM}} = \frac{3Kn_D}{2\psi_E} \tag{12}$$

and also propose that the governing parameter for collisions in the presence of thermal and Coulombic energy will be the minimum of Kn_D and Kn_Ψ. Considering all calculations for which $\Psi_E \geq 0.5$, the ratio of inferred H to the expected continuum limit value, i.e. $H/4\pi Kn_D^2$, is plotted as a function of the minimum of Kn_D, Kn_Ψ in Figure 4.5. Across the entire examined Ψ_E range, these results collapse remarkably well to a single curve, giving further credence to the concept of a capture radius for attractive collisions. Also plotted as a dashed line in Figure 6 is the function:

$$\frac{H}{4\pi Kn_D^2} = \frac{1}{1 + B_1\left(\min\left[Kn_D, Kn_\psi\right]\right)^{B_2}} \tag{13}$$

where $B_1 = 1.598$ and $B_2 = 1.1709$, which are determined via fitting calculation results. For scenarios for which $\min[Kn_D, Kn_\Psi] \leq 2.5$, equation (13) better agrees with calculation results than does a modification to the hard sphere $H(Kn_D)$ curve, with equation (13) predictions within +/- 10% of most calculated points. Thus, for $\Psi_E \geq 0.5$ equation (13) can predict the dimensionless collision kernel in the near-continuum regime with reasonable accuracy. However, it must be noted that equation (13) does not converge to the correct free molecular limiting result, and even with the definition of Kn_Ψ, rendering the prediction of collision kernel in the near free molecular regime with any degree of accuracy a topic of further study. Fortunately, considering charged entities, high Kn_D is correlated with high Ψ_E, in the majority of aerosol systems and a number of dusty plasma systems. Therefore, most high Ψ_E collisions occur with a Kn_Ψ associated with the near continuum collision regime (with the exception of highly charged, supermicrometer particles in a low pressure environment).

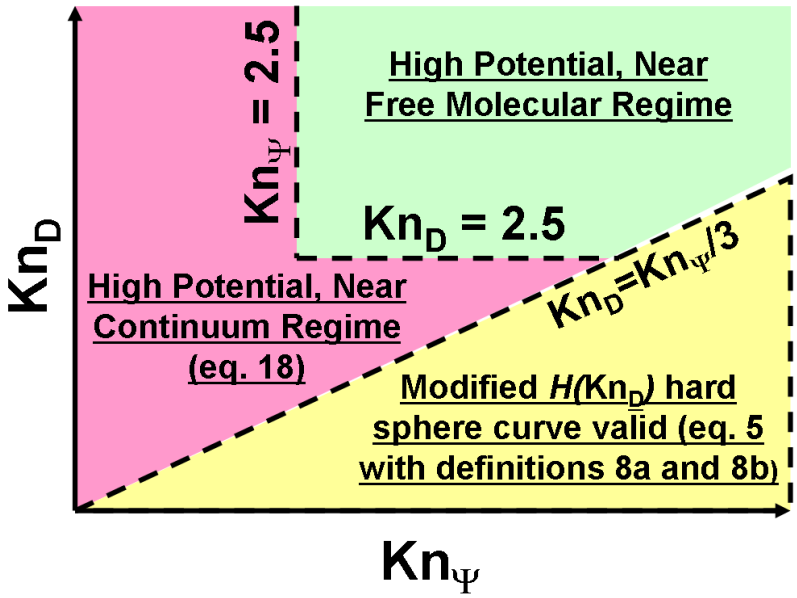

Figure 4.6: Phase space diagram for the calculation of the dimensionless collision kernel, dividing (Kn_D, Kn_Ψ) into three separate regimes.

4.3.4. Collision Kernel Calculation for Population Balance Models

Often, the underlying purpose of calculating collision kernels is for their use in particle/plasma grain population balance models, i.e. systems of ordinary or partial differential equations used to monitor the changes in number concentrations of particles of a given size and charge state over space and time dimensions (Schweigert & Schweigert, 1996; Kortshagen & Bhandarkar, 1999; Warthesen & Girshick, 2007; Ravi & Girshick, 2009). For this reason, a "phase space diagram" which denotes the appropriate collision kernel expression for use in charged entity collision rate calculations at a given Kn_D and Kn_Ψ is shown in Figure 4.6. In the phase space diagram, Kn_Ψ and Kn_D are plotted on the principal axes in the range where Ψ_E is positive. The line $Kn_D = Kn_\Psi/3$ is noted, which corresponds to $\Psi_E = 0.5$ and below which are (Kn_D, Kn_Ψ) pairs where the modified hard sphere $H(Kn_D)$ curve applies in collision kernel calculation. Above this curve, the region bound to the left and below the lines $Kn_D = 2.5$ and $Kn_\Psi = 2.5$ is termed the high potential, near continuum regime, for which equation (13) is

reasonably accurate. Outside these two regions lies the high potential, near free molecular regime, for which mean first passage time calculations can be used for collision kernel calculation, yet a single curve to calculate H is not yet determined. As mentioned in the previous section, however, collisions in the high potential, near free molecular regime are less frequent in aerosol systems than the other two regimes, due to the correlation between high Kn_D and high Ψ_E.

4.4. Conclusions

Dimensional analysis and mean first passage time calculations are used to infer the dimensionless collision kernel H as a function of both Kn_D and Ψ_E for colliding entities which interact via the Coulombic potential. Based on this study the following conclusions are made:

- For $\Psi_E < 0.5$ (weakly attracting entities), the H and Kn_D modified hard sphere curve (developed in Chapter 2) is in excellent agreement with calculations, as are the predictions of flux matching theory (Fuchs, 1963). At 300 K, $\Psi_E < 0.5$ corresponds to singly charged entities with a colliding radius (a_i+a_j) greater than 111 nm.
- For cases where $\Psi_E > 0.5$, we find that the inappropriate speed and impact parameter distributions typically utilized in flux matching theory, combined with difficulties in accounting for three body trapping, lead to underprediction of the collision kernel outside the continuum limit. The alternative linear combination theory, conversely, overestimates the calculation inferred collision kernel. To determine the collision kernel under these conditions, following Gatti and Kortshagen (2008) we define a potential energy based Knudsen number, Kn_Ψ, and show that for cases where the smaller of Kn_D and Kn_Ψ is less than ~2.5, H can be determined as the product of $4\pi Kn_D^2$ and a function of the smaller of Kn_D and Kn_Ψ. This enables collision kernel calculation for colliding entities in a wide size range in atmospheric pressure environments (virtually any sized singly charged particle).

Chapter 5: Unipolar Diffusion Charging of Arbitrary Shaped Aerosol Particles[4]

Building on the length scales from Chapter 3, repulsive Coulombic potential and attractive image potential interactions between an arbitrary shaped particle and a point mass ion are considered here. The hard sphere collision kernel is shown to be applicable for unipolar charging provided the diffusive Knudsen Number is defined appropriately.

5.1. Introduction

The unipolar diffusion charging of aerosol particle (i.e.) particle collisions with gas phase ions of a single polarity, attaining a charge distribution upon timed exposure to ions of a given concentration, is the subject of this chapter. The charging rate, $R_{p,i}$, for particles with p number of excess charges can be calculated from binary reaction kinetics as:

$$\boldsymbol{R_{p,i} = \beta_{p,i} n_p n_i} \quad (1a)$$

where $\boldsymbol{n_p}$ and $\boldsymbol{n_i}$ are the particle and ion number concentrations, respectively, and $\boldsymbol{\beta_{p,i}}$ is the collision rate coefficient/kernel. Correspondingly, the change in number concentration of particles with p charges over time is described by the equation:

$$\boldsymbol{\frac{dn_p}{dt} = R_{p-1,i} - R_{p,i} = n_i\left(\beta_{p-1,i} n_{p-1} - \beta_{p,i} n_p\right)} \quad (1b)$$

for positive ions, with the subscripts *p-1* replaced with *p+1* for negative ions. Evident in equations (1a) and (1b), proper collision kernel evaluation is thus required for both charging rate and charge distribution calculations. As discussed in chapter 4, collision kernels have been predominantly determined using the flux matching approach of Fuchs

[4] Aspects of the results described in this chapter (including some text and figures) have been published in Gopalakrishnan, Thajudeen et al. (2013)

(1963) and Bricard (1962). In the absence of potentials, with an appropriate limiting sphere radius (Wright, 1960) the predictions of flux matching theory agree extremely well with more rigorous derivations of the collision kernel in the transition regime (Sahni, 1966; Loyalka, 1973; Takata *et al.*, 1998). In light of the questionable assumptions about the initialization of the ions on the surface of the limiting sphere in the flux matching theory at high strength of potentials (Filippov, 1993; Gopalakrishnan & Hogan, 2012; López-Yglesias & Flagan, 2013), further examination of the charging process and the development of a collision kernel applicable for unipolar charging are described in this chapter. Moreover, while in earlier studies selected nonspherical particle collisions with ions have been analyzed close to the $Kn_D \rightarrow 0$ and $Kn_D \rightarrow \infty$ limits (Mayya, 1990b; Han, et al., 1991; Han & Gentry, 1993), and Biskos & coworkers (2004) applied a flux matching-like approach to simulate the unipolar charging of selected nonspherical particles, no simple-to-implement expression for the unipolar charging of arbitrary shaped particles under all possible background gas conditions is hitherto available. Specifically, a collision kernel expression which is a function of ion and particle properties, accounts for both repulsive Coulomb and attractive image potentials between ion and particle, and can be extended reasonably to particles of arbitrary size and shape is developed. The mean first passage time calculations discussed before are further extended here, involving a combination of dimensional analysis, molecular dynamics, and Brownian dynamics calculations (Ermak & Buckholz, 1980; Narsimhan & Ruckenstein, 1985). The results presented here demonstrate that the dimensionless collision kernel expression for unipolar charging can be collapsed to a function solely of the diffusive Knudsen number irrespective of the shape of the particle, as it has been for the gas phase collision processes discussed in Chapters 2 – 4.

5.2. Theoretical and Numerical Approach

The development of a collision kernel for unipolar charging requires (1) treatment of the electrostatic interactions involved, (2) analysis in the continuum limit, (3) analysis in the free molecular limit, and (4) analysis in the transition regime. Furthermore, to

examine nonspherical particles, an appropriate set of particle test geometries is necessary. For this purpose ensembles of quasi-fractal point contacting aggregates of spheres are used. (The aggregates satisfy the relationship $\boldsymbol{N = k_f \left(\frac{R_g}{a}\right)^{D_f}}$, where N is the number of primary spheres in each particle, a is the primary sphere radius, k_f is a pre-exponential factor, and D_f is the fractal dimension (Friedlander, 2000)). The computational generation of a wide range of quasi-fractal aggregate test geometries are discussed first, followed by discussion of (1-4).

Table 5.1a: Summary of the test aggregate properties used in trajectory calculations with Coulomb potentials only. R_s and PA for each aggregate are calculated using the methods given in Gopalakrishnan et al. (2011). Noted $\psi_E$values are used in trajectory calculations, and for η_c (eq. 7d), η_f(eq. 8e) calculations, and are determined with R_s as the normalizing length scale.

Quasifractal Parameters	Image	R_s[a]	PA[a]	($\psi_I = 0$) ψ_E	Symbol η_c, η_f, H
N=80 D_f*=2.43*		6.30	121.61	-0.1, -0.5, -1, -2, -3, -5	●, ○, ◇
N=30 D_f*=1.67*		5.47	68.92	-0.21, -0.63, -1.15, -2.7	●, ○, ◇
N=50 D_f*=2.00*	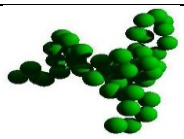	6.22	100.55	-0.33, -0.75, -1.4, -2.8, -4.75	●, ○, ◇
N=80 D_f*=1.95*		8.13	155.91	-0.38, -0.65, -1.3, -2.25	●, ○, ◇
N=60 D_f*=1.63*	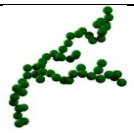	8.35	139.29	-0.44, -0.7, -1.4, -2.4, -3.3	●, ○, ◇
N=45 D_f*=1.78*	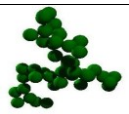	6.50	98.18	-0.5, -1, -2, -3	●, ○, ◇
N=70 D_f*=2.55*		5.73	103.00	-0.15, -0.86, -1.5, -2.5, -3.5	●, ○, ◇
N=65 D_f*=2.32*		6.14	111.19	-0.27, -0.66, -1.55, -2.34, -3.35	●, ○, ◇
N=70 D_f*=2.04*		7.18	133.74	-0.14, -0.44, -1.1, -2.68, -3.67	●,○ , ◇
N=100 D_f*=1.89*		9.28	199.54	-0.05, -0.96, -1.78, -3.58	●, ○, ◇

[a] – Calculated with a primary sphere radius of unity (arbitrary units)

Table 5.1b: Summary of the test aggregate properties used in trajectory calculations with combined Coulomb image-potentials. R_s and PA for each aggregate are calculated using the methods given in Gopalakrishnan et al (2011). Noted ψ_E and ψ_I values are used in trajectory calculations, as well as for η_c (equation 7c) and η_f (equation 8e) calculations, and are determined with R_s as the normalizing length scale.

Quasifractal Parameters	Image	R_s[a]	PA[a]	Cases run		Symbol
				$\psi_E = 0$	$\psi_I = \lvert\psi_E\rvert$ (ψ_E, ψ_I)	η_c, η_f, H
N=2 (Dimer) linear chain	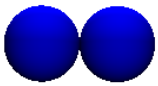	1.39	5.80	0.5, 1, 2, 3, 5	(-0.5, 0.5); (-1, 1); (-2, 2); (-3, 3); (-5, 5)	◐, ◑, ○
N=3 (Trimer) linear cha□n	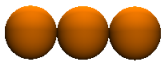	1.72	8.46	3□8, 4.8	(-2.8, 2.8); (-3.8, 3.8); (-4.8, 4.8)	△, ▽, ✚
N=5 (Pentamer) linear chain	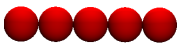	2.32	13.78	3.7, 4.7	(-2.7, 2.7); (-3.7, 3.7); (-4.7, 4.7)	▬, ▬, □
N=5 D_f=1.78		2.19	13.28	3.9, 4.9	(-2.9, 2.9); (-3.9, 3.9)	◩, ◪, □
N=5 D_f=2.50	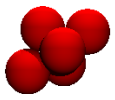	1.97	12.09	3.6, 4.6	(-2.6, 2.6); (-3.6, 3.6); (-4.6, 4.6)	▣, ▣, □
N=10 (Decamer) linear chain		3.59	27.07	3.3, 4.3	(-2.3, 2.3); (-3.3, 3.3); (-4.3, 4.3)	◐, ◑, ○
N=10 D_f=1.78		3.03	24.72	3.2, 4.	(-2.2, 2.2); (-3.2, 3.2); (-4.2, 4.2)	◒, ◓, ○
N=10 D_f=2.50	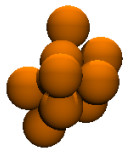	2.58	21.10	3.3, 4.	(-2.3, 2.3); (-3.3, 3.3); (-4.3, 4.3)	◆, ◆, ◇

[a] – Calculated with a primary sphere radius of unity (arbitrary units)

5.2.1. Generation of Quasifractal Aggregates

10 quasifractal aggregates with D_f ranging from 1.63 to 2.55, k_f = 1.3, and 30 to 100 primary particles are used to examine unipolar charging with the Coulomb potential alone considered. All of these aggregates are generated via a cluster-cluster algorithm as described by Filippov et al (2000), with images and properties listed in Table 5.1a. Similarly, Table 5.1b displays images of the aggregates used to examine combined Coulomb and image potentials in unipolar charging. These aggregates are produced via a sequential algorithm, again as described by Filippov et al, and contain fewer primary particles than the aggregates used in examining Coulomb potentials alone; when image potentials are considered the use of aggregates with a large number of primary particles becomes exceedingly computationally expensive. In conjunction with quasifractal aggregates, linear chains of 2 to 10 primary particles are also used when combined Coulomb and image potentials are considered. Finally, for the purpose of plotting results of computations, symbols corresponding to the results for each aggregate are displayed in the furthest right columns of tables 5.1a and 5.1b, with the parameters plotted introduced in the forthcoming sections.

5.2.2. Functional Form of Potentials

As an ion moves about a particle, long range repulsive Coulomb interactions influence motion, and for particles of complex geometry the potential distribution must be appropriately described in charging rate calculations. Similarly, for ions in close vicinity to a conducting particle, the ion itself induces a short range attractive image potential on the particle surface. This has been shown to have a significant effect on aerosol particle charging (Brock, 1970), and thus must be accounted for in the charging of both spherical and nonspherical particles. Here, in calculating potentials, the ion is modeled as a point mass, which considerably simplifies the functional form of the potentials for particles made of conducting and dielectric materials. For spherical particles these functional forms are straightforward (Jeans, 1925; Jackson, 1975) and are

used in most studies of unipolar charging (Fuchs, 1963; Huang, et al., 1991). However, potential functions are complicated when the geometry of the particle is also complex. Therefore, we limit potential function calculations to the aforementioned ensembles of spheres, first presenting the form of the Coulomb potential and second the image potential. For both potentials, the use of ensembles of spheres as test particles drastically simplifies calculations, and the total potential function is obtained by superposition of these two potentials.

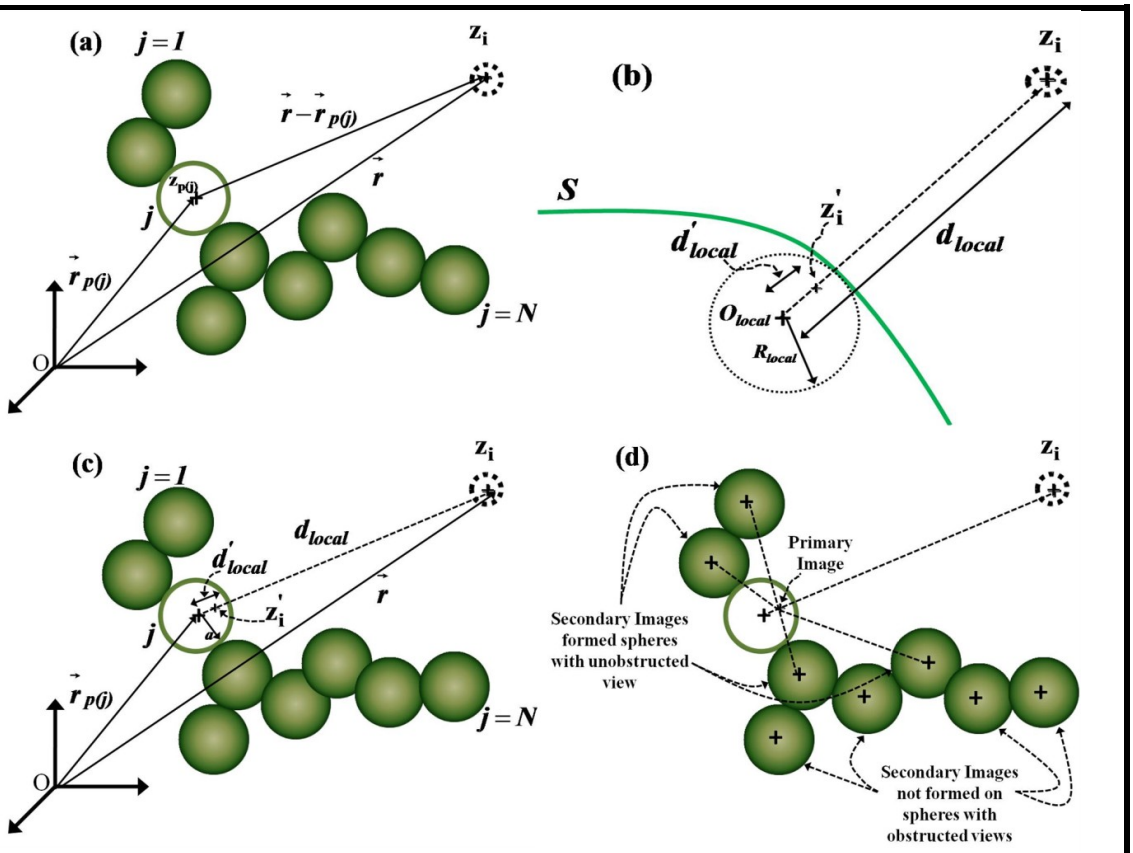

Figure 5.1: (a). A depiction of the Coulomb energy between an ion and primary particle in an aggregate. (b). A depiction noting how an image is formed on a curved surface. (c). A depiction of the calculation of the primary images formed on the primary spheres of the aggregate due to the ion. For a sphere, the local radius of curvature is the radius and local center of curvature is the center. (d.) A depiction of the formation of Secondary images off of other primary spheres from a single image. Images are formed only on those spheres whose view is not hidden by others. By successive reflections, an infinite set of images are formed.

In calculating the Coulomb potential energy of an ion, the primary spheres are assumed to interact with the ion independent of one another and the distribution of charge on the particle is assumed to be unperturbed by the approach of the ion. The charge on each primary sphere is calculated by minimizing the total electrostatic energy of the aggregate, while conserving its total charge, as is described by Brown & Hemingway (1995). The Coulomb potential ($\boldsymbol{\varphi_{coul}}$) of the ion at an arbitrary point outside the particle (whose position vector is $\vec{\boldsymbol{r}}$ from the origin) can be summed from the potentials due to each primary sphere, and is given as:

$$\boldsymbol{\varphi_{coul}}(\vec{\boldsymbol{r}}) = \frac{\boldsymbol{z_i z_p}}{\boldsymbol{4\pi\varepsilon_o}} \sum_{\boldsymbol{j=1}}^{\boldsymbol{N}} \frac{(\boldsymbol{z_{p(j)}/z_p})}{|\vec{\boldsymbol{r}} - \vec{\boldsymbol{r}}_{\boldsymbol{p(j)}}|} \qquad (2)$$

wherein $\boldsymbol{z_p}$ is the total charge on the particle, $\vec{\boldsymbol{r}}_{\boldsymbol{p(j)}}$ and $\boldsymbol{z_{p(j)}/z_p}$ are the position vector of the center of primary sphere $\boldsymbol{j}$ and the fraction of the total charge on it, as is depicted Figure 5.1a.

When an ion approaches a conducting particle, an additional charge density is induced on the particle surface, which ensures the electric field inside the particle remains at the same value in the absence of the ion. The induced charge density depends on the position of the ion relative to the particle and the curvature of the surface. It can be simulated by placing fictitious charges (images) inside the particle (Jackson, 1975). Depicted in figure 5.1b is an insulated, conducting, and uncharged surface $\boldsymbol{S}$ with local radius of curvature $\boldsymbol{R_{local}}$ from the local center of curvature $\boldsymbol{O_{local}}$ as well as a point mass ion (carrying a charge of $\boldsymbol{z_i}$) at a distance $\boldsymbol{d_{local}}$ from $\boldsymbol{O_{local}}$. At the location $\boldsymbol{d'_{local}} = \frac{\boldsymbol{R^2_{local}}}{\boldsymbol{d_{local}}}$ (from $\boldsymbol{O_{local}}$), an image charge of strength $\boldsymbol{z'_i} = -\frac{\boldsymbol{R_{local}}}{\boldsymbol{d_{local}}}\boldsymbol{z_i}$ is induced. The image is always induced on the same side of the surface as $\boldsymbol{O_{local}}$ and opposite in polarity to the external charge $\boldsymbol{z_i}$. Once the image is positioned, the potential energy of the ion due to the image, $\boldsymbol{\varphi_{image}}$, can be calculated as:

$$\boldsymbol{\varphi_{image}} = -\frac{\boldsymbol{z_i^2}}{\boldsymbol{4\pi\varepsilon_o}} \frac{\boldsymbol{R^3_{local}}}{\boldsymbol{2d^2_{local}(d^2_{local} - R^2_{local})}} \qquad (3)$$

For a sphere, the above result is easily recognized as the image potential used in the analysis of charging of aerosol particles in numerous studies (Brock, 1970; Hoppel &

Frick, 1986). For particles composed of point-contacting spheres, the center of curvature is the center of each primary sphere in consideration and the radius of curvature is the corresponding primary sphere radius, as is depicted in Figure 5.1c.

The charge induced on one portion of a particle surface causes charges to accumulate on other surfaces as well, in order to conserve the total charge on the particle. As shown in Figure 5.1d, this is taken into account in calculating the potential energy of the ion by considering secondary images. To determine the position and strength of secondary images, the procedure described previously is applied, with the secondary images induced by the primary images (those induced by the ion itself). A secondary image is formed from a primary image on a surface if and only if the line joining the center of the primary sphere and the primary image is non-intersecting with or tangential to all other primary spheres, with the exception of the primary sphere in which the primary image itself is located. From the primary images, a first generation of secondary images is thus induced. Subsequently, a second generation of secondary images is induced by the first generation; a new generation is always induced by the previous, analogous to optical images formed by reflections in a series of mirrors (Jeans, 1925). The contribution of all images to the total image potential is summed as an infinite series, which is convergent due to the ever decreasing magnitude of the images with each generation. Here, the infinite series is approximated as the sum of the contributions of the primary images and the first two generations of secondary images, as the determination of the positions and strengths of each new generation is computationally more expensive than the previous generation. By superposition, the total potential experienced by the ion considering Coulomb and image effects, $\boldsymbol{\varphi}(\vec{\boldsymbol{r}})$, is then calculated as:

$$\boldsymbol{\varphi}(\vec{\boldsymbol{r}}) = \frac{z_i z_p}{4\pi\varepsilon_o}\sum_{j=1}^{N}\frac{(z_{p(j)}/z_p)}{|\vec{r}-\vec{r}_{p(j)}|} - \frac{z_i^2}{4\pi\varepsilon_o}\sum_{g=1}^{3}\sum_{l=1}^{I_g}\left\{\frac{(-1)^g a^3}{2|\vec{r}-\vec{r}_{p(l)}|^2(|\vec{r}-\vec{r}_{p(l)}|^2-a^2)}\right\} \qquad (4)$$

where g denotes the image generation number (g=1 for primary images) and I_g is the total number of images induced in generation g.

The presented calculations are performed in a dimensionless fashion, enabling determination of a particle-ion collisions kernel applicable under arbitrary background gas conditions. In non-dimensionalizing electrostatic potentials, characteristic length scale for the particle shape in question is needed. From prior studies (Mayya, 1990b; Douglas, et al., 1994; Zhou, et al., 1994), considering Coulomb potentials alone this length scale is identified as the "capacity", also termed the Smoluchowski radius, R_s in chapter 3. Specifically, R_s is the length scale used to evaluate the collision kernel between a point mass and an object in the continuum regime. It is similarly the characteristic length scale for all physical phenomena which are described via Laplace equations, hence its application to electrostatics of conducting media. Calculated R_s values are reported in tables 5.1a and 5.1b.

It is asserted (with later justification) that R_s is also the appropriate length scale for the non-dimensionalization of the image potential. The dimensionless potential energy, normalized by the thermal energy of the ion ($\boldsymbol{kT}$, where k is the Boltzmann constant and T is the ion/background gas temperature) is hence:

$$\frac{\varphi(\vec{r}^*)}{\boldsymbol{kT}} = \frac{R_s}{a}\left\{-\boldsymbol{\psi_E}\sum_{j=1}^{N}\frac{(z_{p(j)}/z_p)}{|\vec{r}^*-\vec{r}^*_{p(j)}|} - \boldsymbol{\psi_I}\sum_{g=1}^{3}\sum_{l=1}^{I_g}\left\{\frac{(-1)^g}{2|\vec{r}^*-\vec{r}^*_{p(l)}|^2(|\vec{r}^*-\vec{r}^*_{p(l)}|^2-1)}\right\}\right\} \tag{5a}$$

where the superscript "*" denotes that the coordinates and distances are expressed in non-dimensional form (normalized by primary radius, a, though this choice is arbitrary), $\boldsymbol{\psi_E}$ is the Coulomb potential energy ratio and $\boldsymbol{\psi_I}$ is the image potential energy ratio:

$$\boldsymbol{\psi_E} = -\frac{z_i z_p}{4\pi\varepsilon_o R_s kT} \tag{5b}$$

$$\boldsymbol{\psi_I} = \frac{z_i^2}{4\pi\varepsilon_o R_s kT} \tag{5c}$$

For spherical particles of radius a_p, these equations reduce to:

$$\frac{\varphi(r^*)}{\boldsymbol{kT}} = -\frac{\psi_E}{r^*} - \frac{\psi_I}{2r^{*2}(r^{*2}-1)} \tag{6a}$$

$$\boldsymbol{\psi_E} = -\frac{z_i z_p}{4\pi\varepsilon_o a_p kT} \tag{6b}$$

$$\boldsymbol{\psi_I} = \frac{z_i^2}{4\pi\varepsilon_o a_p kT} \tag{6c}$$

Repulsive Coulomb interactions between the particle and the ion are characterized by $\boldsymbol{\psi_E} < 0$, and the because the image interaction is always attractive, $\boldsymbol{\psi_I} > 0$. Here, we consider $|\boldsymbol{\psi_E}|$ and $\boldsymbol{\psi_I}$ values between 0 and 5; $\boldsymbol{\psi_E = -5}$ corresponds to a collision between like a charged ion and a singly charged spherical particle ~22 nm in diameter at 300 K. The choice of this absolute limit for the strength of the interaction is constrained by the computation time. To model unipolar charging, only negative values of $\boldsymbol{\psi_E}$ (i.e.) collisions between like charged particles are considered.

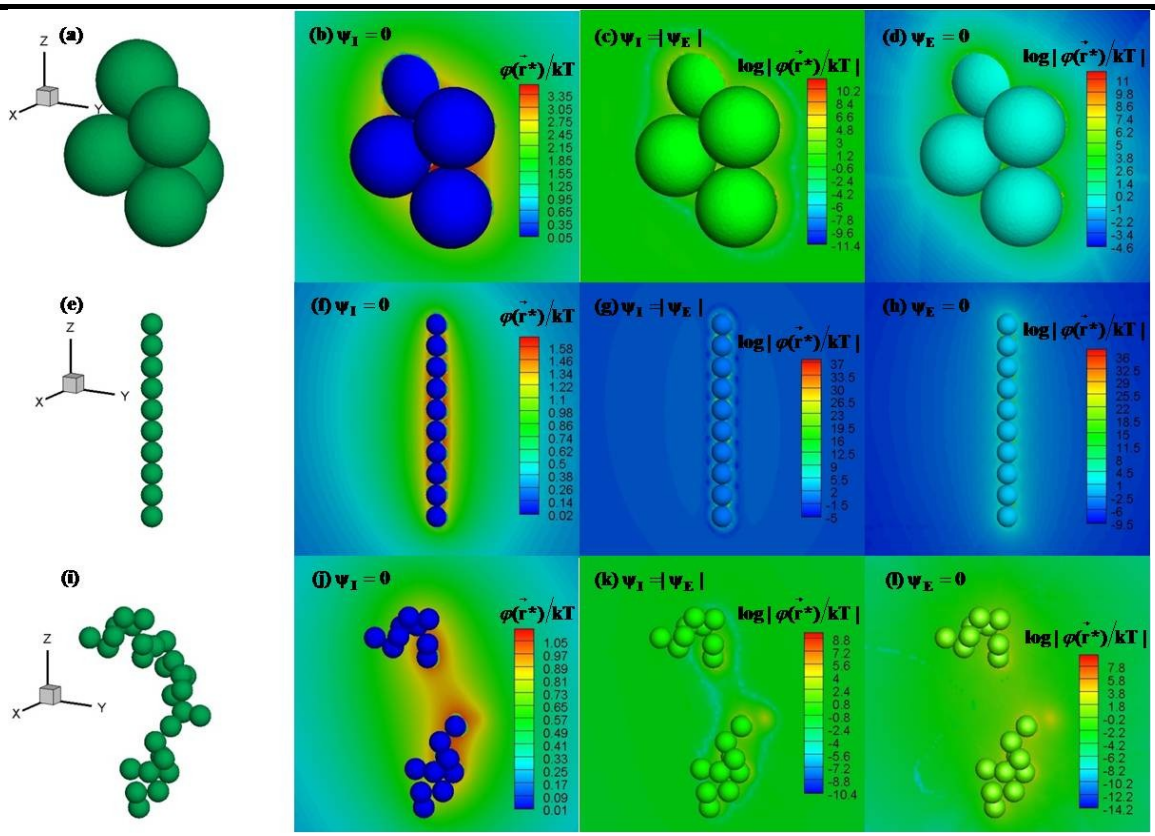

Figure 5.2: Contour plots of the electrostatic potential around selected aggregates. Parts (a,e,i) show the particle geometry alone; Parts (b,f,j) display contour plots in the presence of the Coulomb potential only($\boldsymbol{\psi_E = -5, \psi_I = 0}$); Parts (c,g,k) display contour plots in the presence of the combined Coulomb and image potential ($\boldsymbol{\psi_E = -5, \psi_I = 5}$) with color variation logarithmically. Parts (d,h,l) display contour plots in the presence of the image potential alone ($\boldsymbol{\psi_E = 0, \psi_I = 5}$), also with color variation on a logarithmic scale.

With selected values of $\boldsymbol{\psi_E}$and $\boldsymbol{\psi_I}$, contour plots of the spatial distribution of the ion's potential energy in a cross section are shown in Figures 5.2(a-l). In cases where the image potential is included, the color variation is logarithmic with dimensionless potential as the potential rapidly approaches $-\infty$ at the particle surface. Such potential distributions are used in determining the collision kernel in the continuum, free molecular, and transition regimes through ion trajectory calculations. These trajectory calculations are described in Appendix B, the results of which are compared to the collision kernel expression proposed in subsequent sections.

5.2.3. Continuum Regime Collision Kernel

In the $Kn_D \rightarrow 0$ limit, it has been shown in previous chapters and elsewhere (Laframboise & Chang, 1977; Northrup, et al., 1984; Mayya, 1990b; Filippov, 1994) that the hard sphere collision kernel for spherical and nonspherical particles alike are determined by the Smoluchowski collision kernel. Also, the potential energy of the ions is accounted using a dimensionless continuum enhancement factor $\boldsymbol{\eta_c}$ (Fuchs, 1964) as:

$$\boldsymbol{\beta_c = 4\pi R_s \frac{kT}{f_i} \eta_c} \tag{7a}$$

Based on potential energy considerations, for spherical particles, $\boldsymbol{\eta_c}$ can be evaluated as:

$$\boldsymbol{\eta_c(\psi_E, \psi_I) = \left(\int_1^\infty \frac{1}{r^{*2}} \exp\left(\frac{\varphi(r^*)}{kT}\right) dr^* \right)^{-1}} \tag{7b}$$

For a given set of values for $\boldsymbol{\psi_E}$ and $\boldsymbol{\psi_I}$, equation (7b) can be evaluated with the potential described by equation (6a). From chapter 4, it may be recalled that for purely coulombic potentials, equation 7b can be evaluated analytically as:

$$\boldsymbol{\eta_c(\psi_E) = \frac{\psi_E}{1 - \exp(-\psi_E)}} \tag{7c}$$

For a complex geometry particle, calculation of η_c requires an alternative approach to equation (7b), as the potential not only varies radially, but also with the azimuthal and polar angles. However, nondimensionalization suggests that $\boldsymbol{\eta_c}$ should depend solely on properly defined $\boldsymbol{\psi_E}$and $\boldsymbol{\psi_I}$; thus we propose that $\boldsymbol{\eta_c}$ may be determined using equation (7a), with the potential described in equation (6a) but replacing a_p with R_s for particles of arbitrary shape (i.e. the dimensionless function $\boldsymbol{\eta_c(\psi_E, \psi_I)}$ should not depend on particle

shape). The values of the function $\boldsymbol{\eta_c(\psi_E, \psi_I)}$ determined for a sphere are shown in Appendix B. The applicability of η_c determined in this manner for arbitrary shaped particles is tested through η_c determination from Brownian dynamics (BD) trajectory calculations (Ermak, 1975) of the average time required for an inertialess ion to contact a particle, using the noted test aggregates.

5.2.4. Free molecular collision kernel

Collisions in the $Kn_D \rightarrow \infty$ limit are analyzed using the principles of kinetic gas theory. Building on prior work in dilute systems (Allen, 1992; Zhang *et al.*, 2011), the free molecular collision kernel $\boldsymbol{\beta_f}$ is calculated as follows: in cylindrical coordinates with a particle in a specific orientation, Γ, an ion's position and motion are specified by the impact parameter, b , the cylindrical polar angle θ, and the ion's speed $\boldsymbol{v_i}$,which follows the Maxwell-Boltzmann distribution function, $\boldsymbol{f(v_i)dv_i = 4\pi(m_i/2\pi kT)^{\frac{3}{2}} v_i^2 exp\,(-m_i v_i^2/2kT)dv_i}$ (see Appendix B figure B1 for a schematic displaying the impact parameter and polar angle) when the ion is sufficiently far from the particle (i.e. where the potential energy is zero). The collision kernel for this particle orientation, $\boldsymbol{\beta_{f,\Gamma}}$, is determined by integrating in cylindrical coordinates the ion concentration normalized-flux distribution ($\boldsymbol{vf(v)dv}$) between speeds ($\boldsymbol{v_1, v_2}$), for which the ion collides with the particle. The collision kernel depends on the impact parameter as well as the potential via the relationship:

$$\boldsymbol{\beta_{f,\Gamma} = \int_{b=0}^{\infty} \int_{\theta=0}^{2\pi} \int_{v=v_1(b,\theta,\psi_E,\psi_I)}^{v=v_2(b,\theta,\psi_E,\psi_I)} vf(v)bdvdbd\theta} \qquad (8a)$$

$\boldsymbol{\beta_f}$ is subsequently determined by averaging $\boldsymbol{\beta_{f,\Gamma}}$ over all orientations:

$$\boldsymbol{\beta_f = \int \beta_{f,\Gamma} f(\Gamma) d\Gamma} \qquad (8b)$$

where *f(*Γ*)* denotes the distribution function over all particle orientations (uniform). In the case of hard sphere interactions, the paths of ions are straight lines between collisions and particle-ion collisions take place if these lines intersect with the contours of the particle. Therefore, the hard sphere free molecular kernel $\boldsymbol{\beta_{f(HS)}}$ is calculated as a product of the mean thermal speed of the ion $\boldsymbol{\bar{c}_i = \sqrt{8kT/\pi m_i}}$ and the orientationally

averaged projected area of the particle *PA*. For collisions with a spherical particle of radius a_p, this leads to the well-known result:

$$\boldsymbol{\beta_{f(HS)} = \sqrt{\frac{8\pi kT}{m_i}}\, a_p^2} \tag{8c}$$

For nonspherical particles, $\boldsymbol{PA}$ values were calculated (listed in tables 5.1a and 5.1b) using the Monte-Carlo methods described in (Gopalakrishnan, et al., 2011).

Analogous to the approach in the continuum regime, it is desirable to account for the influence of potential interactions on the collision kernel using a free molecular enhancement factor, $\boldsymbol{\eta_f}$, which can be defined as the ratio of the free molecular collision kernel to the hard sphere kernel:

$$\boldsymbol{\beta_f = \beta_{f(HS)}\eta_f = \sqrt{\frac{8kT}{\pi m_i}}\, PA\eta_f} \tag{8d}$$

For spherical particles, the functional dependence of the range of speeds on the impact parameter has been analytically evaluated for finite contact potentials (Mott-Smith & Langmuir, 1926; Allen, 1992). For cases in which only the (repulsive) Coulomb potential is considered ($\boldsymbol{\psi_I = 0\ and\ \psi_E} < 0$), the free molecular enhancement factor is:

$$\boldsymbol{\eta_f = \exp(\psi_E)} \tag{8e}$$

With singular contact potentials (such as the image potential and combined Coulomb-image potential), the free molecular enhancement factor is calculated for spheres as (Ouyang, et al., 2012):

$$\boldsymbol{\eta_f = 2\int_{v=0}^{\infty} v^{*3} \exp\left(-v^{*2}\right) b_{crit}^{*2}(v^*, \psi_E, \psi_I)\, dv^*} \tag{8f}$$

where $\boldsymbol{v^*}$ is the speed of the ion (normalized by $\sqrt{\boldsymbol{2kT/m_i}}$) and $\boldsymbol{b_{crit}^*}$, the dimensionless critical radial impact parameter (normalized by $\boldsymbol{a_p}$), is the minimum value of the radial impact parameter for a given set of $\boldsymbol{v^*, \psi_E, \psi_I}$ values for which particle-ion collisions occur. Values of $\boldsymbol{\eta_f(\psi_E, \psi_I)}$ calculated with equation (8f) are shown in Appendix B.

Also in parallel to analysis of the continuum regime, calculation of η_f for complex geometries requires use of ion trajectory calculations over varying ion speeds, polar angles, and particle orientations, though in the free molecular regime such calculations

are performed for frictionless, inertial ions (similar to molecular dynamic, MD, simulations). We propose that like its continuum regime counterpart, η_f will collapse to the functional form $\boldsymbol{\eta_f(\psi_E, \psi_I)}$, where the values determined for a sphere are applicable to any geometry, provided $\boldsymbol{\psi_E}$ and $\boldsymbol{\psi_I}$ are determined using the R_s of the particle in question. We test the validity of this assumption by calculating η_f directly for the test aggregates from MD trajectory simulations.

5.2.5. Transition Regime Collision Kernel

In the $Kn_D \rightarrow 0$, limit, equation (7a) can be used to predict the particle-ion collision kernel, while in the $Kn_D \rightarrow \infty$ limit, equation (8d) may be used for collision kernel prediction. Both of these equations require calculation of geometric parameters, R_s and PA, respectively. Further it is proposed that the dimensionless enhancement factors necessary may be evaluated for spheres and generalized to arbitrary shapes by expressing dimensionless energy ratios in terms of R_s. While the validity of this generalization in describing the collision kernel in the intermediate Kn_D range (the transition regime) s later examined, *an priori* assumption that the use of equations (7e) and (8d) are valid in the low and high Kn_D limits, respectively is made at this point.

In the transition regime, ion motion is affected by both inertia and thermal energy; hence, the collision kernel is a function of all and only the parameters which govern the continuum and free molecular collision kernels. Continuing on the approach developed for hard sphere interactions for spheres (chapter 2) and non-spheres (chapter 3), and the effect of potentials (chapter 4), the definitions of $\boldsymbol{Kn_D}$ and $\boldsymbol{H}$ are extended to include the effect of potential interactions (coulombic and image) for arbitrary shaped particles as:

$$\boldsymbol{Kn_D} = \frac{\sqrt{m_i kT}}{f_i}\frac{\pi R_s \eta_c}{PA\eta_f} \quad \text{(non-sphere with potentials)} \tag{9a}$$

$$\boldsymbol{H} = \frac{\beta m_i}{f_i}\left(\frac{\pi^2 R_s \eta_c}{PA^2 \eta_f^2}\right) \quad \text{(non-sphere with potentials)} \tag{9b}$$

With the above definitions and the collision kernels for the continuum (equation 7a) and free molecular regimes (equation 8d), limiting functional forms of $\boldsymbol{H}$ are given as:

$$\boldsymbol{H = 4\pi Kn_D^2} \text{ as } \boldsymbol{Kn_D \to 0} \tag{9c}$$

$$\boldsymbol{H = \sqrt{8\pi} Kn_D} \text{ as } \boldsymbol{Kn_D \to \infty} \tag{9d}$$

In the intermediate Kn_D range, the transition regime expression, found to successfully describe a wide range of collision limited mass transfer problems is repeated here:

$$\boldsymbol{H(Kn_D) = \frac{4\pi Kn_D^2 + C_1 Kn_D^3 + \sqrt{8\pi} C_2 Kn_D^4}{1 + C_3 Kn_D + C_4 Kn_D^2 + C_2 Kn_D^3}} \tag{10}$$

where $\boldsymbol{C_1 = 25.836, C_2 = 11.211, C_3 = 3.502}$ and $\boldsymbol{C_4 = 7.211}$. Along with the results for repulsive interactions described in this chapter, equation (10) has further been found applicable for spherical particles in the presence of the image potential (Ouyang, et al., 2012). Therefore, we propose that it will remain approximately valid for the combined repulsive Coulomb-image potential, not only for spherical particles, but also any particle geometry provided (9a) and (9b) define Kn_D and H, respectively.

Mean first passage time calculations along with other types of trajectory simulations are used to determine H as a function of input Kn_D, $\boldsymbol{\psi_E}$, and $\boldsymbol{\psi_I}$ for the noted test aggregates, to test the validity of equation (10) for spherical and nonspherical particle-ion collisions in the presence of Coulomb-image potentials. The procedure for these calculations is described in detail in Appendix B.

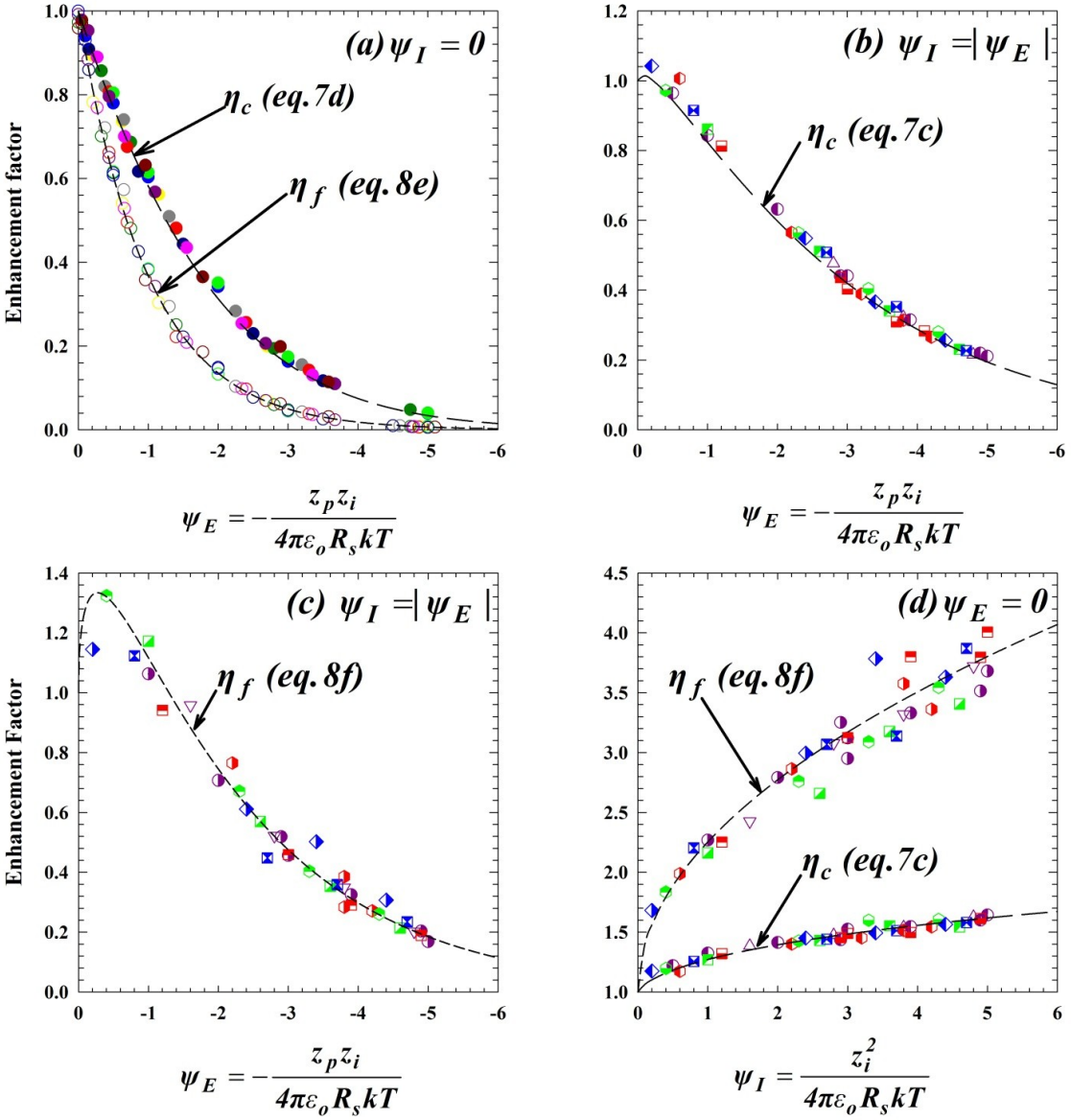

Figure 5.3: The continuum and free molecular enhancement factors computed for various shapes via both trajectory calculations (symbols, with the corresponding aggregates noted in tables 5.1a and 5.1b) and through expressions developed for spherical particles (dashed lines). (a). Continuum and free molecular enhancement factors in instances in which the Coulomb potential only is considered (table 5.1a aggregates). (b). The continuum enhancement factor in instances in which the combined Coulomb-image potential is considered (table 5.1b aggregates). (c). The free molecular enhancement factor in instances in which combined Coulomb-image potential is considered (table 5.1b aggregates). (d). Continuum and free molecular enhancement factors in instances in which the image potential only is considered (table 5.1b aggregates).

5.3. Results & Discussion

5.3.1. Nonspherical Particle-Ion Collisions in the Continuum and Free Molecular Regimes

Considering Coulomb potentials only and the aggregates in table 5.1a, figure 5.3a displays BD trajectory calculation inferred η_c values and MD trajectory calculation inferred η_f values, both as functions of the input values of $\boldsymbol{\psi_E}$ ($\boldsymbol{\psi_E}$noted in table 1a with R_s used as the normalizing value). The symbols used for each aggregate in this plot are also listed in table 1a. Additionally displayed are dashed lines corresponding to the enhancement factors predicted by equation (7c) (η_c) and equation (8e) (η_f) as functions of $\boldsymbol{\psi_E}$. Immediately apparent is the good agreement between the results of trajectory calculations and the equations predicting enhancement factors for spheres; trajectory calculation inferred values and equation calculated values are all within 10% of one another. Considering the inherent statistical nature of both BD and MD trajectory calculation procedures, such agreement verifies the prior proposition (Mayya, 1990b) that for particles of all shape, enhancement factors in both the continuum and free molecular regimes may be calculated using equations developed for spheres, but with $\boldsymbol{\psi_E}$determined using R_s (the capacity/Smoluchowski radius) as the normalizing length scale.

Evidenced in figures 5.3b-d, trajectory calculations also suggest that for the combined Coulomb-image potential and the image potential alone, enhancement factors for arbitrary shaped conducting particles may indeed be determined from equations applicable to spheres. Specifically, figure 5.3b displays η_c inferred from BD trajectory calculations and calculated with equation (7b) as function of $\boldsymbol{\psi_E}$ and under conditions where $\boldsymbol{\psi_I} = |\boldsymbol{\psi_E}|$. Figure 5.3c displays η_f inferred from MD trajectory calculations and calculated with equation (8f) under identical conditions to those in figure 5.3b. Finally, figure 5.3d displays both trajectory calculation inferred η_c and η_f values as well as equation (7b) and equation (8f) predictions as a function of $\boldsymbol{\psi_I}$, with $\boldsymbol{\psi_E} = \mathbf{0}$. For all results displayed in figures 5.3b-d, the aggregate geometries are those listed in table 5.1b

(where the symbols used in plots are noted). Again, trajectory calculation results are within 10% of the equation predictions under all circumstances, within the margin of statistical variation for such calculations. We hence conclude that the approach suggested in prior sections for unipolar charging rate calculation in the continuum and free molecular limits is reasonably valid for conducting particles i.e. we conclude that equations (7a) and (8d) hold valid in these limits, as do the dimensionless equations (9c) and (9d) with Kn_D and H defined by equations (9a) and (9b), respectively.

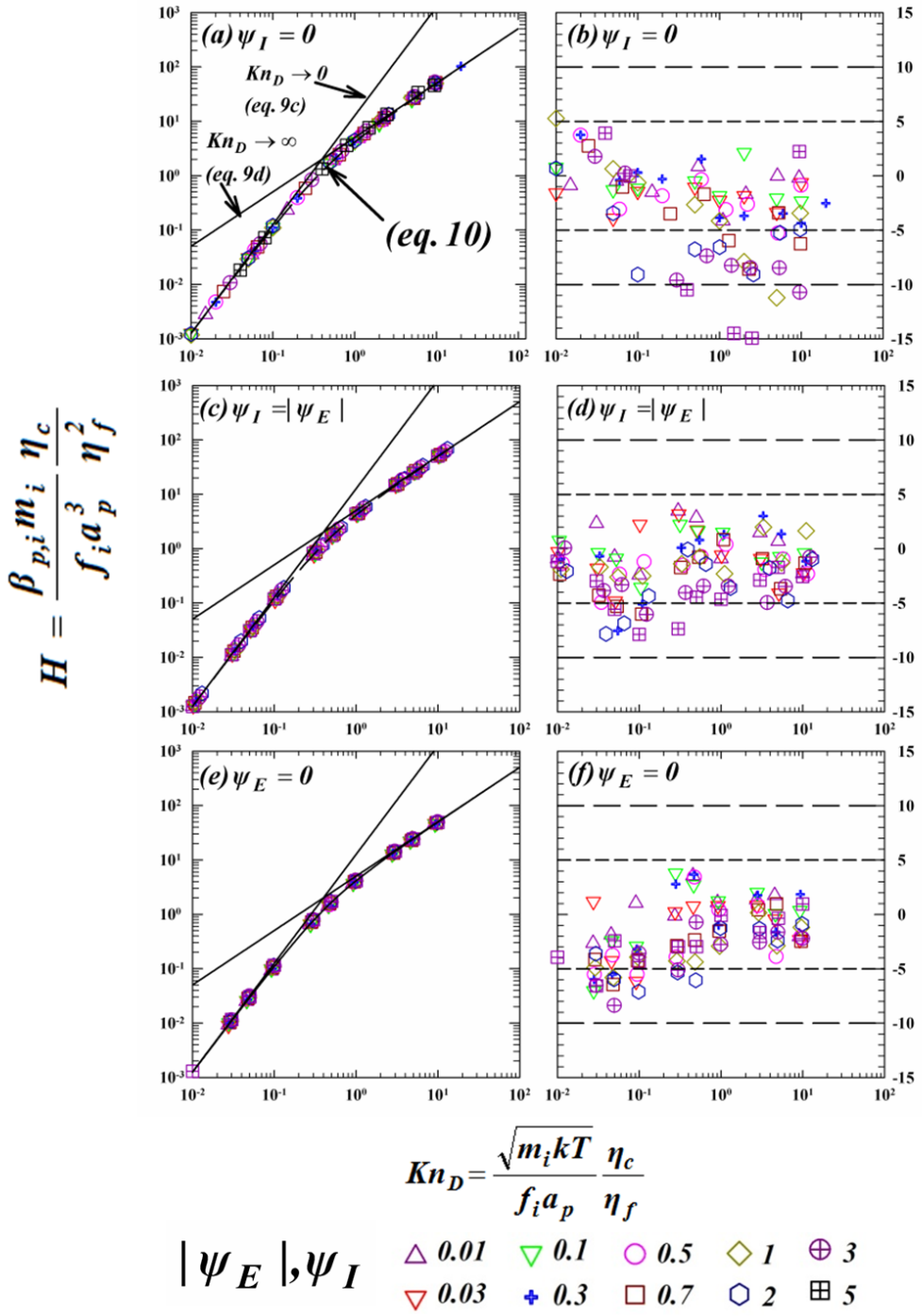

Figure 5.4: MFPT inferred dimensionless collision kernels for spherical particles, compared to equation (10) calculations. (a)., (c)., & (e). display H as a function of Kn_D, while (b)., (d)., & (f). are plots of the relative difference between equation (10) calculations (H_{eq10}) and MFPT inferred values (H_{MFPT}).

5.3.2. Particle-Ion Collisions in the Transition Regime

The values of the dimensionless collision kernel inferred from MFPT trajectory calculations are plotted as a function of Kn_D and compared to the predictions of equation (10) in figures 5.4(a-f), under conditions where $\boldsymbol{\psi_I = 0}$ (a & b), $\boldsymbol{\psi_I = |\psi_E|}$ (c&d), and $\boldsymbol{\psi_E = 0}$ (e & f). For trajectory calculations, Kn_D and H are defined via equation (9a) and (9b) respectively. In figures 5.4b, 5.4d, & 5.4f, H_{MFPT} denotes the value of H determined from MFPT calculations, and H_{eq10} denotes the value determined from regression equation (10). Based on the results of continuum BD and free molecular MD calculations, the agreement found between MFPT calculated and equation (10) determined H values in the low and high Kn_D limits, respectively, is expected, and simply demonstrates that MFPT calculations converge to the correct results in these limits. The results shown in figures 5.4c & 5.4d thus extend the validity of the $H(Kn_D)$ regression curve to spherical particles in the presence of the combined repulsive Coulomb-image potential.

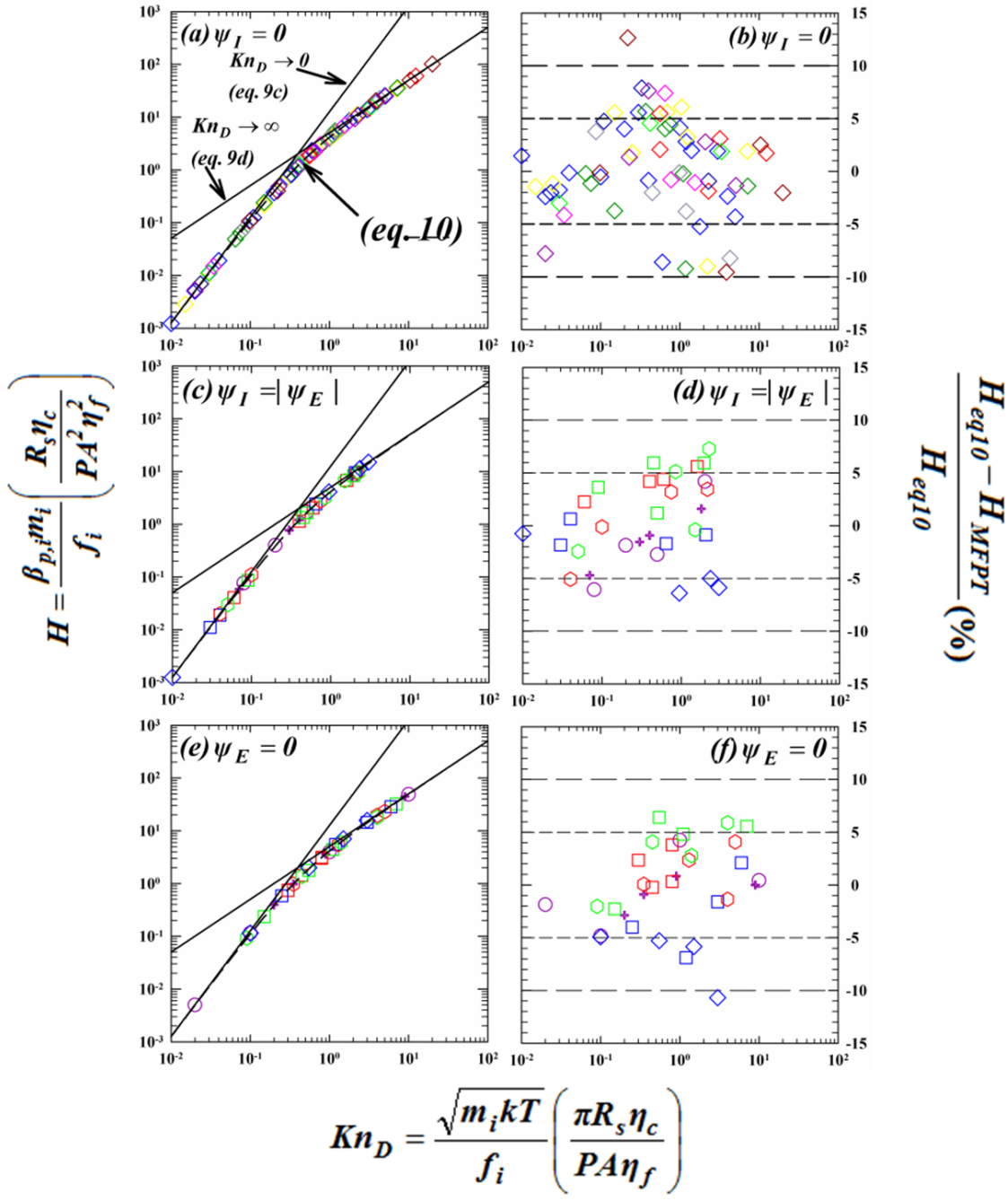

Figure 5.5; MFPT inferred dimensionless collision kernels for the nonspherical particles noted in tables 1a and 1b, compared to equation (10) calculations. (a)., (c)., & (e). display H as a function of Kn_D, while (b)., (d)., & (f). are plots of the relative difference between equation (10) calculations (H_{eq10}) and MFPT inferred values (H_{MFPT}).

Analogous to figures 5.4(a-f), figures 5(a-f) display a comparison of H inferred from trajectory calculations to the predictions of equation (10), with MFPT calculations performed with the aggregates in table 1a ($\boldsymbol{\psi_I = 0}$) and table 1b ($\boldsymbol{\psi_I \neq 0}$). The symbols used for each aggregate are additionally provided in the tables. Overall, MFPT calculation results with aggregates are indistinguishable from MFPT results for spheres, with most MFPT inferred dimensionless collision kernels within 5% of equation (10) calculations. Based on these results, we conclude that the presented calculation approach is not only valid in the $Kn_D \rightarrow 0$ and $Kn_D \rightarrow \infty$ limits, but that equation (10) applies for calculation of the dimensionless particle-ion collision kernel for particles of all shapes and geometric extents, under all background gas conditions (at thermal equilibrium), and for all ion properties.

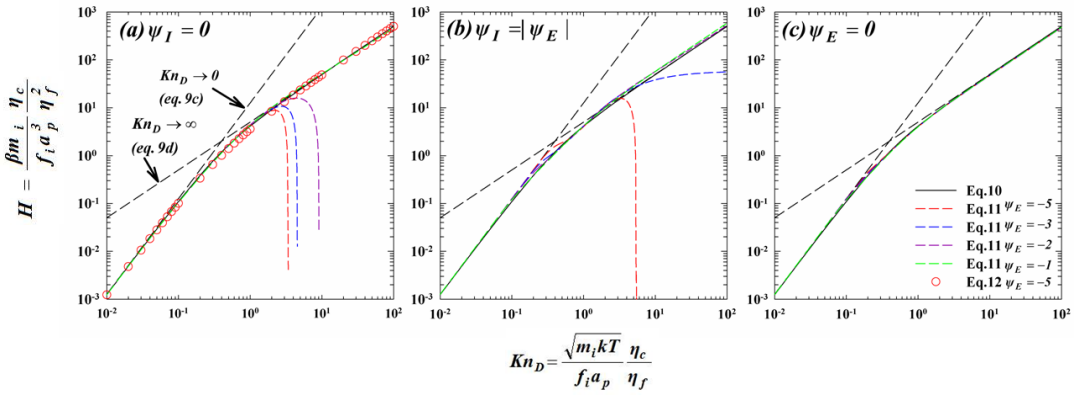

Figure 5.6: Comparison between equation (10) calculations and those of flux matching theory (equations (11) and (12). (a). Instances in which only Coulomb potential is considered (b). Instances in which both the Coulomb and image potential are considered. (c). Instances in which only the image potential is considered.

5.3.3. Comparison to Flux Matching Theory for Spheres

While verification of equation (10) for unipolar charging via trajectory calculations is promising, it is also important to compare equation (10) to the predictions of flux matching theory under similar conditions. We examine two formulations of flux matching theory. First, we examine the version described by Fuchs (1963), in which the

combined Coulomb-image potential is used, but all ions approaching the limiting sphere are assumed to enter the inner, free molecular region at the mean thermal speed. Second, we compare to the more recent version by D'yachkov et al. (2007), in which incoming ions on the limiting sphere surface have Maxwell-Boltzmann distribution speeds, but only the repulsive Coulomb potential is considered to obtain a closed form analytic. Both instances of flux matching are applied to spherical particles. In the framework of the dimensionless collision kernel and the diffusive Knudsen number, Fuch's flux matching theory can be expressed as:

$$\boldsymbol{H = \frac{4\pi Kn_D^2}{\frac{\sqrt{2\pi Kn_D}\eta_f}{\alpha {\delta^*}^2}\exp\left(\frac{\varphi(\delta^*)}{kT}\right)+\frac{\eta_c}{\eta_l}}} \tag{11a}$$

$$\boldsymbol{\delta^* = \frac{1}{\lambda^2}\left(\frac{(1+\lambda)^5}{5} - \frac{(1+\lambda)^3(1+\lambda^2)}{3} + \frac{2(1+\lambda^2)^{5/2}}{15}\right)} \tag{11b}$$

$$\boldsymbol{\eta_l = \int_{\delta^*}^{\infty} exp\left(\frac{\varphi(r^*)}{kT}\right) {r^*}^{-2} dr^*} \tag{11c}$$

$$\boldsymbol{\lambda = 1.329\sqrt{\frac{\pi}{8}}\frac{Kn_D\eta_f}{\eta_c}} \tag{11d}$$

$$\boldsymbol{\alpha = \left(\frac{b_{min}}{\delta^*}\right)^2} \tag{11e}$$

where b_{min} is the minimum value for the function:

$$\boldsymbol{b = r^*\sqrt{1 + \frac{2}{3}\left[\frac{\varphi(\delta^*)}{kT} - \frac{\varphi(r^*)}{kT}\right]}} \tag{11f}$$

in the region 1 to δ^*, and $\frac{\varphi(r^*)}{kT}$ is given by equation (6a), from which $\boldsymbol{\eta_c}$, $\boldsymbol{\eta_f}$, and $\boldsymbol{\eta_l}$ are calculated. The expression of D'yachkov et al. in dimensionless form is given as:

$$\boldsymbol{H = 4\pi Kn_D^2 G(Kn_D, \psi_E)^{-1}} \tag{12a}$$

$$\boldsymbol{G(Kn_D, \psi_E) = \frac{\exp\left(\frac{\psi_E}{\frac{\eta_f}{\eta_c}Kn_D}\right)-1}{\exp(\psi_E)-1} + \sqrt{2\pi}Kn_D} \tag{12b}$$

In figure 5.6, a comparison between equations (10), (11), and (12) is given under conditions where $\boldsymbol{\psi_I = 0}$ (6a), $\boldsymbol{\psi_I = |\psi_E|}$ (figure 5.6b, omitting comparison to equation 12), and $\boldsymbol{\psi_I = 0}$ (figure 5.6c, again omitting comparison to equation 12). In each plot, as Fuchs's flux matching $H(Kn_D)$ curves vary with $\boldsymbol{\psi_E}$and $\boldsymbol{\psi_I}$, multiple curves are shown for equation (11). Equation (10) is independent of these factors once Kn_D is defined, and

similarly the variation in equation (12) with $\boldsymbol{\psi_E}$is minimal. Shown in figure 5.6a, equations (10) and (12) agree well (within 5% of one another throughout the entire Kn_D range), indicating that flux matching theory for repulsive potentials is in line with MFPT calculations (the origin of equation 10) if the ion speed distribution is considered at the limiting sphere surface. However, because of the neglect of the speed distribution, with strong repulsive potentials and at sufficiently high Kn_D, Fuchs's flux matching theory predicts unreasonably low dimensionless collision kernels, eventually predicting a collision kernel of zero once the potential energy on the limiting sphere surface exceeds the ion kinetic energy (based upon the mean thermal speed). This artificial drop in the kernel is further found for the combined Coulomb-image potential with flux matching theory at large potential energies (Ouyang, et al., 2012), and makes the use of Fuchs's flux matching approach particularly problematic in unipolar charging. As a particle becomes multiply charged, $\boldsymbol{\psi_E}$ increases, diminishing the influence of the image potential. The increase in $\boldsymbol{\psi_E}$ additionally leads to an increase in Kn_D, as in instances where repulsive Coulomb potentials are present and $|\boldsymbol{\psi_E}| > \boldsymbol{\psi_I}$, $\boldsymbol{\eta_c} > \boldsymbol{\eta_f}$ (see figure 5.3a), with Kn_D proportional to the ratio $\frac{\boldsymbol{\eta_c}}{\boldsymbol{\eta_f}}$. Therefore, once $|\boldsymbol{\psi_E}|$ becomes critically large, Fuchs's flux matching predictions become extremely inaccurate in unipolar charging.

For collisions between ions and uncharged particles, for which $\boldsymbol{\psi_E} = 0$ and a positive $\boldsymbol{\psi_I}$ leads to attractive forces between particle and ion, the results in figure 5.6c indicate the Fuch's flux matching predictions agree well with equation (10). However, shown in our prior work, in the transition regime, with larger $\boldsymbol{\psi_I}$ than considered here, the use of flux matching to predict $\boldsymbol{\psi_E} = 0$ collision kernels again becomes problematic. Because of its convergence to the appropriate $Kn_D \rightarrow 0$ and $Kn_D \rightarrow \infty$ limiting forms, and its algebraic form (when the tabulated values of $\boldsymbol{\eta_c}$ and $\boldsymbol{\eta_f}$provided in the supplemental information are used), we henceforth propose that equation (10) should be used in future unipolar charging collision kernel calculations for both spherical and nonspherical particles.

5.3.4. Comparison to Nonspherical Collision Kernels

The unipolar charging of nonspherical particles in the transition regime has been sparingly examined theoretically (Laframboise & Chang, 1977) or computationally (Biskos, et al., 2004) in prior work. Nonetheless, comparison to expressions developed previously is warranted. Equation (10) is now treated as an approximately valid relationship describing the dimensionless collision kernel over entire Kn_D range when making comparisons; the validity of previous proposed collision kernel calculations is judged based upon their agreement/disagreement with equation (10). In the absence of the image potential, Laframboise & Chang (1977) proposed a transition regime expression for a prolate spheroid (based upon a more general expression which converges to equation (7a) dimensionally in the $Kn_D \rightarrow 0$ limit), which when non-dimensionalized is given as:

$$\boldsymbol{H = 4\pi K n_D^2 \left[1 - \frac{1}{K_1}\cos^{-1}\left(\frac{1}{L_A}\right) + \frac{K_3}{K_1}\right]} \tag{13a}$$

$$\boldsymbol{K_1 = \frac{4}{3}\sqrt{\frac{2}{\pi}}\frac{1}{Kn_D}\frac{\left(L_A^2-1\right)^{1/2}}{1+\frac{L_A^2}{\left(L_A^2-1\right)^{1/2}}\sin^{-1}\left(1-\frac{1}{L_A^2}\right)^{1/2}}} \tag{13b}$$

$$\boldsymbol{K_2 = \frac{L_A}{\left(L_A^2-1\right)^{1/2}}} \tag{13c}$$

$$\boldsymbol{K_3 = \begin{cases} \frac{2}{\left(1-K_1^2K_2^2\right)^{1/2}}\tan^{-1}\left[\frac{(1-K_1K_2)(L_A-1)}{(1+K_1K_2)(L_A+1)}\right]^{1/2} & \text{if } K_1K_2 < 1 \\ \frac{1}{\left(K_1^2K_2^2-1\right)^{1/2}}\ln\left[\frac{(K_1K_2+1)^{1/2}(L_A+1)^{1/2}+(K_1K_2-1)^{1/2}(L_A-1)^{1/2}}{(K_1K_2+1)^{1/2}(L_A+1)^{1/2}-(K_1K_2-1)^{1/2}(L_A-1)^{1/2}}\right] & \text{if } K_1K_2 > 1 \end{cases}} \tag{13d}$$

where L_A is the spheroid aspect ratio (polar radius/equatorial radius, greater than unity). A comparison of equation (13) to equation (10) is provided in figure 5.7a with L_A = *1.001, 1.01, 1.1, 1.5, 2, 5, & 50*. For $L_A = 1$, equation (13) is not applicable, but evident in figure 5.7a, the agreement between equation (10) and their predictions at $L_A = 1.001$ is reasonable. Incremental increases in L_A however (even a 1% increase), lead to drastic and unreasonable departures in Laframboise & Chang's predictions from equation (10). Although by construction their predictions converge to the correct $Kn_D \rightarrow 0$ limit in all circumstances, for spheroids of appreciable aspect ratio in the transition and free

molecular regimes their collision kernel predictions deviate from the true value by orders of magnitude and never collapse to the correct $Kn_D \rightarrow \infty$ limit.

Table 5.2: Summary of the test aggregate (a.) and high aspect ratio article (b.) properties used example charging rate calculations. Charging rate calculations are performed for particles of equal mobility diameters.

Table 5.2a

Geometry	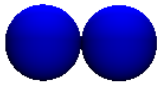		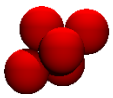		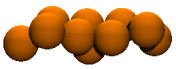					
Quasi Fractal Parameters	*N=2 (Dimer)*		*N=5 D_f=2.50, k_f=1.3*		*N=10, D_f=1.78, k_f=1.3*		*N=80, D_f=1.95, k_f=1.3*		*N=20 (Linear Chain)*	
R_s/a	1.39		1.98		3.03		8.13		5.79	
PA/a^2	5.8		12.1		24.7		155.9		53.1	
$PA/\pi R_s^2$	0.95		0.99		0.86		0.75		0.51	
d_m	75 nm	200 nm	75 nm	200 nm	75 nm	200 nm	75 nm	200 nm	75 nm	200 nm
a (nm)	27.5	72.9	19.1	50.9	13.3	34.8	5.2	13.6	8.8	22.1
Kn	1.74	0.66	1.75	0.66	1.75	0.66	1.8	0.66	1.75	0.66
ψ_I	1.47	0.55	1.48	0.56	1.39	0.53	1.32	0.51	1.10	0.44

Background gas Parameters: Air; Temperature=298 K; density=1.18 kg/m^3; Gas dynamic viscosity = 1.81x10^{-5} Pa.s; hard sphere mean free path = 66.5 nm. *Ion Parameters:* Mass=100 Da; Ion mobility = 1.9 cm^2/s/V, singly charged. Particles are assumed to be conducting.

Table 5.2b

Geometry			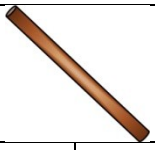		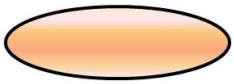	
d_m	75nm	200nm	75nm	200nm	75nm	200nm
Diameter (nm)	10	30	3.5	10	50	130
Length (nm)	510	1080	1400	2720	110	300
L/d	51	36	400	272	2.2	2.3
R_s (nm)	59.3	136.8	107.5	223.87	39.34	104.65
PA (nm^2)	4005.53	25446.9	3848.5	21362.8	4319.7	30630.5
$PA/\pi R_s^2$	0.36	0.43	0.11	0.14	0.89	0.89
Kn	3.05	1.11	5.76	2.16	1.88	0.70
ψ_I	0.95	0.41	0.52	0.25	1.43	0.54

Background gas Parameters: Air; Temperature=298 K; density=1.18 kg/m^3; Gas dynamic viscosity = 1.81x10^{-5} Pa.s; hard sphere mean free path = 66.5 nm. *Ion Parameters:* Mass=100 Da; Ion mobility = 1.9 cm^2/s/V, singly charged. Particles are assumed to be conducting.

As an alternative to Laframboise & Chang's approach, Wen et al (1984a) proposed that to define the steady-state, bipolar ion diffusion charging distribution on a nonspherical particle, a "charging equivalent diameter" may be defined, which is the diameter of a sphere with the same Coulombic surface potential energy as the nonspherical particle in question. From prior work (Northrup, et al., 1984; Mayya, 1990b) as well as the arguments presented here, it is apparent that the charging equivalent diameter would be equivalent to twice the Smoluchowski radius, $2R_s$, with Wen et al's definition. We examine the consequence of using a single length scale to define unipolar charging rates by substituting the charging equivalent diameter for the diameter of a sphere (i.e. by substituting R_s for a_p) in a collision kernel calculation procedure such as flux matching theory, the collision kernel for the nonpsherical particle can be calculated. With the limitations of flux matching theory already noted, we elect to examine Wen et al's assertion by substitution into equation (10). The modified form of equation (10), with the definitions of Kn_D and H maintained by equations (9a) and (9b), is:

$$\boldsymbol{H(Kn_D)} = \frac{4\pi Kn_D^2 + C_1 Kn_D^3\left(\frac{PA}{\pi R_S^2}\right) + \sqrt{8\pi} C_2 Kn_D^4\left(\frac{PA}{\pi R_S^2}\right)^2}{1 + C_3 Kn_D\left(\frac{PA}{\pi R_S^2}\right) + C_4 Kn_D^2\left(\frac{PA}{\pi R_S^2}\right)^2 + C_2 Kn_D^3\left(\frac{PA}{\pi R_S^2}\right)^3} \qquad (14)$$

Deviations in collision kernel calculation with the charging equivalent diameter approach hence arise when $\pi R_s^2 \neq PA$. Only when the length scales (R_s and $(PA/\pi)^{1/2}$, respectively) describing collision rates in the continuum and free molecular regimes are exactly equal to one another can a single length scale, such as a charging equivalent diameter describe collision rates throughout the entire Kn_D range. Rigorously, $\pi R_s^2 \equiv PA$ only applies to spherical particles.

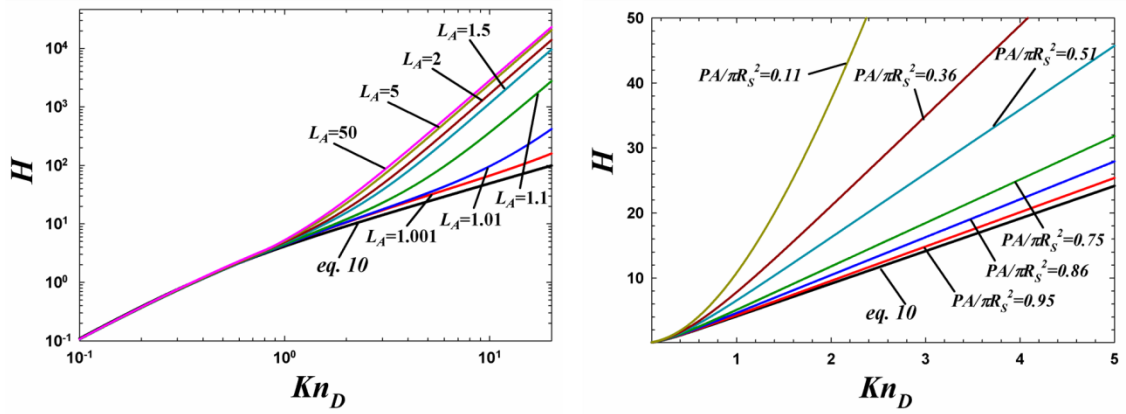

Figure 5.7: (a). Comparison between equation (10) calculations and the predictions of Laframboise & Chang (1977) for prolate spheroids of varying aspect ratio (L_A). (b). Comparison between equation (10) calculations and charging equivalent diameter based predictions (Wen et al, 1984) for varying $PA/\pi R_s^2$, corresponding to the particle geometries in tables 5.2a and 5.2b.

Figure 5.7b displays the function $H(Kn_D)$ calculated with equation (10), and then with equation (14) for the noted values of $PA/\pi R_s^2$, which correspond to the values for the particle geometries listed in table 5.2a and 5.2b. In the transition and free molecular regimes, equation (12) shows substantial deviation from the equation (10) collision kernel (particularly for particles of large aspect ratio), yet remains closer to equation (10) calculations than do the predictions of Laframboise & Chang. In the $Kn_D \rightarrow 0$ limit, R_s is indeed the length scale defining both diffusive ion transport to a particle surface and the electrostatic potential energy. Therefore equation (14), like equation (13), is accurate as $Kn_D \rightarrow 0$. However, based on our analysis we do not advocate the use of charging equivalent diameters to define collision kernels for complex geometry particles in the transition regime, as they cannot be used to predict collision kernels for many shapes outside the $Kn_D \rightarrow 0$ limit.

5.4. Assumptions of the Presented Analysis

A central assumption of the work performed here, as well as in prior analysis of aerosol particle collisions with ions, is that the influence of ion-ion interactions on ion

motion is negligible as an ion approaches a particle. The validity of this assumption can be examined through calculation of the ratio:

$$\boldsymbol{\psi_{ion}} = \frac{e^2 n_{ion}^{-1/3}}{4\pi\varepsilon_0 kT} \tag{15}$$

where n_{ion} is the ion concentration. $\boldsymbol{\psi_{ion}} \rightarrow 0$ indicates that the characteristic strength of the interaction potential between an ion and its nearest neighbor is extremely small compared to the thermal energy, and hence the influence of ion-ion interactions on ion motion can be neglected. At 300 K, for ion concentrations of 10^{12}, 10^{13}, 10^{14}, and 10^{16} m^{-3} $\boldsymbol{\psi_{ion}} = 5.56 \times 10^{-4}$, 1.11×10^{-3}, 2.58×10^{-3}, and 1.20×10^{-2}, respectively. Only in the latter case, for which the background environment can be considered a non-thermal plasma, is the nearest neighbor ion-ion interaction potential more than 1% of the thermal energy. We therefore believe that for most unipolar environments encountered or designed for particle charging, the neglect of ion-ion interactions in collision kernel evaluation is reasonable.

A second assumption in the presented analysis is that charging occurs in the absence of strong external electric fields. The distortion of external fields by particles leads to field charging, in which ion motion is strongly influenced by such distortion (Unger *et al.*, 2004). Further, strong electric fields induce a velocity differential between ions and particles, as uncharged particles will not migrate in such fields, and those that are charged are of much lower electrical mobility than ions, and hence migrate in the external field direction much more slowly than do ions. Future work will be necessary to develop of a combined diffusion charging-field charging ion-particle collision kernel.

5.5. Conclusions

The unipolar charging of particles of spherical and selected non-spherical shapes is examined through BD & MD simulations in an effort to find a dimensionless particle-ion collision kernel expression applicable to conducting particles of any shape and in the transition regime. The determined expression agrees well with those found applicable for

other transition regime collision processes, with a modified form for the dimensionless collision kernel (H) and the diffusive Knudsen number (Kn_D). It is concluded that the $H(Kn_D)$ relationship is more accurate than flux matching theory predictions when large repulsive potentials are present between ion and particle, and utilizes the appropriate descriptors of particle size for collision rate calculations in both the continuum and free molecular regimes.

Chapter 6: Brownian Dynamics Analysis of Bipolar Diffusion Charging of Aerosol Particles[5]

In light of the difficulties identified in Chapter 4 pertaining to the analysis of attractive long range interactions between particles and ions, an alternate method to directly calculate the steady state charge distribution is presented. The utility of the technique is demonstrated by investigating the effect of particle shape and material, as well as polydisperse ion properties on charge distributions.

6.1. Introduction

Aerosol particle size distribution function measurements via differential mobility analysis (Knutson & Whitby, 1975b) or alternative forms ion-mobility spectrometry (Olfert, et al., 2008) rely on accurate knowledge of the charge distributions of aerosol particles entering mobility spectrometers. It is hence necessary to bring particles to a known charge distribution prior to measurement. The most prevalently invoked technique to impart particles with an initial-condition independent (and presumably known) charge distribution is the exposure of particles to bipolar ions (a population of positive and negative ions). After a sufficient time in which particles undergo collisions with such ions (diffusion charging), the number concentration of particles carrying a certain number of charges tends to a steady state, and can be calculated by solving a system of population balance equations:

$$\mathbf{0} \equiv \frac{dn_p}{dt} = \boldsymbol{\beta}_{p-1,+1}\boldsymbol{n}_{p-1}\boldsymbol{n}_{+1} + \boldsymbol{\beta}_{p+1,-1}\boldsymbol{n}_{p+1}\boldsymbol{n}_{-1} - \boldsymbol{\beta}_{p,-1}\boldsymbol{n}_{p}\boldsymbol{n}_{-1} - \boldsymbol{\beta}_{p,+1}\boldsymbol{n}_{p}\boldsymbol{n}_{+1} \quad (1)$$

where n_p is the number concentration of particles carrying p charges (p = ...,-2,-1,0,1,2,…), $n_{\pm 1}$ is the number concentration of ions carrying ±1 charge (with the concentration of multiply charged ions assumed low), and $\beta_{p,\pm 1}$ is the collision rate coefficient (collision kernel) for the collision between a particle carrying p charges and

[5] Aspects of the results described in this chapter (including some text and figures) have been published in Gopalakrishnan, Meredith et al.(2013)

an ion carrying ±1 charge (with charge transfer from ion to particle assumed upon collision). This system of equations can be solved for n_p normalized by the total concentration of particles of all charge states n_T, to yield the steady state fraction f_p of particles carrying p charges (Adachi, et al., 1985; Reischl, et al., 1996):

$$\boldsymbol{f_p = \frac{n_p}{n_T} = \begin{cases} \frac{\prod_{j=1}^{j=p} \beta_{j-1,+1}/\beta_{j,-1}}{\Omega}; p \geq +1 \\ \frac{1}{\Omega}; p = 0 \\ \frac{\prod_{j=p}^{j=-1} \beta_{j+1,-1}/\beta_{j,+1}}{\Omega}; p \leq -1 \end{cases}} \quad (2a)$$

$$\boldsymbol{\Omega = 1 + \sum_{p=+1}^{p=+\infty} \left\{ \prod_{j=1}^{j=p} \frac{\beta_{j-1,+1}}{\beta_{j,-1}} \right\} + \sum_{p=-\infty}^{p=-1} \left\{ \prod_{j=p}^{j=-1} \frac{\beta_{j+1,-1}}{\beta_{j,+1}} \right\}} \quad (2b)$$

Equations (2a) and (2b) are derived assuming the number concentration of positive and negative ions are exactly equal, which is valid in bipolar ionizers provided ions of opposing polarities are lost by diffusive deposition at identical rates (although there have been studies noting the asymmetries in the concentration and rate of diffusive deposition of ions in bipolar ion sources (Hoppel & Frick, 1990; Alonso & Alguacil, 2003), which further note that the validity of the steady-state, equal concentration assumption needs to be checked for bipolar ionizers on a case-by-case basis).

It is apparent from equations (2a) & (2b) that the steady state charge fraction for charge level p depends strongly on the collision kernel ratio $\boldsymbol{\beta_{p\mp1,\pm1}/\beta_{p,\mp1}}$ for p < 0 and p > 0, respectively; hence for their implementation, the collision kernel between ions and particles must be determined *a priori*. To this end studies of collision kernels have been performed (Natanson, 1960b; Fuchs, 1963; Hoppel & Frick, 1986) and, based on the recent work by López-Yglesias & Flagan (2013) and the findings described in Chapter 4, further study of the steady-state bipolar charge distribution is warranted. Many aerosol systems containing nano- and submicrometer particles have a background gas close to atmospheric pressure and a temperature of the order $10^2 - 10^3$ K. Such conditions lead to particle-ion collisions occurring in the transition regime of mass transfer. Ion trajectory calculations have further permitted the determination of a simple-to-apply collision kernel expression for collisions between like charged ions and conducting particles in the

presence of the combined Coulomb and image potentials (chapter 5) and also for collisions between uncharged particles and ions in the presence of image potential alone (Ouyang, et al., 2012). The afore described expression is approximately valid across the entire Kn_D range, for particles of arbitrary shape, and for all values of the Coulomb potential energy to mean thermal energy ratio (Ψ_E) as well as the ion image potential energy to mean thermal energy ratio (Ψ_I). Therefore, equations are available for the collision kernels $\boldsymbol{\beta_{p-1,+1}}$ and $\boldsymbol{\beta_{p+1,-1}}$ for $p > 0$ and $p < 0$, respectively (the numerator of the ratio $\boldsymbol{\beta_{p\mp1,\pm1}/\beta_{p,\mp1}}$ is calculable for conducting particles).

Unfortunately, prior work presented here and elsewhere do not elucidate an appropriate method to determine collision kernels for particle-ion collisions which decrease the absolute level of particle charge, i.e., there is neither consensus between differing theoretical approaches nor experimental verification of approaches to calculate the collision kernels appearing in the dominator of the ratio $\boldsymbol{\beta_{p\mp1,\pm1}/\beta_{p,\mp1}}$. Hoppel & Frick (1986) attempted to modify flux matching theory for $\boldsymbol{\beta_{p,\mp1}}$ calculation using a first order correction (accounting for the influence of ion collisions with one gas molecule very close to the particle surface, as opposed to assuming purely ballistic ion trajectories in this limit) and an empirically determined ion-ion recombination constant, forcing the collision kernel to approach this value for sufficiently small, singly charged particles. An expansion of this approach has been recently developed by López-Yglesias & Flagan (2013). Hoppel & Frick's approach is invoked almost without exception to determine aerosol particle charge distributions in bipolar environments, and their approach serves as the basis for the near-universally applied steady-state charge distribution of Wiedensohler (1988). In chapter 4, through the use of mean first passage time calculations and dimensional analysis, it was found that Fuchs's flux matching approach leads to particle-ion collision kernel expressions which only apply in a limited Kn_D range at low strength of potential interaction between particles and ions. In the related field of dusty/complex plasmas, particles are immersed in a surrounding medium containing free electrons and positive ions at high concentration, leading to prevalent collisions between highly negatively charged particles and positively charged ions. Therefore, as in aerosol

systems, analysis of particle charge reducing collisions is of interest, and a variety of collision kernel calculation approaches have been developed for dusty plasmas (Goree, 1994; Khrapak, et al., 2006; Hutchinson & Patacchini, 2007; Gatti & Kortshagen, 2008; Zobnin *et al.*, 2008; Khrapak & Morfill, 2009), which lead to distinct results from Hoppel & Frick's approach and from one another. Further complicating matters, for the types of collisions in question, long range attractive Coulombic potential energy exists between the ion and particle, and in some cases this energy exceeds thermal energy at separation distances much larger than the particle size. A precise definition of the correct length scale to define a diffusive Knudsen number is not yet clear for all possible potential function forms.

A second problematic aspect of the solution to equation (1) is that the physical properties (mass and mobility) of the ions that are involved in the charging process must be known and input to determine charge fractions. In the comparison of theoretical predictions to experimental results for bipolar diffusion charging of aerosol particles (Liu & Pui, 1974; Kojima, 1978; Porstendorfer *et al.*, 1979a; Hussin, et al., 1983; Reischl, et al., 1983; Porstendörfer *et al.*, 1984; Adachi, et al., 1985; Wiedensohler, et al., 1986; Wiedensohler, 1988; Stober *et al.*, 1991; Reischl, et al., 1996), fixed values for ion properties have been commonly assumed, based either on the results of different studies of the masses and mobility of ions in air (Kilpatrick, 1971; Mohnen, 1977) or chosen to lead to the best possible agreement between flux matching theory predictions and measurements. The use of "best fit" ion properties is clearly not an appropriate method to compare theoretical predictions to measurements, as the agreement observed is forced through fitting. As emphasized recently in the work of Steiner & Reischl (2012), ion properties likely vary from one experimental system to another, as the chemical composition of ions formed by radioactive decay products (the most prevalent method of bipolar ion generation in aerosols) is strongly influenced by small perturbations to background gas composition. Moreover, it has not yet been shown that the use of mean masses and mobilities for ions is appropriate in modeling particle-ion collisions for comparison to experimental measurements. Ion populations, particularly those generated

by radioactive decay products, are not monodisperse in mass and mobility, and the polydisperse properties of the entire ion distribution may need to be considered for correct diffusion charging rate calculations. Using a distribution of ion properties in equation (1) unfortunately complicates its solution considerably. For example, if 50 different types of positive ions and 50 different types of negative ions are present and considered, the number of terms on the right side of equation (1) would increase from 4 to 200.

A final issue of concern in bipolar steady charge distribution calculation is the development of a proper method to extend collision kernel calculation to non-spherical particles. The issues with collision kernel determination for particle-ion collisions which decrease the absolute particle charge level are unresolved for spherical particles and is further exacerbated when particles are non-spherical, and presently no theory has been developed to calculate such collision kernels for non-spherical particles. Instead, for non-spherical particle steady-state charge distribution calculations, simplified assumptions based on "charging equivalent diameters" are often invoked (Wen *et al.*, 1984b; Wen, et al., 1984a; Lall & Friedlander, 2006), which have been tested experimentally only in limited circumstances. Furthermore, the investigation of the unipolar charging of non-spherical particles described in chapter 5 is limited to purely conducting particles, for which the distribution of accumulated charge on a particle surface was assumed to distribute itself in a manner which minimizes the particle's Coulombic potential energy. The influence of particle surface charge distribution (i.e. dielectric properties) on particle-ion collisions is yet to be evaluated.

In light of the pending issues with the use of equation (2) to calculate steady-state charge distributions, the purpose of this work is to develop and test a Brownian/Langevin dynamics calculation (BD calculations, including inertial terms in the equations of motion for ions) approach to determine the steady-state charge distribution as a function of particle size. Collision kernel determination is circumvented entirely in this calculation procedure. The approach can be used for charge distribution calculations in

the continuum, free molecular, and transition regimes, easily extended to examine the influence of polydisperse ion mass and mobility distributions, and used to examine the charge distributions of particles of arbitrary shape. In the following sections, the charge distribution approach is described in detail, followed by a comparison of calculation results to the Weidensohler (1988) distribution, considering both monodisperse and polydisperse ion properties. Calculation results for a number of non-spherical particles are presented and compared to the results for spherical particles under the assumption that the non-spherical particles are perfectly conducting, or are insulating. Finally, regression equations are given for the particle charge distribution as a function of "mobility diameter" for both spherical and non-spherical particles under atmospheric pressure, 300 K temperature, and considering measured ion mass and mobility distributions under these conditions. These equations can be used to invert particle size distribution functions from mobility measurements. In total, presented results demonstrate the influence of complex ion populations, particle morphology, and particle conductivity on the steady-state charge distribution.

6.2. Theoretical and Numerical Approach

6.2.1. Ion Trajectory Simulations

To determine the steady state charge distribution on particles of specified dimensions and shape, ion trajectories about a particle are monitored under dilute conditions in a background gas at a fixed input temperature T. Ions are modeled as point masses which are much heavier than the background gas molecules, but substantially less massive than the particle, allowing tracking of its motion using the Langevin equation introduced in previous chapters. Motion is influenced by inertia, drag, and ion-particle potential interactions, hence each simulated ion is described by its mass m_i, friction factor f_i (where the friction factor is equal to the ratio of the unit electron charge to the ion's electrical mobility), and its polarity (positive or negative). These properties are sampled from an input ion mass-mobility spectrum for the bipolar ion population of interest, and

may describe positive and negative ions which are monodisperse in mass and mobility, or polydisperse in these properties. Simulations commence by initiating a single sampled ion at a random location on the surface of a prescribed simulation domain, as is depicted in Figure 6.1. The particle of interest is fixed with its center of mass at the center of this domain, and is initially neutral. For most particle geometries the domain is spherical (Figure 6.1a), but for cylindrical and linear chain aggregate test particles a cylindrical domain with hemispherical endcaps is employed (Figure 6.1b). After placement on the domain surface, the ion is moved through the domain by calculation of its velocity vector $\vec{\boldsymbol{v}}(\boldsymbol{t}+\Delta\boldsymbol{t})$ and its position vector $\vec{\boldsymbol{r}}(\boldsymbol{t}+\Delta\boldsymbol{t})$ after a small change in time $\Delta\boldsymbol{t}$ via the solution derived by Ermak and Buckholtz (1980) to the Langevin equation of motion (Chandrasekhar, 1943). This solution effectively models motion in the mass transfer transition regime provided that the system in question is at thermal equilibrium and is expressed as:

$$\vec{\boldsymbol{v}}(\boldsymbol{t}+\Delta\boldsymbol{t}) = \vec{\boldsymbol{v}}(\boldsymbol{t})\,\mathbf{exp}\left(-\frac{\boldsymbol{f_i}}{\boldsymbol{m_i}}\Delta\boldsymbol{t}\right) + \frac{\vec{\boldsymbol{F}}(\vec{\boldsymbol{r}}(\boldsymbol{t}))}{\boldsymbol{f_i}}\left(\mathbf{1}-\mathbf{exp}\left(-\frac{\boldsymbol{f_i}}{\boldsymbol{m_i}}\Delta\boldsymbol{t}\right)\right) + \vec{\boldsymbol{A}}_{\mathbf{1}} \tag{3a}$$

$$\vec{\boldsymbol{r}}(\boldsymbol{t}+\Delta\boldsymbol{t}) = \vec{\boldsymbol{r}}(\boldsymbol{t}) + \frac{\boldsymbol{m_i}}{\boldsymbol{f_i}}\left(\vec{\boldsymbol{v}}(\boldsymbol{t}+\Delta\boldsymbol{t}) + \vec{\boldsymbol{v}}(\boldsymbol{t}) - \mathbf{2}\frac{\vec{\boldsymbol{F}}(\vec{\boldsymbol{r}}(\boldsymbol{t}))}{\boldsymbol{f_i}}\right)\left(\frac{\mathbf{1}-\mathbf{exp}\left(-\frac{\boldsymbol{f_i}}{\boldsymbol{m_i}}\Delta\boldsymbol{t}\right)}{\mathbf{1}+\mathbf{exp}\left(-\frac{\boldsymbol{f_i}}{\boldsymbol{m_i}}\Delta\boldsymbol{t}\right)}\right) + \frac{\vec{\boldsymbol{F}}(\vec{\boldsymbol{r}}(\boldsymbol{t}))}{\boldsymbol{f_i}}\Delta\boldsymbol{t} + \vec{\boldsymbol{A}}_{\mathbf{2}} \tag{3b}$$

$$\langle \boldsymbol{A_1^2}\rangle = \frac{\mathbf{3}\boldsymbol{kT}}{\boldsymbol{m_i}}\left(\mathbf{1}-\mathbf{exp}\left(-\mathbf{2}\frac{\boldsymbol{f_i}}{\boldsymbol{m_i}}\Delta\boldsymbol{t}\right)\right) \tag{3c}$$

$$\langle \boldsymbol{A_2^2}\rangle = \frac{\mathbf{6}\boldsymbol{m_i kT}}{\boldsymbol{f_i^2}}\left(\frac{\boldsymbol{f_i}}{\boldsymbol{m_i}}\Delta\boldsymbol{t} - \mathbf{2}\left(\frac{\mathbf{1}-\mathbf{exp}\left(-\frac{\boldsymbol{f_i}}{\boldsymbol{m_i}}\Delta\boldsymbol{t}\right)}{\mathbf{1}+\mathbf{exp}\left(-\frac{\boldsymbol{f_i}}{\boldsymbol{m_i}}\Delta\boldsymbol{t}\right)}\right)\right) \tag{3d}$$

In equations (3a) & (3b), $\vec{\boldsymbol{F}}\left(\vec{\boldsymbol{r}}(\boldsymbol{t})\right)$ is the total electrostatic force acting on the ion due to combined Coulomb and image potential interactions with the particle and k is the Boltzmann's constant. $\vec{\boldsymbol{A}}_{\mathbf{1}}$ and $\vec{\boldsymbol{A}}_{\mathbf{2}}$ are normally distributed random vectors, with zero mean and variances given by equation (3c) and (3d) respectively, and account for the fluctuation in the velocity and position of the ion due to diffusion. When introduced on the domain surface, the initial velocity vector of the ion is determined by sampling a random vector $\vec{\boldsymbol{A}}_{\mathbf{1}}$. Unlike the simulations of particle-ion and particle-particle collisions discussed in previous chapters, it should be noted that equation (3) is solved in a

dimensional fashion with dimensional inputs. A simulation domain that is 500 times the diameter of the particle (in case of spherical particles) and 500-3000 times the diameter of the primary sphere (in case of quasifractal aggregate particles) was found to be sufficient to mitigate the effect of a finite domain volume. For cylindrical particles and linear chain aggregates, the simulation domain is a volume that is identical to the particle in aspect ratio, but larger by a factor of 500 in all directions. The timestep employed is variable with both the magnitude of ion-particle interactions and distance from the ion to the particle, and is determined using the empirical expression:

$$\Delta t = 0.005 \min\left(\frac{1}{|\vec{F}(\vec{r})|}, \frac{|\vec{r}|^2 f_i^2}{2 m_i k T}\right) \tag{3e}$$

Similar to the domain sizes, timesteps chosen in this manner are found to be sufficiently small, such that finite timestep influences are mitigated. After each timestep, an ion will remain in the domain, leave the domain, or collide with the particle. In the event that the ion remains in the domain, equation (3) is again used to model its motion. If an ion exits the domain, a new ion, with its mass, friction factor, and polarity sampled from the input distribution (and hence distinct from the exiting ion) is placed at a random location on the domain surface with a velocity vector by sampling the random vector $\vec{A}_1$. This new ion's motion through the domain is then simulated via equation (3). Finally, if the ion collides with the particle, the particle's charge state is updated to reflect this collision and a new sampled ion is placed on the domain surface. The new ion's motion is monitored with the force experienced by the ion $\vec{F}(\vec{r}(t))$ dependent on the particle's new charge state (as described in a subsequent section).

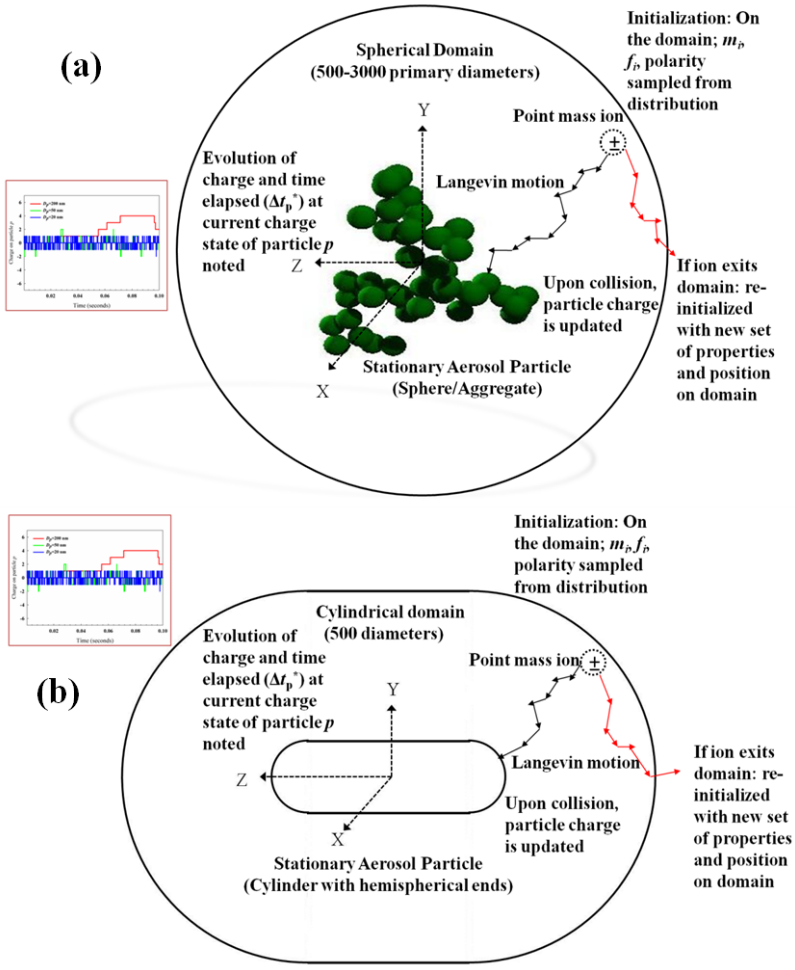

Figure 6.1: Schematic describing the Brownian dynamics simulation procedure using (a.) a spherical domain and (b.) a cylindrical domain.

At all times, one and only one ion is in the domain volume, hence ion-ion interactions are neglected in calculations. In most bipolar ion-containing aerosol systems such interactions are indeed negligible, as the ion concentration is dilute (of order 10^{13} ions m^{-3} or less (Shimada *et al.*, 2002; Han *et al.*, 2003)). If non-dilute (plasma) systems are of interest, ion-ion interactions could be included in calculations by introducing multiple ions into the simulation domain, considering ion-ion potential interactions in monitoring each ion's equation of motion, and using an appropriate distribution from which to sample each ion's initial velocity.

6.2.2. Charge Distribution Inference

The aforementioned simulations monitor the collisions between ions and a single particle over time, similar to the studies of Cui & Goree (1994) and Mangolini & Kortshagen (2009), only in this work the charging process is modeled directly via monitoring ion trajectories. The fraction of time this single particle spends with each charge state, $\boldsymbol{f_{t,p}}$, can be calculated as:

$$\boldsymbol{f_{t,p}} = \frac{\boldsymbol{t_p}}{\sum_i \boldsymbol{t_i}} \tag{4}$$

where t_p is the total amount of simulation time in which the particle has charge state p. Following a sufficiently long total time ($\sum_i \boldsymbol{t_i}$), the values $\boldsymbol{f_{t,p}}$ will become time-invariant, hence the simulation reaches a steady-state. All simulations are performed such that this steady-state has been attained for low charge states. This is monitored by defining the moments of the charge distribution as:

$$\boldsymbol{M_j} = \sum_p \boldsymbol{p^j f_{t,p}} \tag{5}$$

M_1, M_2, and M_3 are evaluated over the course of simulations, and simulations proceed until each of these moments ceases to vary with increasing time. Generally, 10,000-100,000 ion-particle collisions are modeled to ensure that $\boldsymbol{f_{t,p}}$ converges to a steady-state value for p = 0, +1, -1, +2 and -2. Determination of the steady-state values for the fraction of time a particle spends with higher charge states ($|p|>2$) requires monitoring more than 100,000 ion-particle collisions (though the sum of fractions for these charge states can be determined). Steady-state can only be attained in instances where particles are exposed to both positive and negative (bipolar) ions (though they need not be equal concentrations); $\boldsymbol{f_{t,p}}$ values will not attain steady-state in a unipolar environment (Boisdron & Brock, 1970).

While simulations reveal the fraction of time a single particle will spend in each charge state when exposed to bipolar ions, in bipolar charging experiments, what is truly of interest is the fraction of particles of specified size and shape which have charge state p have after exiting a bipolar charging device, i.e. at a specific instant in time. As noted

in equation (2), this distribution, $\boldsymbol{f_p}$, also reaches a steady-state, provided particles are exposed to bipolar ions for a sufficiently long time and appreciable diffusion losses of ions does not occur. Without proof, the ergodic hypothesis is conjectured to be applicable to aerosol particles attaining their steady-state charge distribution; and that the steady state fraction of time a single particle spends with charge state p is inferred as the fraction of particles at charge state p once steady-state is attained ($\boldsymbol{f_{t,p} \equiv f_p}$), provided the particles in both situations are of the same size and shape. This hypothesis is frequently invoked to determine the properties of systems at equilibrium, though we note the charging of particles in a bipolar environment does not reach true equilibrium, as the reverse charging reaction rate (the rate at which neutral vapor molecules collide with particles, leave the particle surface ionized, and alter the particle charge state) appears to be negligibly small for particles appreciably larger than gas molecules, under most circumstances (Premnath, et al., 2011).

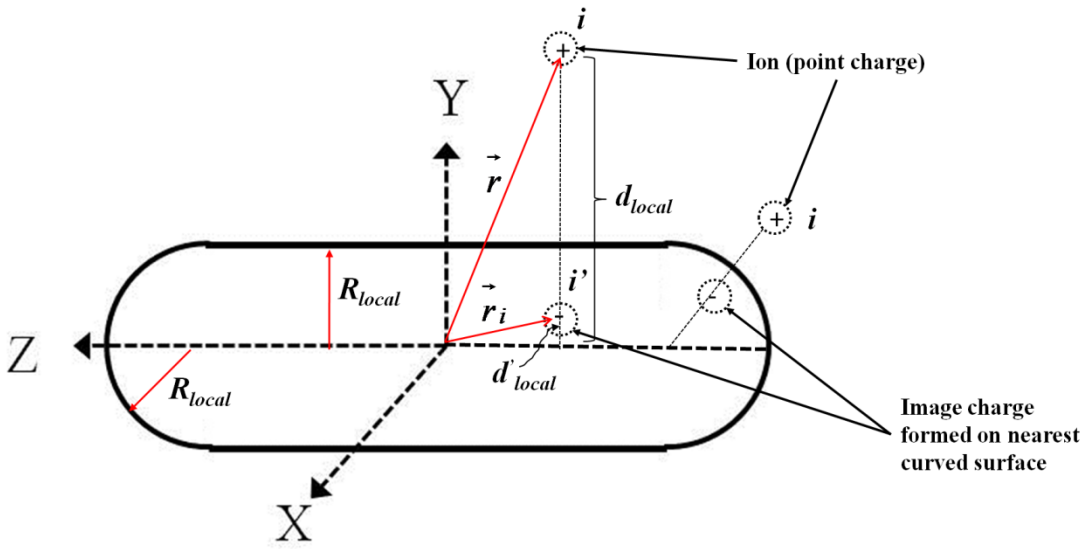

Figure 6.2: Depiction of the calculation procedure to determine the placement of "image" charge on cylindrical particles.

6.2.3. Ion-Particle Potentials

We consider combined Coulomb and image potentials in BD calculations. For spherical particles of diameter d_p, the force experienced by the ion subject to combined Coulomb-image potential interactions is expressed as:

$$\vec{F}(\vec{r}) = \frac{pie^2}{4\pi\varepsilon_o|\vec{r}|^3}\vec{r} - \frac{i^2e^2}{4\pi\varepsilon_o|\vec{r}|^4}\frac{\left(2|\vec{r}|^2-\left(d_p/2\right)^2\right)}{\left(|\vec{r}|^2-\left(d_p/2\right)^2\right)^2}\vec{r} \quad (6)$$

where ε_0 is the permittivity of free space, e is the unit electron charge, and i is the integer charge on the ion. In the investigation of cylindrical particles of diameter $\boldsymbol{d_p}$, hemispherical ends of the same diameter, and an end to end length $\boldsymbol{L_p}$, the Coulomb potential is computed assuming that the charge on the particle is uniformly distributed over the entire particle surface area. Subsequently, the Coulomb force experienced by the ion, $\vec{\boldsymbol{F}}_{\boldsymbol{c}}(\vec{\boldsymbol{r}})$, is calculated as the sum of all the coulomb interactions between the ion and a finite number of finely divided surface charge elements (whose local position vector expressed in suitable surface coordinates is denoted by $\vec{\boldsymbol{r}}_{\boldsymbol{e}}$):

$$\vec{F}_c(\vec{r}) = \frac{pie^2}{\pi\varepsilon_o d_p L_p}\iint\frac{(\vec{r}-\vec{r}_e)}{|\vec{r}-\vec{r}_e|^3}\boldsymbol{dA} \quad (7a)$$

To evaluate the image potential with cylindrical particles, as demonstrated in Figure 6.2, the effect of the induced charge density on the surface of a cylinder (wholly convex in curvature) can be accounted for by placing a single image charge inside the cylinder whose position is determined by the ion's position (Jackson, 1975). In the vicinity of an ion, (with a position vector $\vec{\boldsymbol{r}}$ at a distance d_{local} from the nearest center of curvature), an image charge of magnitude $i' = -\boldsymbol{i}\frac{\boldsymbol{R_{local}}}{\boldsymbol{d_{local}}}$ is placed at a distance $\boldsymbol{d'_{local}} = \frac{\boldsymbol{R^2_{local}}}{\boldsymbol{d_{local}}}$ from the same center of curvature, where R_{local} is the local radius of curvature. In Figure 6.2, the position vector of the image is labeled as $\vec{\boldsymbol{r}}_{\boldsymbol{i}}$. With the image charge positioned, the image force $\vec{\boldsymbol{F}}_{\boldsymbol{i}}(\vec{\boldsymbol{r}})$ acting on the ion is computed using Coulomb's law:

$$\vec{F}_i(\vec{r}) = -\frac{i^2e^2}{4\pi\varepsilon_o}\frac{2d^2_{local}-R^2_{local}}{d^3_{local}\left(d^2_{local}-R^2_{local}\right)^2}\frac{(\vec{r}-\vec{r}_i)}{|\vec{r}-\vec{r}_i|} \quad (7b)$$

The total electrostatic force on an ion in the presence of a cylindrical particle is then computed using superposition of the coulomb and image forces, to obtain $\vec{F}(\vec{r})$ used in equations (3a&b).

Finally, when calculations are performed on aggregates, which are ensembles of point contacting spheres, the Coulomb force acting on an ion is calculated via two separate methods. First, it is assumed that aggregates are conducting and the total charge on an aggregate is dispersed in a manner that minimizes the electrostatic potential energy within the aggregate itself. With this assumption the Coulomb force is calculated in the manner described in chapter 5, building on the methods of Brown & Hemmingway (1995). Second, aggregates are treated as insulating with immobile surface charge, and the charges an aggregate obtains are assumed to remain on the spheres at which ions collided throughout the entire simulation. This can lead to Coulomb interactions influencing ion motion even for neutral particles, as a positive charge and a negative charge may occupy different primary spheres within an aggregate. For aggregates with more than 5 primary particles, the influence of image potential interactions are neglected due to the high computational cost which comes with including this potential; for the (two) aggregates examined with 5 primary particles and less, the image potential is calculated using the procedure described in chapter 5.

6.2.4. Particle & Ion Properties

Table 6.1: Summary of the properties of the cylinders (length, L_p and diameter, d_p) and aggregates used in Brownian dynamics calculations. For all quasifractal aggregates, k_f = *1.3*. In each column where the mobility diameter (d_m) is specified, the cylinder and primary particle diameter (d_o) employed are noted in nanometers.

Geometry					d_m **(nm)**					
	L_p/d_p	$\frac{2R_s}{d_p}$	$\frac{4PA}{d_p^2}$	$\frac{PA}{\pi R_s^2}$	**20**	**50**	**70**	**85**	**100**	**125**
Cylinder	**10**	3.73	31.42	0.72	6.30	15.6	21.7	26.4	31.0	38
	25	6.98	78.54	0.51	3.95	9.8	13.6	16.3	19.1	23.5
	50	11.7	157.1	0.37	2.80	6.9	9.5	11.4	13.3	16.4
	100	20.0	314.2	0.25	1.97	4.8	6.7	8.0	9.3	11.4
	300	48.5	942.5	0.13	1.14	3.0	3.8	4.5	5.3	6.4
Quasi-Fractal Aggregates (k_f=1.3)	***Quasi-Fractal Parameters***	$\frac{2R_s}{d_0}$	$\frac{4PA}{d_0^2}$	$\frac{PA}{\pi R_s^2}$	**20**	**50**	**70**	**85**	**100**	**125**
	N_p=*5* D_f=**2.50**	1.97	12.09	0.987	-	25.4	35.8	-	50.8	-
	N_p =**50** D_f=**2.00**	6.22	100.55	0.83	3.52	8.8	13.2	14.8	17.4	20.8
	N_p =**80** D_f=**1.95**	8.13	155.91	0.75	2.82	7.0	9.8	11.8	13.8	17.2
	N_p =**60** D_f=**1.63**	8.35	139.29	0.64	3.00	7.4	5.3	12.4	14.6	18.0
Linear Aggregates	***Number of primary spheres***	$\frac{2R_s}{d_0}$	$\frac{4PA}{d_0^2}$	$\frac{PA}{\pi R_s^2}$	**20**	**50**	**70**	**85**	**100**	**125**
	N_p =*2*	1.39	5.82	0.96	-	36.6	51.2	-	73.8	-
	N_p =*30*	7.81	77.97	0.41	3.96	9.8	13.	16.2	19.0	23.4
	N_p =*70*	14. 9	181.44	0.26	2.60	6.3	8.8	10.5	12.2	15.0
	N_p =*200*	34.7	516.73	0.14	1.54	3.7	5.1	6.1	7.1	8.7
	N_p =*500*	74.8	1292.2	0.07	0.97	2.3	3.2	3.8	4.4	5.4

Table 6.1: (continued).

Geometry					d_m (nm)					
	L_p/d_p	$\frac{2R_s}{d_p}$	$\frac{4PA}{d_p^2}$	$\frac{PA}{\pi R_s^2}$	**150**	**180**	**200**	**500**	**1000**	**2000**
Cylinder	**10**	3.73	31.4	0.72	45.5	54.5	60.0	144	280.0	555.0
	25	6.98	78.5	0.51	28.0	33.4	36.5	84.0	160.0	305.0
	50	11.7	157.1	0.37	19.4	22.7	25.0	55.5	101.0	190.0
	100	20.0	314.2	0.2	13.4	□5.6	17.1	36.9	65.2	118.3
	300	48.5	942.5	0.13	7.5	8.7	9.5	19.5	33.0	56.0
Quasi-Fractal Aggregates (k_f=1.3)	***Quasi-Fractal Parameters***	$\frac{2R_s}{d_0}$	$\frac{4PA}{d_0^2}$	$\frac{PA}{\pi R_s^2}$	**150**	**180**	**200**	**500**	**1000**	**2000**
	N_p **=5** D_f**=2.50**	1.97	12.09	0.987	-	-	-	25.0	510.0	-
	N_p **=50** D_f**=2.00**	6.22	100.6	0.83	26.0	31.0	34.1	84.0	165.0	326.0
	N_p **=80** D_f**=1.95**	8.13	155.9	0.75	20.6	24.6	27.0	66.0	127.8	251.6
	N_p **=60** D_f**=1.63**	8.35	139.3	0.64	21.4	25.4	28.0	66.0	127.8	248.8
Linear Aggregates	***Number of primary spheres***	$\frac{2R_s}{d_0}$	$\frac{4PA}{d_0^2}$	$\frac{PA}{\pi R_s^2}$	**150**	**180**	**200**	**500**	**1000**	**2000**
	N_p *=2*	1.39	5.82	0.956	-	-	-	360.0	720.0	-
	N_p *=30*	7.81	78.0	0.41	27.6	32.6	36.0	80.0	148.0	280.0
	N_p *=70*	14.9	181.4	0.26	17.6	20.8	22.8	49.0	87.0	158.0
	N_p *=200*	34.5	516.7	0.1	10.2	11.9	13.0	26.8	45.0	78.0
	N_p *=500*	74.8	1292.2	0.07	6.3	7.4	8.0	16.0	26.0	43.0

As noted in the prior sections, four types of particles are examined in this work: spheres, cylinders with hemispherical endcaps, straight linear chain aggregates, and quasifractal aggregates, which statistically obey the relationship $\boldsymbol{N_p = k_f \left(\frac{2R_g}{d_0}\right)^{D_f}}$, where $\boldsymbol{N_p}$ is the number of primary spheres in the aggregate, $\boldsymbol{k_f}$ is the dimensionless pre-exponential factor, R_g is the aggregate radius of gyration, D_f is the fractal dimension, and $\boldsymbol{d_0}$ is the primary sphere diameter. The properties of the non-spherical particles are displayed in Table 6.1, which includes cylinders with length (end to end distance) to diameters ratios ranging from 10 to 300, linear chain aggregates with N_p = 2-500, and quasifractal aggregates with N_p = 5-80, k_f = 1.3, and D_f = 1.63-2.50. The quasifractal

aggregates are generated via a cluster-cluster algorithm as described by Filippov et al (2000). The precise dimensions of cylinders, scaled by their diameters, and both types of aggregates, scaled by their primary sphere diameters, are chosen in an effort to scale the "mobility diameter", d_m, of these particles in a T = 300 K, atmospheric pressure, air environment (in which the mean free path is 66.5 nm and the dynamic viscosity is 1.82 x 10^{-5} Pa.s). Although dependent upon Knudsen number (Dahneke, 1973c; Sorensen, 2011; Zhang *et al.*, 2012), mobility diameter is selected as the length scale for comparison because it is directly inferred from electrical mobility measurements, which are frequently made under the noted conditions. For a particle with net number of charges p, d_m is calculated from the electrical mobility, Z_p as:

$$\boldsymbol{Z_p = \frac{pe}{3\pi\mu d_m}\left(1 + \frac{2\lambda}{d_m}\left[1.257 + 0.4\exp\left(\frac{-0.55 d_m}{\lambda}\right)\right]\right)} \quad (8a)$$

where the coefficient 1.257, 0.4, and 0.55 are taken from Davies (1945). Based on the work of Dahneke (1973c) and supported by direct simulation Monte Carlo as well as experiments, the work of Zhang et al. (2012) suggests that for a particle which does not preferentially align with the direction of an electric field during mobility measurements, the electrical mobility is calculated as:

$$\boldsymbol{Z_p = \frac{pe}{6\pi\mu R_s}\left(1 + Kn\left[1.257 + 0.4 exp\left(\frac{-1.1}{Kn}\right)\right]\right)} \quad (8b)$$

where the Knudsen number, Kn, is evaluated as:

$$\boldsymbol{Kn = \frac{\lambda \pi R_s}{PA}} \quad (8c)$$

Two shape descriptors for a particle are needed to compute electrical mobility: R_s, the Smoluchowski radius/capacity, which is assumed equivalent to the particle's orientationally averaged hydrodynamic radius via the Hubbard-Douglas approximation (Douglas, et al., 1994), and PA, the particle's orientationally averaged project area (Larriba & Hogan, 2013). The algorithms given in (Gopalakrishnan, et al., 2011) are used here to compute R_s and PA for quasifractal aggregates, while for cylinders R_s values are computed using the results of Hansen (2004) and PA is computed with Cauchy's theorem (Appendix D). Although Hansen's results apply for cylinders without hemispherical ends, we find that the addition of hemispherical ends negligibly changes R_s values (by less than 1%) from his calculations. Normalized values of R_s and PA for test

particles are shown in Table 6.1. An important point to note is that the ratio $PA/\pi R_s^2$ is not equal to unity for non-spherical objects, and approximately decreases with increasing particle aspect ratio. With these values calculated, by setting equations (8a) & (8b) equal to one another, the diameter of both cylinders and primary particles in quasifractal aggregates can be specified, such that the cylinders and aggregates have a specified mobility diameter. In BD simulations, mobility diameters for non-spherical particles in the 20-2000 nm range are examined. For varying aspect ratios and quasifractal descriptors, respectively, the cylinder and primary particle diameters required for particles to have selected mobility diameters in the range are also noted in Table 6.1.

In the regression equations developed by Wiedensohler (1988) for the steady-state charge distribution in air at 300 K and atmospheric pressure, all positive ions have a mass of 140 Da and an electrical mobility of 1.35 $cm^2\ V^{-1}\ s^{-1}$, while all negative ions have a mass of 101 Da and an electrical mobility of 1.60 $cm^2\ V^{-1}\ s^{-1}$, with positive and negative ions in equal concentration to one another. Simulations using these ion properties are performed for direct comparison to this distribution. In addition, polydisperse ion mass and mobility distributions which were measured directly are examined. Specifically, the properties of the 50 most abundant positive and 50 most abundant negative ions from the measurements of Meredith et al (In Prep.) were used in calculations. These measurements will be described in detail in a forthcoming manuscript, briefly, ions were generated via a 10 mCi Po-210 alpha particle source from high purity, water free (zero) air and directed in to a parallel-plate differential mobility analyzer (P5 SEADM, Valladolid, Spain) coupled to a time-of-flight mass spectrometer (QSTAR XL, MDS Sciex, Ontario, Canada) for mobility and mass measurement (Hogan & Fernandez de la Mora, 2009; Rus *et al.*, 2010; Larriba, et al., 2011). The tubing connecting the air cylinder to the Po-210 housing (which was made of Delrin plastic) was a combination of brass, stainless steel, and Teflon; hence, measurements of ion properties were made under conditions similar to many laboratory scale aerosol experiments. Lists of the measured ion masses and mobilities are provided in Appendix C. Also given are the relative abundances of each

ion; in simulations ions are sampled randomly in proportional to their relative abundances. Equal total concentrations of positive and negative ions are assumed.

6.3. Results and Discussion

6.3.1. Simulation Convergence

The charge distribution moments M_1, M_2, and M_3 are plotted as functions of the number of simulated particle-ion collisions for a 100 nm diameter spherical particle in Figure 6.3a. Simulations are performed using the polydisperse ion properties noted in the supplemental information. All moments tend to constant values after ~8000 collisions, though to ensure that results are reliable, reported values derive from simulations with a larger number of collisions. Once steady values are reached, M_1 and M_3 converge to values close to zero, as the contributions of positively and negatively charged particles roughly balance with one another in odd number moment calculations.

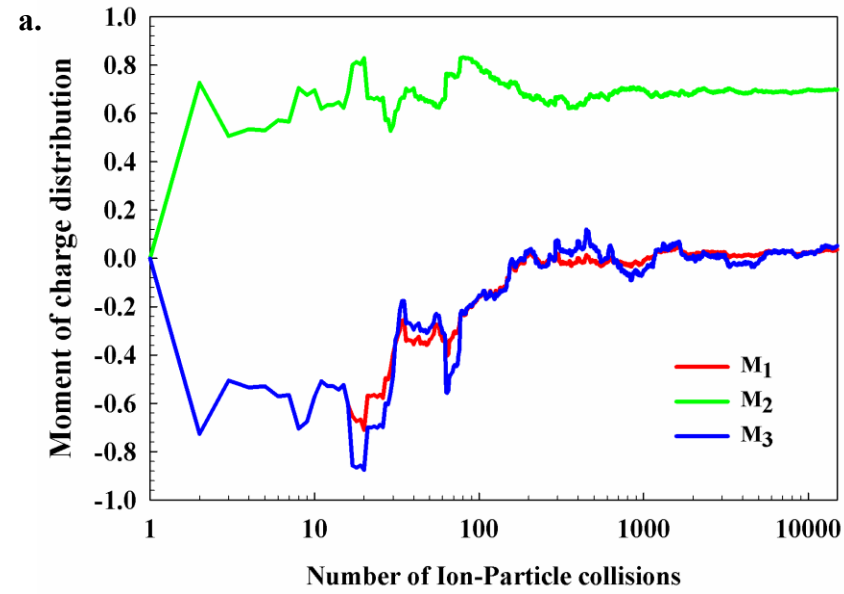

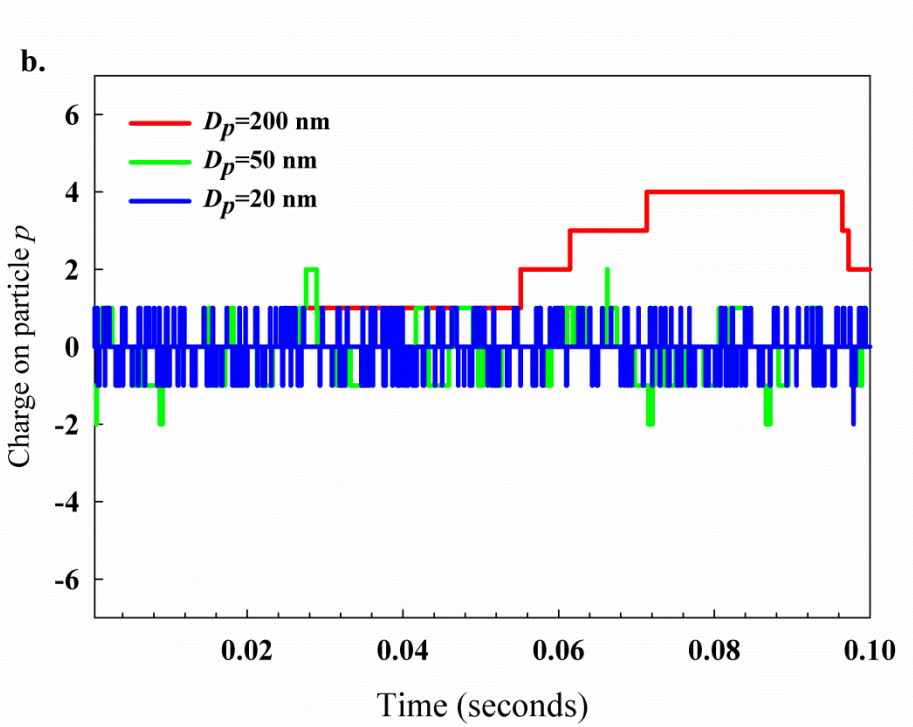

Figure 6.3: (a.) The first, second, and third moments of the charge distribution on a 100 nm particle as a function of the number of ion-particle collisions in a typical Brownian dynamics simulation. (b.) Fluctuations of the charge level on selected spherical particles in Brownian dynamics simulations, as a function of dimensional simulation time.

While moments of a charge distribution converge to specific values, the charge on particles oscillates at all times. Figure 6.3b is a plot of the charges on 20 nm, 50 nm and 200 nm diameter spheres as functions of dimensional time, again using the tabulated polydisperse ion properties. The charge levels on all particles oscillate about zero, with the frequency of fluctuations and the deviations from neutral greater for the larger particles. Such results are anticipated, from prior work the fraction of particles which remain neutral at steady-state is known to decrease monotonically with particle size in bipolar ion environments.

6.3.2. Comparison to Flux Matching Derived Charge Distribution

For spherical particles in the 5 – 2000 nm size range, the fractions containing 0, +1, -1, +2, -2, and $|p| > 2$ calculated from simulations are shown in Figure 6.4. Results with the measured polydisperse ion properties (red circles) and the monodisperse ion properties noted by Wiedensohler (1988) (blue squares) are displayed. Also shown for comparison are the regression curves developed by Wiedensohler based upon the collision kernels of Hoppel & Frick (1986). Both sets of simulation results agree well with one another at all mobility diameters, though simulations with polydisperse ion properties lead to slightly more positive singly charged particles and slightly fewer negative singly charged particles in the 10 – 200 nm size range. This suggests that the overall consequence of using monodisperse ion properties in charge distribution calculations is minor for the measured polydisperse distribution, provided that appropriate values for ion properties are chosen. However, it should be noted that the monodisperse ion properties used are not the mean masses and mobilities of the polydisperse ions, and further that the same conclusion may not hold valid for all polydisperse ion populations. Future work, combining experimental measurements and improved collision rate calculations for oppositely charged ions and particles, will be necessary to reveal a method to determine the most appropriate monodisperse ion properties to invoke for a given polydisperse ion population.

More evident is the disagreement between simulations and the regression curves in the 20-2000 nm size range. For singly charged particles, the regression based distribution is highly skewed towards negative ions, while the simulated distributions only show a slight negative bias. The difference observed is substantial enough to influence electrical mobility based size distribution inversions; at 20 nm, the fraction of positive singly charged particles is ~26% greater in simulations with polydisperse ions than is expected by the regression equation and at 150 nm the fraction of negative singly charged particles is 10% less than is expected by the regression equation. Additionally, simulation results reveal significantly more positive doubly charged particles in the nanoparticle size range and a much higher fraction of particles with charge levels $|p| > 2$ in the submicrometer size range. For example, polydisperse ion simulations reveal fractions of positive doubly charged particles 48% and 38% greater than the regression equations at mobility diameters of 40 nm and 70 nm, respectively. As these trends are also evident when comparing the results with monodisperse ions to the regression curve, the differences are not brought about by the choice of ion properties, but rather must be due to differences between charging rates determined from ion trajectory calculations and from flux matching theory. Flux-matching calculations can lead to an artificially reduced number of particle-ion collisions in the presence of strong repulsive interactions as shown in chapter 5. Although ions moving at the mean thermal speed may be unable to collide with particles, there is a non-negligible fraction of ions with speeds higher than the mean, and these ions may indeed collide with like-charged particles, which, in turn, increases the fraction of particles with multiple charges. At larger sizes, the assumption that the fraction of particles at charge states $|p| > 5$ is negligibly small, made by Wiedensohler when developing the regression equations, leads to further underestimation of total number of multiply charged particles (Lòpez-Yglesias & Flagan, 2013). Conversely, the reason an increase in the fraction of positive singly charged particles and decrease in the fraction of negatively charged particles is found with simulations is not immediately clear. As polydisperse and monodisperse ions properties employed both have negative ions which are less massive and more mobile (in the polydisperse case this is true for the average ion properties, though certain negative ions are more massive and less mobile

than certain positive ions), a bias in the charge distribution towards negatively charged is still expected (and is found, just to a lesser extent than is found with flux matching theory). Presumably, this observed difference is brought about by differences in the particle charge reducing collision kernels ($\boldsymbol{\beta_{p,\mp 1}}$) calculated using the approach of Hoppel & Frick (1986) and that which would arise from simulating ion trajectories directly.

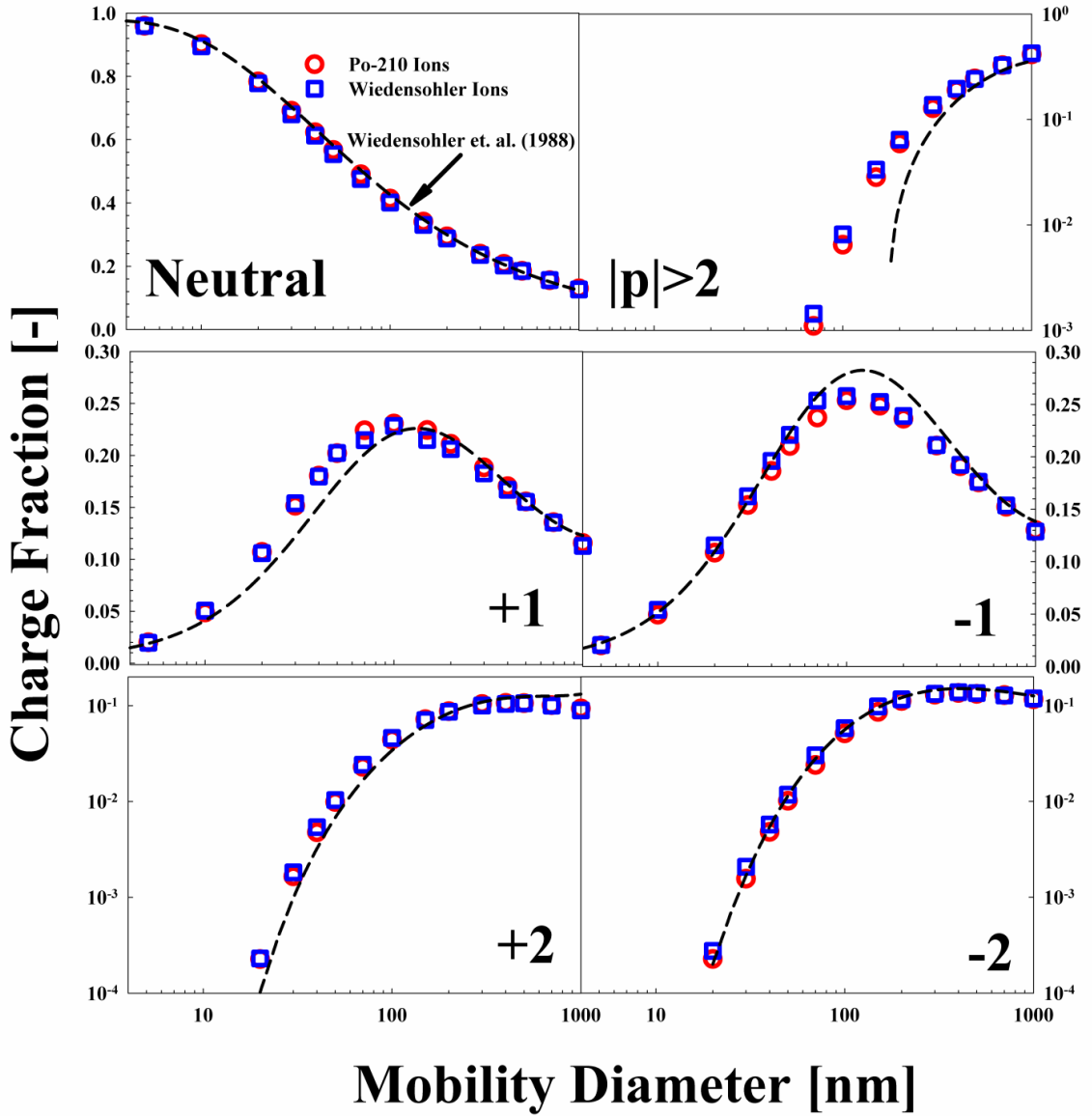

Figure 6.4: The fractions of neutral and charged spherical particles determined by Brownian dynamics calculations considering the Coulomb and image potentials, as functions of mobility diameter. Results considering polydisperse (Po-210) ions and the ion properties used by Wiedsensohler (1988) are displayed. The Wiedensohler (1988) regression curve is also noted.

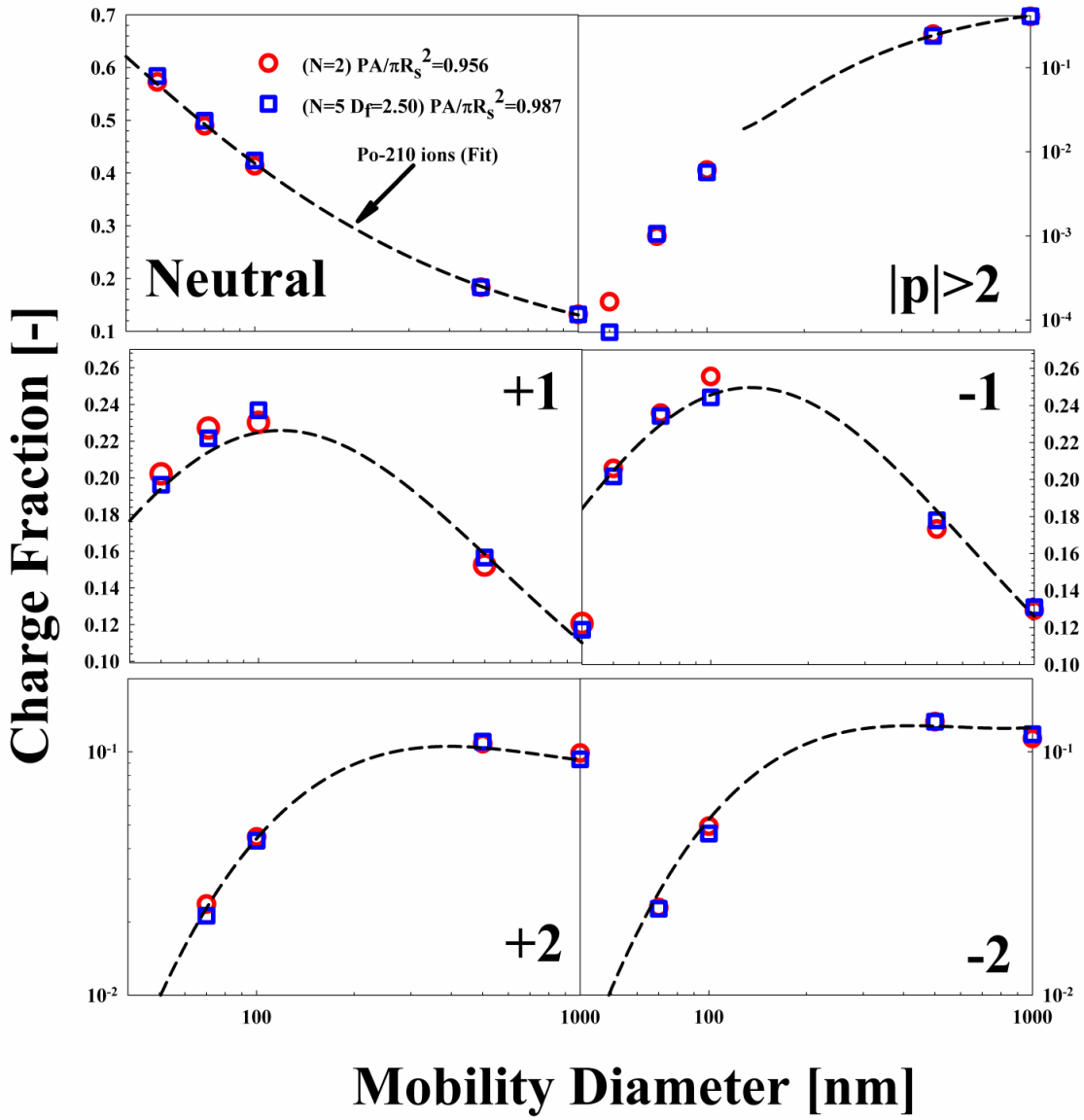

Figure 6.5: The fractions of neutral and charged nonspherical particles determined by Brownian dynamics calculations considering the Coulomb and image potential. The properties of the particles examined are shown in Table 6.1. Calculations are performed assuming the accumulated particle charge distributes itself to minimize Coulombic potential energy and considering polydisperse ion properties measured from a Po-210 radioactive source.

6.3.3. Non-Spherical Particle Charge Distributions Including Image Potential Interactions

In comparing non-spherical particle charge distributions to those of spheres, instances where the excess charge distributes itself in a manner minimizing Coulombic potential energy as well as image potential interactions are first considered. All reported results for non-spherical particles derive from simulations using polydisperse ions. Shown in Figure 6.5 are the charged (+1, -1, +2, -2, & $|p| > 2$) and uncharged fractions of particles for the dimer ($N_p = 2$) and $N_p = 5$ test aggregates, as functions of mobility diameter. Regression curves based upon simulations for spheres with polydisperse ions (described in sub-section 6.3.6.) are displayed via dashed lines. Charged fractions for these aggregates agree well with the regression expressions, indicating that in these instances steady-state charge distributions are not strongly influenced by morphology.

However, for the two noted aggregates, the ratio $PA/\pi R_s^2$ is close to unity. It is seen from previous chapters and elsewhere (Thajudeen *et al.*, 2012; Zhang, et al., 2012) that free molecular momentum transfer and particle-ion collision rates depend upon PA, while continuum momentum transfer and particle-ion collision rates depend on R_s. Agreement is hence expected in these instances. Conversely, for cylinders, the ratio $PA/\pi R_s^2$ decreases monotonically with increasing aspect ratio. The fractions of cylindrical particles described in Table 6.1 with 0, +1, -1, +2, -2, and $|p| > 2$ at steady-state are shown in Figure 6.6 as functions of mobility diameter, with different aspect ratio cylinders distinguished from one another by the $PA/\pi R_s^2$ values noted in the legend. The sphere-based regression curve is again shown for comparison. With an aspect ratio of 10 ($PA/\pi R_s^2 = 0.72$), charge distributions are found to be similar to those of spheres of the same mobility diameter. For the higher aspect ratio cylinders, below 200 nm in mobility diameter, the fractions of neutral particles and the fractions of multiply charged (doubly charged and $|p| > 2$) particles decrease and increase, respectively, with decreasing $PA/\pi R_s^2$. The +1 and -1 fractions show little dependency on $PA/\pi R_s^2$ at most mobility diameters for $PA/\pi R_s^2 > 0.25$. However, with $PA/\pi R_s^2 \leq 0.25$, the +1 and -1 fractions are

higher than is found for spheres below mobility diameters of ~70 nm, but lower than what is found for spheres in the 70-200 nm mobility diameter range. Further, for almost all cylinders in the 50-100 nm mobility diameter range, the singly charged particle fractions are nearly independent of mobility diameter. These results, in combination, show that higher aspect ratio particles become charged more prevalently than equivalent mobility diameter spheres below 200 nm. Therefore, if the charge fractions of spheres were assumed to apply to high aspect ratio particles, size distribution functions would be incorrectly inverted due to both incorrect calculations of the fractions of singly and multiply charged particles.

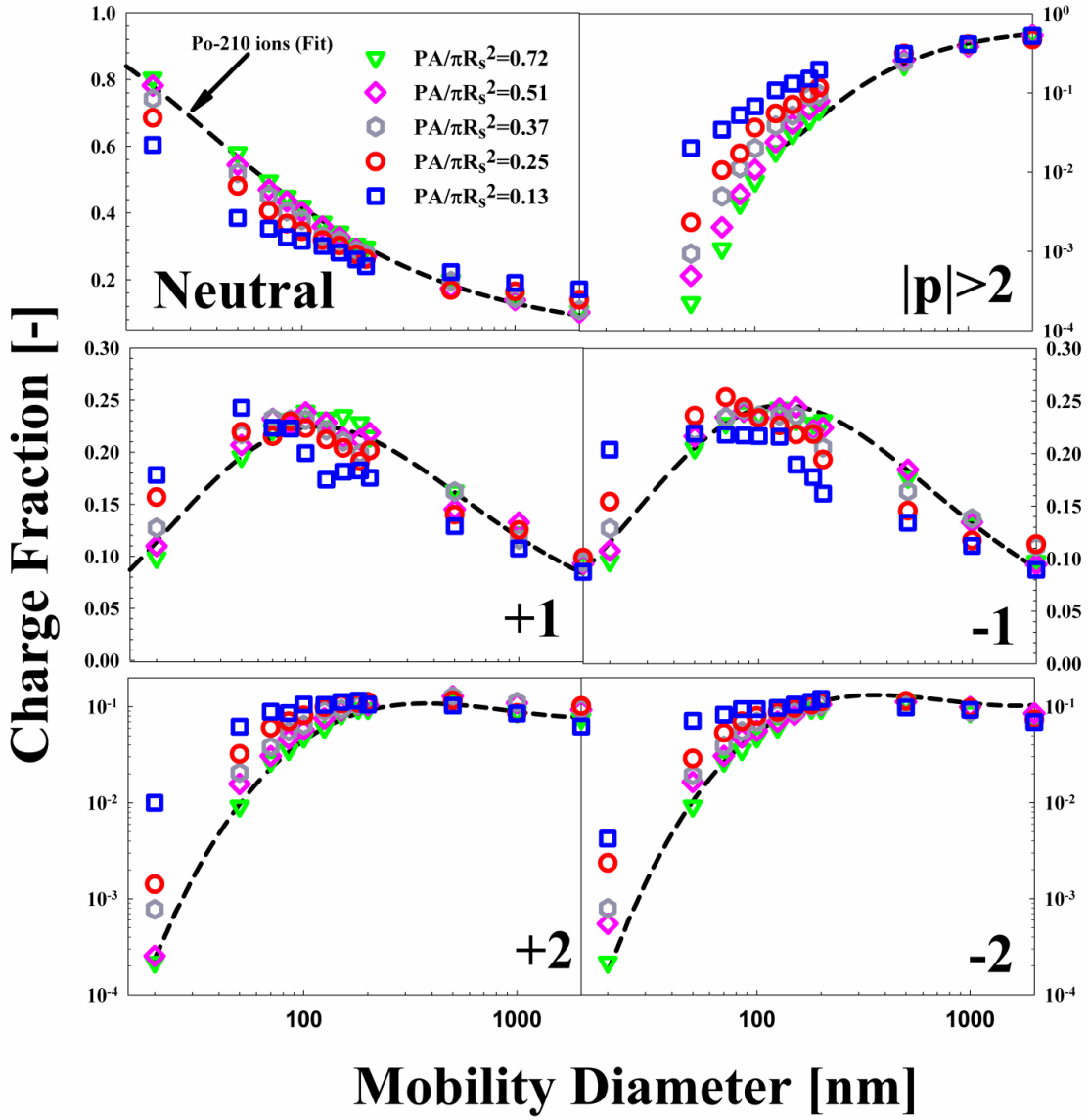

Figure 6.6: The fractions of neutral and charged cylindrical particles determined by Brownian dynamics calculations considering the Coulomb and image potential. The properties of the particles examined are shown in Table 6.1. Calculations are performed assuming the accumulated particle charge distributes itself to minimize Coulombic potential energy and considering polydisperse ion properties measured from a Po-210 radioactive source.

As mobility diameter increases, both momentum and mass transfer processes approach the continuum limit for all particles, in which particles of identical mobility diameter will have identical capacities/Smoluchowksi radii (equal to half the mobility diameter). Continuum limit particle-ion collision rates depend solely on Smoluchowski

radii (Laframboise & Chang, 1977; Mayya, 1990b); thus, particles of identical mobility diameter have identical steady-state charge distributions when both momentum and mass transfer occur in the continuum limit, irrespective of particle morphology and ion properties. At the largest mobility diameter examined (2000 nm), the cylinders with an aspect ratio of 50 have $Kn = 0.16$, leading to particle-ion collisions occurring at the near continuum limit rate for them, as well as lower aspect ratio cylinders (though note this is not determined strictly by Kn alone). It is not surprising then, that in the supermicrometer mobility diameter range, spheres and cylinders with aspect ratios below 50 have near identical steady-state charge distributions to one another. It should be noted that an exception would arise if particles preferentially align during mobility measurements, which appears to occur for large particles at high electric field strengths in differential mobility analyzers (Kasper & Shaw, 1982; Zelenyuk & Imre, 2007; Shin *et al.*, 2010).

Above 200 nm but below the size at which cylinders reach both the momentum and mass transfer continuum limits (Thajudeen, et al., 2012), high aspect ratio cylinders are surprisingly found to be less charged overall than their spherical counterparts. This is most evident for the cylinders of aspect ratio 300; at mobility diameters of 500 nm and 2000 nm there are ~20% and ~85%, respectively, more neutral cylinders than spheres. At the same time, however, the fractions of multiply charged particles remain close to or above those for spheres. Although the fractions of neutral particles decrease monotonically for all cylinders, the rate of change is substantially smaller than is found for spheres, which leads to cylinders appearing more charged than spheres at small mobility diameters, but less charged at large mobility diameters.

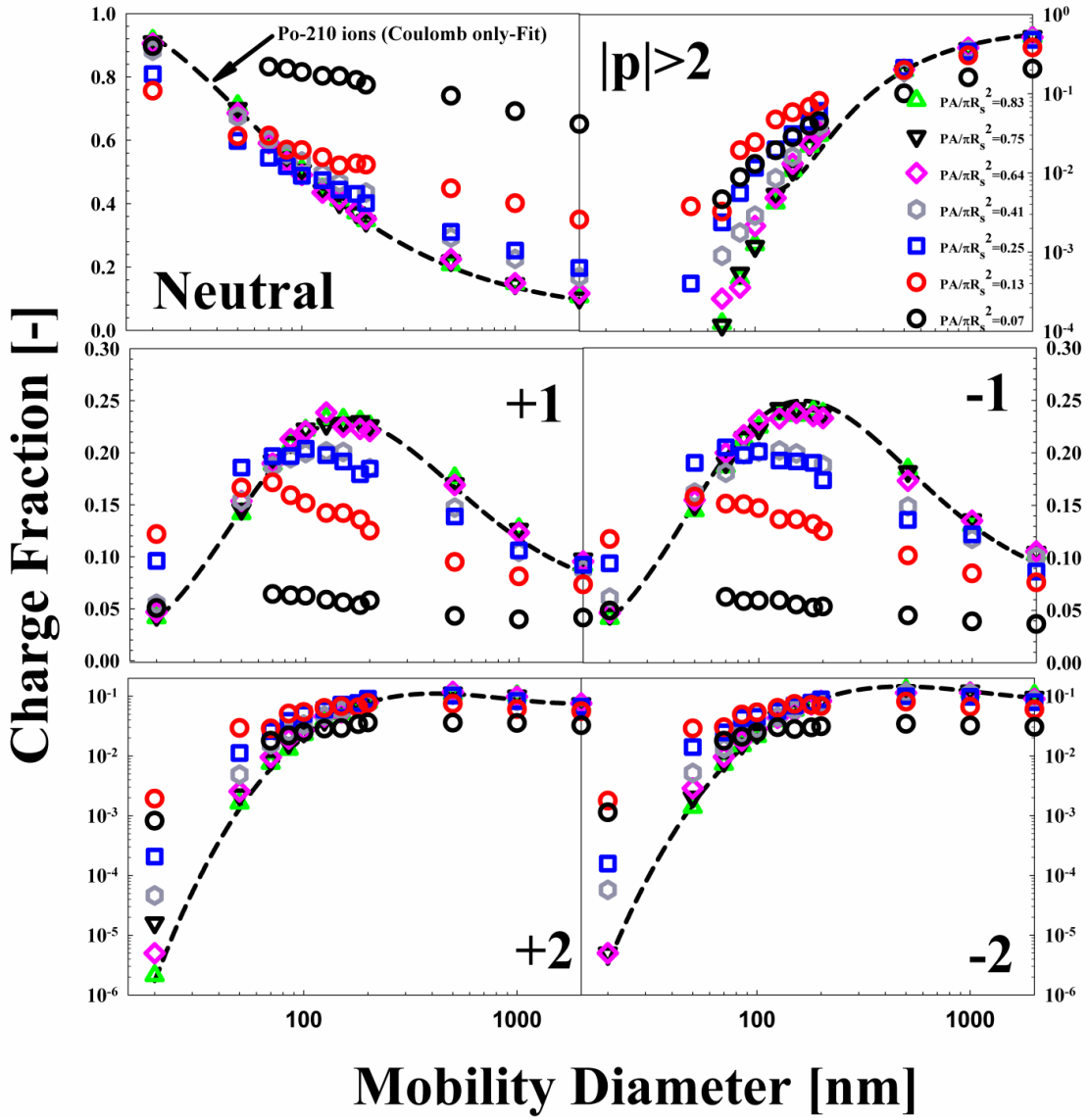

Figure 6.7(a.): The fractions of neutral and charged non-spherical particles determined by Brownian dynamics calculations considering the Coulomb and image potential. The properties of the particles examined are shown in Table 6.1. Calculations are performed assuming the accumulated particle charge distributes itself to minimize Coulombic potential energy.

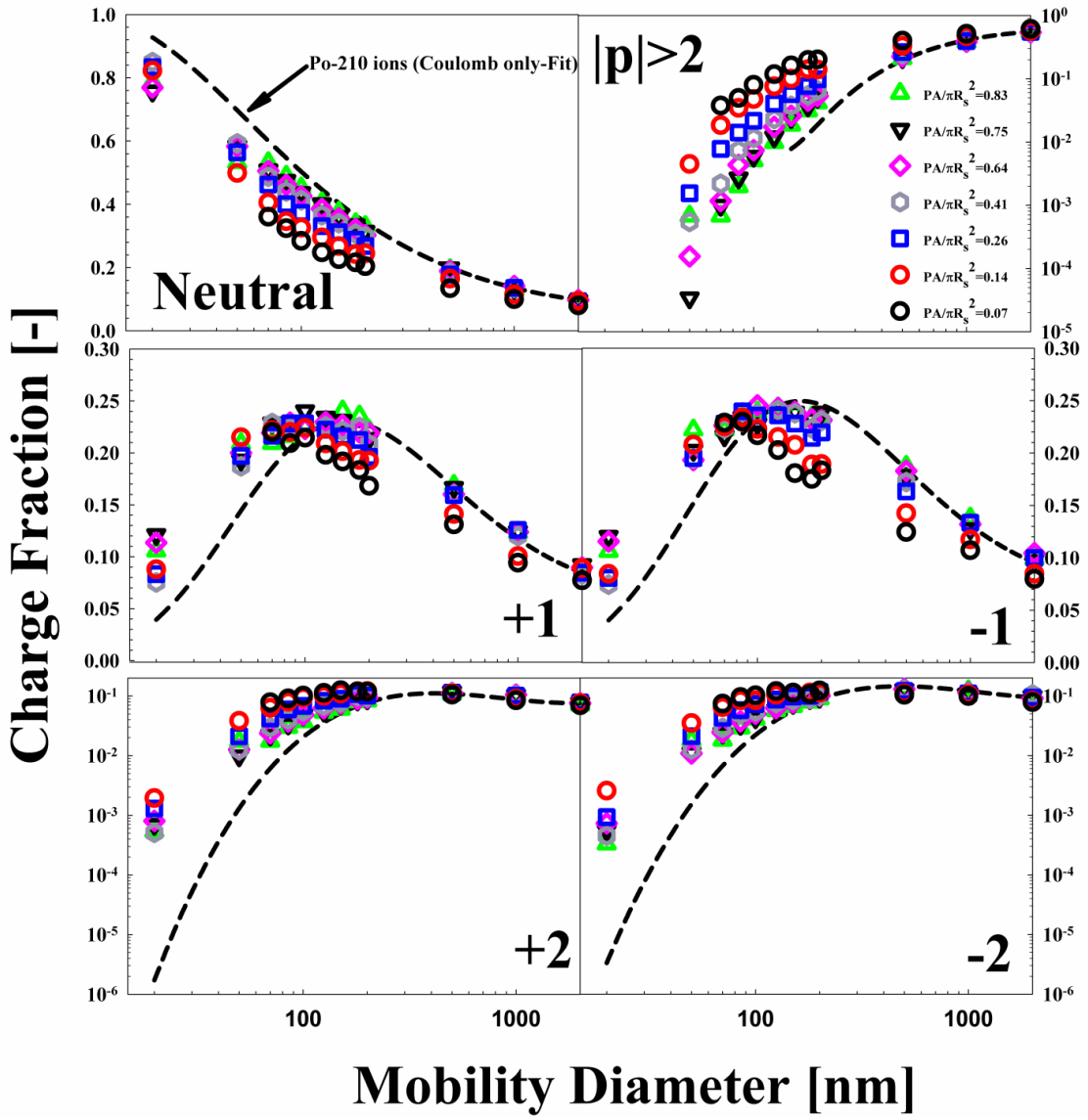

Figure 6.7(b.): The fractions of neutral and charged non-spherical particles determined by Brownian dynamics calculations considering the Coulomb and image potential. The properties of the particles examined are shown in Table 6.1. Calculations are performed assuming accumulated charges remain fixed at the location at which they collide with a particle.

6.3.4. Non-Spherical Particle Charge Distributions Excluding Image Potential Interactions

Excluding image potentials but maintaining the assumption that particle excess charge distributes itself to minimize internal Coulombic potential energy, particle-ion collision rates are still expected to depend on R_s and PA as length scale descriptors, and we hence expect charge distributions to depend on mobility diameter and the ratio $PA/\pi R_s^2$. The results of simulations without image potentials for cylinders, linear chains, and quasifractal aggregates are shown in Figure 6.7a. Results for different shapes are distinguished from one other via the $PA/\pi R_s^2$ values noted on the legend and in Table 6.1. Regression results for spheres, also obtained from results without image potentials included, are noted via dashed curves. Charge distributions determined without the image potential are qualitatively similar to those determined with its inclusion, though for spheres the fraction of neutral particles slightly increases with the exclusion of image potentials. Again, for the more modestly aspherical particles ($PA/\pi R_s^2 \geq 0.64$), charge distributions are similar to those found for spheres of the same mobility diameter. More pronounced than when image potentials are accounted for, however, is the shift from higher aspect ratio particles attaining more charge (lower neutral fractions, more multiply charged particles) in the sub-100 nm size range to higher aspect ratio objects attaining less charge at steady-state in the submicrometer range. Further, this transition is not limited to cylinders, as the degree of deviation from sphere regression curves also scales directly with $PA/\pi R_s^2$ for quasifractal aggregates and linear chains.

The finding that the image potential so drastically influences the charge distributions of non-spherical particles suggests that the bipolar charging of nonspherical particles is more dependent on particle material properties (conductivity) than is the charging of their spherical counterparts. This is further demonstrated through the results of simulations in which the charges attained by particles are immobile. Figure 6.7b displays the results of such simulations for linear chains and quasifractal aggregates, analogous to Figure 6.7a. In contrast to the results obtained with the conducting particle

model, particles of lower $PA/\pi R_s^2$ are found to have higher fractions of singly and multiply charged particles across the entire mobility range examined. These substantial differences are presumably brought about by differences in particle-ion collision rates between the conducting and non-conducting particle models. Without the assumption that particle charge distributes itself to minimize potential energy, particle-ion collision rates are not necessarily dependent on the size scales R_s and PA alone, as R_s is not necessarily the length scale defining the characteristic Coulomb energy for a non-conducting particle.

The drastic differences in charge distributions between the two models of how charge distributes itself on a non-spherical particle surface have considerable implications for size distribution inversion. Tandem differential mobility analyzer measurements of the charge distributions on non-spherical soot particles by Maricq (2008) are qualitatively similar to those predicted by the conducting particle model, as the soot particles examined had slightly more singly charged particles than spheres at a mobility diameter of 50 nm but slightly less at a mobility diameter of 400 nm. Conversely, the neutral fractions of non-covalently bound ensembles of multi-walled carbon nanotubes (likely with substantially lower electrical conductivities than isolated or aligned, single-walled nanotubes) measured by Ku et al (2011) were equal to or lower than those of spheres of equivalent mobility diameter in the submicrometer range, which is in line with the results found for non-conducting particles here. Unfortunately, in prior experimental studies, R_s and PA have not been not measured, efforts have not been made to infer particle conductivity, consistent ion properties have not been ensured (e.g. (Xiao *et al.*, 2012)), and alignment influences during mobility measurement have not been considered when comparing the charge distributions of spheres to non-spheres. It is therefore difficult to make direct comparison between model predictions and prior measurements in the transition regime. Measurement systems such as those recently constructed and tested by Beranek *et al* (2012) would enable R_s and PA determination without offline electron microscopy, and would hence aid in future efforts to compare model predictions to experiments.

6.3.5. Comparison to Prior Work on Non-spherical Particles

Aside from the application of the Wiedensohler (1988) charge distribution curves, the most prevalently used theory to estimate the charge distribution on non-spherical aerosol particles is that proposed by Wen et al. (1984a, 1984b). Specifically, they proposed that the charge distribution on linear-chain aggregates can be described using a Boltzmann-like distribution:

$$\boldsymbol{f_p = \left(\frac{\psi_E}{2\pi}\right)^{1/2} \exp\left(-\frac{(p-\bar{p})^2 \psi_E}{2}\right)} \quad (9a)$$

where $\boldsymbol{\psi_E}$ is the potential to thermal energy ratio, defined as:

$$\boldsymbol{\psi_E = \frac{e^2}{2\pi k T \epsilon_0 D_{qe}}} \quad (9b)$$

$\boldsymbol{\bar{p}}$ is the approximate mean charge, defined as:

$$\boldsymbol{\bar{p} = \frac{1}{\psi_E} \ln\left(\frac{f_{i,-}}{f_{i,+}}\right)} \quad (9c)$$

$f_{i,-}$ and $f_{i,+}$ are the friction factors of negative and positive ions, respectively, and D_{qe} is the "charging equivalent" diameter for the spherical particle in question. For straight chain aggregates, Wen et al (1984a) approximate D_{qe} as:

$$\boldsymbol{D_{qe} = \frac{d_0 N_p}{\ln(2N_p)}} \quad (9d)$$

which is adapted from an equation for twice the Smoluchowski radius of an ellipsoid. From this, we can extend the definition of D_{qe} to $D_{qe} = 2R_s$. Notably, equations (9a-9d) have been employed by Lall & Friedlander (2006) in an effort to develop an approach to measure surface area and volume distributions for aggregates with electrical mobility measurements in the transition regime. However, the validity of equations (9a-9d) has been examined sparingly, and further, they are simply modifications of the approximate equations put forth by Gunn (1955) to evaluate the charge distribution on spherical particles in a bipolar ion environment, solely in the continuum regime of mass transfer. Nanometer and submicrometer particles at room temperature fall outside of the mass transfer continuum regime, thus there is cause for concern if (9a-9d) are extrapolated to these sizes. Shown in Figure 8a is comparison of (9a-9d) to the simulated distributions of quasifractal aggregates ($N_p = 80$, $D_f = 1.95$ and $N_p = 60$, $D_f = 1.63$) and in Figure 6.8b to

the simulated distributions of chain aggregates (30 and 500 primary particles) in the absence of image potential (which equations (9a-9d) do not account for). Equation (9) predictions are made both employing equation (9d) and equating D_{qe} with $2R_s$. Irrespective of the choice of D_{qe}, equation (9) predictions do not agree well with neither simulations results for conducting particles nor those for nonconducting particles, except at several mobility diameters where equation (9) predictions and simulation results cross one another. We hence do not advocate the continued use of equation (9) to approximate the charge distribution on nonpsherical particles in the transition regime.

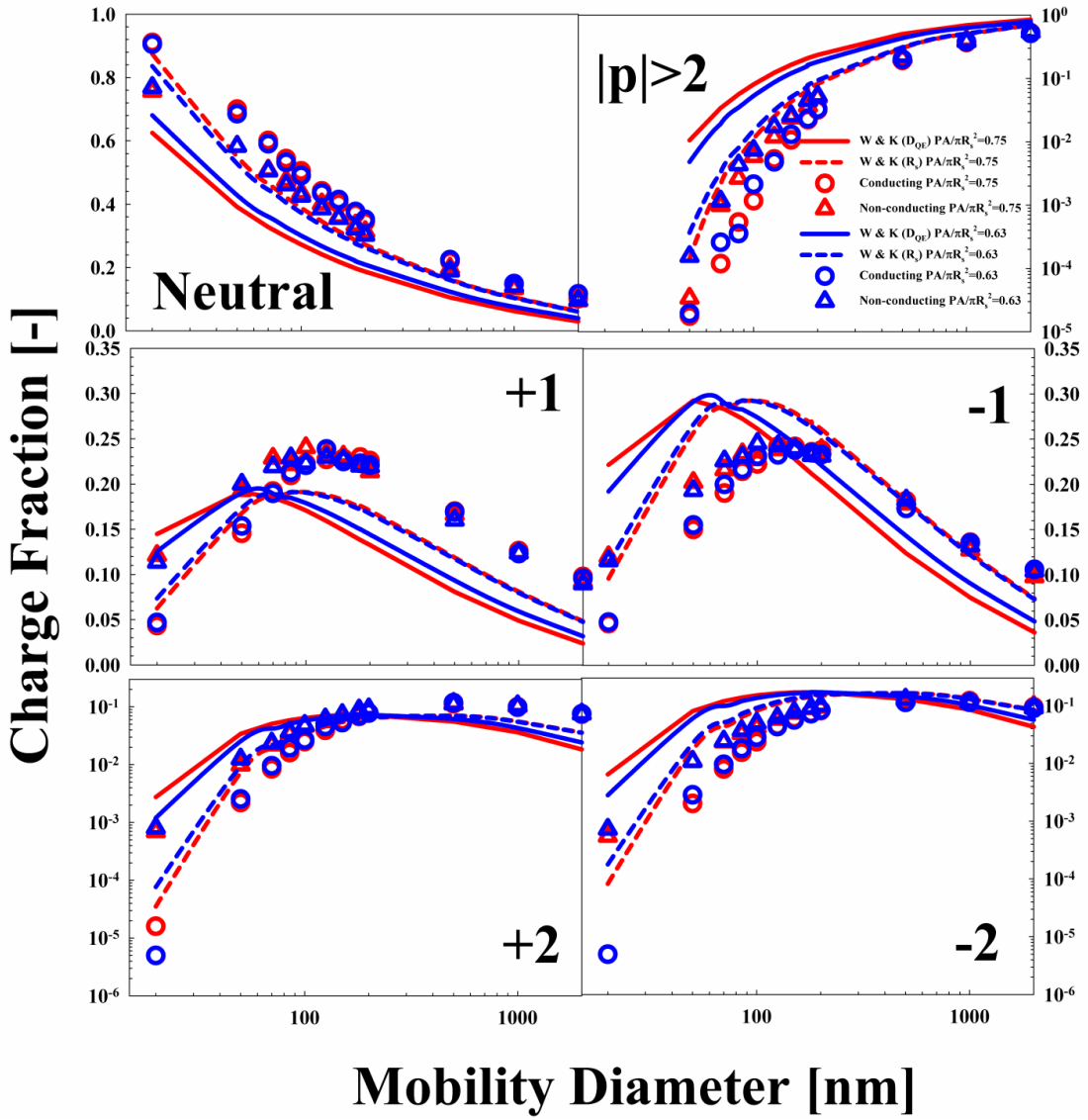

Figure 6.8(a): A comparison of the predictions of the model by Wen et al (1984a) to Brownian dynamics determined charge distributions for quasifractal aggregates. Particles are identified by their noted $PA/\pi R_s^2$ values, with their complete properties listed in Table 6.1. The predictions of Wen et al are performed with (1) D_{qe} is defined by equation (9d) (solid curves) and (2) $D_{qe} = 2R_s$ (dashed curves).

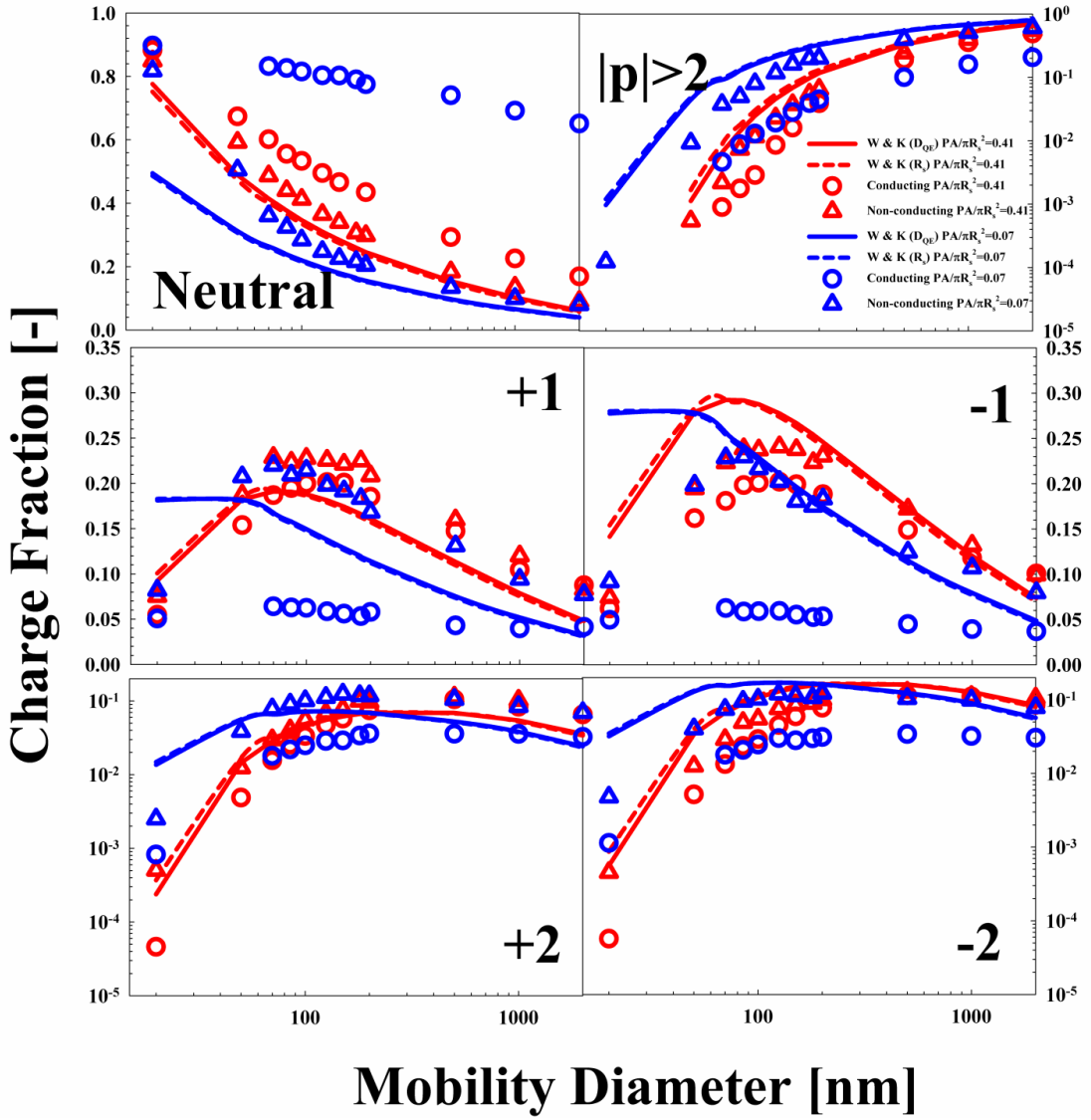

Figure 6.8(b): A comparison of the predictions of the model by Wen et al (1984a) to Brownian dynamics determined charge distributions for straight chain aggregates. Particles are identified by their noted $PA/\pi R_s^2$ values, with their complete properties listed in Table 6.1. The predictions of Wen et al are performed with (1) D_{qe} is defined by equation (9d) (solid curves) and (2) $D_{qe} = 2R_s$ (dashed curves).

6.3.6. Revised Charge Distribution Equations

Simulations with spheres and non-spherical particles, including and excluding image potentials, enable the development of regression equations to approximate the charge distributions on particles. Such regression equations are provided here in the form:

$$\boldsymbol{f_p(d_m) = \exp\left(\sum_{i=0}^{3} a_i\left(p, \frac{PA}{\pi R_s^2}\right)(\ln(d_m))^i\right)} \quad (10)$$

where d_m is given in nanometers and the coefficients a_i depend upon p, $PA/\pi R_s^2$, and the manner in which charge distributes on a particle surface. Equation (10) is highly similar in form to that used by Wiedensohler (1988), except that Wiedsensohler used 6 coefficients instead of 4 (we note that most R-square coefficients are > 0.99 with the 4 parameter regressions), and also used the common (base 10) log in lieu of the natural log. Tables 6.2, 6.3, & 6.4 listed the coefficients for $p = -2, -1, 0, 1, \& 2$ for selected values of $PA/\pi R_s^2$ considering conducting particles and the image potential, conducting particles without the image potential, and nonconducting particles, respectively. To determine the values $PA/\pi R_s^2$, both parameters can be calculated as described by Gopalakrishnan et al (2011), or regression equations developed for quasifractal aggregates and cylinders may be used (Thajudeen, et al., 2012). Linear interpolation may be used to find f_p for $PA/\pi R_s^2$ values between those listed in tables. Moreover, the values for $PA/\pi R_s^2 = 1.00$ apply to spherical particles, and they can be used generally to approximate the steady-state bipolar charge distribution in lieu of using the Wiedensohler distribution for $|p| \leq 2$.

Table 6.2. The coefficients necessary for equation (10) with the Coulomb and image potential considered between particles and ions, and particles assumed conducting.

	$p = 0$			
$PA/\pi R_s^2$	a_0	a_1	a_2	a_3
0.1	1.8168	-1.12□2	0.1301	-0.0058
0.25	-0.2859	0.4199	-0.1937	0.0144
0.37	0.8966	-0.3534	-0.0181	0.0014
0.51	-0.3265	0.4902	-0.1910	0.0122
0.72	0.2207	0.1269	-0.1101	0.0067
1.00	-0.3880	0.4545	-0.1634	0.0091

	$p = -1$				$p = +1$			
$PA/\pi R_s^2$	a_0	a_1	a_2	a_3	a_0	a_1	a_2	a_3
0.13	-4.8006	2.0267	-0.3838	0.0209	-4.6451	1.9779	-0.3817	0.0210
0.25	-9.4638	4.6930	-0.8693	0.0497	-6.8841	3.0381	-0.5394	0.0288
0.37	-8.9901	4.1032	-0.7082	0.0377	-8.6720	3.9012	-0.6679	0.347
0.5	-9.0270	3.8284	-0.6029	□.028 3	-9.9368	4.5129	-0.7623	0.0395
0.72	-10.183	4.4594	-0.7168	0.0350	-10.488	4.6738	-0.7643	0.0381
1.00	-7.8696	3.1036	-0.4557	0.0187	-8.0157	3.2536	-0.5018	0.0223

	$p = -2$				$p = +2$			
$PA/\pi R_s^2$	a_0	a_1	a_2	a_3	a_0	a_1	a_2	a_3
0.13	-21.452	9.4514	-1.5021	0.0767	-23.569	10.682	-1.7377	0.0915
0.25	-37.604	17.611	-2.8771	0.1541	-28.592	12.306	-1.8693	0.0922
0.37	-35.931	15.751	-2.4120	0.1213	-36.697	16.257	-2.5109	0.1266
0.51	-43.98	19.643	□3.036	0.1543	-36.973	16.038	-2.4299	0.1207
0.72	-46.825	20.741	-3.1709	0.1595	-42.005	18.142	-2.7132	0.1327
1.00	-45.405	20.049	-3.0570	0.1534	-40.714	17.487	-2.6146	0.1282

Table 6.3: The coefficients necessary for equation (10) with the image potential between particles and ions neglected, and particles assumed conducting.

	$p = 0$			
$PA/\pi R_s^2$	a_0	a_1	a_2	a_3
0.07	0.1549	-0.1250	0.0164	-0.0013
0.13	0.9498	-0.6477	0.0972	-0.0061
0.25	1.2357	-0.6768	0.0802	-0.0054
0.41	0.5466	-0.1663	-0.0202	0.0002
0.64	-0.7□02	0.8009	-0.2335	0.0137
0.75	-0.5228	0.6345	-0.1945	0.0106
0.83	-1.2925	1.1534	-0.3035	0.0178
1.00	-1.2120	1.1068	-0.2934	0.0169

	$p = -1$				$p = +1$			
$PA/\pi R_s^2$	a_0	a_1	a_2	a_3	a_0	a_1	a_2	a_3
0.07	-6.5562	2.2142	-0.4126	0.02□4	-7.8718	3.1083	-0.6000	0.0358
0.13	-6.5942	2.7818	-0.5178	0.0292	-7.9102	3.6690	-0.6973	0.0403
0.25	-9.9795	4.4756	-0.7605	0.0399	-10.601	4.8872	-0.8466	0.0455
0.41	-13.667	6.3072	-1.0596	0.0561	-14.743	6.8263	-1.1365	0.0594
0.64	-16.000	7.3453	-1.1909	0.0609	-15.901	7.2709	-1.1749	0.0596
0.75	-15.527	6.9673	-1.1038	0.0548	-16.320	7.4402	-1.1961	0.0605
0.83	-16.123	7.2505	-1.1475	0.0570	-15.966	7.1258	-1.1181	0.0547
1.00	-16.801	7.5947	-1.1975	0.0590	-16.704	7.5438	-1.1938	0.0589

	$p = -2$				$p = +2$			
$PA/\pi R_s^2$	a_0	a_1	a_2	a_3	a_0	a_1	a_2	a_3
0.07	-27.824	11.709	-1.8496	0.0962	-30.318	12.883	-2.0246	0.1047
0.13	-29.651	12.978	-2.0417	0.1052	-29.431	12.932	-2.0441	0.1056
0.25	-47.488	21.564	-3.3989	0.1765	-43.897	19.423	-2.9821	0.1501
0.41	-46.358	19.532	-2.8485	0.1367	-50.532	21.924	-3.2791	0.1609
0.64	-66.767	29.811	-4.5508	0.2295	-66.169	29.374	-4.4517	0.2222
0.75	-63.115	27.357	-4.0501	0.1978	-52.123	21.601	-3.0613	0.1416
0.83	-68.767	30.127	-4.5037	0.2226	-69.998	30.805	-4.6157	0.2276
1.00	-63.185	26.833	-3.8723	0.1835	-71.051	31.209	-4.6696	0.2301

Table 6.4. The coefficients necessary for equation (10) with the image potential between particles and ions neglected, and particles assumed nonconducting.

	$p = 0$			
$PA/\pi R_s^2$	a_0	a_1	a_2	a_3
0.07	2.1247	-0.7971	0.0008	0.0031
0.13	2.1382	-0.9206	0.0532	-0.0013
0.25	1.5571	-0.6327	0.0222	-0.0009
0.41	0.968	-0.308	-0.025	0.001
0.64	-0.4974	0.5023	-0.1686	0.0093
0.75	-0.8128	0.6497	-0.1866	0.0098
0.83	-0.8286	0.6728	-0.1873	0.0094
1.00	-1.212	1.1068	-0.2934	0.0169

	$p = -1$				$p = +1$			
$PA/\pi R_s^2$	a_0	a_1	a_2	a_3	a_0	a_1	a_2	a_3
0.07	-12.653	6.185	-1.0987	0.0607	-13.646	6.6929	-1.1826	0.0651
0.13	-12.835	6.1403	-1.0622	0.0572	-14.152	6.9706	-1.2293	0.0678
0.25	-12.66	5.8842	-0.9865	0.0516	-11.424	5.1354	-0.8418	0.0424
0.41	-13.081	6.0188	-0.992	0.0509	-12.485	5.6607	-0.923	0.0463
0.64	-8.393	3.4777	-0.5432	0.0252	-8.5893	3.628	-0.5784	0.0274
0.75	-7.7041	3.0775	-0.4672	0.0204	-8.0471	3.3366	-0.5267	0.0244
0.83	-8.4271	3.3863	-0.5076	0.0221	-7.9352	3.0531	-0.4369	0.017
1.00	-16.801	7.5947	-1.1975	0.059	-16.704	7.5438	-1.1938	0.0589

	$p = -2$				$p = +2$			
$PA/\pi R_s^2$	a_0	a_1	a_2	a_3	a_0	a_1	a_2	a_3
0.07	-27.546	12.436	-1.9855	0.103	-34.124	15.898	-2.5738	0.1352
0.13	-32.69	14.873	-2.3706	0.1234	-34.576	15.896	-2.5452	0.1327
0.25	-35.342	15.581	-2.4022	0.1215	-31.578	13.534	-2.038	0.1
0.41	-37.88	16.397	-2.4818	0.1239	-34.698	14.41	-2.0806	0.0973
0.64	-28.775	11.021	-1.4691	0.0625	-28.837	10.936	-1.472	0.0631
0.75	-31.173	12.332	-1.712	0.0774	-27.99	10.488	-1.3632	0.0556
0.83	-32.972	12.887	-1.7559	0.0778	-27.452	9.8612	-1.2119	0.0452
1.00	-63.185	26.833	-3.8723	0.1835	-71.051	31.209	-4.6696	0.2301

6.4. Conclusions

From the results of the Brownian Dynamics study of the charging of spherical and non-spherical particles as presented in the previous sections, the following conclusions are drawn:

- The ions generated by commonly used bipolar ionizers (e.g. Po-210 sources) have complex mass-mobility spectra, strongly dependent on the composition of the carrier gas and the impurities present in the aerosol. Nonetheless, with the monodisperse mass and mobility values of Wiedensohler (1988) employed, the differences in the BD calculated fractions of charged and uncharged particles from those calculated with a polydisperse input ion population are found minimal. The extent to which this conclusion holds valid for polydisperse ion populations under alternative conditions (e.g. with ambient air) remains to be verified.
- The underprediction of the fraction of charged particles by the Wiedensohler (1988) in the sub-100 nm size range for spheres appears to be due to the underprediction of the charging rate by the flux matching theory. At sizes larger than 100 nm, the Wiedensohler expression derives from calculations neglecting the fraction of highly charged ($|p| > 5$) particles and thus overpredicts the fraction of particles carrying lower numbers of charges.
- The BD-calculated charge distributions of slightly non-spherical particles ($\boldsymbol{PA/\pi R_s^2 \geq 0.50}$) are similar to the charge distributions found on spherical particles of the similar mobility diameter. For the most open/aphserical structures examined ($\boldsymbol{PA/\pi R_s^2} < 0.50$), the fraction of higher charges ($|p|>2$ and $p=\pm 2$) are higher than spheres of the same mobility diameter below 150 nm and lower than spheres above 200 nm. Aerosol particle material is seen to have a greater effect on the bipolar charging of non-spherical particles than spherical particles in calculations, and previously developed predictions for the bipolar charge distribution on non-spherical particles are in pronounced disagreement with BD calculations for all simulated circumstances.

Chapter 7: Drag on Nonspherical Nanoparticles

The transition regime drag law, invoked in Chapter 6, is experimentally verified by measuring the drag on spherical and cylindrical nanoparticles. It is also seen that the DMA transfer function can be measured by analyzing the size distributions of mobility classified particles collected on TEM grids. The verification serves as a step towards diffusion charging measurements on cylindrical nanoparticles, described in Chapter 8.

7.1. Introduction

Accurate knowledge of the drag experienced by aerosol particles is important to characterize them using electrical mobility measurements. In instances of low Mach number and low Reynolds number gas flows, the drag force $\vec{F}$ can be calculated as a product of a scalar friction factor f_p and the first power of the relative drift velocity $\vec{U}$ of the particle with respect to the gas ($\vec{F} = f_p\vec{U}$). The nature of momentum transfer between the gas molecules and an aerosol particle is described by the momentum transfer Knudsen number *Kn* defined as λ_g/a_p where λ_g is the mean free path of gas molecules and a_p is the radius (or a suitable measure of size) of the particle. In calculating the transition regime momentum transfer to spherical particles, a slip correction factor C_c, which is a regression fit of experimentally measured drag on spherical particles at various *Kn* values to obtain a smooth interpolation between the continuum and the free molecular limit, is applied to Stokes law to account for the velocity slip of gas molecules on the surface of the particle (Eglin, 1923; Millikan, 1923; Davies, 1945; Allen & Raabe, 1982; Rader, 1990; Kim *et al.*, 2005):

$$f_p = \frac{6\pi\mu_g a_p}{C_c} \tag{1a}$$

$$C_c(Kn) = 1 + Kn\left(a_1 + a_2\exp\left(-\frac{a_3}{Kn}\right)\right) \tag{1b}$$

Here, $\boldsymbol{a_1, a_2, a_3}$ are semi-empirical slip correction coefficients whose values depend on the type of gas (Rader, 1990) and $\boldsymbol{\mu_g}$ is the gas viscosity. The applicability of equation (eq. 1), a settled issue so far as determining friction factor for spherical particles is concerned, is examined in this work for nonspherical particles. Apart from some limited attention to drag on nonspherical particles (Pich, 1969; Rogak & Flagan, 1990; Filippov, 2000; Vainshtein & Shapiro, 2005; Gmachowski, 2010), the Adjusted Sphere Model (Dahneke, 1973a, 1973b, 1973c) and the more recent expression proposed by Zhang *et al.*(2012) enable friction factor calculation for arbitrary shaped particles at all *Kn* (introduced through equations (8a) and (8b) of Chapter 6).

Rogak *et al.* (1993) have studied the relationship between the projected area diameter and the mobility diameter of aggregates in the transition and the free molecular regimes. By using electron microscopy, they have carefully characterized TiO_2/Si aggregates synthesized in a flame. By eliminating multiply charged aggregates seen on the microscopy grids, it is seen that, for aggregates of mobility diameter less than 400 nm, the projected area diameter follows the mobility diameter approximately. The discrepancies seen in bigger size ranges suggest the existence of a different length scale for which they postulate that the radius of gyration of aggregates is appropriate in the continuum regime and point to agreement between their model and measurements to within 25% as evidence. A similar study using gold nanorods has been done by Song *et al.* (2005) to compared measured drag with the predictions of eq. 2 with the volume equivalent diameter (obtained via TEM measurements) and the shape factors derived for spheroidal particles. The same approach is adopted here, coupling electron microscopy measurements to obtain the true size of mobility classified non-spherical particles and for direct comparison as described in this chapter.

In this chapter, friction factor measurements done using well characterized cylindrical nanoparticles to experimentally verify the predictions of the transition regime

drag expression proposed by Zhang *et al.* (2012) are described. New measurements are required for such verification, as the theory requires well defined particle length scales (R_s and PA) that were not measured in previous studies. The generation of aerosol nanoparticles is described along with details of the mobility distribution measurement using the DMA and geometric characterization by transmission electron microscopy (TEM). The principle of the measurement is laid out and considerations of preferential alignment of non-spherical particles while flowing through the DMA is discussed and put in context with other instances of preferential alignment reported in the literature. Finally, the results of mobility distribution histograms for each data set of particles along with the degree of agreement between experiment and theory are presented and discussed.

7.2. Experimental Methods

7.2.1. Aerosol Generation

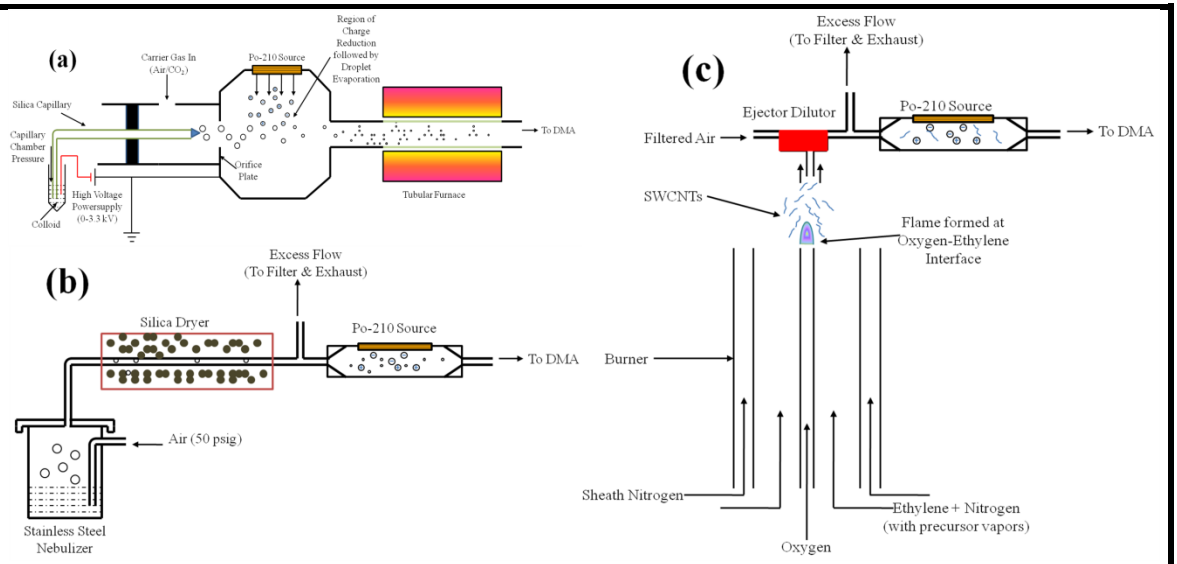

Figure 7.1: Schematic Representation of Aerosol Generation techniques employed. (a) Electrospray aerosolization using TSI 3480 Electrospray Aerosol Generator (b) Collision Nebulization of PSL solution (c) Flame synthesis of SWCNTs using an inverse diffusion flame. See Appendix D for details of generation methods.

Spherical and nonspherical particles (cylinders and doublets of spheres) were generated for measurement using three generation techniques: 1) Electrospray aerosolization of colloidal gold solutions to generate spheres and cylindrical particles (fig. 7.1a) 2) Collision Nebulization of PSL solutions to generate doublets of spheres (fig. 7.1b) 3) Flame synthesis of Single walled Carbon nanotubes (SWCNTs) (fig. 7.1c). A detailed description of these methods can be found in Appendix D. TEM images of the particles examined here are given in Fig. 7.2 and the mean dimensions for all of the datasets are listed in Table 7.1.

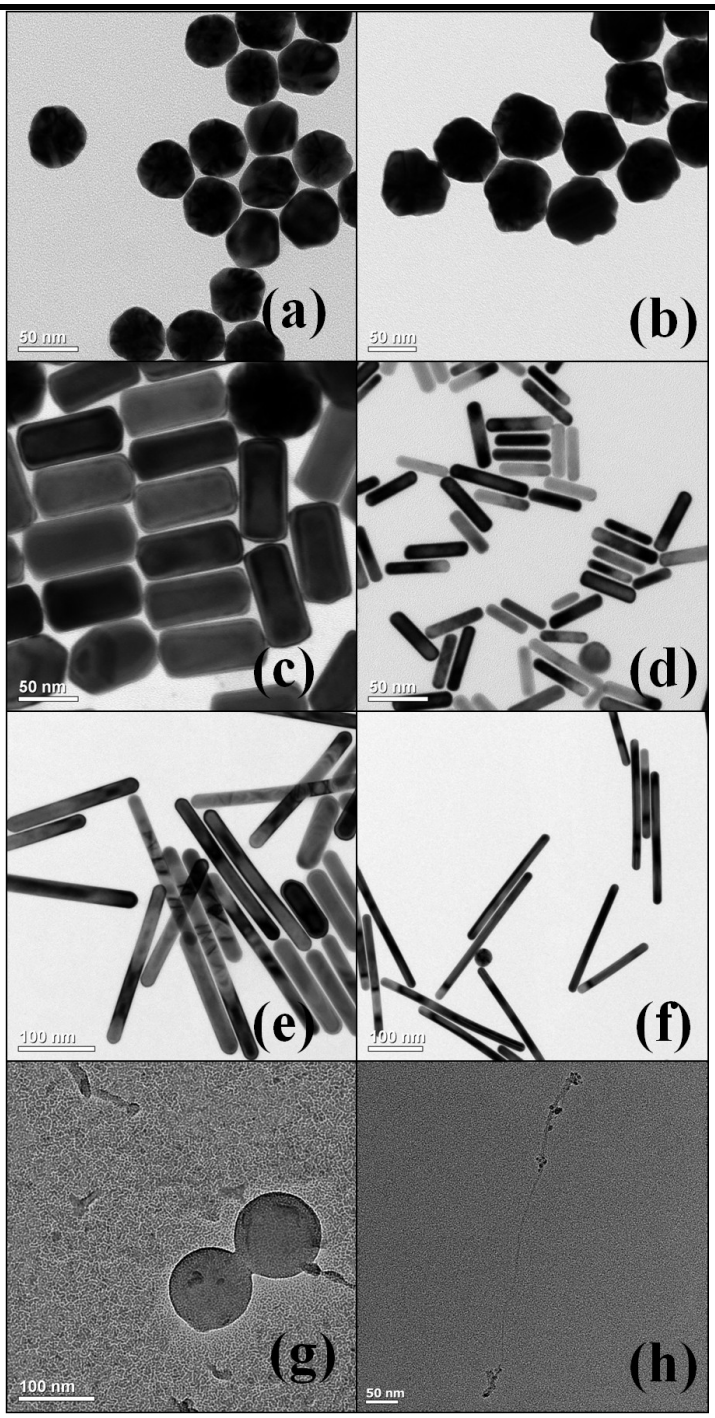

Figure 7.2: TEM images of nanoparticles considered for drag measurement: (a) 50 nm spheres (b) 70 nm spheres (c) $\frac{l_p}{d_p}$=1.8 nanorods (d) $\frac{l_p}{d_p}$=3.8 nanorods (e) $\frac{l_p}{d_p}$=9.4 nanorods (f) $\frac{l_p}{d_p}$=14 nanorods (g) PSL doublets (h) SWCNTs

Dataset	Nominal Dimensions				Sample TEM image
	$\overline{d_p}$ (nm)	$\overline{l_p}$ (nm)	$\overline{\left(\frac{l_p}{d_p}\right)}$	$\overline{\left(\frac{PA}{\pi R_s^2}\right)}$	
50 nm spheres	49±2.0	-	-	1.00	Fig. 7.2(a)
70 nm spheres	70±1.9	-	-	1.00	Fig. 7.2(b)
$\frac{l_p}{d_p}$=1.8 □anoro□s	46±3.2	81±6.0	1.8	0.81	Fig. 7.2(c)
$\frac{l_p}{d_p}$=3.8 nanorods	15±1.5	56±4.3	3.8	0.85	Fig. 7.2(d)
$\frac{l_p}{d_p}$=9.4 nanorods	23±4.9	200±49	9.4	0.74	Fig. 7.2(e)
$\frac{l_p}{d_p}$=14 nanorods	17±2.1	230±49	14	0.66	Fig. 7.2(f)
SWCNTs d_m=4.3 nm	7.5±3.3	140 – 1140	9.5 – 175	0.19 – 0.77	Fig. 7.2(h)
SWCNTs d_m=53.9 nm	6.3±2.0	280 – 1040	44 – 243	0.19 – 0.50	
SWCNTs d_m=60.3 nm	7.2±2.0	360 – 1090	39 – 176	0.19 – 0.47	
PSL doublets $\boldsymbol{d_{p1}}$and $\boldsymbol{d_{p1}}$ are diameters of primary spheres	$\overline{d_{p1}}$=116±6.7 nm $\overline{d_{p2}}$=115±7.7 nm			0.96	Fig. 7.2(g)

Table 7.1: Mean dimensions of spherical, cylindrical and doublet shaped nanoparticles.

7.2.2. Determination of Mobility Distribution

A TSI nano® DMA 3085 was used for mobility characterization of all samples (fig. 7.3), with the exception of PSL doublets for which a University of Minnesota built long DMA (Knutson & Whitby, 1975a) was used. The sheath flow through the DMA and CPC sample flowrates were calibrated against a Gilian® Gilibrator flowcell to within 1% accuracy in Air and Carbon dioxide. The DMA was operated at a fixed sheath flow rate (closed loop) with the voltage being stepped (as opposed to being scanned) to acquire mobility distributions (see fig. 7.4 for representative mobility spectra for selected datasets). The temperature of the sheath flow entering the DMA was measured using a K-type thermocouple (Omega, resolution of 0.5° C and accuracy of about 1%). The classifying voltage to the DMA was applied using a Bertan (205B-10R) powersupply with a range of 0-10000 V, resolution of 5 V and an accuracy of 1% of the full scale reading. For obtaining number concentrations, the TSI 3025A ultrafine condensation particles counter (UCPC) was used (Stolzenburg & Mcmurry, 1991).

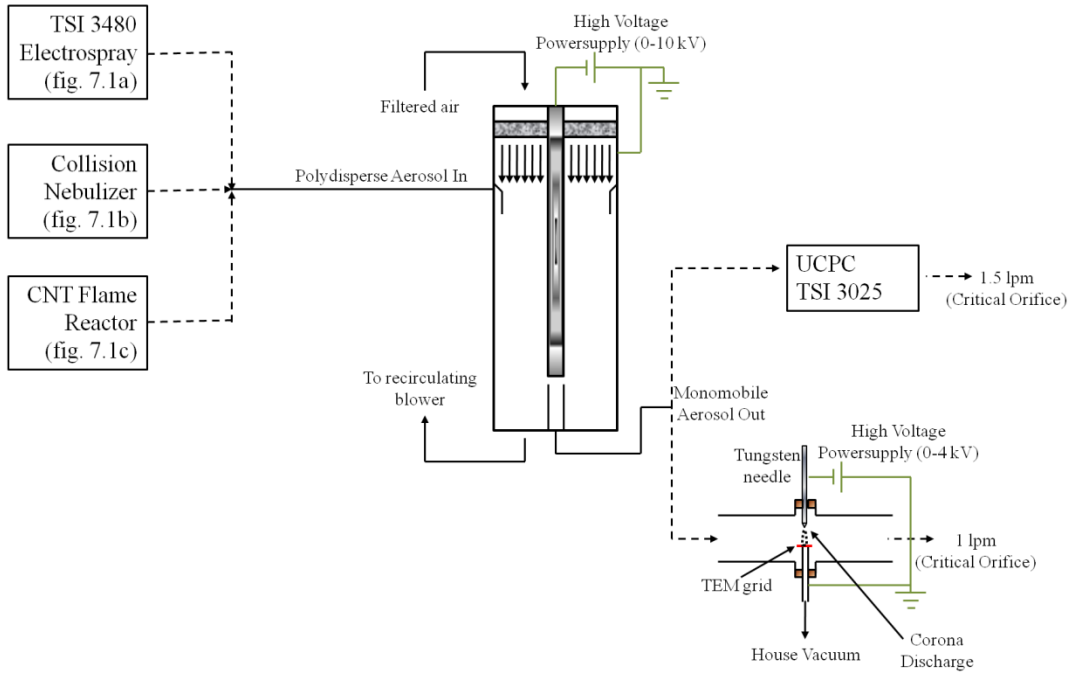

Figure 7.3: Schematic representation of the mobility and size distribution measurements.

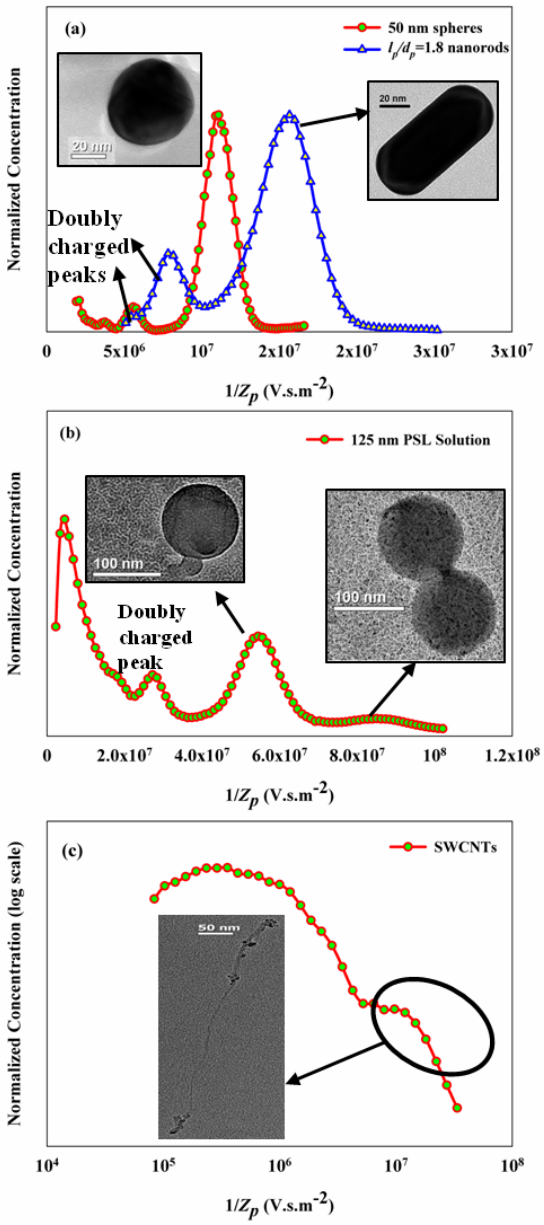

Figure 7.4: Representative mobility spectra of nanoparticle aerosol particles considered (Z_p is the electrical mobility). DMA voltage is set to classify the peak mobility found in such spectra to deposit particles onto TEM grids. (a) Electrosprayed 50 nm spheres and $\frac{l_p}{d_p}$=1.8 nanorods in air. (b) Nebulized PSL particles: The doublets are used for measurement, while the singly and doubly charged PSL spherical particles are not used. (c) Flame generated SWCNTs are obtained as a part of a bimodal distribution. The dominant peak found at lower $1/Z_p$ (not labeled) corresponds to unreacted catalyst particles that are not of interest to us.

7.2.3. Determination of Geometric Size using Electron Microscopy

To facilitate comparison between theory and experiment, precise knowledge of the size of each nanoparticle is necessary. Based on the mobility distribution for a given sample, the DMA is set at a voltage corresponding to the peak mobility and a point-to-plane electrostatic sampler (Cheng *et al.*, 1981; Miller *et al.*, 2010) is used downstream (fig. 7.3) to deposit particles onto a TEM grid (Tedpella Inc. 01811). A flow rate of 1.080 lpm was pulled through the sampler using a critical orifice to draw aerosol flow through the DMA. The collected nanoparticles are imaged using the Tecnai T-12 TEM to obtain digital images in .jpeg format and analyzed using ImageJ (distributed free of cost by NIH). Using the scale bar found on each TEM image, the true dimensions of the particles are determined manually. For each image, the diameter and length (in cases of cylinders) is measured several times for statistical averaging. The diameter (and length) distribution of mobility classified particles is constructed by analyzing a batch of 60-200 images for each particle population. The DMA settings for each data set during TEM sample preparation are listed in Table D2 in Appendix D.

7.3. Design of Experiment

The expression proposed by Zhang *et al.* (2012) for the scalar friction factor of a non-spherical particle for any Kn is

$$\boldsymbol{f_{p,theoretical} = \frac{6\pi\mu_g R_s}{1+Kn\left(a_1+a_2\exp\left(-\frac{a_3}{Kn}\right)\right)}} \tag{2a}$$

$$\boldsymbol{Kn = \frac{\lambda_g \pi R_s}{PA}} \tag{2b}$$

$$\boldsymbol{f_{p,continuum} = 6\pi\mu_g R_s} \tag{2c}$$

$$\boldsymbol{f_{p,free\ molecular} = 2.67\frac{\mu_g}{\lambda_g}\xi PA} \tag{2d}$$

The continuum and free molecular limits are defined by eq. 2c and 2d, respectively. The prediction of $\boldsymbol{f_p}$ thus requires the evaluation of two parameters, namely the

Smoluchowski Radius $\boldsymbol{R_s}$ and the orientation averaged Projected Area $\boldsymbol{PA}$, along with gas parameters such as viscosity, mean free path and slip correction coefficients. Details of particle and gas parameters required to evaluate the friction factor using eq. 4a is given in Appendix D. Based on the DMA voltage $\boldsymbol{V}$ and sheath flow rate $\boldsymbol{Q_{sh}}$ at which particles were collected for electron microscopy, the centroid mobility $\boldsymbol{Z_p}$ of particles collected on the TEM grid can be calculated from DMA theory (Knutson & Whitby, 1975b). The experimental friction factor is calculated from the definition of electrical mobility:

$$\boldsymbol{f_{p,experimental}} = \frac{\boldsymbol{n_p e}}{\boldsymbol{Z_p(V,Q_{sh})}} \quad (3)$$

$\boldsymbol{n_p}$ is the number of integer charge(s) on the particle (1 or 2) and $\boldsymbol{e}$ is the fundamental quantum of electronic charge. For each of the mobility classified particles imaged on the TEM grid, the experimental friction factor (eq. 3) is compared with the prediction of (eq. 2) for assessing the theory.

7.4. Particle Orientation inside the DMA

The theoretical expression (eq. 2a) assumes that gas molecules impinge on the nonspherical particle without any preferred orientation (Zhang et al. 2012) . Hence, it is important that cylindrical and doublet aerosol particles do not undergo preferential alignment due to dielectric polarization in the presence of applied electric field as they flow through the DMA. Such alignment will alter both the Projected Area (*PA*) and the Smoluchowski Radius (R_s) of the particle exposed to the flow in a manner that has not yet been quantified.

Kasper & Shaw (1983) argue that the nonspherical particles undergo preferential orientation during measurement in electrical, centrifugal or inertial force fields. It is generally known that in the size ranges where the momentum transfer is continuum in nature ($Kn \rightarrow 0$) and the $Re \sim 1$, particles have a preferred orientation to minimize their resistance to bulk gas motion (Davies, 1979) as opposed to random rotations due to

diffusion. They have shown that aerodynamic classification (aerosol centrifuges and inertial impactors) lead to the measurement of drag of particles tend to be oriented parallel to the flow field (Kasper, 1982), while electrical mobility classification techniques yield the drag of the particle oriented perpendicular to the flow as particles tend to align along field lines due to dielectric polarization (Wen & Kasper, 1984). It is known that the drag force (which is proportional to the DSF) undergoes a reduction as field strength is increased leading to the conclusion that doublets of spheres orient themselves parallel to the field (Horvath, 1979; Hansson & Ahlberg, 1985). However, that conclusion cannot be necessarily extended to triplets and quadruplets which do not undergo such alignment leading to ambiguities about the orientation of elongated particles at comparable field intensities. The measurements of Kousaka *et al.* (1996) confirm the notion that doublets and triangular/compact triplets are in random orientation at low field strengths (average intensity < 200,000 V/m) while aligning themselves parallel to the field at high field strengths (average intensity > 500,000 V/m) with a region of transition. They have also shown that the effect is also a strong function of the *Kn* (defined based on the volume equivalent diameter), with larger particles ($Kn \leq 0.5$) being more amenable to orientation than smaller particles ($Kn > 1$). Zelenyuk *et al.* (2006) and later Zelenyuk & Imre (2007) have measured the DSF of PSL aggregates and other nonspherical particles (NaCl crystals, NH_4SO_4 particles and mineral dust) and clearly show the decrease in the drag (DSF) as particles align with the field. They have characterized doublets and triangular triplets with primary particle size varying from 100 – 300 nm and show the effect of both field strength and primary particle size. From their work it can be concluded, aggregates with larger primary size particles (200 nm and above) undergo alignment whereas the orientation of smaller aggregates (125 nm and lesser in primary sphere diameter) can be inferred as random even at high field strengths. In the continuum regime, the dielectric effect being proportional to volume (Jackson, 1975), leads to a higher alignment torque on the particle thereby leading to alignment of large particles (> 200 nm in size). In the transition regime where the thermal energy of particles are comparable to the polarization energy, high field strengths ($> 5 \times 10^6$ V/m)

are generally required to induce alignment as is evident from numerous measurements done on doublets, triplets and high aspect ratio fibers (Kim *et al.*, 2007; Li *et al.*, 2012).

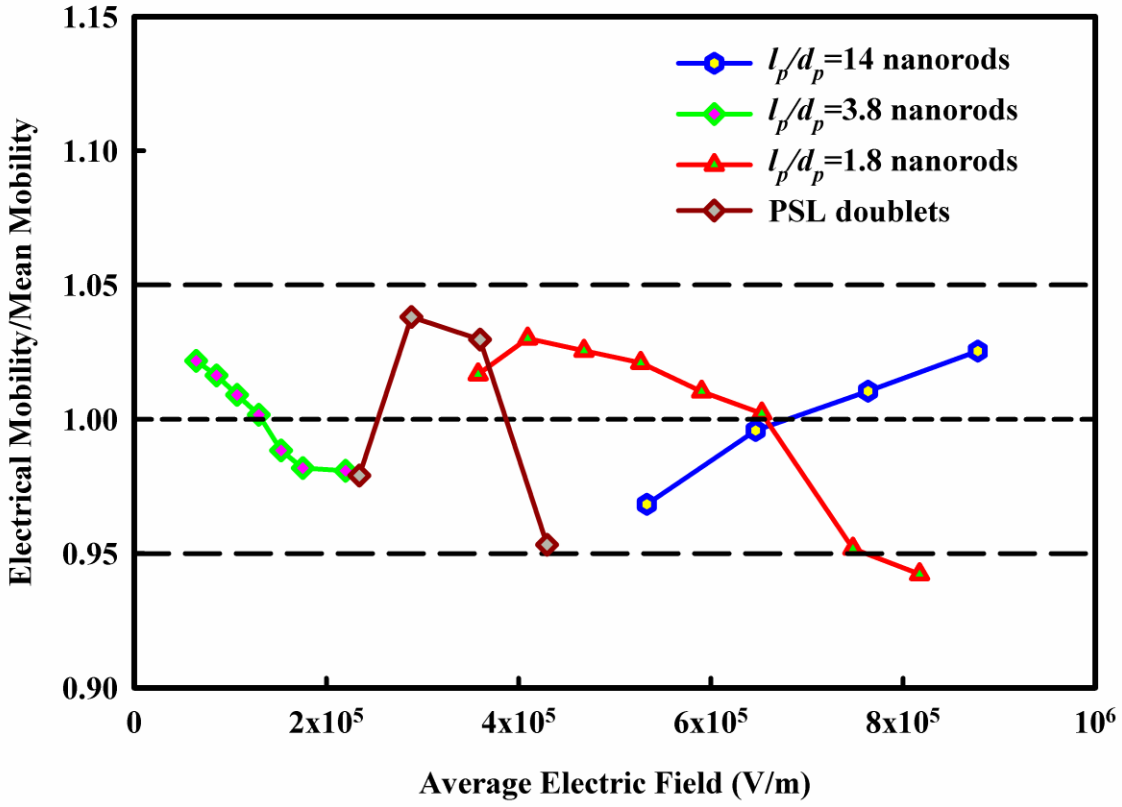

Figure 7.5: plot showing the variation of measured electrical mobility as a function of the field strength in the DMA. Electrical mobility is non-dimensionalized by the mean mobility over all field strengths for a given dataset.

As stated previously in this beginning of this section, it is not our objective to align these nanoparticles but to make mobility measurements using the DMA operated at electric field intensities for which the orientation distribution of the particle can be safely considered uniform. Here, we present mobility of nanoparticles measured at different field strengths in the DMA. The field strengths were varied by operating at different sheath flow rates which accordingly changes the voltage at which particles of given mobility exit the DMA. Shown in fig. 7.5 is the electrical mobility of various

nanoparticles considered in this work as a function of the average electric field strength during classification$\left(\boldsymbol{E_{avg}} = \frac{\boldsymbol{V}}{\boldsymbol{r_{outer} - r_{inner}}}\right)$. The mobility is normalized by the average mobility over all the field strengths at which measurements were done for a given data set. Evident from the figure is that the scatter in the mobility values is within ±5% for all data sets, while in most cases 10% is the maximum resolution with which mobility is measured (based on the ratio of sample flow to sheath flow in the DMA). Hence, we infer that there is no significant variation in mobility beyond measurement uncertainty. We do note that the mobility of all data sets (except for $\frac{\boldsymbol{l_p}}{\boldsymbol{d_p}}$=14 cylinders) tend to decrease in mobility with field strength. Again, such variation is within 5%, we chose to do mobility measurements at the field strengths corresponding to voltages applied at 10 lpm sheath flow in the nano and long DMA and consider such measurements to be consistent with the derivation of eq. 2a.

7.5. Results and Discussion

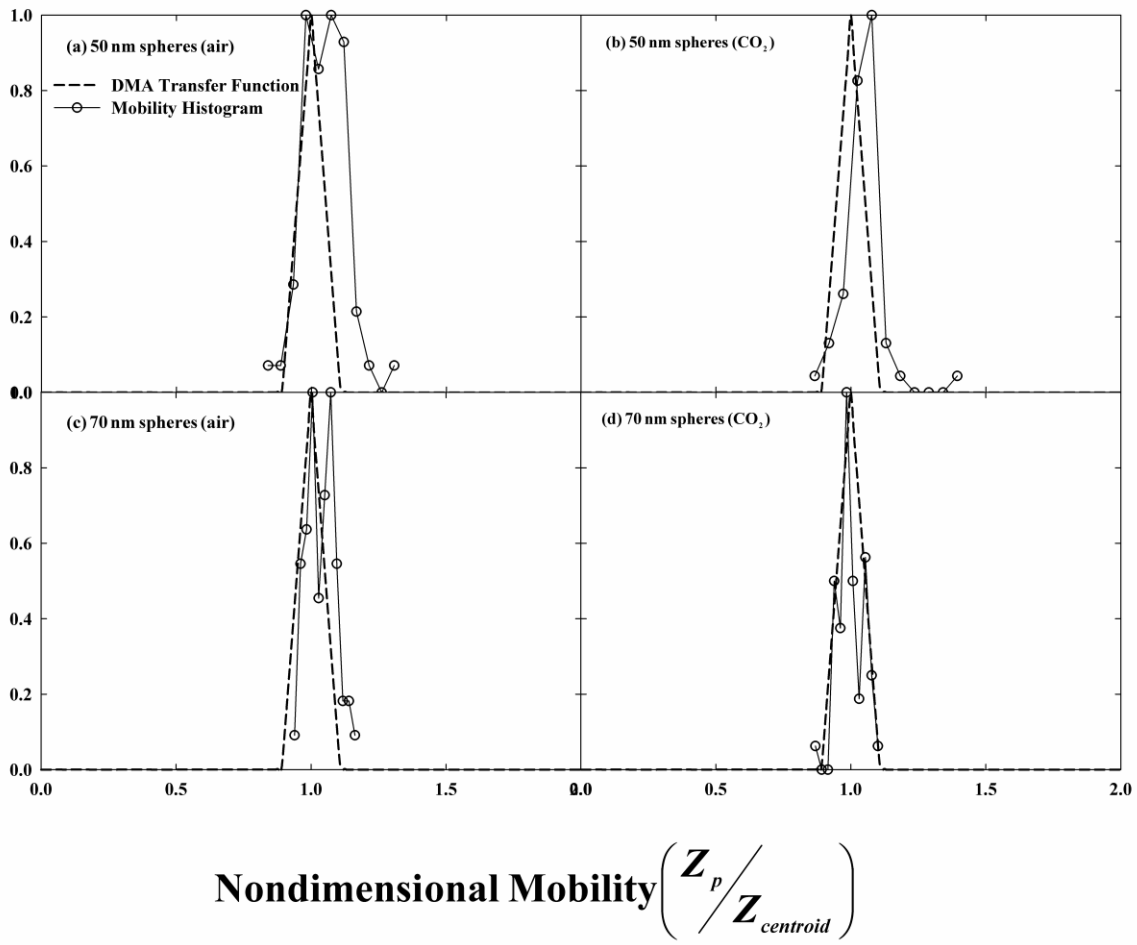

Figure 7.6: Predicted mobility histogram and the DMA transfer function plotted as function of non-dimensional mobility for spherical particles (see label on each plot). (Z_p is electrical mobility of the particle, $Z_{centroid}$ corresponds to the classifying voltage, sheath flow rate through the DMA and the sample flow rate drawn through the sampler)

7.5.1 DMA Transfer function

For each dataset, mobility classified particles were collected on a TEM grid and imaged. Based on the measured dimensions, a prediction of friction factor (via eq. 2a) and thereby electrical mobility was made for each particle. Due to the non-zero spread in the mobilities transmitted by the DMA, a distribution of particle sizes are found on the TEM grid and a normalized frequency histogram was constructed by binning the particles

in uniform mobility intervals. If the variation of the mobility of particles over the transmission window of the DMA ($\frac{\Delta Z_p}{Z_p}$=0.1 in all cases) can be considered negligible, the mobility distribution of particles collected on the grid is a convolution of the transfer function of the DMA and the mobility dependent collection efficiency of the electrostatic sampler. While the latter is known to have only a weak, yet undetermined dependence on electrical mobility (Cheng, et al., 1981), the frequency histogram of particles binned by predicted mobility is compared to the transfer function of the DMA in fig. 7.6 for spheres and fig. 7.7 for non-spheres. The non-dimensional transfer function of the DMA (Knutson & Whitby, 1975b) is shown along with the normalized number fractions as a function of the mobility (normalized by the centroid mobility corresponding to the DMA operating conditions). In all of the plots, it can be seen that some particles with mobility outside the window transmitted by the DMA have made their way to the grid. This may be due to the DMA resolution being less than the theoretical value of $\frac{Q_{sheath}}{Q_{aerosol}}$ (Wen & Kasper, 1984; Wen, et al., 1984b). Figures 7.6a – 7.6d show results for spherical particles of mean sizes (49±2.0) nm and (70±1.9) nm measured in air and CO_2. The qualitative agreement of the theory-predicted mobility histogram with the DMA transfer function confirms the validity of instrument operation and the accuracy of measurements on cylindrical particles. The coarseness of the histograms is due to the finiteness of the sample size (60 – 70) particles for each dataset. Further, figures 7.7a – 7.7d show similar comparisons for singly and doubly charged gold nanorods of $\frac{l_p}{d_p}$=1.8 in air and CO_2. It can be seen that there is reasonable agreement in the mean mobility predicted as well as the shape of the distribution as predicted by the drag expression (eq. 2a). Fig. 7e shows results obtained for gold nanorods of $\frac{l_p}{d_p}$=3.8 in air, having the most scatter of all datasets, while the data obtained for gold nanorods of $\frac{l_p}{d_p}$=9.4 in air (fig. 7.7f) show substantial difference in the shape and width between predicted mobility and DMA transfer function. These datasets contain 54 and 32 particles each, respectively. The histogram for nanorods of $\frac{l_p}{d_p}$=14 in air (fig. 7.7g), constructed by imaging 30 particles show better agreement

with the transfer function, with the mean predicted mobility matching the centroid mobility transmitted by the DMA within 1%. These measurements can be substantially improved by considering larger number of samples for each dataset. Some of these measurements can be affected by setting the DMA to classify mobilities that are not the peak of the respective distribution, leading to a skew/shift from the centroid mobility. We also note that a skew towards higher mobilities seen in most datasets can be a feature of the electrostatic sampler capturing particles of higher mobility particles than lower mobility. This can be due to the former acquiring more charges in the corona discharge prior to collection on the grid while the latter may not be charged to the same extent and thus may escape deposition in more numbers. Finally, data obtained for PSL doublets in air are shown in fig. 7.7h which further confirms the capability of the theory to reproduce the DMA transfer function. We note that the friction factor measurements for SWCNTs are not analyzed for consistency with the DMA transfer function as the number of particles imaged is too few, which is further complicated by relatively high polydispersity in length compared to other data sets due to multiple charging.

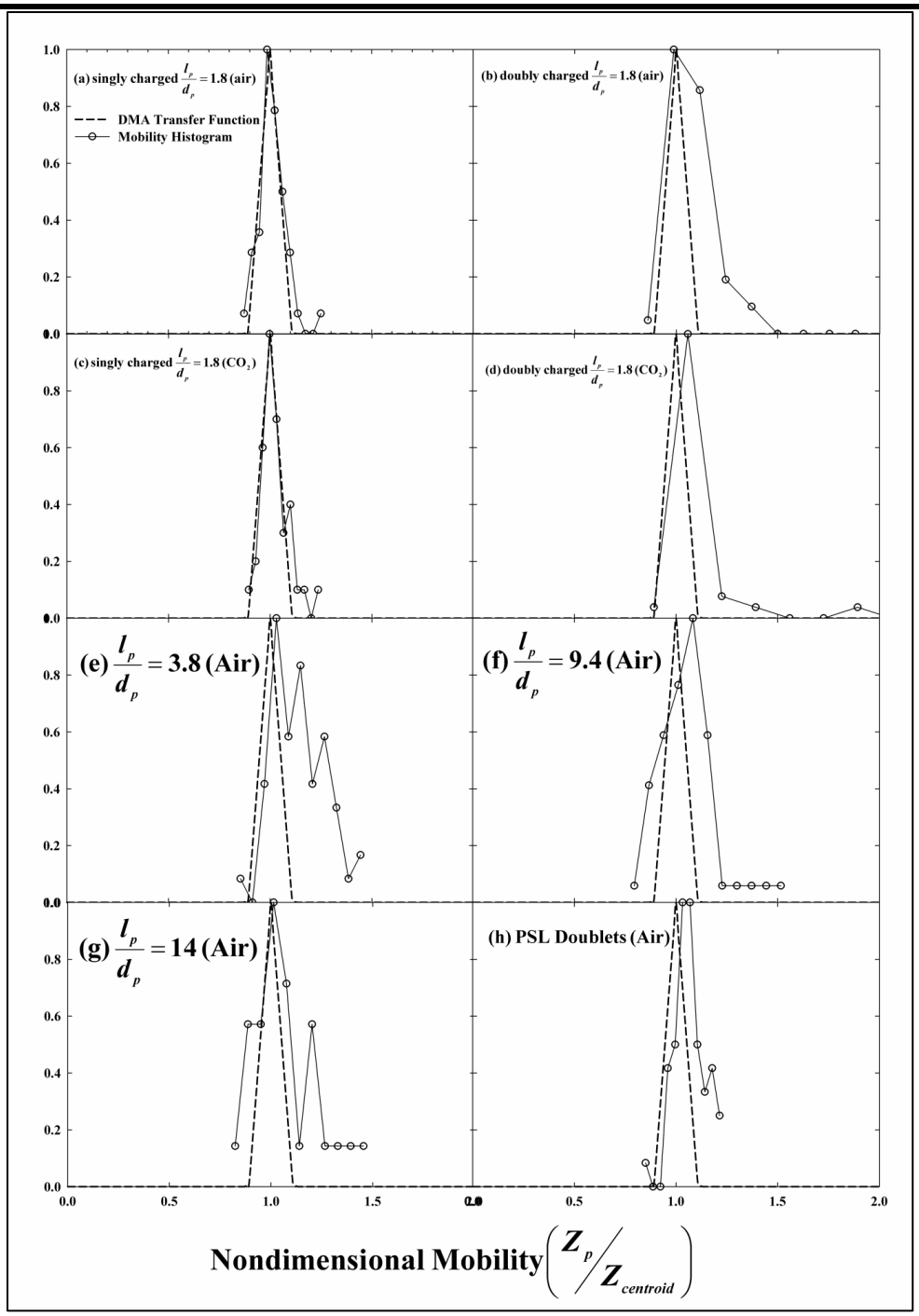

Figure 7.7: Predicted mobility histogram and the DMA transfer function plotted as function of non-dimensional mobility for nonspherical particles (see label on each plot). (Z_p is electrical mobility of the particle, $Z_{centroid}$ corresponds to the classifying voltage, sheath flow rate through the DMA and the sample flow rate drawn through the sampler)

7.5.2. Direct Comparison of Measurements and Theory

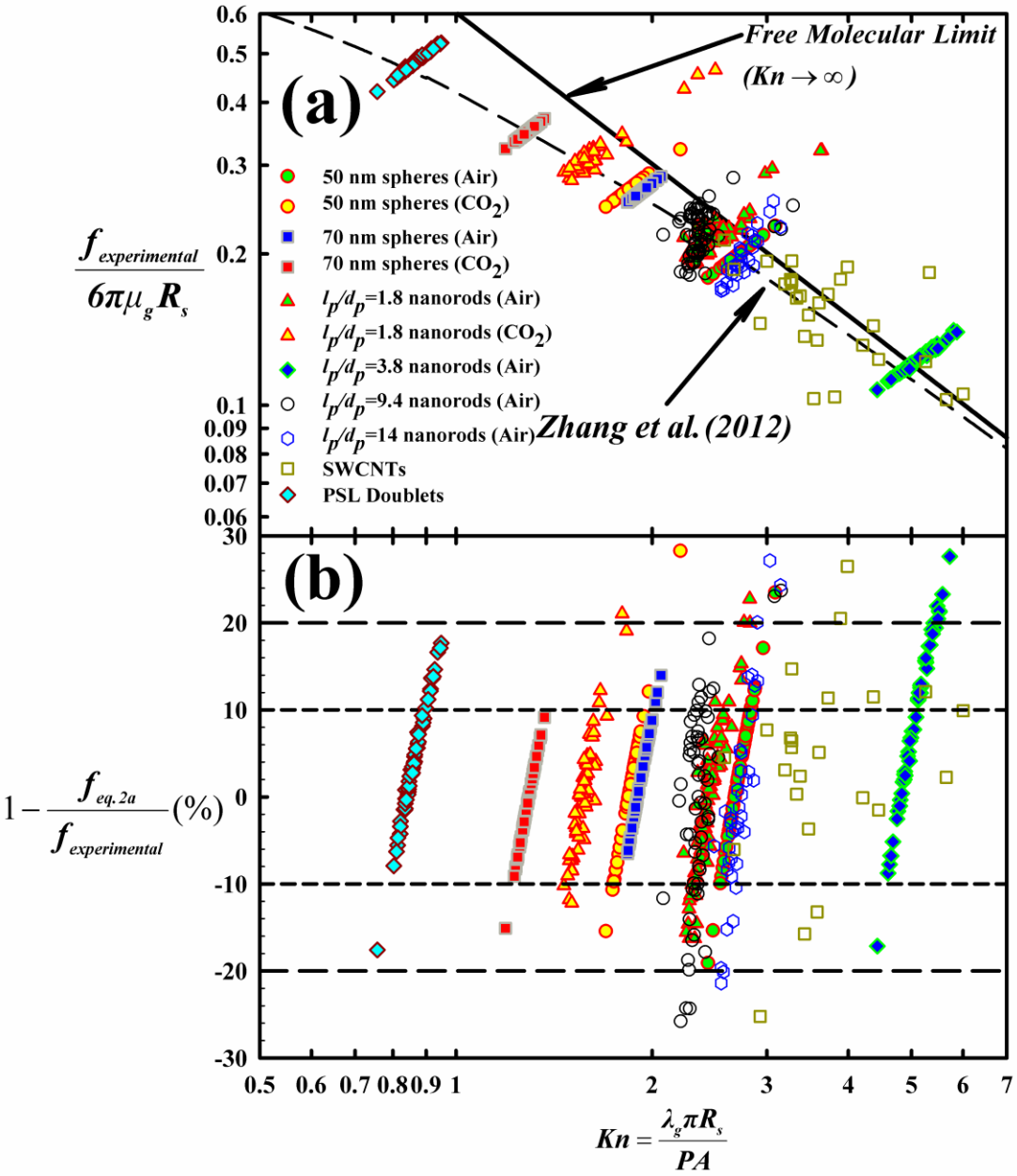

Figure 7.8: (a) Compilation of measured friction factors for all datasets as a function of *Kn*. The expression of Zhang *et al.* and the free molecular expression are also shown. (b) Plot showing the corresponding % deviation of the predictions of Zhang et al. (2012) actors from measured friction factors.

It is instructive to make a direct comparison of the predicted friction factor against the experimentally inferred friction factor to assess the accuracy of eq. 2a as a transition

regime drag law for nonspherical particles. For each particle in a dataset, the experimental friction factor $\boldsymbol{f_{experimental}}$ (using DMA voltage and sheath flow in eq. 7) normalized by the continuum friction factor (eq. 2c) is plotted as a function of *Kn* (eq. 2b) in fig. 7.8a. For guiding the reader, the friction factor expression (eq. 2a) and the free molecular drag expression (eq. 2d) are shown with the same normalization. Analogously, in fig. 7.8b, the % deviation of eq. 2 from experiment $\left(\mathbf{1} - \frac{f_{eq.2}}{f_{experimental}}\right)$ is plotted as a function of *Kn*. The measured friction factors for 50 nm and 70 nm spheres in air and CO_2 agree excellently with the predictions of eq. 2a and the deviation is strictly within ±10% without any bias in the *Kn* range of 1.2 – 2.2. The scatter in the data points with a well defined slope on fig. 8a is a result of the spread in friction factor (ordinate) and the spread in diameter (abscissa) due to the width of the DMA mobility window as discussed in the previous section. The degree of aspehericity of a particle can be quantified by the ratio $\frac{\overline{PA}}{\pi R_s^2}$, with the ratio being exactly equal to 1 for a sphere, and approaching 0 for an infinite cylinder. The mean $\frac{\overline{PA}}{\pi R_s^2}$ for all the datasets considered in this work are listed in table 1 along with other parameters. Focusing on the data obtained for gold nanorods of $\frac{l_p}{d_p}$=1.8 in air and CO_2 $\left(\frac{\overline{PA}}{\pi R_s^2} = \mathbf{0.85}\right)$, we again find excellent agreement to within ±10% with a few outliers. Data for nanorods of $\frac{l_p}{d_p}$=3.8 in air $\left(\frac{\overline{PA}}{\pi R_s^2} = \mathbf{0.85}\right)$ show more scatter than others with the theory under-predicting for a significant fraction of the particles considered. We attribute this to the fact that we were unable to completely evaporate the surfactant coating on the electrosprayed particles without sintering them. The size of gold nanorods was measured by setting a threshold for the pixels on the particle compared to the background seen on digital images. Any surfactant coating, if present, may not create sufficient thickness contrast on TEM images when compared to the gold and hence not accounted for in the size determination. The use of smaller diameters and lengths than the true dimensions, while the nanorods were flowing through the DMA, in eq. 2a accounts for the under-prediction, These rods have mean $\boldsymbol{d_p = 15 \pm 1.5}$ nm, and hence surfactant coating uncertainty of about 1.5 – 2.0 nm (which was the nominal thickness observed in

images obtained without using a furnace) has a significant effect on $\boldsymbol{R_s \propto d_p^{2/3}}$ and $\boldsymbol{PA \propto d_p}$. Data obtained for high aspect ratio particles, nanorods of $\frac{l_p}{d_p}$=9.4 and $\frac{l_p}{d_p}$=14, with $\frac{\overline{PA}}{\pi R_s^2}$ of 0.74 and 0.66 respectively, show unbiased agreement with the theory to within ±10% for 90% of the particles examined with the rest within ±15%. The data points obtained by imaging SWCNTs of three mobility diameters (48.3 nm, 53.9 nm and 60.3 nm) are plotted collectively to qualitatively prove that the theory is capable of handling very high aspect ratio particles ($\frac{\overline{PA}}{\pi R_s^2}$ for these particles vary from 0.19 – 0.77). We reiterate the fact that a lot of approximations had to be made to analyze SWCNTs which were not perfectly straight cylinders. However, it should be noted that even with such approximations the agreement with theory is within ±10% in most cases. An explainable pattern of scatter however is not present. Finally, we examine PSL doublets in air (mean dimensions listed in table 1). As mentioned before, PSL particles collected on the TEM grid underwent some evaporation under the electron beam and the true size distribution is expected to have shifted to a lower size range (in an undetermined manner). This notion is well supported by a significant fraction of particles having deviations in the 10 – 20% range while most had a deviation in the ±10% range. These measurements with spherical and nonspherical particles in the *Kn* range of 0.8 – 5 clearly demonstrate the validity of eq. 2a to predict the friction factor of nonspherical particles.

7.5.3 Comparison with Other Theories

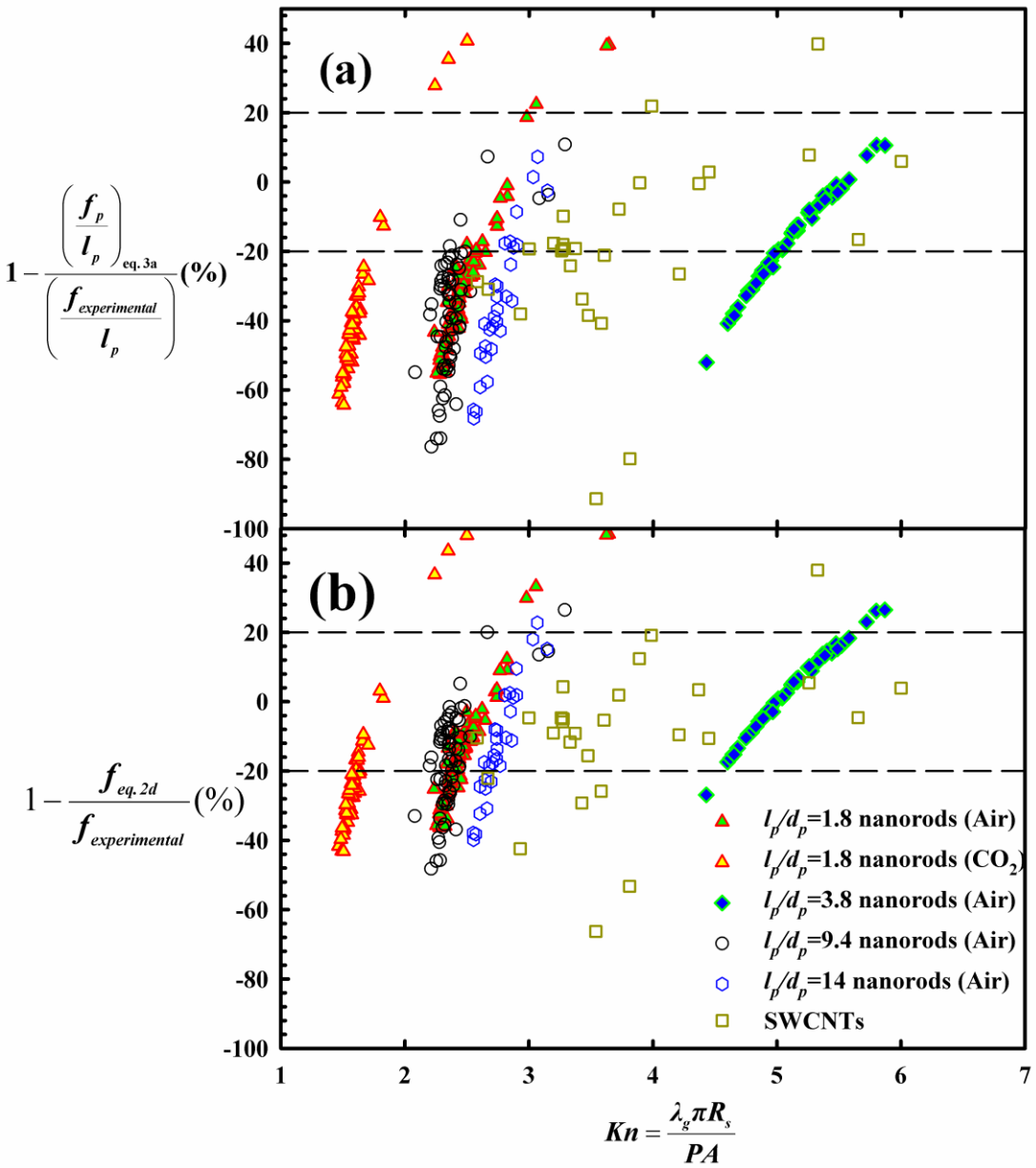

Figure 7.9: Plots showing the percentage deviation of friction factors predicted by (a) the Infinite Cylinder theory of Pich and (b) Free Molecular friction factor expression as a function of *Kn* for cylindrical particles only.

In addition to the comparison made previously, we also compare measured friction factors to the predictions of two expressions found in the literature that are commonly used for nonspherical particles, especially cylinders. Firstly, Pich (1969) has derived the friction factor per unit length for an infinite cylinder as a function of the *Kn*

and *Re* (defined based on gas properties and the radius of the cylinder) in the transition regime ($0.25 < Kn < 10$):

$$\frac{f_p}{l_p} = \frac{4\pi\mu_g}{2.0022 - \ln(Re_P) + 1.747 Kn_P - \ln(1 + 0.749 Kn_P)} \quad (3a)$$

$$Kn_P = \frac{2\lambda_g}{d_p} \quad (3b)$$

$$Re_P = \frac{\rho_g U d_p}{\mu_g} \quad (3c)$$

The characteristic velocity U is equal to $\overline{c_g}$, the mean thermal speed of the gas inside the DMA. The other expression considered for comparison is the free molecular friction factor applied for nonspherical particles and macromolecules (eq. 2d). In figure 7.9a and 7.9b, the % deviation of the predictions of eq. 3a and eq. 2d are plotted as a function of the *Kn* (defined by eq. 2b) for consistency). Even though the aspect ratios of cylinders considered here cannot be considered as large ($\rightarrow \infty$), eq. 3a has been used to predict drag in the transition regime due to absence of viable expressions. It can be readily seen from fig. 7.9a that most data points are 20 – 60 % above the experimentally determined friction factors for the datasets of nanorods of $\frac{l_p}{d_p}$=1.8 (in air and CO_2), 9.4 and 14 in air. Considering the uncertainties that exist around the determination of the surfactant coating thickness and the fact that eq. 3a performs poorly for higher aspect ratio particles, we conclude that the data obtained for $\frac{l_p}{d_p}$=3.8 in air showing reasonably good agreement with theory more as an anomaly than as a meaningful physical trend. The comparison to high aspect ratio SWCNTs, the dataset most consistent with the infinite cylinder approximation yield agreement within ±20% for most particles. The quality of the comparison is also low due to very small sample size but it can be concluded that the expression is reasonably good for cylinders of aspect ratio > 100.

The free molecular friction factor expression performs better than Pich's expression (fig. 7.9b), yet over-predicts by up to 45% for all datasets except for $\frac{l_p}{d_p}$=3.8 nanorods in air and SWCNTs. For the former, the agreement is excellent. For *Kn* > 5, this agreement can be taken as proof that the free molecular expression is adequate for

friction factor calculation. However, for the same reasons cited for Pich's expression, we consider this observation and arrive at that conculsion. For SWCNTs, the agreement is very good, with the scatter considerably less than with the other two expressions (eq. 2a and eq. 3a).

7.6. Conclusions

The transition regime drag law measured proposed by Zhang *et al.* (2012) was experimentally evaluated using well characterized cylindrical particles by performing DMA-TEM measurements.

- Firstly, the direct comparison of theory and measurements show that the proposed expression in Zhang et al. is accurate to within ±10% in most cases. The degree of agreement can be further increased by operating the DMA at higher resolution. The systematic scatter found is a feature of the DMA transfer function, and not a physical aspect of the theoretical expression.
- Secondly, the ability of the theory to accurately predict the mobility distribution of particles collected downstream of a DMA operated at a fixed voltage and sheath flow rate was assessed. It was found that the theory reproduces the transfer function of the DMA quite well in all the datasets considered and the quality of the comparison can be greatly improved by using large sample sizes.
- Thirdly, on comparing measurements to the drag expressions for infinite cylinders (Pich, 1969) and the free molecular friction factor expression, it is concluded that, these expressions are erroneous if used in the transition regime, as is commonly done in the absences of viable transition regime drag theories for nonspherical particles.
- Finally, it is concluded that the expression of Zhang *et al.* (2012) be used for the calculation of transition regime drag on nonspherical particles. This is believed to be of great utility for characterizing such particles by electrical mobility analysis or other drag force based measurement techniques, especially for the bipolar diffusion charging experiments discussed in the next chapter.

Chapter 8: Experimental Investigation of the Bipolar Diffusion Charging of Spherical and Cylindrical Aerosol Particles

To validate the theoretical and computational approaches developed in this thesis, bipolar diffusion charging experiments are performed. The mass and mobility distributions are simulataneously measured to enable computations using the methods developed in Chapter 6. Comparison between experiment and simulations is performed to understand the effect of particle shape and ion polydispersity.

8.1. Introduction

Bipolar diffusion charging of aerosol particles is a problem of fundamental importance. Historically, the flux matching theory (Bricard, 1962; Fuchs, 1963; D'yachkov, et al., 2007), and the regression expression (Wiedensohler, 1988) based on the approach of Hoppel & Frick (1986) are used widely to determine the steady state charge fraction in such instances. The velocity and impact parameter distribution of the incoming ions on the surface of the limiting sphere are improperly specified in such approaches, leading to substantial under prediction of collision kernel at high strength of attractive long range (Coulombic) potential between particles and ions (Chapter 4). While a universal collision kernel expression applicable for charge transfer processes which increase the net charge on the particle (unipolar charging) was derived for arbitrary shaped particles in Chapter 5, an analogous expression for the bipolar charging process (bipolar charging) is still elusive even for spheres. To deal with the bipolar diffusion charging of spherical and nonspherical particles, BD based calculation approach which circumvents collision kernel calculation altogether and yields the steady state charge fraction for ion populations with arbitrary mass-mobility distributions in Chapter 6. The Brownian Dynamics approaches to calculate aerosol particle collision kernels and steady state charge fractions are experimentally tested against measurement of the charge distributions in the mass transfer transition regime.

Measurements in the size range of 5-100 nm (Hussin, et al., 1983; Reischl, et al., 1983; Wiedensohler, et al., 1986) agree well with the limiting sphere model (Fuchs, 1963). Later works by Wiedensohler and coworkers, Reischl and coworkers (Wiedensohler & Fissan, 1988, 1991; Reischl, et al., 1996) note that measured charge distributions are increasingly deviant from the limiting sphere theory predictions in gases other than air (high purity argon and nitrogen), at elevated temperatures and at particles sizes less than about 20 nm. Also in these studies, the key parameters in obtaining charge fraction predictions from theory (i.e.) the mass and electrical mobility values of the ions are taken from previously published data (Wellisch, 1909; Kilpatrick, 1971; Mohnen, 1977; Steiner & Reischl, 2012) or obtained by fitting experimentally inferred ion-particle combination coefficients and corresponding theoretical predictions. Thus, it can be argued that experiments in which the ion properties were not independently measured are not true tests of charging theories. It is known that the uncertainty in the ion properties can lead to incorrect inferences about the ability of the theory to correctly explain experimentally observed charge fractions (Wiedensohler & Fissan, 1991; Reischl, et al., 1996).

Advances in the synthesis and usage of novel shaped nanomaterials have generated interest to understand the diffusion charging characteristics of non-spherical particles. Measurements with straight chain aggregates (composed of iron oxide) with primary particles of diameter 40-80 nm and length to diameter ratios in the range of 10 to 1000 (Wen, et al., 1984b), and carbon nanotubes with mobility diameters in the range of 200-700 nm (Ku, et al., 2011) show that the use of the continuum model of Boltzmann charge distribution with the charging equivalent diameter, introduced by Wen *et al. (1984a)*, are not accurate in the transition regime. Measurements on agglomerates (Yu, et al., 1987; Rogak & Flagan, 1992a; Ntziachristos, et al., 2004; Oh, et al., 2004; Biskos, et al., 2005; Jung & Kittelson, 2005; Maricq, 2008) and carbon nanotubes (Kulkarni, et al., 2009) in the transition regime show that open structures attain higher fraction of multiply charge states than mobility equivalent spheres. These measurements clearly show that particle morphology has a significant effect on charging and viable theories of charging need to be verified in this context. It should also be noted that, the uncertainty in ion

properties that is found in the experiments done with spheres, holds true with these measurements also.

In this chapter, bipolar diffusion charging experiments performed using spherical and cylindrical particles with accompanying ion mass-mobility measurements are described. Comparisons to theoretical predictions performed using the BD methods of Gopalakrishnan, Meredith, *et al.* (2013) are made to understand the effect of shape and complex ion properties. The generation of particles, tandem-DMA (TDMA) experiments to measure charge fractions and the determination of the mass-mobility distribution of the charging ions are presented. The TDMA experiments for each dataset are exactly simulated by using the size distribution of generated aerosol particles, ion mass-mobility distribution and DMA transfer function as inputs. The dynamics of bipolar charging in a Po-210 neutralizer is simulated by the BD calculation procedure to facilitate one-to-one comparison. Finally, experimental and simulation results are presented and discussed to evaluate the utility of the BD procedure as a tool to predict steady state bipolar charge fractions.

8.2. Experimental Methods

8.2.1. Aerosol Generation

Spherical and cylindrical gold nanoparticles (Chapter fig. 7.1 a – f) were produced by aerosolizing colloidal solutions (Nanopartz Inc.) using the TSI 3480 Electrospray Aerosol Generator (schematically depicted in fig. 8.1). The purchased solutions were diluted in suitable proportions in Ammonium Acetate (Sigma Aldrich) buffer and sprayed using silica capillaries (Polymicro™). The OD of the capillaries used for all solutions was 360 μm while different IDs were used to spray particles of longest dimension varying from 50 – 250 nm. Particles were generated in two different gases: 1) Ultra-High-Purity (UHP) air (99.99% pure, Matheson Inc.) 2) Industrial Grade Carbon dioxide

(99.9% pure, Matheson Inc.). In the case of UHP air, a very small amount (<2% of the total flow rate) of CO_2 was added to prevent corona discharge inside the electrospray chamber. The charge reduced aerosol particles from the TSI 3480 were flown through a tubular furnace (Lindberg TF5503A-1) to evaporate surfactant coating on the particle after solvent evaporation. Table 8.1 provides a summary of the mean dimensions for all of the datasets considered here (Electrospray settings are provided in Appendix E, table E1).

Table 8.1: Mean dimensions of electrosprayed gold nanoparticles.

Dataset	Nominal Dimensions				Sample TEM Images
	d_p (nm)	l_p (nm)	$\overline{\left(\frac{l_p}{d_p}\right)}$	$\overline{\left(\frac{PA}{\pi R_s^2}\right)}$	
50 nm spheres	52.4±1.0	-	-	1.00	fig. 7.1a
70 nm spheres	73.2±2.0	-	-	1.00	fig. 7.1b
$\frac{l_p}{d_p}$=2.2 nanorods	43.3±2.4	94.9±5.1	2.2	0.84	fig. 7.1c
$\frac{l_p}{d_p}$=4.3 nanorods	11.2±0.6	47.4±2.8	4.3	0.84	fig. 7.1d
$\frac{l_p}{d_p}$=11.3 nanorods	2□.9	232	11.3	0.70	fig. 7.1e
$\frac{l_p}{d_p}$=14.9 nanorods	17.3	257	14.9	0.63	fig. 7.1f

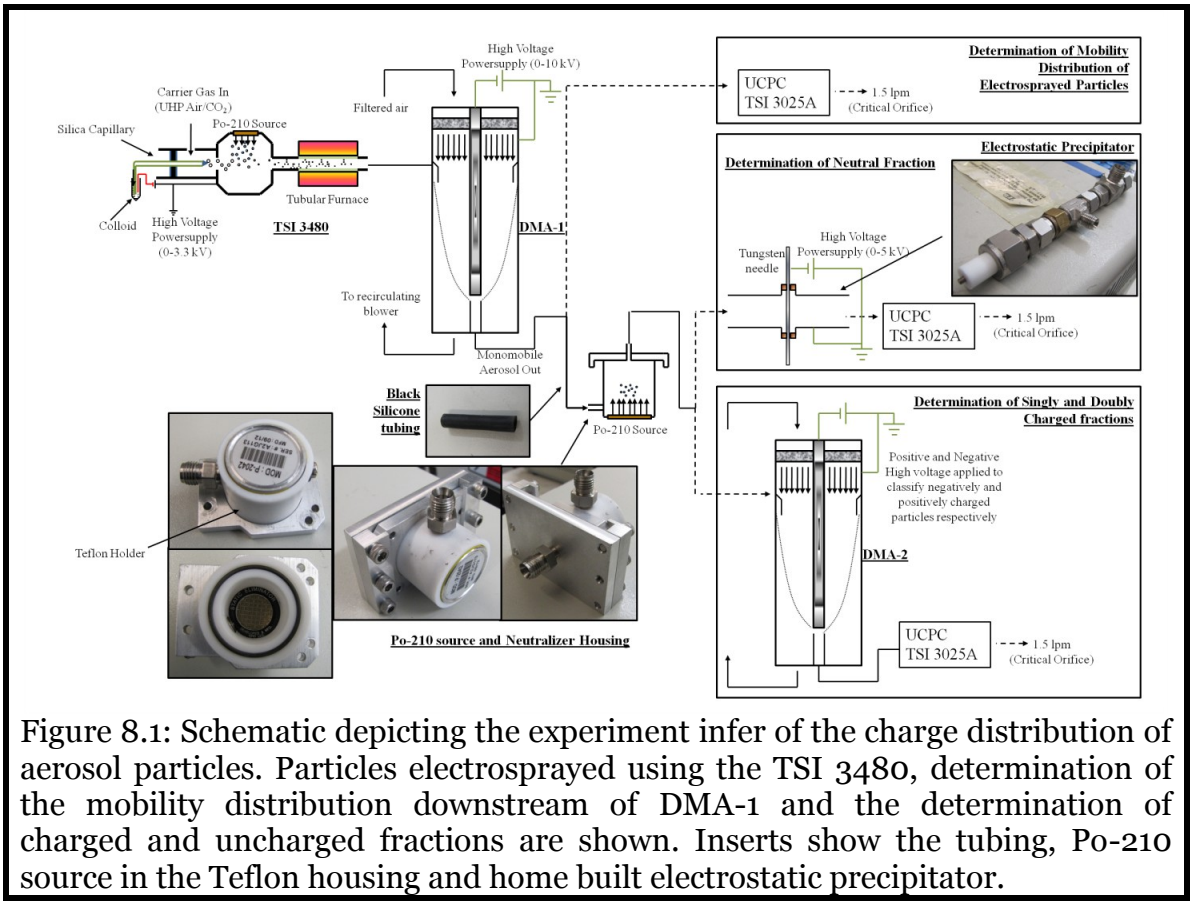

Figure 8.1: Schematic depicting the experiment infer of the charge distribution of aerosol particles. Particles electrosprayed using the TSI 3480, determination of the mobility distribution downstream of DMA-1 and the determination of charged and uncharged fractions are shown. Inserts show the tubing, Po-210 source in the Teflon housing and home built electrostatic precipitator.

8.2.2. Measurement of Charge Fractions

The measurement of the fraction of charged and uncharged particles is schematically depicted in fig. 8.1. For each dataset, after determination of the mobility distribution of electrosprayed particles using a TSI nano® DMA 3085 and a TSI Ultrafine Condensation Particle Counter (UCPC) 3025A (sample spectra shown in fig. 8.2a and 8.2b for 50 nm spheres and l_p/d_p=2.2 nanorods, respectively), DMA-1 was set at a voltage corresponding to the singly charged particles peak mobility found in the spectrum, thereby acting as a source of monodisperse particles for charging measurements. During the course of each experiment, the electrospray particle current was monitored for steady operation and was found not to fluctuate more than ±5%. A 10 mCi Po-210 source housed in a Teflon holder is placed in line, which ionizes vapors present in the carrier gas (sourced mainly from "Black" tubing made of

Polydimethylsiloxane (PDMS) blend polymers) to generate bipolar ions that impart a steady state charge distribution to the aerosol particles. The fraction of uncharged particles is determined by using an electrostatic precipitator (ESP) and the UCPC. The ESP consists of a Tungsten rod (1/8'') to which high voltage is applied, electrically isolated from the Swagelok® flow fittings (ground). The electric field existing inside the ESP collects particles of both polarities and was tested for 100% collection efficiency for sizes corresponding to all datasets and operational flow rates considered here. Neglecting losses due to diffusion as the particles are monodisperse, the uncharged fraction f_0 is directly determined as:

$$\boldsymbol{f_0 = \frac{N_{ESP\ ON}}{N_{ESP\ OFF}}} \tag{1a}$$

where $\boldsymbol{N_{ESP\ ON}}$ and $\boldsymbol{N_{ESP\ OFF}}$ are the concentrations recorded by the UCPC when the high voltage to the ESP was applied and turned off, respectively. The fraction of charged particles is obtained by using a second DMA (also a nano® TSI 3085) in series. Mobility spectra for each data set is obtained by stepping the DMA-2 voltage (as opposed to the more common scanning mode) in positive and negative mode to measure negative and positively charged particles, respectively. At each voltage, sufficient number of particles N are counted to so that the counting uncertainty ($=N^{-1/2}$) is less than 1% at the peak mobility. The concentration recorded by the UCPC as a function of the voltage set on DMA-2 can be expressed as a function of the mobility distribution function $\boldsymbol{\frac{dn}{dZ_p'}}$, DMA transfer function $\boldsymbol{\Omega}$ and various mobility depedent loss coefficients (transmission efficiency $\boldsymbol{\eta_T}$, diffusion lossess of particles in the tubing $\boldsymbol{\eta_D}$ and counting efficiency of the UCPC $\boldsymbol{\eta_{CPC}}$) as:

$$\boldsymbol{R_2(V_2, Q_{sh2}, Q_{a2}) = \int_0^\infty \frac{dn}{dZ_p'}\Big|_{Z_p} \Omega\left(\frac{Z_p'}{Z_c(V_2,Q_{sh2},Q_{a2})}, \frac{Q_{a2}}{Q_{sh2}}\right) \eta_T \eta_D \eta_{CPC} dZ_p'} \tag{1b}$$

($\boldsymbol{Z_p'}$ is an integration variable, $\boldsymbol{Z_p}$ is a given particle mobility and $\boldsymbol{Z_c}$ is the centroid mobility evaluated as a function of the DMA-2 voltage $\boldsymbol{V_2}$, sheath flow rate $\boldsymbol{Q_{sh2}}$ and

aerosol flow rate $\boldsymbol{Q_{a2}}$.) A piecewise constant approximation of $\frac{\boldsymbol{dn}}{\boldsymbol{dZ_p'}}$ allows evaluation of the same as:

$$\left.\frac{\boldsymbol{dn}}{\boldsymbol{dZ_p'}}\right|_{Z_p} = \frac{R_2(V_2,Q_{sh2},Q_{a2})}{\eta_T\eta_D\eta_{CPC}\int_0^\infty \Omega\left(\frac{Z_p'}{Z_c(V_2,Q_{sh2},Q_{a2})},\frac{Q_{a2}}{Q_{sh2}}\right)dZ_p'} \tag{1c}$$

For monodisperse particles transmitted by DMA-1, the loss coefficients can be considered identical, and close to 1 for all particles exiting DMA-2 throughout the entire voltage range and from DMA theory $\int_0^\infty \boldsymbol{\Omega}\left(\frac{\boldsymbol{Z_p'}}{\boldsymbol{Z_c(V_2,Q_{sh2},Q_{a2})}},\frac{\boldsymbol{Q_{a2}}}{\boldsymbol{Q_{sh2}}}\right)\boldsymbol{dZ_p'} = \mathbf{1}$ (Stolzenburg & McMurry, 2008). Thus, the number concentration recorded by the UCPC is inferred as the approximate mobility distribution of particles exiting DMA-2, differing by a few percentage points from the exact distribution. A Gaussian function is fitted to the singly and doubly charged peaks and the peak concentration fit value is reported as the total absolute concentrations of the same (figs. 8.2c & 8.2e show DMA-2 mobility distributions for 50 nm spheres, similar data for l_p/d_p=2.2 nanorods are shown in figs. 8.2d & 8.2f). Table E1 in Appendix E shows DMA-1 and DMA-2 settings for each dataset. The ratio of concentrations is inferred as the ratio of the fraction of singly to doubly charged particles, the metrics of comparison of experimentally inferred charge distributions with theoretical predictions:

$$\frac{\boldsymbol{f_{\pm1}}}{\boldsymbol{f_{\pm2}}} = \frac{\boldsymbol{(N_{\pm1})_{fit}}}{\boldsymbol{(N_{\pm2})_{fit}}} \tag{1d}$$

$$\frac{\boldsymbol{f_{-1}}}{\boldsymbol{f_{+1}}} = \frac{\boldsymbol{(N_{-1})_{fit}}}{\boldsymbol{(N_{+1})_{fit}}} \tag{1e}$$

$$\frac{\boldsymbol{f_{-2}}}{\boldsymbol{f_{+2}}} = \frac{\boldsymbol{(N_{-2})_{fit}}}{\boldsymbol{(N_{+2})_{fit}}} \tag{1f}$$

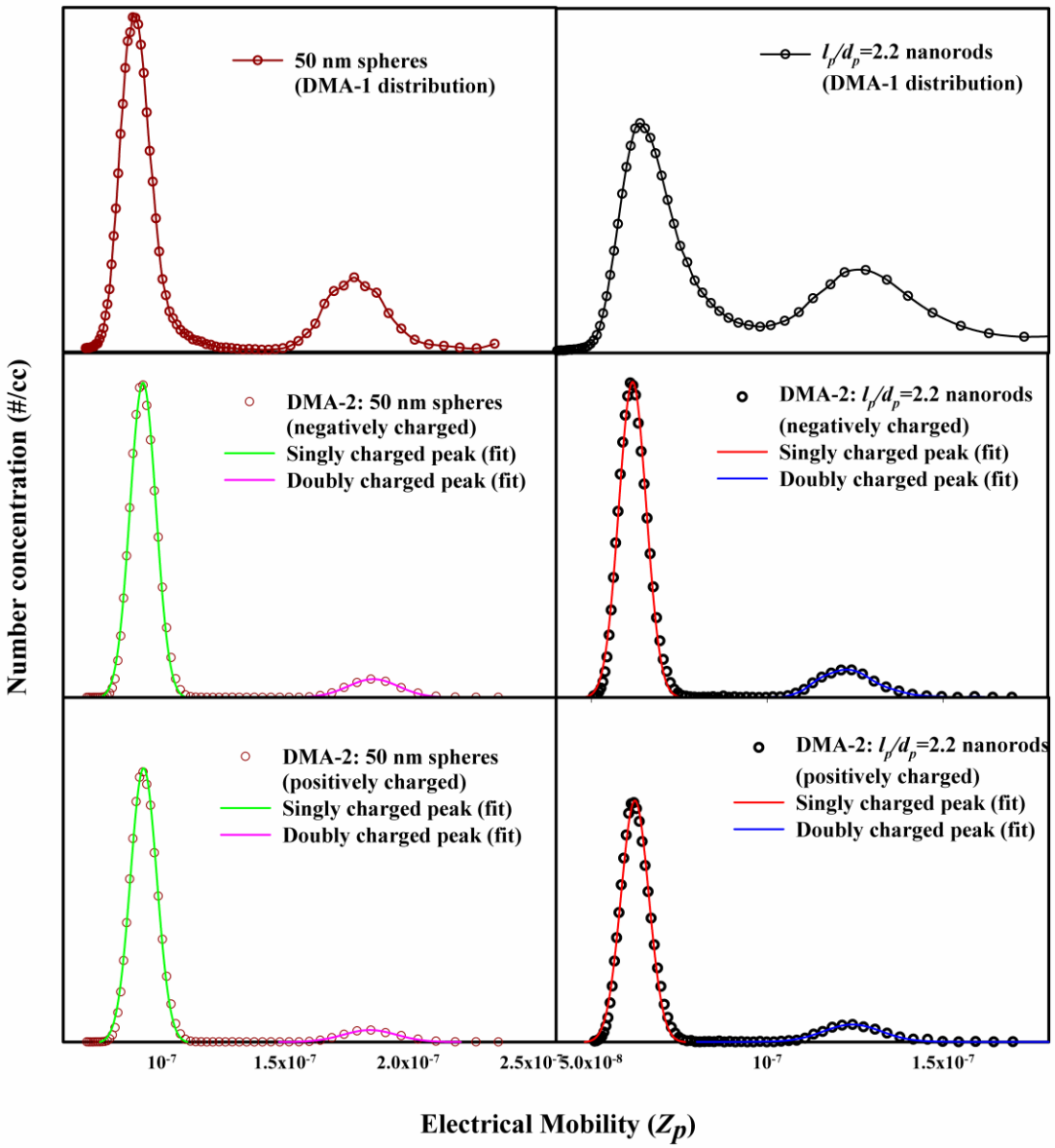

Figure 8.2: Sample mobility distributions for and representation of Gaussian fits to experimental data. (a) & (b) DMA-1 mobility distribution for 50 nm spheres and l_p/d_p=2.2 nanorods respectively. (c) & (e) Number concentration downstream of DMA-2 as function of electrical mobility ($\propto \mathbf{1}/\boldsymbol{V_2}$) for 50 nm spheres. (d) & (f) Number concentration downstream of DMA-2 as function of electrical mobility ($\propto \mathbf{1}/\boldsymbol{V_2}$) for l_p/d_p=2.2 nanorods.

8.2.3. Measurement of Ion Mass-Mobility Distribution

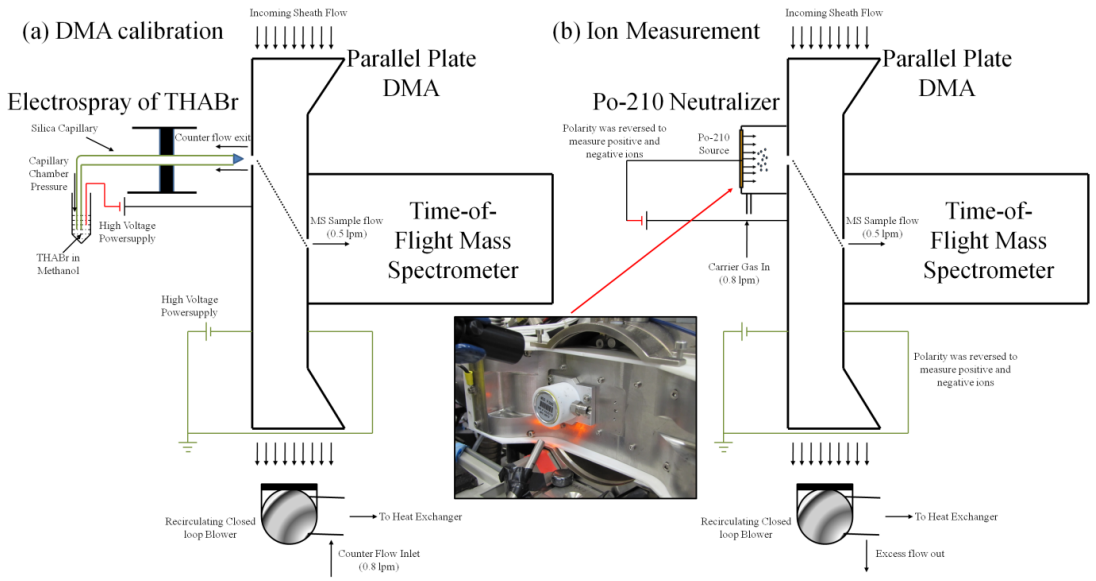

Figure 8.3: Schematic representation of DMA-MS characterization of ion properties. (a) Calibration of parallel plate DMA using electrosprayed THA^+ ions. (b) Measurement of charging ions generated in the housing. Insert shows the neutralizer housing attached to the sampling portion of the DMA.

The mass-mobility distributions of the complex ions generated by ionization of trace vapors present in the carrier gas (UHP air/CO_2) by alpha particles emitted by 10 mCi Po-210 source were measured using a tandem DMA-MS system consisting of a parallel plate Differential Mobility Analyzer (P5 SEADM, Vallidolid, Spain) coupled to a Time of Flight Mass Spectrometer (QSTAR XL, MDS, Sciex, Ontario, Canada). Measurements were conducted using the same tubing and gas drawn from the same cylinder that was used in the TDMA experiments to the neutralizer housing with the Po-210 source to ensure that the composition of the charging ions was unaltered during mass-mobility characterization. Prior to measurement, tetraheptylammonium bromide (THA-Br) dissolved in methanol was electrosprayed (see fig. 8.3a) to generate $(THA)^+$, $(THABr)THA^+$ and other larger clusters of positive ions that were used as a mobility standard to obtain a reference voltage V_{ref} corresponding to the undetermined sheath flow (~ 700 lpm) through the DMA. A flow of 0.8 lpm was introduced through the counterflow inlet, of which 0.5 lpm is sampled by the MS. The reminder of the flow exits

the system via the DMA inlet and the ions are sampled electrostatically for classification. With the sheath setting unaltered, the neutralizer housing with the Po-210 source was attached to the front plate of the DMA (see fig. 8.3b). In this case, a flow of 0.8 lpm was pushed through the housing into the inlet and the Po-210 metal casing was held 1000 V above the front plate of the DMA to drive the generated ions into the DMA-MS inlet. With all other flows in the system being unchanged, it is assumed that the switch from counter flow to co-flow operation of the ion sampling creates a negligible difference in the sheath flow for unaltered settings on the blower controls. The reminder of 0.3 lpm, after sampling by the MS, leaves the system through the counterflow inlet. The mobility of an ion Z_{ion} which exits the DMA at a voltage V_{ion}: $\boldsymbol{Z_{ion} = Z_{ref}\frac{V_{ref}}{V_{ion}}}$. The temperature of the sheath flow was regulated using an air cooled heat exchanger and was observed to be T_{sh}=23.0±0.5 °C when measurements were made. The reported mobilities are not corrected for temperature variation $\propto \left(\frac{\boldsymbol{T_{sh}+273}}{\boldsymbol{298}}\right)^{\boldsymbol{1/2}}$ and polarization $\propto \left(\frac{\boldsymbol{T_{sh}+273}}{\boldsymbol{298}}\right)$ which were found to be negligible. Mass-Mobility contours of measured ions is shown in fig. 8.4, with higher size images, reference mobility and voltages of the standards used in each gas (table E2), and the mass, relative abundance and mobility of the bipolar ions measured in UHP air and CO_2 (table E3) are provided in Appendix E.

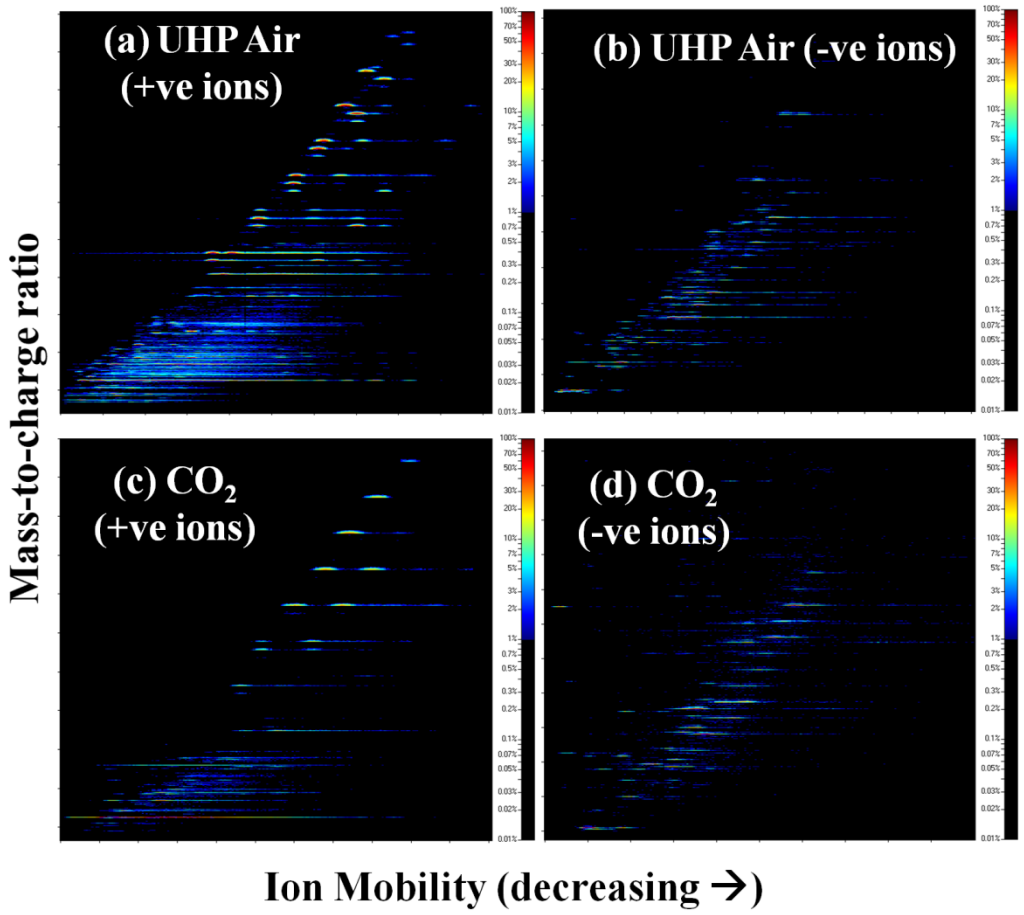

Figure 8.4: Mass-Mobility contours of charging ions. (a) positive ions in UHP air (b) negative ions in UHP air (c) positive ions in CO_2 (d) negative ions in CO_2. The ions are primarily generated by ionization of trace vapors released by the tubing material into the carrier gas stream.

8.3. Simulation Methods

TDMA experiments to measure charge distributions were simulated by taking into account the size distribution (PSD) of aerosol particles and ion mass-mobility distribution as inputs. The effect of DMA resolution was modeled by using the non-diffusing transfer function Ω (Knutson & Whitby, 1975b) for the corresponding sheath flow rates and measured voltages for each dataset (fig. 8.5). Firstly, the PSD of particles entering DMA-1, assumed to be changed negligibly by the furnace upstream, was measured by analyzing particles collected on a TEM grid by evaporating a droplet of the colloidal solution. The

PSD, (a diameter d_p distribution for spheres, bi-variate d_p and length l_p distribution for cylinders) was constructed by sizing about 100 particles in each dataset, was convoluted with Ω to infer the size distribution (<PSD* Ω>) of particles downstream of DMA-1 that is exposed to the charging ions in the Po-210 housing (fig. 8.5a). Using the Brownian Dynamics charge fraction calculation procedure for dilute charging kinetics of aerosol particles, described in detail by Gopalakrishnan, Meredith *et al.* (2013), a particle size, sampled from <PSD*Ω> is placed at the center of a sufficiently large simulation domain with initial charge p=0. An ion with mass m_i, friction factor f_i and charge c_i, sampled from the measured ion mass-mobility distribution measured using the DMA-MS, is initialized on the surface of the domain with a Maxwell Boltzmann distributed velocity (fig. 8.5b). The ion is tracked using a solution to the Langevin equation of motion (Chandrasekhar, 1943) derived by Ermak and Buckholtz (1980) taking into account Coulombic and Image potentials. In the instance of the ion leaving the simulation domain, the ion and particle are re-initialized by sampling from relevant distributions and the simulation is continued. The time elapsed (Δt_p) for the ion to collide with the particle at charge state (p) is inferred as the concentration of particles carrying p charges. The particle charge is updated as $p = p + c_i$ upon each collision. About 20,000 collisions are simulated to calculate the response of the CPC downstream of DMA-2:

$$\boldsymbol{R(V_2) = \Delta t_p \Omega \left(\frac{Z_p(p,d_p,l_p)}{Z_c(V_2,Q_{sh2})}, \frac{Q_{a2}}{Q_{sh2}} \right)} \tag{2a}$$

$\boldsymbol{Z_p(p, d_p, l_p)}$ is the electrical mobility of the particle calculated as $\frac{pe}{\chi_p(d_p,l_p)}$ where e is the fundamental quantum of electronic charge and $\boldsymbol{\chi_p}$ is the scalar friction factor of the particle calculated using the expression for arbitrary shaped particles proposed by Zhang *et al.* (2012) and experimentally verified, as described in chapter 7 (equation 2): Details of particle parameters (R_s and PA) as well as gas parameters are provided in Appendix D. The normalized mobility distribution as measured by DMA-2 (fig. 8.5c) is calculated as:

$$\boldsymbol{R^*(V_2) = \frac{\Delta t_p \Omega \left(\frac{Z_p(p,d_p,l_p)}{Z_c(V_2,Q_{sh2})} \right)}{\sum_{V_2 range} \Delta t_p \Omega \left(\frac{Z_p(p,d_p,l_p)}{Z_c(V_2,Q_{sh2})} \right)}} \tag{2b}$$

Analogous to the Gaussian fits of experimentally measured mobility scans, simulated peak concentrations of singly and doubly charged particles (of both polarities) are used to calculate the ratios defined by eqs. 1d – 1f for comparison. Finally, the fraction of neutral particles is calculated directly as:

$$f_0 = \frac{\Delta t_0}{\sum_{p=-\infty}^{p=+\infty} \Delta t_p} \tag{3}$$

In the above simulations, diffusion losses of particles were neglected and the counting efficiency of the UCPC for particles in the size ranges considered is to be 100%.

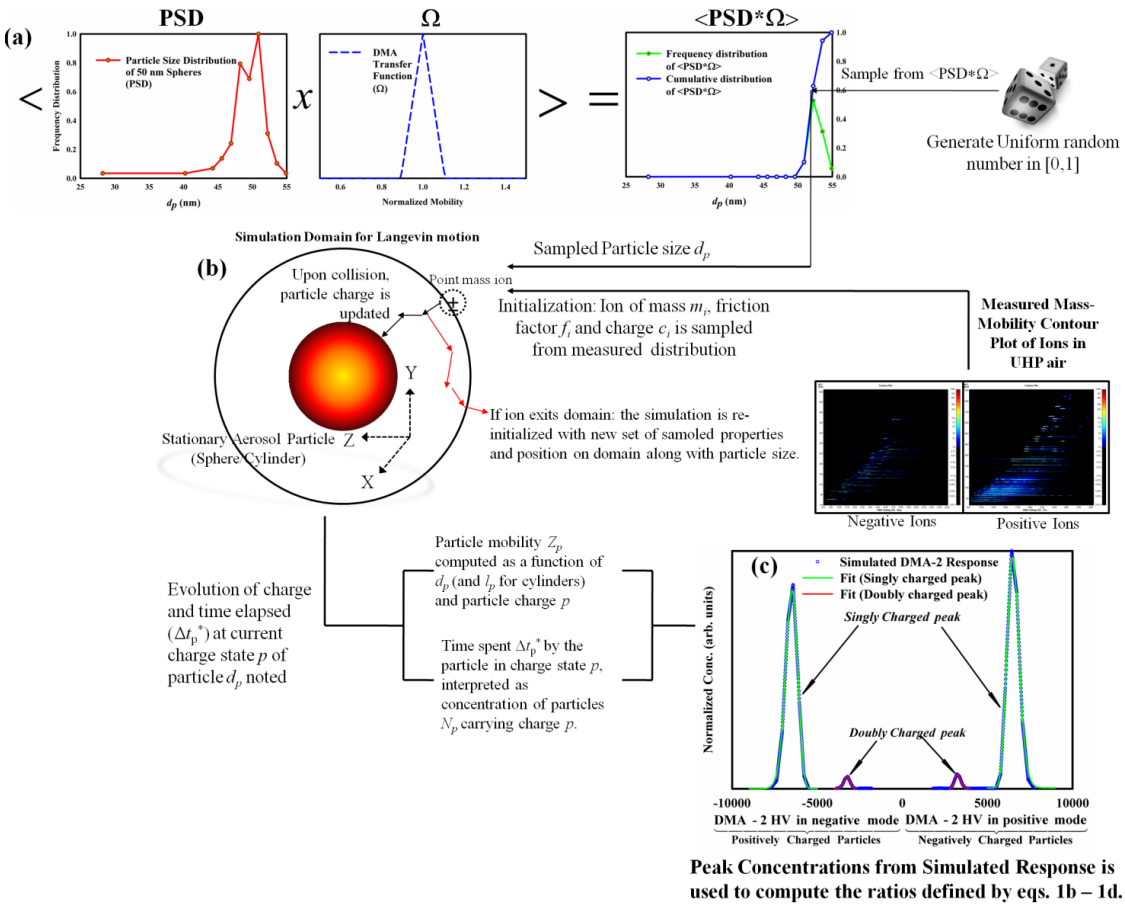

Figure 8.5: Schematic representation of the simulation of charging TDMA experiments using statistical sampling and Brownian Dynamics calculations (a) Sampling of aerosol particles and ions entering the Po-210 housing for charging dynamics simulation (b) Depiction of BD simulation technique (c) simulation of DMA-2 response and fitting of Gaussian functions to concentration of charged particles.

8.4. Results and Discussion

8.4.1. Properties of Charging Ions

Radioactive sources such as Po-210 used in this study and numerous others, generate alpha particles (Helium nuclei), which ionize trace vapors present in the gas stream leading to the generation of bipolar ions through a series of complex reactions. We have used high purity gases (UHP air and CO_2) are used to eliminate the effect of undetermined contaminants, pre-existing vapors and the effect of water vapor. To understand the nature of charge steady states attained in commonly used Silicone "Black" tubes (see insert in fig. 8.1) are used to transport aerosol in both ion and particle characterization. The tubing material is known to be composed of low vapor pressure Polydimethylsiloxane (PDMS) blend polymers, and release heavy molecules into the gas stream, at a very slow, yet steady rate. It is assumed that, since dry gases are used here, water attachment to the measured ions leading to change in their mobility (structure) is not dominant. Also, in such instances, loss of water clusters from macromolecules inside the MS is also believed to be rare. Measured mass-mobility spectra reveal that the charging ions are primarily composed of PDMS units. Fig. 8.4 shows the mass-mobility contours of positive and negative ions measured in UHP air and CO_2 (Bigger figures are provided in the supplemental information). In fig. 8.4a is shown the positive ion spectrum in UHP air, which clearly shows bands of PDMS units appearing in various cluster sizes, ranging from 85 Da to 800 Da. On the other hand, the negative ion distribution in UHP air is relatively polydisperse with the absence of such clearly defined bands (fig. 8.4b). This shows the PDMS polymeric units are more likely to be positively ionized and the negative charge carriers are likely to be lighter molecules, possibly organic in composition. The ion spectra in CO_2 (fig. 8.4c and 8.4d) is qualitatively similar to that of UHP air, with the positive ions exhibiting band like behavior and negative ions being composed of low molecular mass species. Ion-gas molecule collision cross sections are larger in CO_2, owing to CO_2 being a "larger" molecule than oxygen/nitrogen owing to its

high polarizability and van der Waals radius. This leads to the ions having a lower mobility than in air (see tables E4 & E5 listed in Appendix E). Chemical identification of such charging ions and deduction of their structure from measured mobilities via density functional theory modeling is required to understand their source and repeatability in different circumstances (Meredith, Ouyang, Larriba-Andaluz *et al.*, In Prep.). About 50 most abundant ions each of positive and negative polarity are used for charge fraction calculations for both gases. Finally, it should be noted that the DMA-MS can measure only the ions that were not lost to diffusion in the timeframe of the measurement. More mobile species (high energy ions generated during ionization, free electrons) would have been lost in the sampling lines or inside the instrument before reaching the Time-of-Flight detector. The properties of such species will remain undetermined even though they might have participated in the charging reactions with particles in the charger housing. The possibility of free electrons generated during ionization having a significant lifetime and participating in direct collisions (low energy electrons) with particles to induce charge transfer leading to the absolute charge of the particle to decrease, or ionization of particle surface (high energy electrons) can be expected in CO_2 owing to its polarizable nature.

8.4.2. Attainment of Steady State Charge Distribution

The charger made of Teflon used to provide a sealed housing for the Po-210 source was designed to provide enough residence time for particles to undergo sufficient number of collisions with bipolar ions for attainment of steady state charge distribution. This was experimentally verified by measuring the charge distribution attained by 50 nm spheres in UHP air, at several flow rates through the charger to vary the mean the mean residence time of particles. The flow field inside the charger is expected to be complex, with recirculation, leading to particles spending more time on average than a simplistic plug flow profile. In fig. 8.6a, the measured neutral fraction f_0 and the ratios f_{-1}/f_{-2}, f_{+1}/f_{+2} are plotted, normalized by the average ratio over all the flow rates measured. Hence, the ordinate can be directly read as the % deviation from the mean at a given flow rate. Immediately apparent is that, f_0 and the ratios f_{-1}/f_{-2} and f_{+1}/f_{+2} are within ±10% of each other for all mean residence times considered. The measurements reported here, are performed at a flow rate of 1.5 lpm (drawn by the critical orifice downstream of the UCPC), are within ±5% of the measurements made at 0.96 lpm, corresponding to the longest mean residence time in the charger and it is clear that, due to recirculation, steady state is attained even at 3.0 lpm.

To experimentally verify that the charger housing used here imparts an initial condition independent steady state charge distribution to particles, the polarity of particles entering the charger is varied keeping other parameters fixed (50 nm spheres in UHP air). In all the reported measurements, DMA-1 is set to a voltage of negative polarity leading to positively charged particles entering the charger. In fig. 8.6b, measurements done for positively as well as negatively charged particles (DMA-1 operated in positive polarity) are shown. f_0 and f_{+1}/f_{+2} show very small difference (noted in the figure) while f_{-1}/f_{-2} exhibits a 17% difference. We note that this difference is not negligible and that the charger is likely to have a higher concentration of negative charge carriers leading to a slight bias in neutralizing particles with pre-existing negative charge. However, since all reported measurements are done with particles that are initially positively charged, we expect this effect to be negligible. We note that the ratios f_{-1}/f_{+1}

and f_{-2}/f_{+2} are not included in these comparisons as the measurements were performed on different days, the electrospray aerosol generator produced different absolute concentrations that make such comparisons invalid.

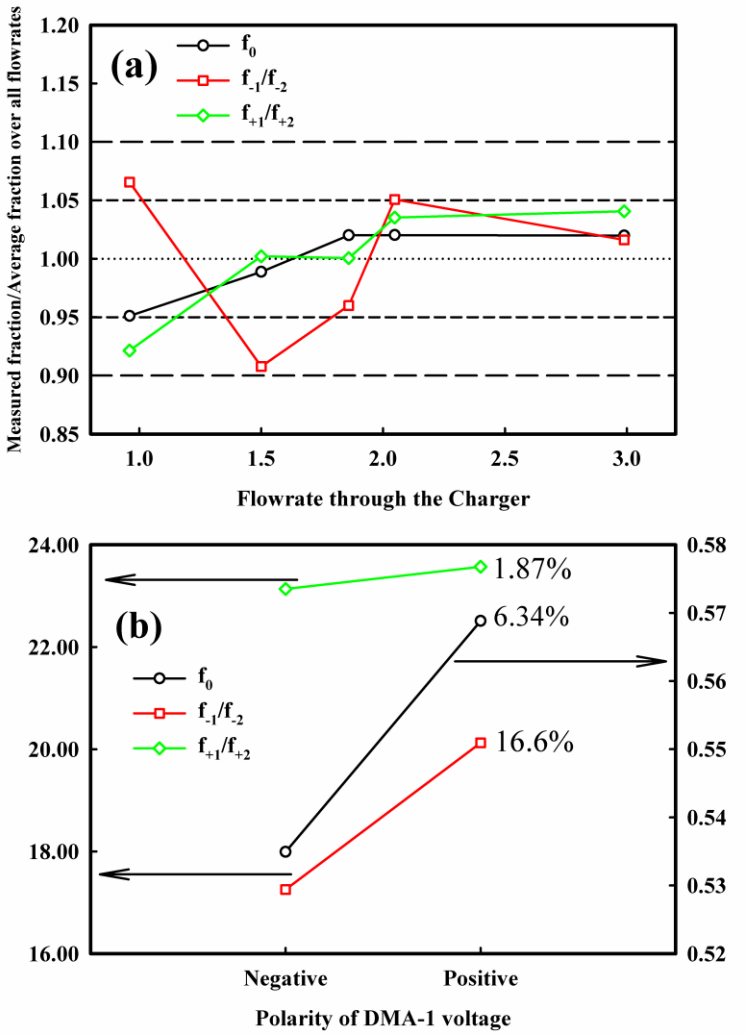

Figure 8.6: (a) plot showing charge fraction ratios normalized by the average at all measured flow rates as a function of the flow rate through the neutralizer. The ordinate can be directly read as the factor of deviation of measurements reported. (b) measured charge fraction ratios for positive and negatively charged particles entering the Po-210 housing. Also noted is the % difference between the values obtained in positive and negative voltage on DMA-1.

8.4.3. Validation of Simulation Methods

The experimental and simulated peak mobilities of particles (singly and doubly charged) as well as the width of the peaks in mobility space for all datasets are compared with each other in figs. 8.7a & 8.7b respectively. Electrical mobility, calculated based on the friction factor law (eq. 2c) for nonspherical particles is expected to give good agreement with the measured mobilities as shown in fig. 8.7a. The surfactant coating found on l_p/d_p=4.3 nanorods was not completely removed by passing through the tubular furnace and hence the rods, while flowing through the DMA were bigger than their dimensions observed in TEM, due to the surfactant being invisible due to insufficient contrast, as described in chapter 7 (Gopalakrishnan *et al.*, (In Prep.)). in UHP air and CO_2 can be seen. To overcome the under-prediction of mobility based on TEM size (which is lower than the true size), a coating of uniform thickness of 3 nm was assumed to minimize the difference between predicted and experimentally observed mobility. Other datasets do not suffer from this issue and their mobilities are obtained directly using the TEM size. The width of DMA-2 mobility distribution function serves as a validation of the simulation procedure used here (fig. 8.7b). Again, excellent agreement can be seen as most data points are found to fall close to the 1:1 line. Based on these results, it is concluded that the simulated distributions closely follow the experimental distributions and are appropriate for comparison.

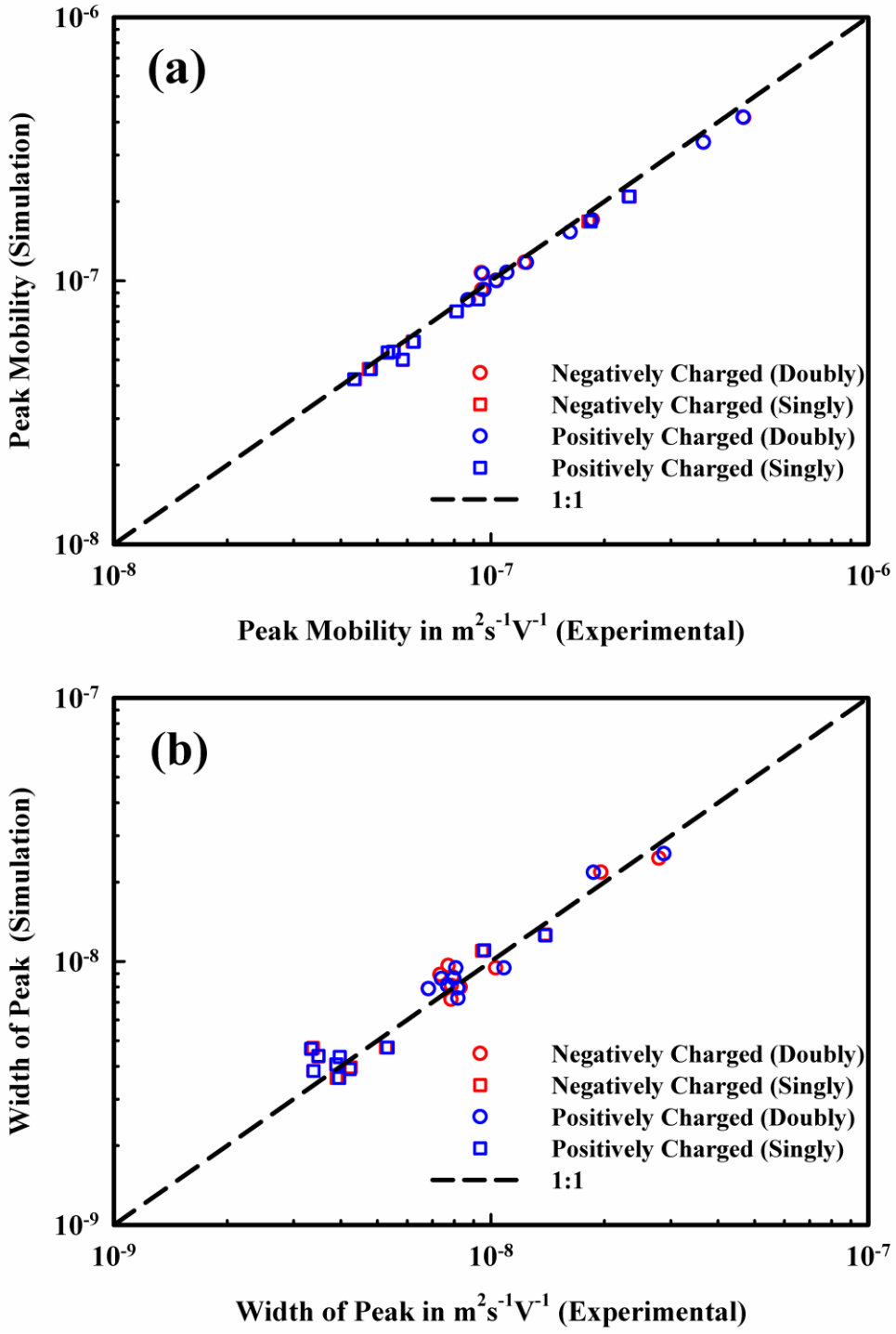

Figure 8.7: Comparison of simulated and experimentally measured charged particle (a) peak mobility and (b) width. For brevity, all datasets are plotted together grouped by the polarity and charge state of the peak. A 1:1 line is shown to guide the eye.

8.4.4. Charging Results: Spheres

Using the methods described previously, the neutral fraction f_0 and ratios of charged fractions (defined by eqs. 1d – 1f) for 50 nm and 70 nm spherical particles measured in UHP air and CO_2 are presented in figure 8.8. Also, shown are charge distributions predicted by the commonly used regression expression for bipolar steady state charge fractions derived by Wiedensohler (1988) based on mean mass and mobility measured for gas phase ions in air (Wellisch, 1909) with collision kernels required to solve population balances of charged particles calculated using the theory of Hoppel & Frick (1986). The BD simulation derived regression expression developed in Chapter 6 based on ions measured in UHP air (transported using a combination of stainless steel and Teflon tubing) which takes into account the combined Coulombic and image potential, is also given for comparison.

Ratios f_0, f_{-1}/f_{-2} and f_{+1}/f_{+2} are calculated based on particles with the same size distribution function, and instances when the particle absolute concentration was different between the positive and negative mode measurements are noted and the ratios f_{-1}/f_{+1} and f_{-2}/f_{+2} excluded from comparison in such cases.

Firstly, the experimentally determined ratios and simulated ratios exhibit similar qualitative behavior for all metrics of comparison which shows that the BD simulation procedure is capable of predicting bipolar diffusion charging kinetics. It also been shown earlier using BD simulations that the expression of Wiedensohler over predicts charge fractions by about 15-30% in the size range of 20-150 nm in air at STP (Gopalakrishnan, et al., 2013). This notion is supported by the deviation of the Wiedensohler charge distribution from experiment, which shows that the charge distributions strongly depend on the properties of the charging ions as well. The difference between the regression expression from Chapter 6 is not negligible either, but less than that of the Wiedensohler expression and illustrate the difference between the ions generated while using Black Silicone tubing and clean SS & Teflon tubing. Hence it is important to characterize neutralizer ions as a function of the tubing, and as the flow profile through neutralizer housing is also critical (Alonso & Alguacil, 2003). For both sizes in UHP air, the

measured and calculated neutral fractions (fig. 8.8a) are within ±2% of each other, while the deviation in CO_2 is 14% for 50 nm spheres and 6% for 70 nm spheres. Similarly, the ratio f_{-1}/f_{-2} (fig. 8.8b) show good agreement (maximum deviation 9%) but the ratio f_{+1}/f_{+2} (fig. 8.8c) values are under-predicted by about 10% for both sizes of spheres, especially 50 nm spheres in CO_2 (deviation of 38%). The simulations show agreement within 15% except for ratios f_{-1}/f_{+1} and f_{-2}/f_{+2} (figs. 8.8d & 8.8e), for 50 nm particles in CO_2. This shows there was a stronger bias for particles to acquire negative charge than positive, likely to have been caused by high mobility negative charge carriers that might have escaped detection and hence were not accounted in simulations.

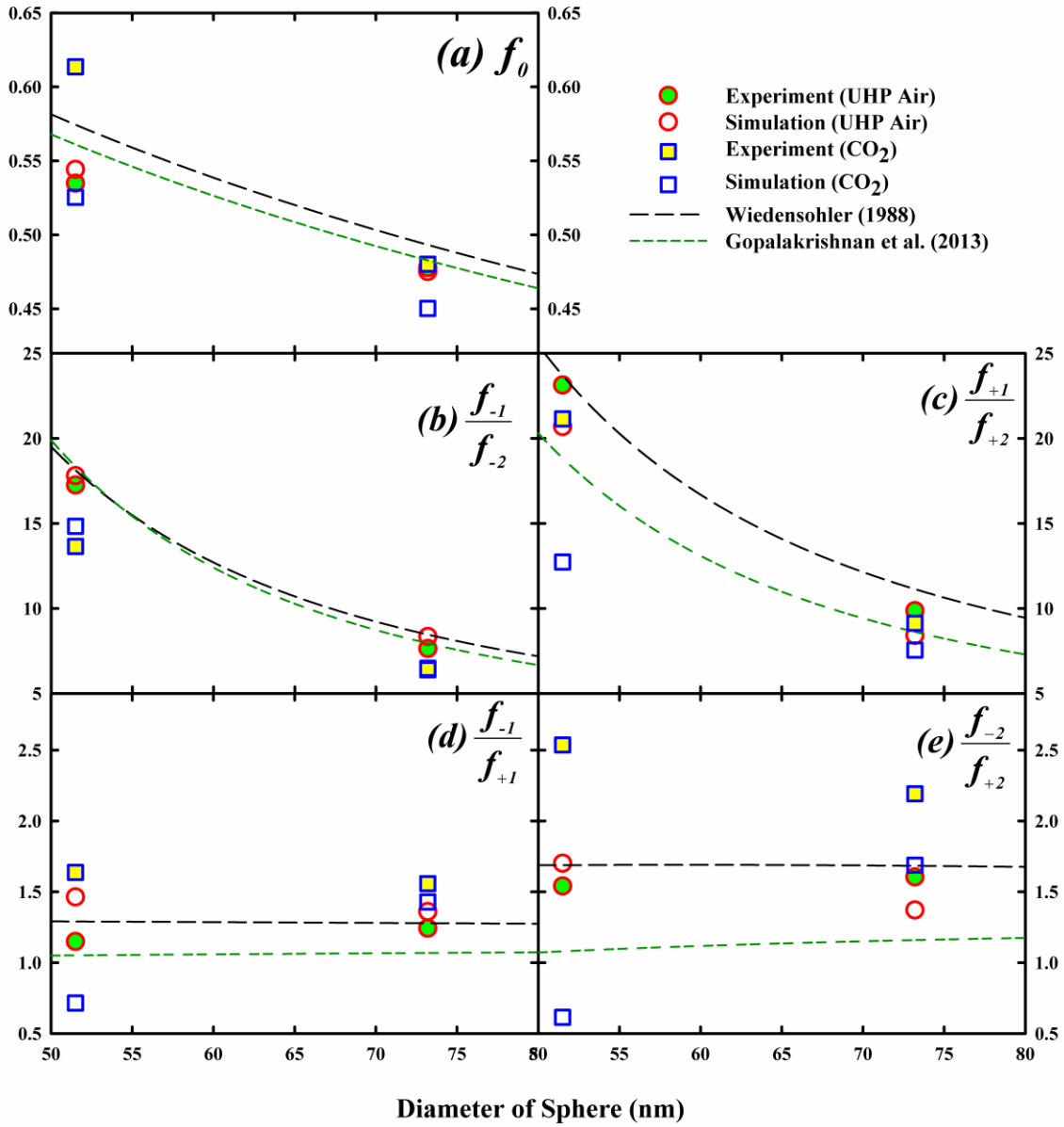

Figure 8.8: Experimental (filled symbols) and simulation derived (open symbols) charge fraction ratios for spherical particles. (a) f_0 (b) f_{-1}/f_{-2} (c) f_{+1}/f_{+2} (d) f_{-1}/f_{+1} (e) f_{-2}/f_{+2}. Also shown on each plot are the Wiedensohler regression and regression for spheres developed in Chapter 6 (Gopalakrishnan, Meredith et al. 2013).

8.4.5. Charging Results: Cylinders

The data collected in this study are analyzed to delineate the effect of two parameters, 1) nondimensional parameter that provides information on particle nonsphericity $\frac{PA}{\pi R_s^2}$ (i.e.) ratio of the orientation averaged projected area (PA) to the continuum momentum transfer based surface area (πR_s^2) noted in table 1 and 2) the electrical mobility equivalent diameter d_m (introduced in Chapter 6).

Firstly, f_0 and other ratios (eqs. 1d – 1f) are plotted as a function of $\frac{PA}{\pi R_s^2}$ in the range of 0.63 to 1.00 (fig. 8.9) for cylinders whose d_m values are close to each other. Nanorods of l_p/d_p 14.9, 11.3, 2.2 and 70 nm spheres, respectively, have $\frac{PA}{\pi R_s^2}$ values of 0.63, 0.70, 0.84 and 1.00. The d_m of these datasets vary from 62.5 to 70 nm. As an approximation, they are considered to be of fixed d_m to understand the effect of $\frac{PA}{\pi R_s^2}$. From fig. 8.9a, it is seen that the neutral fraction decreases for higher aspect ratio particles and this observation is also confirmed by simulations. From fig. 8.9b, the experimentally determined f_{-1}/f_{-2} and f_{+1}/f_{+2} show a monotonic decrease with decreasing $\frac{PA}{\pi R_s^2}$, which is consistent with prior experimental evidence that longer or open structures tend to acquire more charges than spheres of same mobility. The simulation derived ratios show similar trends but over-predict the ratios. The ratios of f_{-1}/f_{+1} and f_{-2}/f_{+2} which are expected to be about 1.0 for positive and negative ions of equal concentration and similar properties. However, the observed ratios in the range of 1.0 to 3.0 suggest asymmetries in concentrations and mobilities of ions. While the difference in mobility can be seen in the observed DMA-MS data (ratio of most mobile negative to positive ion is 1.16 in UHP air and 1.06 in CO_2), the concentrations of negative and positive ions were assumed to be equal as measurements of absolute number concentrations were not attempted. These can be possible reasons for a maximum difference of about a factor of 2.5 between experimental values and simulation-derived charge distributions.

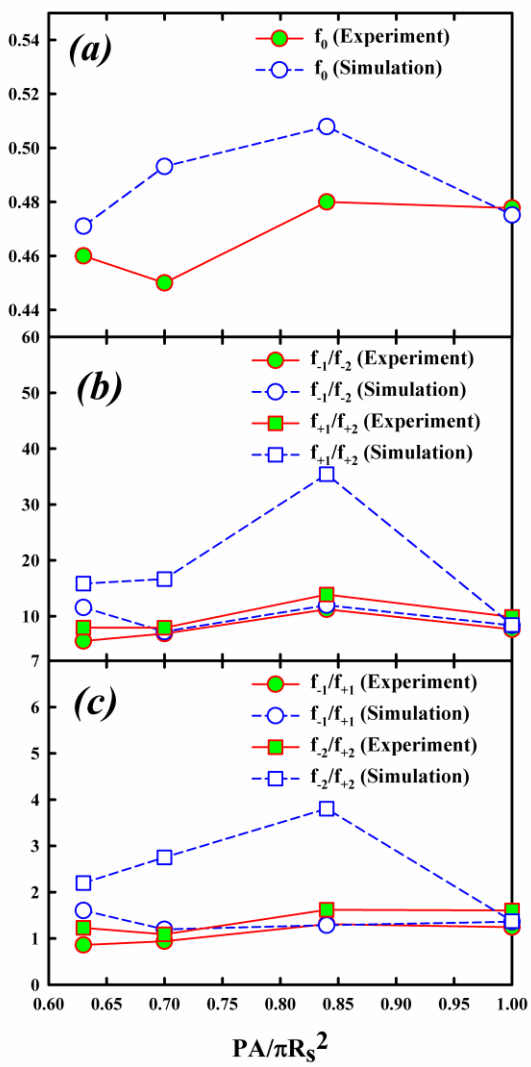

Figure 8.9: Experimental (solid lines) and simulation derived (dashed lines) charge fraction ratios for cylindrical particles as a function of $PA/\pi R_s^2$ for datasets with mobility diameter about 65 nm. Shown in (a) f_0, (c) f_{-1}/f_{-2} & f_{+1}/f_{+2} and (e) f_{-1}/f_{+1} & f_{-2}/f_{+2}. (b), (d) & (e) present the corresponding % deviation of simulation from experiments.

To understand the effect of mobility diameter, charge distributions of nanorods of l_p/d_p 4.3 and 2.2 (having the same $\frac{PA}{\pi R_s^2}$ value of 0.84) are plotted in fig. 8.10 along with the regression expression for spheres and non-spheres of $\frac{PA}{\pi R_s^2}$=0.84 from Chapter 6. In this size range, experimental charge distributions for both datasets behave like spheres of the

same mobility diameter with the dataset l_p/d_p=4.3 having decreasing tendency to attain doubly charge state than l_p/d_p=2.2. Simulation results for f_0 (fig. 10a) show reasonable agreement (within 15%) f_{-1}/f_{-2} (fig. 8.10b) and significant deviation for the ratio f_{+1}/f_{+2} but reproduce qualitative trends as before. The large deviation of f_{-1}/f_{+1} and f_{-2}/f_{+2} simulation values from experimental values, highlight the importance of determining ion properties along with absolute concentration for accurate theoretical predictions using BD methods.

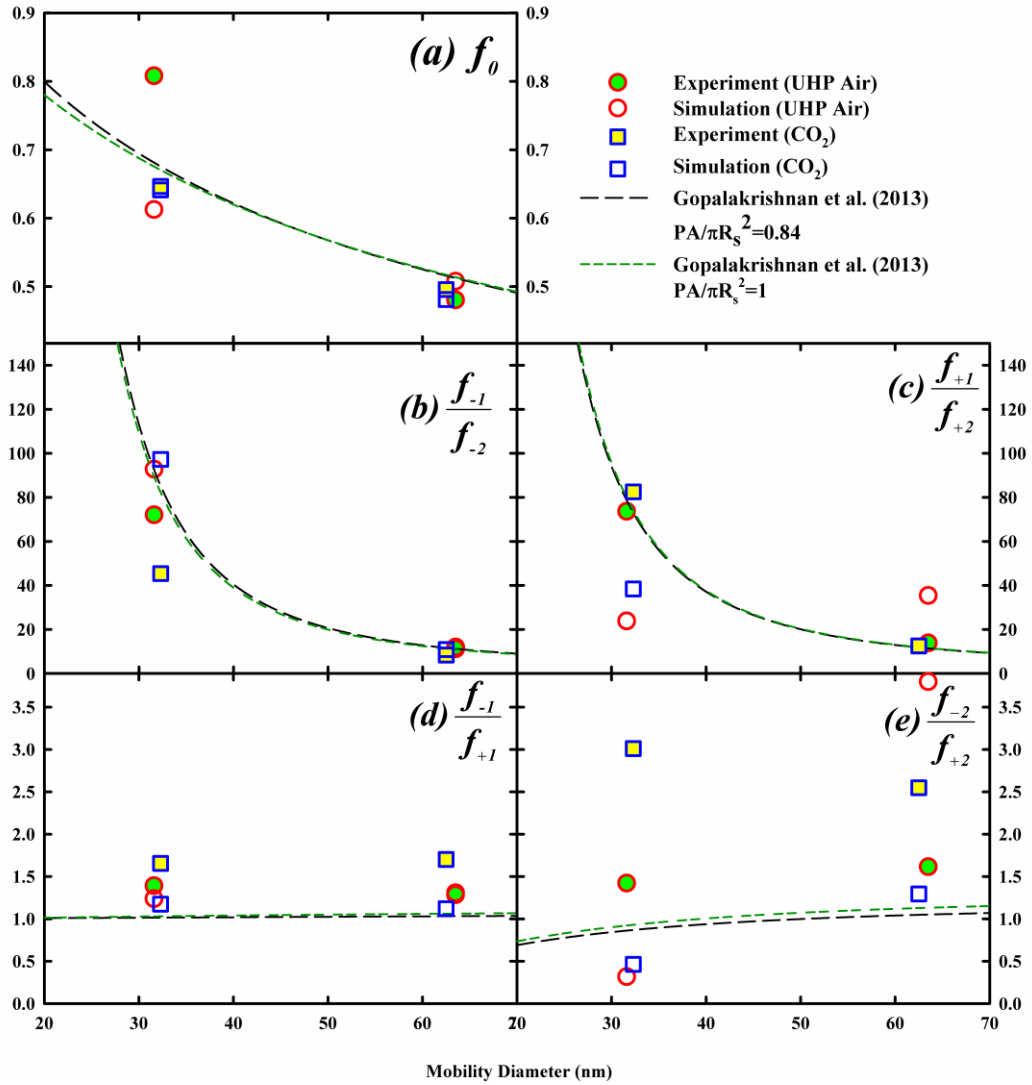

Figure 8.10: Experimental (filled symbols) and simulation derived (open symbols) charge fraction ratios for cylindrical particles as function of mobility diameter for $PA/\pi R_s^2$=0.84. (a) f_0 (b) f_{-1}/f_{-2} (c) f_{+1}/f_{+2} (d) f_{-1}/f_{+1} (e) f_{-2}/f_{+2}. Also shown on each plot are the regression expression for spheres ($PA/\pi R_s^2$=1.00) and non-spheres with $PA/\pi R_s^2$=0.84 from Chapter 6.

8.5. Conclusions

In summary, the measurements of charge distribution of well defined spherical and cylindrical particles lead us to the following conclusions:

- The ions generated by radioactive neutralizers were traced to the tubing material used as is evident from measured mass-mobility spectra.
- The measured and simulated charge distribution for spheres show good agreement in UHP air, while in CO_2 the presence of high mobility negative charge carriers (free electrons) is hypothesized to be the reason for the large difference.
- From measured charge distributions of cylinders, it is clear that particles that are highly nonspherical ($\frac{\boldsymbol{PA}}{\boldsymbol{\pi R_s^2}}$ of 0.70 and 0.63) attain higher charge levels than mobility equivalent spheres (d_m ~ 65 nm). The effect of mobility diameter was also studied, and for the particles considered here ($\frac{\boldsymbol{PA}}{\boldsymbol{\pi R_s^2}}$ of 0.84) behave akin to mobility equivalent spheres (<65 nm).
- The simulation technique used here reproduced the experimental trends while the specific difference was large in many instances. We attribute this to the following factors:
    - Finiteness of samples size used to construct particle size distribution produced by the electrospray.
    - Presence of high mobility charge carriers (free electrons) that were not "seen" by the DMA-MS and thus not accounted in mass-mobility distributions used.
    - Possible imbalance in the concentration of positive and negative ions generated in the neutralizer housing leading to asymmetric charge distribution. Careful flow profile analysis and exposure time characterization will be required in the future to accurately simulate the charging process.

Chapter 9: Summary and Future Work

9.1 Summary

The theoretical, computational and experimental studies described in this thesis deal with some fundamental problems in aerosol science, specifically, the modification of the size and shape of aerosol particles by collisional growth and the charging of particles by collisions with gas phase ions has been studied in detail. These problems are tied by the common theme of diffusion limited transport of species to the surface of an aerosol particle in the mass transfer transition regime and find numerous applications in the design and operation of instruments and aerosol synthesis reactors.

Scaling/dimensional analysis, a simple yet powerful tool that yields global constraints and enables the prediction of the correct functional form has been the principle theoretical tool employed to analyse collisional mass transfer in dilute aerosol particle systems. Coupled to mean first passage time calculations, a viable transition regime collision kernel for hard sphere and long range repulsive interactions has been derived. To deal with bipolar diffusion charging, an alternate approach was employed to calculate the steady state charge distribution directly. This enabled us to show that particle shape and material have a profound effect on the charging properties. Using cylindrical shaped aerosol particles, drag measurements were used to verify a scalar friction factor law that can be widely applied to mobility characterization of fractal aggregates and other nonspherical particles in the transition regime. Finally, bipolar diffusion charging experiments were used to demonstrate the predictive abilities of the computational approaches developed.

9.2 Recommendations for Future Work

The body of accumulated knowledge about nanoparticle physics can be advanced by focusing on the topics (sorted by the chapters in which they appeared previously) described herein, which are by no means exhaustive.

Chapters 2 & 3:

The mean mean first passage time calculations performed using solutions to the Langevin equations assume that the diffusing entity is much heavier than the background molecules. While this assumption was shown to be not important for transition regime collisions between vapor clusters and gas molecules by comparing expressions that were derived by assuming $Z \rightarrow 0$ and $Z \rightarrow \infty$ produce similar results, the effect of Z on calculated collision kernel need to be investigated in detail. Direct modeling of vapor clusters and gas molecules using the Boltzmann equation may be employed. Many atmospherically relevant condensable vapors have molecular masses that are comparable to the background gas molecules, hence assumptions of $Z \rightarrow \infty$ needs to be re-examined.

The transition regime expression $H(Kn_D)$ assumes that the colliding entities either have correlated masses and friction factors ($\boldsymbol{\theta_m = \theta_f}$) or one of the collision partners is much larger and massive than the other ($\boldsymbol{\theta_m, \theta_f} \rightarrow 0$). While this assumption holds satisfactorily for particles of the same material, collisions with particles whose densities are different need to be re-examined. The dependence of $H(Kn_D)$ on $\boldsymbol{\theta_m, \theta_f}$ should be established.

Also, all of the simulations conducted here assume complete thermal equilibrium of all entities including gas molecules. While this is a very good model for many aerosol systems, it may not be valid for dusty plasmas where ions, free electrons and dust grains have different temperatures, making the analysis quite intriguing. Extension of Brownian Dynamics methods to include collisional heat transfer can prove challenging.

Chapter 4:

The foremost outstanding problem pertaining to potential interactions in the transition regime is the definition of the correct length scale that is relevant for long range attractive interactions as pointed out in the discussions about coulombic capture radius in

chapter 4. In future work it will be necessary to find a suitable functional form to calculate collision kernels in the large Ψ_E, large Kn_D range, termed the high potential, near free molecular regime. Further, more sophisticated potential functions, and non-spherical colliding entities need to be considered. Such instances are also amenable to dimensional analysis and mean first passage time calculations, allowing for an appropriately defined H to be expressed as a function of Kn_D and the dimensionless parameters required to define the functional form of the potential. A kernel for attractive inverse squared (coulombic/gravitational) interaction between particles in high vacuum environments like plasmas and outerspace, where high Knudsen transport of mass and momentum take place, is of great interest.

Chapter 5 & 6:

The identification of R_s and PA as the relevant length scales describing collisions involving nonspherical particles requires that the dependence of these parameters on shape needs to be clearly understand through computational studies. Further, experimental determination of R_s and PA requires tedious microscopy. Hence, online techniques (differential mobility analysis for e.g.) that will yield information about the R_s and PA distribution should be developed, which when coupled to the afore said theoretical studies will help in identifying particles shapes with unique charging and mass transfer characteristics.

Secondly, the analysis and expressions presented in Chapter 5 are applicable to conducting particles only. As seen from the discussion in Chapter 6, particle material plays a strong role in the charging of highly nonspherical particles. hence, theoretical studies along the lines of Chapter 5 need to be undertaken for dielectric materials as well. This theoretical development is believed to have profound applications in dealing with nanomaterials whose properties differ from commonly handled metallic (gold, silver, iron, etc.) nanoparticles.

The neglect ion-ion interactions is a valid assumption for aerosol particle systems as pointed out in Chapter 5. However, extension of simulation methods to include ion concentration effects and screening of ion potentials due to other charge carriers needs to be undertaken. Such developments can prove valueable to analysis of collisions in dusty plasmas and highly concentrated aerosols.

Diffusion charging (i.e.) ion transport by thermal diffusion and electrokinetic motion due to electrostatic interactions in the absence of external fields have been the sole focus here. Field charging of micrometer and nanometer particles are interesting problems with applications in designing high efficiency chargers for measurement and manufacturing.

Chapters 7 & 8:

The measurements of drag on cylindrical nanoparticles helped to verify the transition regime drag expression. Further validation using fractal aggregates is important. Techniques to get information about 3-D structure from 2-D images obtained from microscopy, to compute R_s and PA exactly will be a natural extension of the work presented here.

Finally, bipolar and unipolar charging experiments to investigate the effect of particle shape and material across a wide size range should be undertaken. The principle innovation of the measurements reported here, is the simultaneous characterization of ion properties using a DMA-MS. Such characterization should be considered routine in the future to enable accurate validation of models developed to describe charging phenomena. Also, in typical aerosol application, the effect of contaminants and pre-existing vapors (especially water vapor) is important and should be understood. Loss of water clusters during characterization can make such measurements tricky to carry out.

Bibiliography

Adachi, M., Kousaka, Y., & Okuyama, K. (1985). Unipolar and Bipolar Diffusion Charging of Ultrafine Aerosol-Particles. *Journal of Aerosol Science,* **16**, 109-123.

Adachi, M., Romay, F.J., & Pui, D.Y.H. (1992). High-efficiency unipolar aerosol charger using a radioactive alpha source. *J. Aerosol. Sci.,* **23**, 123-137.

Allen, J.E. (1992). Probe Theory - The Orbital Motion Approach. *Phys. Scr.,* **45**, 497-503.

Allen, M.D., & Raabe, O.G. (1982). Re-Evaluation of Millikan Oil Drop Data for the Motion of Small Particles in Air. *Journal of Aerosol Science,* **13**, 537-547.

Alonso, M., & Alguacil, F.J. (2003). The effect of ion and particle losses in a diffusion charger on reaching a stationary charge distribution. *Journal of Aerosol Science,* **34**, 1647-1664.

Amadon, A.S., & Marlow, W.H. (1991a). Cluster-Collision Frequency .1. The Long-Range Intercluster Potential. *Physical Review A,* **43**, 5483-5492.

Amadon, A.S., & Marlow, W.H. (1991b). Cluster-Collision Frequency .2. Estimation of the Collision Rate. *Physical Review A,* **43**, 5493-5499.

Azarov, I.B., & Veshchunov, M.S. (2010). Development of the New Approach to the Brownian Coagulation Theory: Transition Regime. *Journal of Engineering Thermophysics,* **19**, 128-137.

Beranek, J., Imre, D., & Zelenyuk, A. (2012). Real-Time Shape-Based Particle Separation and Detailed in Situ Particle Shape Characterization. *Anal Chem,* **84**, 1459-1465.

Biskos, G., Mastorakos, E., & Collings, N. (2004). Monte-Carlo simulation of unipolar diffusion charging for spherical and non-spherical particles. *J. Aerosol. Sci.,* **35**, 707-730.

Biskos, G., Reavell, K., & Collings, N. (2005). Unipolar diffusion charging of aerosol particles in the transition regime. *J. Aerosol. Sci.,* **36**, 247-265.

Biswas, P., & Wu, C.Y. (1998). Control of toxic metal emissions from combustors using sorbents: A review. *J Air Waste Manage,* **48**, 113-127.

Biswas, P., & Zachariah, M.R. (1997). In situ immobilization of lead species in combustion environments by injection of gas phase silica sorbent precursors. *Environmental Science & Technology,* **31**, 2455-2463.

Boisdron, Y., & Brock, J.R. (1970). On the stochastic nature of the acquisition of electrical charge and radioactivity by aerosol particles. *Atmospheric Environment (1967),* **4**, 35-50.

Bricard, J. (1962). La fixation des petits ions atmosphériques sur les aérosols ultra-fins. *Pure and Applied Geophysics,* **51**, 237-242.

Brock, J.R. (1966). Diffusion to Particles in the Near Free Molecular Regime. *Journal of Colloid and Interface Science,* **22**, 513-516.

Brock, J.R. (1970). Aerosol Charging: The Role of Image Force. *Journal of Applied Physics,* **41**, 843-844.

Brown, R.C., & Hemingway, M.A. (1995). Electric charge distribution and capacitance of agglomerates of spherical particles: Theory and experimental simulation. *J. Aerosol. Sci.,* **26**, 1197-1206.

Buckingham, E. (1914). On physical similar systems; illustrations of the use of dimensional equations. *Physical Review,* **4**, 345-376.

Buckingham, E. (1915). Model experiments and the forms of empirical equations. *Transactions of the ASME,* **37**, 263-296.

Cai, J., Lu, N.L., & Sorensen, C.M. (1995). Analysis of Fractal Cluster Morphology Parameters - Structural Coefficient and Density Autocorrelation Function Cutoff. *Journal of Colloid and Interface Science,* **171**, 470-473.

Cauchy, A. (1908). *Oeuvres Completes leserie. Tone II, Paris.*

Chandrasekhar, S. (1943). Stochastic Problems in Physics and Astronomy. *Reviews of Modern Physics,* **15**, 1-89.

Chapman, S., & Cowling, T.G. (1970). *The Mathematical Theory of Non-uniform Gases*. Cambridge University Press, Cambridge.

Chatterjee, A., Kerker, M., & Cooke, D.D. (1975). Brownian coagulation of Aerosols in the Transition Regime. *Journal of Colloid and Interface Science,* **53**, 71-82.

Chaudhuri, M., Khrapak, S.A., & Morfill, G.E. (2010). Effect of ionization/recombination processes on the electrical interactions between positively charged particles in highly collisional plasmas. *Physics of Plasmas,* **17**, 034503.

Chen, D.R., & Pui, D.Y.H. (1997). Experimental investigation of scaling laws for electrospraying: Dielectric constant effect. *Aerosol Science and Technology,* **27**, 367-380.

Chen, D.R., & Pui, D.Y.H. (1999). A high efficiency, high throughput unipolar aerosol charger for nanoparticles. *J. Nanopart. Res.,* **1**, 115-126.

Cheng, Y.-S., & Yeh, H.-C. (1981). Equilibrium bipolar charge distribution of aerosols consisting of chains of uniform spheres. *Journal of Colloid and Interface Science,* **84**, 444-450.

Cheng, Y.S., Yeh, H.C., & Kanapilly, G.M. (1981). Collection Efficiencies of a Point-to-Plane Electrostatic Precipitator. *Am Ind Hyg Assoc J,* **42**, 605-610.

Chernyak, V. (1995). The Kinetic Theory of Droplet Evaporation. *Journal of Aerosol Science,* **26**, 873-885.

Cui, C., & Goree, J. (1994). Fluctuations of the Charge on a Dust Grain in a Plasma. *IEEE Transactions on Plasma Science,* **22**, 151-158.

D'yachkov, L.G., Khrapak, A.G., Khrapak, S.A., & Morfill, G.E. (2007). Model of grain charging in collisional plasmas accounting for collisionless layer. *Physics of Plasmas,* **14**, 042102.

Dahneke, B.E. (1973a). Slip Correction Factors for Nonspherical Bodies- I Introduction and Continuum Flow. *Journal of Aerosol Science,* **4**, 139-145.

Dahneke, B.E. (1973b). Slip Correction Factors for Nonspherical Bodies- II Free Molecular Flow. *Journal of Aerosol Science,* **4**, 147-161.

Dahneke, B.E. (1973c). Slip Correction Factors for Nonspherical Bodies- III The Form of the General Law. *Journal of Aerosol Science,* **4**, 163-170.

Dahneke, B.E. (1983). Simple Kinetic Theory of Brownian Diffusion in Vapors and Aerosols. In *Theory of Dispersed Multiphase Flow*(Edited Meyer, R.E.), *Theory of Dispersed Multiphase Flow*. Academic Press, New York.

Davies, C.N. (1945). Definitive equations for the fluid resistance of spheres. *Proceedings of the Physical Society,* **57**, 259-270.
Davies, C.N. (1979). Particle-fluid interaction. *Journal of Aerosol Science,* **10**, 477-513.
Davis, E.J., & Ray, A.K. (1978). Submicron Droplet Evaporation in the Continuum and Non-Continuum Regimes. *J. Aerosol. Sci.,* **9**, 411.
de la Mora, J.F., Borrajo-Pelaez, R., & Zurita-Gotor, M. (2012). Capillary and Coulombic Effects on the Gas Phase Structure of Electrosprayed Concanavalin A Ions and Its Clusters C-n(+z) (n=1-6). *Journal of Physical Chemistry B,* **116**, 9882-9898.
Douglas, J.F., Zhou, H.X., & Hubbard, J.B. (1994). Hydrodynamic Friction and the Capacitance of Arbitrarily-Shaped Objects. *Physical Review E,* **49**, 5319-5337.
Eglin, J.M. (1923). The Coefficients of Viscosity and Slip of Carbon Dioxide by the Oil Drop Method and the Law of Motion of an Oil Drop in Carbon Dioxide, Oxygen, and Helium, at Low Pressures. *Physical Review,* **22**, 161-170.
Ermak, D.L. (1975). Computer-Simulation of Charged-Particles in Solution. 1.Technique and Equilibrium Properties. *Journal of Chemical Physics,* **62**, 4189-4196.
Ermak, D.L., & Buckholz, H. (1980). Numerical-Integration of the Langevin Equation - Monte-Carlo Simulation. *J Comput Phys,* **35**, 169-182.
Filippov, A.V. (1993). Charginf of Aerosol in the Transition Regime. *J. Aerosol. Sci.,* **24**, 423-436.
Filippov, A.V. (1994). Charge-Distribution among Nonspherical Particles in a Bipolar Ion Environment. *J. Aerosol. Sci.,* **25**, 611-615.
Filippov, A.V. (2000). Drag and Torque on Clusters of N Arbitrary Spheres at Low Reynolds Number. *J Colloid Interf Sci,* **229**, 184-195.
Filippov, A.V., Zurita, M., & Rosner, D.E. (2000). Fractal-like aggregates: Relation between morphology and physical properties. *Journal of Colloid and Interface Science,* **229**, 261-273.
Friedlander, S.K. (2000). *Smoke, Dust, and Haze*. Oxford University Press, New York.
Fuchs, N.A. (1934). *Physik. Z. Sowjet.,* **6**, 225.
Fuchs, N.A. (1959). *Evaporation and Droplet Growth in Gaseous Media*. Pergamon Press, London.
Fuchs, N.A. (1963). On the Stationary Charge Distribution on Aerosol Particles in a Bipolar Ionic Atmosphere. *Geofis. Pura Appl.,* **51**, 185-193.
Fuchs, N.A. (1964). *The mechanics of aerosols* (Rev. and enl. ed.). Macmillan, New York,.
Fuchs, N.A., & Stechkina, I.B. (1962). Resistance of a gaseous medium to the motion of a spherical particle of a size comparable to the mean free path of the gas molecules. *Transactions of the Faraday Society,* **58**, 1949-1952.
Fuchs, N.A., & Sutugin, A.G. (1970). *Highly dispersed aerosols*. Ann Arbor Science Publishers, Ann Arbor,.
Gatti, M., & Kortshagen, U. (2008). Analytical model of particle charging in plasmas over a wide range of collisionality. *Physical Review E,* **78**, 046402.
Gentry, J., & Brock, J.R. (1967). Unipolar Diffusion Charging of Small Aerosol Particles. *The Journal of Chemical Physics,* **47**, 64-69.
Gentry, J.W. (1972). Charging of aerosol by unipolar diffusion of ions. *J. Aerosol. Sci.,* **3**, 65-76.

Girshick, S.L., Agarwal, P., & Truhlar, D.G. (2009). Homogenous Nucleation with Magic Numbers: Aluminum. *Journal of Chemical Physics,* **131**, 134305.

Given, J.A., Hubbard, J.B., & Douglas, J.F. (1997). A first-passage algorithm for the hydrodynamic friction and diffusion-limited reaction rate of macromolecules. *Journal of Chemical Physics,* **106**, 3761-3771.

Gmachowski, L. (2010). Mobility radius of fractal aggregates growing in the slip regime. *Journal of Aerosol Science,* **41**, 1152-1158.

Gopalakrishnan, R., & Hogan, C.J. (2011). Determination of the Transition Regime Collision Kernel from Mean First Passage Times. *Aerosol Science and Technology,* **45**, 1499-1509.

Gopalakrishnan, R., & Hogan, C.J. (2012). Coulomb-Influenced Collisions in Aerosols and Dusty Plasmas. *Physical Review E,* **85**, 026410.

Gopalakrishnan, R., McMurry, P.H., & Hogan Jr, C.J. ((In Prep.)). Experimental Verification of a Transition Regime Drag Law using High Aspect Ratio Aerosol Particles.

Gopalakrishnan, R., Meredith, M.J., Larriba-Andaluz, C., & Hogan Jr, C.J. (2013). Brownian dynamics determination of the bipolar steady state charge distribution on spheres and non-spheres in the transition regime. *Journal of Aerosol Science,* **63**, 126-145.

Gopalakrishnan, R., Thajudeen, T., & Hogan, C.J. (2011). Collision Limited Reaction Rates for Arbitrarily Shaped Particles across the Entire Diffusive Knudsen Number Range. *Journal of Chemical Physics,* **135**, 054302.

Gopalakrishnan, R., Thajudeen, T., Ouyang, H., & Hogan Jr, C.J. (2013). The Unipolar Diffusion Charging of Arbitrary Shaped Aerosol Particles. *J. Aerosol. Sci.,* **64**.

Goree, J. (1992). Ion Trapping by a Charged Dust Grain in a Plasma. *Physical Review Letters,* **69**, 277-280.

Goree, J. (1994). Charging of particles in a plasma. *Plasma Sources Sci. Technol.,* **3**, 400-406.

Griffin, J.L., & Loyalka, S.K. (1994). Vapor Condensation on Multiple Spheres and Spheroids in the Near-Continuum Regime. *J. Aerosol. Sci.,* **25**, 1271-1289.

Gunn, R. (1955). The statistical electrification of aerosols by ionic diffusion. *Journal of Colloid Science,* **10**, 107-119.

Gurav, A., Kodas, T., Pluym, T., & Xiong, Y. (1993). Aerosol Processing of Materials. *Aerosol Science and Technology,* **19**, 411-452.

Gutsch, A., Pratsinis, S.E., & Loffler, F. (1995). Agglomerate Structure and Growth-Rate by Trajectory Calculations of Monomer-Cluster Collisions. *J. Aerosol. Sci.,* **26**, 187-199.

Han, B., Shimada, M., Choi, M., & Okuyama, K. (2003). Unipolar charging of nanosized aerosol particles using soft X-ray photoionization. *Aerosol Science and Technology,* **37**, 330-341.

Han, R.J., & Gentry, J.W. (1993). Unipolar diffusional charging of fibrous aerosols—Theory and experiment. *J. Aerosol. Sci.,* **24**, 211-226.

Han, R.J., & Gentry, J.W. (1994). Evolution of Charge-Distributions of Nonspherical Particles undergoing Unipolar Charging. *J. Aerosol. Sci.,* **25**, 499-508.

Han, R.J., Ranade, M.B., & Gentry, J.W. (1991). Rate of Unipolar Charging of Ultrafine Thin Platelets. *Aerosol Science and Technology,* **15**, 184-190.

Hansen, S. (2004). Translational friction coefficients for cylinders of arbitrary axial ratios estimated by Monte Carlo simulation. *Journal of Chemical Physics,* **121**, 9111-9115.

Hansson, H.-C., & Ahlberg, M.S. (1985). Dynamic shape factors of sphere aggregates in an electric field and their dependence on the Knudsen number. *Journal of Aerosol Science,* **16**, 69-79.

Heine, M.C., & Pratsinis, S.E. (2007). Brownian coagulation at high concentration. *Langmuir,* **23**, 9882-9890.

Hernandez-Sierra, A., Alguacil, F.J., & Alonso, M. (2003). Unipolar charging of nanometer aerosol particles in a corona ionizer. *J. Aerosol. Sci.,* **34**, 733-745.

Hogan, C.J., & Fernandez de la Mora, J. (2009). Tandem ion mobility-mass spectrometry (IMS-MS) study of ion evaporation from ionic liquid-acetonitrile nanodrops. *Phys. Chem. Chem. Phys.,* **11**, 8079-8090.

Hoppel, W.A., & Frick, G.M. (1986). Ion-aerosol attachment coefficients and the steady-state charge distribution on aerosols in a bipolar ion environment. *Aerosol Science and Technology,* **5**, 1-21.

Hoppel, W.A., & Frick, G.M. (1990). The Nonequilibrium Character of the Aerosol Charge Distributions Produced by Neutralizes. *Aerosol Science and Technology,* **12**, 471-496.

Horvath, H. (1979). Method for the determination of dynamic shape factors of sphere aggregates by measuring the sedimentation velocity in a capacitor. *Journal of Aerosol Science,* **10**, 309-315.

Huang, D.D., & Seinfeld, J.H. (1990). Fokker-Planck Equation Solution of Aerosol Brownian Coagulation with an Interparticle Potential. *Journal of Colloid and Interface Science,* **139**, 213-237.

Huang, D.D., Seinfeld, J.H., & Marlow, W.H. (1990). Bgk Equation Solution of Coagulation for Large Knudsen Number Aerosols with a Singular Attractive Contact Potential. *Journal of Colloid and Interface Science,* **140**, 258-276.

Huang, D.D., Seinfeld, J.H., & Okuyama, K. (1991). Image Potential between a Charged-Particle and an Uncharged Particle in Aerosol Coagulation Enhancement in All Size Regimes and Interplay with Vanderwaals Forces. *Journal of Colloid and Interface Science,* **141**, 191-198.

Huang, H., Oh, C., & Sorensen, C.M. (1998). Structure factor scaling in aggregating systems. *Physical Review E,* **57**, 875-880.

Hussin, A., Scheibel, H.G., Becker, K.H., & Porstendörfer, J. (1983). Bipolar diffusion charging of aerosol particles—I: experimental results within the diameter range 4–30 nm. *J. Aerosol. Sci.,* **14**, 671-677.

Hutchinson, I.H., & Patacchini, L. (2007). Computation of the effect of neutral collisions on ion current to a floating sphere in a stationary plasma. *Physics of Plasmas,* **14**.

Hwang, C.O., & Mascagni, M. (2004). Electrical capacitance of the unit cube. *Journal of Applied Physics,* **95**, 3798-3802.

Isella, L., & Drossinos, Y. (2010). Langevin agglomeration of nanoparticles interacting via a central potential. *Physical Review E,* **82**, 011404.

Jackson, J.D. (1975). *Classical Electrodynamics*. John Wiley and Sons, New York.

Jeans, J. (1925). *Mathematical Theory of Electricity and Magnetism*. Cambridge University Press, Cambridge.

Jeans, J. (1954). *The Dynamical Theory of Gases*. Dover, New York.

Jiang, J.K., Hogan, C.J., Chen, D.R., & Biswas, P. (2007). Aerosol charging and capture in the nanoparticle size range (6-15 nm) by direct photoionization and diffusion mechanisms. *Journal of Applied Physics,* **102**, 034904.

Jung, H., & Kittelson, D.B. (2005). Characterization of Aerosol Surface Instruments in Transition Regime. *Aerosol Science and Technology,* **39**, 902-911.

Kasper, G. (1982). Dynamics and Measurement of Smokes. II The Aerodynamic Diameter of Chain Aggregates in the Transition Regime. *Aerosol Science and Technology,* **1**, 201-215.

Kasper, G., & Shaw, D.T. (1982). Comparative Size Distribution Measurements on Chain Aggregates. *Aerosol Science and Technology,* **2**, 369-381.

Kasper, G., & Shaw, D.T. (1983). Comparative Size Distribution Measurements on Chain Aggregates. *Aerosol Science and Technology,* **2**, 369-381.

Keefe, D. (1959). Charge equilibrium in aerosols according to the Boltzmann law. *Proceedings of the Royal Irish Academy. Section A, Mathematical, astronomical, and physical science,* **60**, 27-45.

Khrapak, S., & Morfill, G. (2009). Basic Processes in Complex (Dusty) Plasmas: Charging, Interactions, and Ion Drag Force. *Contrib. Plasma Phys.,* **49**, 148-168.

Khrapak, S.A., Morfill, G.E., Khrapak, A.G., & D'Yachkov, L.G. (2006). Charging properties of a dust grain in collisional plasmas. *Physics of Plasmas,* **13**, 052114.

Khrapak, S.A., Ratynskaia, S.V., Zobnin, A.V., Usachev, A.D., Yaroshenko, V.V., Thoma, M.H., Kretschmer, M., Höfner, H., Morfill, G.E., Petrov, O.F., & Fortov, V.E. (2005). Particle charge in the bulk of gas discharges. *Physical Review E,* **72**, 016406.

Kilpatrick, W.D. (1971). An experimental mass-mobility relation for ions in air at atmospheric pressure. *Proceedings of the 19th Annual Conference on Mass Spectroscopy*.

Kim, D.S., Park, S.H., Song, Y.M., Kim, D.H., & Lee, K.W. (2003). Brownian coagulation of polydisperse aerosols in the transition regime. *J. Aerosol. Sci.,* **34**, 859-868.

Kim, I.C., & Torquato, S. (1991). 1st-Passage-Time Calculation of the Conductivity of Continuum Models of Multiphase Composites. *Phys Rev A,* **43**, 3198-3201.

Kim, J.H., Mulholland, G., Kukuck, S.R., & Pui, D.Y.H. (2005). Slip Correction Measurements of Certified PSL Nanoparticles Using a Nanometer Differential Mobility Analyzer (Nano-DMA) for Knudsen Number From 0.5 to 83. *J. Res. Natl. Inst. Stand. Technol.,* **110**, 31-54.

Kim, S.H., Mulholland, G.W., & Zachariah, M.R. (2007). Understanding ion-mobility and transport properties of aerosol nanowires. *Journal of Aerosol Science,* **38**, 823-842.

Kirsch, A.A., & Zagnitko, A.V. (1981). Diffusion Charging of Submicrometer Aerosol-Particles by Unipolar Ions. *Journal of Colloid and Interface Science,* **80**, 111-117.

Klein, G. (1952). Mean First-Passage Times of Brownian Motion and Related Problems. *Proceedings of the Royal Society of London- Series A,* **211**, 431-443.

Knutson, E.O., & Whitby, K.T. (1975a). Accurate measurement of aerosol electric mobility moments. *J. Aerosol. Sci.,* **6**, 453-460.

Knutson, E.O., & Whitby, K.T. (1975b). Aerosol classification by electric mobility: apparatus, theory, and applications. *Journal of Aerosol Science,* **6**, 443-451.

Kojima, H. (1978). Measurements of equilibrium charge distribution on aerosols in bipolar ionic atmosphere. *Atmospheric Environment (1967),* **12**, 2363-2368.

Kortshagen, U., & Bhandarkar, U. (1999). Modeling of particulate coagulation in low pressure plasmas. *Physical Review E,* **60**, 887-898.

Kousaka, Y., Endo, Y., Ichitsubo, H., & Alonso, M. (1996). Orientation-specific dynamic shape factors for doublets and triplets of spheres in the transition regime. *Aerosol Science and Technology,* **24**, 36-44.

Koylu, U.O., Xing, Y.C., & Rosner, D.E. (1995). Fractal morphology analysis of combustion-generated aggregates using angular light scattering and electron microscope images. *Langmuir,* **11**, 4848-4854.

Ku, B.K. (2010). Determination of the ratio of diffusion charging-based surface area to geometric surface area for spherical particles in the size range of 100–900 nm. *Journal of Aerosol Science,* **41**, 835-847.

Ku, B.K., & de la Mora, J.F. (2009). Relation between Electrical Mobility, Mass, and Size for Nanodrops 1-6.5 nm in Diameter in Air. *Aerosol Science and Technology,* **43**, 241-249.

Ku, B.K., Deye, G.J., Kulkarni, P., & Baron, P.A. (2011). Bipolar diffusion charging of high-aspect ratio aerosols. *Journal of Electrostatics,* **69**, 641-647.

Kuang, C., McMurry, P.H., & McCormick, A.V. (2009a). Determination of cloud condensation nuclei production from measured new particle formation events. *Geophys Res Lett,* **36**, -.

Kuang, C., McMurry, P.H., & McCormick, A.V. (2009b). Determination of cloud condensation nuclei production from measured new particle formation events. *Geophys Res Lett,* **36**, L09822.

Kulkarni, P., Deye, G.J., & Baron, P.A. (2009). Bipolar diffusion charging characteristics of single-wall carbon nanotube aerosol particles. *J. Aerosol. Sci.,* **40**, 164-179.

Kulkarni, P., & Wang, J. (2006). New fast integrated mobility spectrometer for real-time measurement of aerosol size distribution - I: Concept and theory. *J. Aerosol. Sci.,* **37**, 1303-1325.

Laframboise, J.G., & Chang, J.-S. (1977). Theory of charge deposition on charged aerosol particles of arbitrary shape. *J. Aerosol. Sci.,* **8**, 331-338.

Lall, A.A., & Friedlander, S.K. (2006). On-line measurement of ultrafine aggregate surface area and volume distributions by electrical mobility analysis: I. Theoretical analysis. *Journal of Aerosol Science,* **37**, 260-271.

Larriba, C., & Hogan, C.J. (2013). Ion Mobilities in Diatomic Gases: Measurement versus Prediction with Non-Specular Scattering Models. *The Journal of Physical Chemistry A,* **117**, 3887-3901.

Larriba, C., Hogan, C.J., Attoui, M., Borrajo, R., Fernandez-Garcia, J., & Fernandez de la Mora, J. (2011). The Mobility-Volume Relationship below 3.0 nm examined by

Tandem Mobility-Mass Measurement. *Aerosol Science and Technology,* **45**, 453-467.
Lawless, P.A. (1996). Particle charging bounds, symmetry relations, and an analytic charging rate model for the continuum regime. *J. Aerosol. Sci.,* **27**, 191-215.
Lee, M.H., Cho, K., Shah, A.P., & Biswas, P. (2005). Nanostructured sorbents for capture of cadmium species in combustion environments. *Environmental Science & Technology,* **39**, 8481-8489.
Lee, T.G., Biswas, P., & Hedrick, E. (2001). Comparison of Hg-0 capture efficiencies of three in situ generated sorbents. *Aiche Journal,* **47**, 954-961.
Lee, T.G., Biswas, P., & Hedrick, E. (2004). Overall kinetics of heterogeneous elemental mercury reactions on TiO2 sorbent particles with UV irradiation. *Industrial & Engineering Chemistry Research,* **43**, 1411-1417.
Li, M., Mulholland, G.W., & Zachariah, M.R. (2012). The Effect of Orientation on the Mobility and Dynamic Shape Factor of Charged Axially Symmetric Particles in an Electric Field. *Aerosol Science and Technology,* **46**, 1035-1044.
Li, W., & Davis, E.J. (1996). Aerosol Evaporation in the Transition Regime. *Aerosol Science and Technology,* **25**, 11-21.
Li, Z., & Wang, H. (2003). Drag force, diffusion coefficient, and electric mobility of small particles. I. Theory applicable to the free-molecule regime. *Phys Rev E,* **68**, 061206.
Liu, B.Y.H., & Pui, D.Y.H. (1974). Equilibrium bipolar charge distribution of aerosols. *Journal of Colloid and Interface Science,* **49**, 305-312.
Liu, B.Y.H., & Pui, D.Y.H. (1977). On unipolar diffusion charging of aerosols in the continuum regime. *Journal of Colloid and Interface Science,* **58**, 142-149.
López-Yglesias, X., & Flagan, R.C. (2013). Ion–Aerosol Flux Coefficients and the Steady-State Charge Distribution of Aerosols in a Bipolar Ion Environment. *Aerosol Science and Technology,* **47**, 688-704.
Lòpez-Yglesias, X., & Flagan, R.C. (2013). Population Balances of Micron-Sized Aerosols in a Bipolar Ion Environment. *Aerosol Science and Technology,* **47**, 681-687.
Loyalka, S.K. (1973). Condensation on a spherical droplet. *J Chem. Physics,* **58**, 354.
Loyalka, S.K. (1976). Brownian Coagulation of Aerosols. *Journal of Colloid and Interface Science,* **57**, 578-579.
Loyalka, S.K. (1982). Condensation on a spherical droplet, II. *Journal of Colloid and Interface Science,* **87**, 216.
Loyalka, S.K., & Griffin, J.L. (1993). Condensation on Nonspherical Aerosol-Particles - Numerical Solutions in the Continuum Regime. *Nuclear Science and Engineering,* **114**, 135-140.
Lushnikov, A.A., & Kulmala, M. (2004a). Charging of aerosol particles in the near free-molecule regime. *Eur Phys J D,* **29**, 345-355.
Lushnikov, A.A., & Kulmala, M. (2004b). Flux-matching theory of particle charging. *Physical Review E,* **70**, 046413.
Lushnikov, A.A., & Kulmala, M. (2005). A kinetic theory of particle charging in the free-molecule regime. *J. Aerosol. Sci.,* **36**, 1069-1088.

Madler, L., Lall, A.A., & Friedlander, S.K. (2006). One-step aerosol synthesis of nanoparticle agglomerate films: simulation of film porosity and thickness. *Nanotechnology,* **17**, 4783-4795.

Maisels, A., Kruis, F.E., & Fissan, H. (2002). Determination of coagulation coefficients and aggregation kinetics for charged aerosols. *Journal of Colloid and Interface Science,* **255**, 332-340.

Makela, J.M., Riihela, M., Ukkonen, A., Jokinen, V., & Keskinen, J. (1996). Comparison of mobility equivalent diameter with Kelvin-Thomson diameter using ion mobility data. *Journal of Chemical Physics,* **105**, 1562-1571.

Mangolini, L., & Kortshagen, U. (2009). Selective nanoparticle heating: Another form of nonequilibrium in dusty plasmas. *Physical Review E,* **79**.

Mangolini, L., Thimsen, E., & Kortshagen, U. (2005). High-yield plasma synthesis of luminescent silicon nanocrystals. *Nano Letters,* **5**, 655-659.

Maricq, M.M. (2008). Bipolar Diffusion Charging of Soot Aggregates. *Aerosol Science and Technology,* **42**, 247-254.

Marlow, W.H. (1978). Unipolar Aerosol Diffusion Charging .1. Particle Dielectric-Constant and Ion Mobility Distribution Effects. *Journal of Colloid and Interface Science,* **64**, 543-548.

Marlow, W.H. (1980a). Derivation of Aerosol Collision Rates for Singular Attractive Contact Potentials. *Journal of Chemical Physics,* **73**, 6284-6287.

Marlow, W.H. (1980b). Lifshitz-Vanderwaals Forces in Aerosol-Particle Collisions .1. Introduction - Water Droplets. *Journal of Chemical Physics,* **73**, 6288-6295.

Marlow, W.H., & Brock, J.R. (1975a). Calculations of Bipolar Charging of Aerosols. *Journal of Colloid and Interface Science,* **51**, 23-31.

Marlow, W.H., & Brock, J.R. (1975b). Unipolar Charging of Small Aerosol-Particles. *Journal of Colloid and Interface Science,* **50**, 32-38.

Matsoukas, T. (1997). The coagulation rate of charged aerosols in ionized gases. *Journal of Colloid and Interface Science,* **187**, 474-483.

Matsoukas, T., & Russell, M. (1997). Fokker-Planck description of particle charging in ionized gases. *Physical Review E,* **55**, 991-994.

Matsoukas, T., Russell, M., & Smith, M. (1996). Stochastic charge fluctuations in dusty plasmas. *Journal of Vacuum Science & Technology a-Vacuum Surfaces and Films,* **14**, 624-630.

Mayya, Y.S. (1990a). Theory of diffusion charging of fractal aerosol aggregates. *Journal of Colloid and Interface Science,* **140**, 185-191.

Mayya, Y.S. (1990b). Theory of Diffusion Charging of Fractal Aerosol Aggregates. *Journal of Colloid and Interface Science,* **140**, 185-191.

Meredith, M.J., Ouyang, H., Larriba-Andaluz, C., & Hogan, C.J. (In Prep.).

Meredith, M.J., Ouyang, H., Larriba, C., Oberreit, D., & Hogan, C.J. (In Prep.). *In Prep.*

Michael, M., Tripathi, S.N., Arya, P., Coates, A., Wellbrock, A., & Young, D.T. (2011). High-altitude charged aerosols in the atmosphere of Titan. *Planet Space Sci.,* **59**, 880-885.

Miller, A., Frey, G., King, G., & Sunderman, C. (2010). A Handheld Electrostatic Precipitator for Sampling Airborne Particles and Nanoparticles. *Aerosol Science and Technology,* **44**, 417-427.

Millikan, R.A. (1923). The General Law of Fall of a Small Spherical Body through a Gas, and its Bearing upon the Nature of Molecular Reflection from Surfaces. *Physical Review,* **22**, 1-23.

Mohnen, V.A. (1977). Formation, Nature and Mobility of Ions of Atmospheric Importance. *Electrical Processes in Atmospheres*, 1-17.

Mott-Smith, H.M., & Langmuir, I. (1926). The Theory of Collectors in Gaseous Discharges. *Physical Review,* **28**, 727-763.

Narsimhan, G., & Ruckenstein, E. (1985). Monte-Carlo Simulation of Brownian Coagulation over the Entire Range of Particle Sizes from near Molecular to Colloidal - Connection between Collision Efficiency and Interparticle Forces. *Journal of Colloid and Interface Science,* **107**, 174-193.

Natanson, G. (1960a). *Zh. Tech. Fiz.,* **30**, 573-588.

Natanson, G. (1960b). On the theory of charging of amicroscopic aerosol particles resulting from the capture of gaseous ions. *Soviet Physics Technical Physics,* **5**, 538-551.

Nolan, P.J., & Kennan, E.L. (1949). Condensation nuclei from hot platinum: size, coagulation coefficient and charge-distribution. *Proceedings of the Royal Irish Academy, Section A (Mathematical, Astronomical and Physical Science)* **52**, 171-190.

Northrup, S.H., Allison, S.A., & McCammon, J.A. (1984). Brownian Dynamics Simulation of Diffusion-Influenced Bimolecular Reactions. *Journal of Chemical Physics,* **80**, 1517-1526.

Northrup, S.H., Curvin, M.S., Allison, S.A., & Mccammon, J.A. (1986). Optimization of Brownian Dynamics Methods for Diffusion-Influenced Rate-Constant Calculations. *Journal of Chemical Physics,* **84**, 2196-2203.

Nowakowski, B., & Sitarski, M. (1981). Brownian coagulation of aerosol particles by Monte Carlo simulation. *Journal of Colloid and Interface Science,* **83**, 614-622.

Ntziachristos, L., Giechaskiel, B., Ristimäki, J., & Keskinen, J. (2004). Use of a corona charger for the characterisation of automotive exhaust aerosol. *J. Aerosol. Sci.,* **35**, 943-963.

Oh, H., Park, H., & Kim, S. (2004). Effects of Particle Shape on the Unipolar Diffusion Charging of Nonspherical Particles. *Aerosol Science and Technology,* **38**, 1045-1053.

Olfert, J.S., Kulkarni, P., & Wang, J. (2008). Measuring aerosol size distributions with the fast integrated mobility spectrometer. *J. Aerosol. Sci.,* **39**, 940-956.

Ouyang, H., Gopalakrishnan, R., & Christopher J. Hogan, J. (2012). Nanoparticle collisions in the gas phase in the presence of singular contact potentials. *The Journal of Chemical Physics,* **137**, 064316.

Pich, J. (1969). The drag of a cylinder in the transition region. *J Colloid Interf Sci,* **29**, 91-96.

Pollak, L.W., & Metnieks, A.L. (1962). On the validity of Boltzmann's distribution law for the charges of aerosol particles in electrical equilibrium. *Geofisica Pura e Applicata,* **53**, 111-132.

Porstendörfer, J., Hussin, A., Scheibel, H.G., & Becker, K.H. (1984). Bipolar diffusion charging of aerosol particles—II. Influence of the concentration ratio of positive

and negative ions on the charge distribution. *Journal of Aerosol Science,* **15**, 47-56.

Porstendorfer, J., Robig, G., & Ahmed, A. (1979a). Experimental-Determination of the Attachment Coefficients of Atoms and Ions on Monodisperse Aerosols. *Journal of Aerosol Science,* **10**, 21-28.

Porstendorfer, J., Robig, G., & Ahmed, A. (1979b). Experimental Determination of the Attachment Coefficients of Atoms and Ions on Monodisperse Aerosols. *J. Aerosol. Sci.,* **10**, 21-28.

Potter, M.J., Luty, B., Zhou, H.X., & McCammon, J.A. (1996). Time-dependent rate coefficients from Brownian dynamics simulations. *Journal of Physical Chemistry,* **100**, 5149-5154.

Pratsinis, S.E. (1998). Flame aerosol synthesis of ceramic powders. *Progress in Energy and Combustion Science,* **24**, 197-219.

Pratsinis, S.E. (2010). Aerosol-based Technologies in Nanoscale Manufacturing: from Functional Materials to Devices through Core Chemical Engineering. *Aiche Journal,* **56**, 3028-3035.

Premnath, V., Oberreit, D., & Hogan, C.J. (2011). Collision Based Ionization: On the Limit Between Diffusion Charging and Chemical Ionization. *Aerosol Science and Technology,* **45**, 712-726.

Pui, D.Y.H., Fruin, S., & McMurry, P.H. (1988). Unipolar Diffusion Charging of Ultrafine Aerosols. *Aerosol Science and Technology,* **8**, 173-187.

Qi, C., Chen, D.-R., & Pui, D.Y.H. (2007). Experimental study of a new corona-based unipolar aerosol charger. *J. Aerosol. Sci.,* **38**, 775-792.

Rader, D.J. (1985). *Application of the Tandem Differential Mobility Analyzer to Studies of Droplet Evaporation and Growth.* University of Minnesota, Minneapolis, MN.

Rader, D.J. (1990). Momentum slip correction factor for small particles in nine common gases. *Journal of Aerosol Science,* **21**, 161-168.

Ravi, L., & Girshick, S.L. (2009). Coagulation of nanoparticles in a plasma. *Physical Review E,* **79**, 026408.

Ray, A.K., Davis, E.J., & Ravindran, P. (1979). Determination of Ultra-Low Vapor Pressures by Submicron Droplet Evaporation. *Journal of Chemical Physics,* **71**, 582.

Reischl, G.P., Mäkelä, J.M., Karch, R., & Necid, J. (1996). Bipolar charging of ultrafine particles in the size range below 10 nm. *Journal of Aerosol Science,* **27**, 931-949.

Reischl, G.P., Scheibel, H.G., & Porstendörfer, J. (1983). The bipolar charging of aerosols: Experimental results in the size range below 20-nm particle diameter. *Journal of Colloid and Interface Science,* **91**, 272-275.

Rogak, S.N., Baltensperger, U., & Flagan, R.C. (1991). Measurement of Mass-Transfer to Agglomerate Aerosols. *Aerosol Science and Technology,* **14**, 447-458.

Rogak, S.N., & Flagan, R.C. (1990). Stokes Drag on Self-Similar Clusters of Spheres. *J Colloid Interf Sci,* **134**, 206-218.

Rogak, S.N., & Flagan, R.C. (1992a). Bipolar diffusion charging of spheres and agglomerate aerosol particles. *J. Aerosol. Sci.,* **23**, 693-710.

Rogak, S.N., & Flagan, R.C. (1992b). Coagulation of Aerosol Agglomerates in the Transition Regime. *Journal of Colloid and Interface Science,* **151**, 203-224.

Rogak, S.N., Flagan, R.C., & Nguyen, H.V. (1993). The Mobility and Structure of Aerosol Agglomerates. *Aerosol Science and Technology,* **18**, 25-47.

Romay, F.J., & Pui, D.Y.H. (1992). On the Combination Coefficient of Positive ions with Ultrafine Neutral Particles in the Transition and Free-molecule Regimes. *Aerosol Science and Technology,* **17**, 134-147.

Romay, F.J., Pui, D.Y.H., & Adachi, M. (1991). Unipolar Diffusion Charging of Aerosol Particles at Low Pressure. *Aerosol Science and Technology,* **15**, 60-68.

Rubinstein, J., & Torquato, S. (1988). Diffusion-Controlled Reactions - Mathematical Formulation, Variational-Principles, and Rigorous Bounds. *J Chem Phys,* **88**, 6372-6380.

Rus, J., Moro, D., Sillero, J.A., Royuela, J., Casado, A., Estevez-Molinero, F., & Fernandez de la Mora, J. (2010). IMS–MS studies based on coupling a differential mobility analyzer (DMA) to commercial API–MS systems. *International Journal of Mass Spectrometry,* **298**, 30-40.

Sahni, D.C. (1966). The Effect of a Black Sphere on the Flux Distribution in an Infinite Moderator. *Journal of Nuclear Energy,* **20**, 915.

Sahni, D.C. (1983). An Exact Solution of Fokker-Planck Equation and Brownian Coagulation in the Transition Regime. *Journal of Colloid and Interface Science,* **91**, 418-429.

Sceats, M.G. (1989). Brownian Coagulation in Aerosols- The Role of Long Range Forces. *Journal of Colloid and Interface Science,* **129**, 105-112.

Schweigert, V.A., & Schweigert, I.V. (1996). Coagulation in a low-temperature plasma. *Journal of Physics D: Applied Physics,* **29**, 655-659.

Seaver, A.E. (1984). Closed Form Equations for the Evaporation Rate and Droplet Size of Knudsen Droplets. *Aerosol Science and Technology,* **3**, 177.

Shimada, M., Han, B.W., Okuyama, K., & Otani, Y. (2002). Bipolar charging of aerosol nanoparticles by a soft X-ray photoionizer. *J Chem Eng Jpn,* **35**, 786-793.

Shin, W.G., Mulholland, G.W., & Pui, D.Y.H. (2010). Determination of volume, scaling exponents, and particle alignment of nanoparticle agglomerates using tandem differential mobility analyzers. *Journal of Aerosol Science,* **41**, 665-681.

Shon, S.-N., Kasper, G., & Shaw, D.T. (1980). An experimental study of Brownian coagulation in the transition regime. *Journal of Colloid and Interface Science,* **73**, 233-243.

Sitarski, M., & Nowakowski, B. (1979). Condensation rate of a trace vapor on Knudsen aerosol from the solution of the Boltzmann equation. *J Colloid Int Sci,* **72**, 113-122.

Sitarski, M., & Seinfeld, J.H. (1977). Brownian Coagulation in the Transition Regime. *Journal of Colloid and Interface Science,* **61**, 261-271.

Song, D.K., Lenggoro, I.W., Hayashi, Y., Okuyama, K., & Kim, S.S. (2005). Changes in the shape and mobility of colloidal gold nanorods with electrospray and differential mobility analyzer methods. *Langmuir,* **21**, 10375-10382.

Sorensen, C.M. (2011). The Mobility of Fractal Aggregates: A Review. *Aerosol Science and Technology,* **45**, 765-779.

Spicer, P.T., Artelt, C., Sanders, S., & Pratsinis, S.E. (1998). Flame synthesis of composite carbon black-fumed silica nanostructured particles. *J. Aerosol. Sci.,* **29**, 647-659.

Steiner, G., & Reischl, G.P. (2012). The effect of carrier gas contaminants on the charging probability of aerosols under bipolar charging conditions. *Journal of Aerosol Science,* **54**, 21-31.

Stober, J., Schleicher, B., & Burtscher, H. (1991). Bipolar Diffusion Charging of Particles in Noble Gases. *Aerosol Science and Technology,* **14**, 66-73.

Stolzenburg, M.R., & Mcmurry, P.H. (1991). An Ultrafine Aerosol Condensation Nucleus Counter. *Aerosol Science and Technology,* **14**, 48-65.

Stolzenburg, M.R., & McMurry, P.H. (2008). Equations governing single and tandem DMA configurations and a new lognormal approximation to the transfer function. *Aerosol Science and Technology,* **42**, 421-432.

Swihart, M.T. (2003). Vapor-phase synthesis of nanoparticles. *Curr. Opin. Colloid Interface Sci.,* **8**, 127-133.

Szymanski, W.W., Majerowicz, A., & Wagner, P.E. (1989). Measurement of Brownian coagulation in monodispersed and bidispersed liquid aerosols. *Aerosol Science and Technology,* **11**, 1-10.

Takata, S., Sone, Y., Lhuillier, D., & Wakabayashi, M. (1998). Evaporation from or condensation onto a sphere: Numerical analysis of the Boltzmann equation for hard-sphere molecules. *Computers & Mathematics with Applications,* **35**, 193-214.

Tandon, P., & Rosner, D.E. (1999). Monte Carlo simulation of particle aggregation and simultaneous restructuring. *Journal of Colloid and Interface Science,* **213**, 273-286.

Thajudeen, T., Gopalakrishnan, R., & Hogan, C.J. (2012). The Collision Rate of Non-spherical Particles and Aggregates for all Diffusive Knudsen Numbers. *Aerosol Science and Technology,* **46**.

Torquato, S., & Avellaneda, M. (1991). Diffusion and Reaction in Heterogeneous Media - Pore-Size Distribution, Relaxation-Times, and Mean Survival-Time. *J Chem Phys,* **95**, 6477-6489.

Trzeciak, T.M., Podgorski, A., & Marijnissen, J.C.M. (2004). Langevin dynamics simulation of aerosol coagulation in highly concentrated systems. *Inzynieria Chemiczna I Procesowa,* **25**, 1741-1746.

Ude, S., & de la Mora, J.F. (2005). Molecular monodisperse mobility and mass standards from electrosprays of tetra-alkyl ammonium halides. *Journal of Aerosol Science,* **36**, 1224-1237.

Unger, L., Boulaud, D., & Borra, J.P. (2004). Unipolar field charging of particles by electrical discharge: effect of particle shape. *Journal of Aerosol Science,* **35**, 965-979.

Unrau, C.J., & Axelbaum, R.L. (2010). Gas-phase synthesis of single-walled carbon nanotubes on catalysts producing high yield. *Carbon,* **48**, 1418-1424.

Unrau, C.J., Axelbaum, R.L., Biswas, P., & Fraundorf, P. (2007a). Online size characterization of nanofibers and nanotubes. *Molecular Building Blocks for*

Nanotechnology: From Diamondoids to Nanoscale Materials and Applications, **109**, 212-245.

Unrau, C.J., Axelbaum, R.L., Biswas, P., & Fraundorf, P. (2007b). Synthesis of single-walled carbon nanotubes in oxy-fuel inverse diffusion flames with online diagnostics. *Proceedings of the Combustion Institute,* **31**, 1865-1872.

Vainshtein, P., & Shapiro, M. (2005). Mobility of permeable fractal agglomerates in slip regime. *J Colloid Interf Sci,* **284**, 501-509.

Verlet, L. (1967). Computer "Experiments" on Classical Fluids. I. Thermodynamical Properties of Lennard-Jones Molecules. *Physical Review,* **159**, 98-103.

Veshchunov, M.S. (2010). A new approach to the Brownian coagulation theory. *J. Aerosol. Sci.,* **41**, 895-910.

Veshchunov, M.S. (2011). A new approach to diffusion-limited reaction rate theory. *Journal of Engineering Thermophysics,* **20**, 260-271.

Vincenti, W.G., & Kruger, C.H. (1975). *Introduction to Physical Gas Dynamics*. Krieger, Huntington, NY.

Wagner, P.E., & Kerker, M. (1977). Brownian coagulation of aerosols in rarified gases. *Journal of Chemical Physics,* **66**, 638-646.

Wang, S.C., & Flagan, R.C. (1990). Scanning Electrical Mobility Spectrometer. *Aerosol Science and Technology,* **13**, 230-240.

Warthesen, S.J., & Girshick, S.L. (2007). Numerical simulation of the spatiotemporal evolution of a nanoparticle-plasma system. *Plasma Chemistry and Plasma Processing,* **27**, 292-310.

Wellisch, E.M. (1909). The Mobilities of the Ions Produced by Rontgen Rays in Gases and Vapours. *Philosophical Transactions of the Royal Society of London. Series A, Containing Papers of a Mathematical or Physical Character,* **209**, 249-279.

Wen, H.Y., & Kasper, G. (1984). Dynamics and Measurement of Smokes .3. Drag and Orientation of Chain Aggregates in an Electrical Mobility Spectrometer. *Aerosol Science and Technology,* **3**, 397-403.

Wen, H.Y., Reischl, G.P., & Kasper, G. (1984a). Bipolar Diffusion Charging of Fibrous Aerosol-Particles .1. Charging Theory. *J. Aerosol. Sci.,* **15**, 89-101.

Wen, H.Y., Reischl, G.P., & Kasper, G. (1984b). Bipolar Diffusion Charging of Fibrous Aerosol-Particles .2. Charge and Electrical Mobility Measurements on Linear-Chain Aggregates. *J. Aerosol. Sci.,* **15**, 103-122.

Wiedensohler, A. (1988). An Approximation of the Bipolar Charge-Distribution for Particles in the Sub-Micron Size Range. *J. Aerosol. Sci.,* **19**, 387-389.

Wiedensohler, A., Büscher, P., Hansson, H.C., Martinsson, B.G., Stratmann, F., Ferron, G., & Busch, B. (1994). A novel unipolar charger for ultrafine aerosol particles with minimal particle losses. *J. Aerosol. Sci.,* **25**, 639-649.

Wiedensohler, A., & Fissan, H.J. (1988). AEROSOL CHARGING IN HIGH-PURITY GASES. *J. Aerosol. Sci.,* **19**, 867-870.

Wiedensohler, A., & Fissan, H.J. (1990). Bipolar Ion and Electron-Diffusion Charging of Aerosol-Particles in High-Purity Argon and Nitrogen. *Particle & Particle Systems Characterization,* **7**, 250-255.

Wiedensohler, A., & Fissan, H.J. (1991). Bipolar Charge-Distributions of Aerosol-Particles in High-Purity Argon and Nitrogen. *Aerosol Science and Technology,* **14**, 358-364.

Wiedensohler, A., Lutkemeier, E., Feldpausch, M., & Helsper, C. (1986). Investigation of the Bipolar Charge-Distribution at Various Gas Conditions. *Journal of Aerosol Science,* **17**, 413-416.

Wright, P.G. (1960). On the Discontinuity Involved in Diffusion Across an Interface (The Delta of Fuchs). *Discussions of the Faraday Society,* **30**, 100-112.

Xiao, K., Swanson, J.J., Pui, D.Y.H., & Kittelson, D.B. (2012). Bipolar Diffusion Charging of Aggregates. *Aerosol Science and Technology,* **46**, 794-803.

Yu, P.Y., Wang, C.C., & Gentry, J.W. (1987). Experimental measurement of the rate of unipolar charging of actinolite fibers. *J. Aerosol. Sci.,* **18**, 73-85.

Zelenyuk, A., Cai, Y., & Imre, D. (2006). From Agglomerates of Spheres to Irregularly Shaped Particles: Determination of Dynamic Shape Factors from Measurements of Mobility and Vacuum Aerodynamic Diameters. *Aerosol Science and Technology,* **40**, 197-217.

Zelenyuk, A., & Imre, D. (2007). On the Effect of Particle Alignment in the DMA. *Aerosol Science and Technology,* **41**, 112-124.

Zhang, C., Thajudeen, T., Larriba, C., Schwartzentruber, T.E., & Hogan, C.J. (2012). Determination of the Scalar Friction Factor for Nonspherical Particles and Aggregates Across the Entire Knudsen Number Range by Direct Simulation Monte Carlo (DSMC). *Aerosol Science and Technology,* **46**, 1065-1078.

Zhang, Y., Li, S., Yan, W., Yao, Q., & Tse, D. (2011). Role of dipole-dipole interaction on enhancing Brownian coagulation of charge-neutral nanoparticles in the free molecular regime. *The Journal of Chemical Physics,* **134**, 084501.

Zhou, H.X. (1995). Calculation of translational friction and intrinsic viscosity .1. General formulation for arbitrarily shaped particles. *Biophys. J.,* **69**, 2286-2297.

Zhou, H.X., Szabo, A., Douglas, J.F., & Hubbard, J.B. (1994). A Brownian Dynamics Algorithm for Calculating the Hydrodynamic Friction and the Electrostatic Capacitance of an Arbitrarily-Shaped Object. *J Chem Phys,* **100**, 3821-3826.

Zobnin, A.V., Usachev, A.D., Petrov, O.F., & Fortov, V.E. (2008). Ion current on a small spherical attractive probe in a weakly ionized plasma with ion-neutral collisions (kinetic approach). *Physics of Plasmas,* **15**.

Appendix A: Fortran Codes developed for Brownian Dynamics Simulations

This section contains titles of the computer programs used to perform various simulations for this thesis. Source codes with detailed instruction files for compilation and execution are made available on a DVD accompanying this thesis and free of cost public access through Google© drive (https://drive.google.com/folderview?id=0B-sJpKnVrC80UzNDV3lkM28ycTQ&usp=sharing)

Code F1: Program to calculate Mean First Passage Times for collisions between a point mass and an aggregate composed of point contacting spheres. This code was used to derive dimensionless collision kernels for vapor condensation onto spherical particles (single entity calculations, chapter 2) and aggregates (chapter 3) for hard sphere interactions.

Code F2: Program to calculate Mean First Passage Times for collisions between two finite sized spherical particles. This code was used to derive dimensionless collision kernels for coagulation of spherical aerosol particles for hard sphere interactions, also referred to as two entity calculations (chapter 2).

Code F3: Program to calculate Mean First Passage Times for collisions between a point mass and a sphere considering attractive Coulombic potential interaction (chapter 4).

Code F4: Program to calculate Mean First Passage Times for collisions between a point mass and an aggregate composed of point contacting spheres considering combined Coulombic and image potential interactions (chapter 5).

Code F5: Program to calculate continuum enhancement factor for collisions between a point mass and an aggregate composed of point contacting spheres considering combined Coulombic and image potential interactions (chapter 5).

Code F6: Program to calculate free molecular enhancement factor for collisions between a point mass and an aggregate composed of point contacting spheres considering combined Coulombic and image potential interactions (chapter 5).

Code F7: Program to calculate steady state charge distribution of spherical particles exposed to bipolar ions of arbitrary mass-mobility distributions considering combined Coulombic and image potential interactions (chapter 6).

Code F8: Program to calculate steady state charge distribution of an aggregate composed of point contacting spheres exposed to bipolar ions of arbitrary mass-mobility distributions considering combined Coulombic and image potential interactions (chapter 6).

Code F9: Program to calculate steady state charge distribution of cylindrical particles exposed to bipolar ions of arbitrary mass-mobility distributions considering combined Coulombic and image potential interactions (chapter 6).

Code F10: Program to simulate experimental charging distribution measurements by tandem differential mobility using Brownian Dynamics for spherical particles exposed to bipolar ions of arbitrary mass-mobility distributions considering combined Coulombic and image potential interactions (chapter 8).

Code F11: Program to simulate experimental charging distribution measurements by tandem differential mobility using Brownian Dynamics for cylindrical particles exposed to bipolar ions of arbitrary mass-mobility distributions considering combined Coulombic and image potential interactions (chapter 8).

Appendix B: Details of Brownian Dynamics and Molecular Dynamics Simulations

INFORMATION AVAILABLE

In this section, the information available includes:

1. Determination of the force experienced by an ion in trajectory calculations.
2. Brownian dynamics (BD) calculations in the continuum regime
3. Molecular dynamics (MD) calculations in the free molecular regime
4. BD calculations in the transition regime.
5. Tabulated values of $\boldsymbol{\eta_c}$ and $\boldsymbol{\eta_f}$ as a function of $\boldsymbol{\psi_E}$and $\boldsymbol{\psi_I}$.

Please note that all parameters not defined here are defined in the main text.

1. The Force experienced by Ion

The potential energy of the ion in the presence of an aggregate, normalized by the thermal energy of the ion $\boldsymbol{kT}$, as noted in the main text, is given as:

$$\frac{\varphi(\vec{r}^*)}{kT} = \frac{R_s}{a}\left\{-\psi_E \sum_{j=1}^{N} \frac{(z_{p(j)}/z_p)}{|\vec{r}^* - \vec{r}^*_{p(j)}|} - \psi_I \sum_{g=1}^{3} \sum_{l=1}^{I_g} \left\{\frac{(-1)^g}{2|\vec{r}^* - \vec{r}^*_{p(l)}|^2(|\vec{r}^* - \vec{r}^*_{p(l)}|^2 - 1)}\right\}\right\} \quad \text{(S1)}$$

From this expression, the force on the ion at any point in space outside the aggregate $(\vec{F} = -\nabla\varphi)$ is calculated as:

$$\vec{F}^*(\vec{r}^*) = \frac{a\vec{F}(\vec{r}^*)}{kT} =$$
$$\frac{R_s}{a}\left(-\psi_E \sum_{j=1}^{N} \frac{(z_{p(j)}/z_p)}{|\vec{r}^* - \vec{r}^*_{p(j)}|^3}\left(\vec{r}^* - \vec{r}^*_{p(j)}\right) - \psi_I \sum_{g=1}^{3} \sum_{l=1}^{I_g} \left\{\frac{(-1)^g\left(2|\vec{r}^* - \vec{r}^*_{p(j)}|^2 - 1\right)}{|\vec{r}^* - \vec{r}^*_{p(j)}|^4(|\vec{r}^* - \vec{r}^*_{p(j)}|^2 - 1)^2}\left(\vec{r}^* - \right.\right.\right.$$
$$\boldsymbol{rp(j)*} \quad \text{(S2)}$$

2. Brownian Dynamics Calculations in the Continuum Regime

To determine the continuum regime enhancement factor for a particle, inertialess (massless) ion trajectory calculations are performed, in which an ion is initiated on the surface of a cubical domain (of volume $\boldsymbol{V_{box}}$) with the particle center of mass coinciding with the origin. The particle is assumed to be at rest, and the ion velocity is assumed to relax to the gas molecule velocity instantly. The drag force experienced by the ion, the

potential force of interaction between the particle and ion and the diffusion of the ion are accounted for to obtain an expression for the position as a function of time. The ion position is normalized in terms of the primary sphere radius $\vec{r}^* = \vec{r}/a$ (the choice of a normalizing length for position is arbitrary), the time scale associated with the ion motion is scaled with $f_i R_s^2/kT$, (with dimensionless time denoted as t^*) and the force is obtained using equation (S2). With these choices, the non-dimensional position of the ion as a function of dimensionless time is:

$$\vec{r}^*(t^* + \Delta t^*) = \vec{r}^*(t^*) + \left(\frac{R_s}{a}\right)^2 \vec{F}^*(\psi_E, \psi_I) + \vec{D} \tag{S3a}$$

$$\langle \vec{D} \cdot \vec{D} \rangle = 6\left(\frac{R_s}{a}\right)^2 \Delta t^* \tag{S4b}$$

$\vec{D}$ is a normally distributed random vector, with zero mean and variance given by equation (S3b), to model the diffusion of the ion. At the beginning of each trial, the ion is allowed to move inside the box according to equation (S3a) until impact with the particle. Sufficiently large box sizes (100-2500 times the primary sphere radius) are chosen to simulate the far field conditions for each particle and sufficiently small time steps were used to obtain results in the limit of $\Delta t^* \to 0$. The timestep used for simulation is chosen at each step by an empirical condition involving the instantaneous position $\vec{r}^*$ and the instantaneous force $\vec{F}^*$

$$\Delta t^* = 0.0005 \cdot \min\left(\frac{|\vec{r}^*|^2}{2(R_s/a)}, \frac{1}{(R_s/a)^2|\vec{F}^*|}\right) \tag{S5}$$

Upon collision, the process is reset, and repeated several times and the total time for all collisions is monitored. Periodic boundary conditions are employed on the domain surface, such that if the ion leaves the domain, it re-enters on the opposing face. These periodic boundary conditions are only employed to simplify the computation; more exactly, in BD calculations the motion of the nearest neighbor ion to a particle is examined (neglecting ion-ion interactions, as is justified in the main text). When this ion leaves the domain, it is no longer considered to be the nearest neighbor (it is a new ion in the domain, whose motion is monitored.

The dimensionless mean first passage time is calculated by performing enough trials for statistical accuracy

$$t^*_{mean} = \frac{1}{N_c}\sum_{k=1}^{N_c} t^*_k \tag{S6}$$

Typically, 10000-15000 collisions (N_c) are sufficient to calculate the mean first passage time time to within 1% of the average over the latest 200 collisions. From the mean first passage time, the continuum enhancement factor is calculated directly using the non-dimensional domain volume $V^*_{box} (= V_{box}/a^3)$:

$$\eta_c = \frac{V^*_{box}}{t^*_{mean}} \frac{1}{4\pi} \left(\frac{a}{R_s}\right)^3 \tag{S7}$$

where R_s is the Smoluchowksi radius for the particle under examination.

3. Molecular Dynamics (Ballistic) Trajectory Calculations

To determine the free molecular regime enhancement factor, an ion is initiated at a distance $\boldsymbol{l_o}$ away from a particle (chosen sufficiently large for forces on the ion to be negligible) with velocity directed along the z axis, whose magnitude $\boldsymbol{c_o}$ is sampled randomly from the Maxwell-Boltzmann speed distribution. The starting radial and azimuthal impact parameters of the ion are chosen by randomly choosing a point from a square region of side $\boldsymbol{s_o}$ symmetrical about the z axis and on the plane $\boldsymbol{z = l_o}$ (Figure B1). The ion trajectory is calculated using the velocity-verlet algorithm (Verlet, 1967) taking into account the force experienced by the ion (equation S2) until the ion impacts with the particle or is deemed to have missed the collision and escaped a sufficient distance from the particle (representing infinity):

$$\vec{\boldsymbol{r}}^*(\boldsymbol{t}^* + \Delta\boldsymbol{t}^*) = \vec{\boldsymbol{r}}^*(\boldsymbol{t}^*) + \sqrt{\frac{\boldsymbol{PA}}{\boldsymbol{\pi a^2}}}\vec{\boldsymbol{v}}^*(\boldsymbol{t}^*)\Delta\boldsymbol{t}^* + \frac{\boldsymbol{1}}{\boldsymbol{2}}\frac{\boldsymbol{PA}}{\boldsymbol{\pi a^2}}\vec{\boldsymbol{F}}^*(\vec{\boldsymbol{r}}^*(\boldsymbol{t}^*), \boldsymbol{\psi_E}, \boldsymbol{\psi_I})\Delta\boldsymbol{t}^* \quad \text{(S8a)}$$

$$\vec{\boldsymbol{v}}^*(\boldsymbol{t}^* + \Delta\boldsymbol{t}^*) = \vec{\boldsymbol{v}}^*(\boldsymbol{t}^*) + \frac{\boldsymbol{1}}{\boldsymbol{2}}\sqrt{\frac{\boldsymbol{PA}}{\boldsymbol{\pi a^2}}}\left\{\vec{\boldsymbol{F}}^*(\vec{\boldsymbol{r}}^*(\boldsymbol{t}^*), \boldsymbol{\psi_E}, \boldsymbol{\psi_I}) + \vec{\boldsymbol{F}}^*(\vec{\boldsymbol{r}}^*(\boldsymbol{t}^* + \Delta\boldsymbol{t}^*), \boldsymbol{\psi_E}, \boldsymbol{\psi_I})\right\}\Delta\boldsymbol{t}^* \quad \text{(S8b)}$$

The following choices are made for normalizing the simulation variables: position vector and distances by the primary sphere radius $\boldsymbol{a}$, velocity is scaled by $\sqrt{\boldsymbol{kT/m_i}}$ and the time scale of ion motion is taken as $\sqrt{\boldsymbol{m_i PA/\pi kT}}$. After each trial, the ion is restarted from the starting plane from a new point $(\boldsymbol{b}, \boldsymbol{\theta})$, with the z-component of velocity $\boldsymbol{c_o}$ sampled from the Maxwell-Boltzmann speed distribution and the particle is rotated about the *x*, *y*, and *z* axis in that sequence by uniformly distributed random angles. A large number of trials (typically 20000-30000) are performed so that the distributions are adequately sampled to yield an orientation averaged value of the enhancement factor. For each trial, the outcome of the ion motion (collision with particle or escape to infinity) is noted and the free molecular enhancement is calculated as:

$$\boldsymbol{\eta_f} = \frac{\sum_{i=1}^{M_c} \boldsymbol{c_o}}{\sum_{i=1}^{M_t} \boldsymbol{c_o}} \frac{\boldsymbol{s_o^2}}{\boldsymbol{PA}} \quad \text{(S9)}$$

where M_c is the number of trials resulting in collisions, and M_t is the total number of trials. As was mentioned in the description of the continuum enhancement factor calculations, simulation parameters such as the side $\boldsymbol{s_o}$ of the square region from which ions are launched, the time step $\Delta\boldsymbol{t}^*$ used are chosen to ensure high accuracy, insensitivity of the simulation results to these parameters and optimal computational effort. Typically, a starting distance of $\boldsymbol{l_o = 50}$ (expressed as a multiple of the particle primary sphere radius for test aggregates) ensures that the ions start in conditions of mechanical

equilibrium. For purely repulsive interactions, the value of $\boldsymbol{s_o}$ is exactly taken to be the maximum extent of the particle (ions starting outside the geometric extent of the particle escape to infinity due to repulsion) and for cases of combined coulomb and image potentials, a value 5 times the maximum extent is used to capture the close range attraction of the ions towards the particle. The time step $\boldsymbol{\Delta t^*}$ is calculated based on this empirical condition involving the instantaneous speed and acceleration (force) of the ion:

$$\boldsymbol{\Delta t^* = 0.0005 \cdot \min\left(\frac{1}{\sqrt{\frac{PA}{\pi a^2}}|\vec{v}^*|}, \frac{1}{\frac{PA}{\pi a^2}|\vec{F}^*|}\right)} \tag{S10}$$

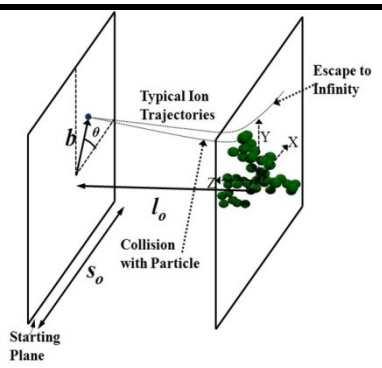

Figure B1: Ion trajectories are simulated using the Verlet Algorithm for a given set of impact parameters, z-component velocity sampled from the Maxwell-Boltzmann speed distribution. The particle is rotated by about the x, y and z axis randomly for each trial. Several trials are performed to obtained orientation averaged free molecular enhancement factor.

4. Brownian Dynamics Calculations in the Transition Regime

For determination of the dimensionless collision kernel in the transition regime, an ion is initiated on the surface of a cubical domain (of volume $\boldsymbol{V_{box}}$) with the particle center of mass coinciding with the origin. The particle is assumed to be at rest, and the ion velocity is assumed to be much more massive than the gas molecules it collides with en route to the particle. The drag force experienced by the ion, the potential force of interaction between the particle and ion and the diffusion of the ion are accounted for to obtain an expression for the position and velocity of the ion as a function of time. The particle position is normalized in terms of the primary sphere radius $\boldsymbol{\vec{r}^* = \vec{r}/a}$ (the choice of a normalizing length for position is again arbitrary), the time scale associated with the ion motion is scaled with $\boldsymbol{f_i PA^2 \eta_f^2/(\pi^2 R_s^2 \eta_c^2 kT)}$ and the force given by equation (S2). With these choices, the non-dimensional velocity and position of the ion as a function of time is expressed as:

$$\vec{v}^*(t^* + \Delta t^*) = \vec{v}^*(t^*)\exp(-\Delta t^*) + \left(\frac{PA\eta_f}{\pi R_s \eta_c}\right)^2 Kn_D^2 \vec{F}^*(\vec{r}^*(t^*), \psi_E, \psi_I)\left(1 - \exp(-\Delta t^*)\right) + \vec{A}_1 \tag{S11a}$$

$$\vec{r}^*(t^* + \Delta t^*) = \vec{r}^*(t^*) + \frac{PA\eta_f}{\pi R_s \eta_c}\left(\vec{v}^*(t^* + \Delta t^*) + \vec{v}^*(t^*) - \frac{PA\eta_f}{\pi R_s \eta_c} Kn_D^2 \vec{F}^*(\vec{r}^*(t^*), \psi_E, \psi_I)\right)\left(\frac{1-\exp(-\Delta t^*)}{1+\exp(-\Delta t^*)}\right) + \left(\frac{PA\eta_f}{\pi R_s \eta_c}\right)^2 Kn_D^2 \vec{F}^*(\vec{r}^*(t^*), \psi_E, \psi_I)\Delta t^* + \vec{A}_2 \tag{S11b}$$

$$\langle \vec{A}_1 \cdot \vec{A}_1 \rangle = 3Kn_D^2(1 - \exp(-2\Delta t^*)) \tag{S11c}$$

$$\langle \vec{A}_2 \cdot \vec{A}_2 \rangle = 6\left(\frac{PA\eta_f}{\pi R_s \eta_c}\right)^2 Kn_D^2\left(\Delta t^* - 2\left(\frac{1-\exp(-\Delta t^*)}{1+\exp(-\Delta t^*)}\right)\right) \tag{S11d}$$

$\vec{A}_1$ and $\vec{A}_2$ are normally distributed random vectors, with zero mean and variances given by equations (S11c) & (S11d), and model the random fluctuations in the velocity and position due diffusion of the ion. At the beginning of each trial, the ion is initialized at a random location on the surface of the cubical domain and allowed to move inside the box according to equations (S11 a) & (S11b) until impact with the particle. As in continuum limit BD simulations, only the motion of the nearest neighbor ion to the particle is considered. Sufficiently large box sizes (100-2500 times the primary sphere radius) are chosen to simulate the far field conditions for each particle and sufficiently small time steps are used to obtain results in the limit of $\Delta t^* \to 0$. The timestep used for simulation is chosen at each step by an empirical condition involving the instantaneous position $\vec{r}^*$ and the instantaneous force $\vec{F}^*$

$$\Delta t^* = 0.005 \cdot \min\left(\frac{|\vec{r}^*|^2}{2\left(\frac{PA\eta_f}{\pi R_s \eta_c}\right)^2 Kn_D^2}, \frac{1}{\left(\frac{PA\eta_f}{\pi R_s \eta_c}\right)^2 Kn_D^2 |\vec{F}^*|}\right) \tag{S12}$$

Upon collision, the process is reset and repeated several times, and the total time for all collisions is monitored. The mean first passage time is calculated by performing enough trials for statistical accuracy.

$$t^*_{mean} = \frac{1}{N_c}\sum_{k=1}^{N_c} t^*_k \tag{S13}$$

Typically, 10000-15000 collisions (N_c) are sufficient to calculate the mean first passage time to within 1% of the average over the latest 200 collisions. The collision kernel is calculated directly using the mean first passage time and the non-dimensional domain volume $V^*_{box}(= V_{box}/a^3)$ as

$$H = \frac{V^*_{box}}{t^*_{mean}} \frac{\pi^2 R_s \eta_c a^3}{PA^2 \eta_f^2} \tag{S14}$$

Tabulated values of η_c and η_f

Table B1. The continuum enhancement factor as a function of the Coulomb and image potential energy ratios.

$$\eta_c(\psi_E, \psi_I) = \begin{cases} \dfrac{\psi_E}{1 - \exp(-\psi_E)}, \psi_I = 0 \\ \left(\displaystyle\int_1^\infty \frac{1}{r^{*2}} \exp\left(\frac{\varphi(r^*)}{kT} \right) dr^* \right)^{-1}, \psi_I = \alpha|\psi_E| \\ 1 + 0.3475\psi_I^{0.3802}, 0 \le \psi_I \le 266, \psi_E = 0 \end{cases}$$

ψ_E	α=0.2	α=0.4	α=0.6	α=0.8	α=1.0
0.00E+00	1.00E+00	1.00E+00	1.00E+00	1.00E+00	1.00E+00
-1.00E-01	9.70E-01	9.84E-01	9.95E-01	1.00E+00	1.01E+00
-2.00E-01	9.36E-01	9.57E-01	9.74E-01	9.90E-01	1.00E+00
-3.00E-01	9.01E-01	9.28E-01	9.50E-01	9.69E-01	9.86E-01
-4.00E-01	8.66E-01	8.98E-01	9.24E-01	9.46E-01	9.66E-01
-5.00E-01	8.31E-01	8.68E-01	8.97E-01	9.22E-01	9.44E-01
-6.00E-01	7.98E-01	8.38E-01	8.69E-01	8.97E-01	9.21E-01
-7.00E-01	7.65E-01	8.08E-01	8.42E-01	8.71E-01	8.97E-01
-8.00E-01	7.33E-01	7.78E-01	8.15E-01	8.45E-01	8.72E-01
-9.00E-01	7.02E-01	7.50E-01	7.88E-01	8.20E-01	8.48E-01
-1.00E+00	6.71E-01	7.22E-01	7.61E-01	7.94E-01	8.24E-01
-1.10E+00	6.42E-01	6.94E-01	7.35E-01	7.69E-01	7.99E-01
-1.20E+00	6.14E-01	6.67E-01	7.09E-01	7.44E-01	7.75E-01
-1.30E+00	5.86E-01	6.41E-01	6.84E-01	7.20E-01	7.52E-01
-1.40E+00	5.60E-01	6.16E-01	6.59E-01	6.96E-01	7.28E-01
-1.50E+00	5.35E-01	5.91E-01	6.35E-01	6.73E-01	7.05E-01
-1.60E+00	5.10E-01	5.67E-01	6.12E-01	6.50E-01	6.83E-01
-1.70E+00	4.86E-01	5.44E-01	5.89E-01	6.28E-01	6.61E-01
-1.80E+00	4.64E-01	5.22E-01	5.67E-01	6.06E-01	6.39E-01
-1.90E+00	4.42E-01	5.00E-01	5.46E-01	5.84E-01	6.18E-01
-2.00E+00	4.21E-01	4.79E-01	5.25E-01	5.64E-01	5.98E-01
-2.10E+00	4.01E-01	4.59E-01	5.05E-01	5.44E-01	5.78E-01
-2.20E+00	3.81E-01	4.40E-01	4.85E-01	5.24E-01	5.58E-01
-2.30E+00	3.63E-01	4.21E-01	4.66E-01	5.05E-01	5.39E-01
-2.40E+00	3.45E-01	4.03E-01	4.48E-01	4.87E-01	5.20E-01

-2.50E+00	3.28E-01	3.85E-01	4.30E-01	4.69E-01	5.02E-01
-2.60E+00	3.12E-01	3.68E-01	4.13E-01	4.51E-01	4.85E-01
-2.70E+00	2.96E-01	3.52E-01	3.97E-01	4.34E-01	4.68E-01
-2.80E+00	2.81E-01	3.37E-01	3.81E-01	4.18E-01	4.51E-01
-2.90E+00	2.67E-01	3.22E-01	3.65E-01	4.02E-01	4.35E-01
-3.00E+00	2.54E-01	3.07E-01	3.50E-01	3.87E-01	4.20E-01
-3.10E+00	2.41E-01	2.93E-01	3.36E-01	3.72E-01	4.04E-01
-3.20E+00	2.28E-01	2.80E-01	3.22E-01	3.58E-01	3.90E-01
-3.30E+00	2.16E-01	2.67E-01	3.09E-01	3.44E-01	3.76E-01
-3.40E+00	2.05E-01	2.55E-01	2.96E-01	3.31E-01	3.62E-01
-3.50E+00	1.94E-01	2.43E-01	2.83E-01	3.18E-01	3.48E-01
-3.60E+00	1.84E-01	2.32E-01	2.71E-01	3.05E-01	3.36E-01
-3.70E+00	1.74E-01	2.21E-01	2.60E-01	2.93E-01	3.23E-01
-3.80E+00	1.65E-01	2.11E-01	2.49E-01	2.81E-01	3.11E-01
-3.90E+00	1.56E-01	2.01E-01	2.38E-01	2.70E-01	2.99E-01
-4.00E+00	1.48E-01	1.92E-01	2.28E-01	2.59E-01	2.88E-01
-4.10E+00	1.40E-01	1.83E-01	2.18E-01	2.49E-01	2.77E-01
-4.20E+00	1.33E-01	1.74E-01	2.09E-01	2.39E-01	2.66E-01
-4.30E+00	1.25E-01	1.66E-01	1.99E-01	2.29E-01	2.56E-01
-4.40E+00	1.19E-01	1.58E-01	1.91E-01	2.20E-01	2.46E-01
-4.50E+00	1.12E-01	1.50E-01	1.82E-01	2.11E-01	2.37E-01
-4.60E+00	1.06E-01	1.43E-01	1.74E-01	2.02E-01	2.28E-01
-4.70E+00	1.00E-01	1.36E-01	1.67E-01	1.94E-01	2.19E-01
-4.80E+00	9.46E-02	1.30E-01	1.59E-01	1.86E-01	2.10E-01
-4.90E+00	8.93E-02	1.23E-01	1.52E-01	1.78E-01	2.02E-01
-5.00E+00	8.44E-02	1.17E-01	1.45E-01	1.71E-01	1.94E-01
-5.10E+00	7.97E-02	1.11E-01	1.39E-01	1.64E-01	1.87E-01
-5.20E+00	7.52E-02	1.06E-01	1.33E-01	1.57E-01	1.79E-01
-5.30E+00	7.10E-02	1.01E-01	1.27E-01	1.50E-01	1.72E-01
-5.40E+00	6.70E-02	9.58E-02	1.21E-01	1.44E-01	1.65E-01
-5.50E+00	6.32E-02	9.10E-02	1.15E-01	1.38E-01	1.59E-01
-5.60E+00	5.96E-02	8.65E-02	1.10E-01	1.32E-01	1.52E-01
-5.70E+00	5.63E-02	8.22E-02	1.05E-01	1.26E-01	1.46E-01
-5.80E+00	5.31E-02	7.81E-02	1.00E-01	1.21E-01	1.40E-01
-5.90E+00	5.00E-02	7.41E-02	9.57E-02	1.16E-01	1.35E-01
-6.00E+00	4.72E-02	7.04E-02	9.13E-02	1.11E-01	1.29E-01
-6.10E+00	4.45E-02	6.69E-02	8.71E-02	1.06E-01	1.24E-01
-6.20E+00	4.19E-02	6.35E-02	8.31E-02	1.01E-01	1.19E-01
-6.30E+00	3.95E-02	6.03E-02	7.93E-02	9.71E-02	1.14E-01
-6.40E+00	3.72E-02	5.72E-02	7.56E-02	9.29E-02	1.09E-01

-6.50E+00	3.51E-02	5.43E-02	7.20E-02	8.88E-02	1.05E-01
-6.60E+00	3.30E-02	5.15E-02	6.87E-02	8.50E-02	1.01E-01
-6.70E+00	3.11E-02	4.89E-02	6.55E-02	8.13E-02	9.64E-02
-6.80E+00	2.93E-02	4.64E-02	6.24E-02	7.77E-02	9.24E-02
-6.90E+00	2.76E-02	4.40E-02	5.95E-02	7.43E-02	8.86E-02
-7.00E+00	2.60E-02	4.17E-02	5.67E-02	7.10E-02	8.49E-02
-7.10E+00	2.44E-02	3.96E-02	5.40E-02	6.79E-02	8.14E-02
-7.20E+00	2.30E-02	3.75E-02	5.14E-02	6.49E-02	7.80E-02
-7.30E+00	2.17E-02	3.56E-02	4.90E-02	6.20E-02	7.47E-02
-7.40E+00	2.04E-02	3.37E-02	4.67E-02	5.93E-02	7.16E-02
-7.50E+00	1.92E-02	3.20E-02	4.45E-02	5.67E-02	6.86E-02
-7.60E+00	1.80E-02	3.03E-02	4.23E-02	5.41E-02	6.57E-02
-7.70E+00	1.70E-02	2.88E-02	4.03E-02	5.17E-02	6.30E-02
-7.80E+00	1.60E-02	2.72E-02	3.84E-02	4.94E-02	6.03E-02
-7.90E+00	1.50E-02	2.58E-02	3.66E-02	4.72E-02	5.78E-02
-8.00E+00	1.41E-02	2.45E-02	3.48E-02	4.51E-02	5.53E-02
-8.10E+00	1.33E-02	2.32E-02	3.31E-02	4.31E-02	5.30E-02
-8.20E+00	1.25E-02	2.20E-02	3.15E-02	4.11E-02	5.07E-02
-8.30E+00	1.17E-02	2.08E-02	3.00E-02	3.93E-02	4.86E-02
-8.40E+00	1.10E-02	1.97E-02	2.86E-02	3.75E-02	4.65E-02
-8.50E+00	1.04E-02	1.87E-02	2.72E-02	3.58E-02	4.45E-02
-8.60E+00	9.76E-03	1.77E-02	2.59E-02	3.42E-02	4.26E-02
-8.70E+00	9.17E-03	1.68E-02	2.46E-02	3.27E-02	4.08E-02
-8.80E+00	8.62E-03	1.59E-02	2.34E-02	3.12E-02	3.90E-02
-8.90E+00	8.10E-03	1.50E-02	2.23E-02	2.98E-02	3.74E-02
-9.00E+00	7.61E-03	1.42E-02	2.12E-02	2.84E-02	3.57E-02
-9.10E+00	7.15E-03	1.35E-02	2.02E-02	2.71E-02	3.42E-02
-9.20E+00	6.72E-03	1.27E-02	1.92E-02	2.59E-02	3.27E-02
-9.30E+00	6.31E-03	1.21E-02	1.82E-02	2.47E-02	3.13E-02
-9.40E+00	5.93E-03	1.14E-02	1.73E-02	2.36E-02	3.00E-02
-9.50E+00	5.57E-03	1.08E-02	1.65E-02	2.25E-02	2.87E-02
-9.60E+00	5.23E-03	1.02E-02	1.57E-02	2.15E-02	2.74E-02
-9.70E+00	4.91E-03	9.69E-03	1.49E-02	2.05E-02	2.62E-02
-9.80E+00	4.62E-03	9.17E-03	1.42E-02	1.95E-02	2.51E-02
-9.90E+00	4.33E-03	8.67E-03	1.35E-02	1.86E-02	2.40E-02
-1.00E+01	4.07E-03	8.21E-03	1.28E-02	1.78E-02	2.30E-02
-1.01E+01	3.82E-03	7.77E-03	1.22E-02	1.69E-02	2.20E-02
-1.02E+01	3.59E-03	7.35E-03	1.16E-02	1.62E-02	2.10E-02
-1.03E+01	3.37E-03	6.95E-03	1.10E-02	1.54E-02	2.01E-02
-1.04E+01	3.16E-03	6.58E-03	1.05E-02	1.47E-02	1.92E-02

-1.05E+01	2.97E-03	6.22E-03	9.95E-03	1.40E-02	1.84E-02
-1.06E+01	2.79E-03	5.89E-03	9.46E-03	1.34E-02	1.76E-02
-1.07E+01	2.62E-03	5.57E-03	8.99E-03	1.28E-02	1.68E-02
-1.08E+01	2.46E-03	5.27E-03	8.54E-03	1.22E-02	1.60E-02
-1.09E+01	2.30E-03	4.98E-03	8.12E-03	1.16E-02	1.53E-02
-1.10E+01	2.16E-03	4.71E-03	7.71E-03	1.11E-02	1.47E-02
-1.11E+01	2.03E-03	4.45E-03	7.33E-03	1.05E-02	1.40E-02
-1.12E+01	1.90E-03	4.21E-03	6.96E-03	1.00E-02	1.34E-02
-1.13E+01	1.79E-03	3.98E-03	6.62E-03	9.58E-03	1.28E-02
-1.14E+01	1.68E-03	3.77E-03	6.28E-03	9.13E-03	1.22E-02
-1.15E+01	1.57E-03	3.56E-03	5.97E-03	8.71E-03	1.17E-02
-1.16E+01	1.48E-03	3.37E-03	5.67E-03	8.30E-03	1.12E-02
-1.17E+01	1.39E-03	3.18E-03	5.39E-03	7.91E-03	1.07E-02
-1.18E+01	1.30E-03	3.01E-03	5.12E-03	7.54E-03	1.02E-02
-1.19E+01	1.22E-03	2.84E-03	4.86E-03	7.18E-03	9.76E-03
-1.20E+01	1.14E-03	2.69E-03	4.62E-03	6.85E-03	9.32E-03
-1.21E+01	1.07E-03	2.54E-03	4.38E-03	6.53E-03	8.91E-03
-1.22E+01	1.01E-03	2.40E-03	4.16E-03	6.22E-03	8.51E-03
-1.23E+01	9.44E-04	2.27E-03	3.95E-03	5.93E-03	8.13E-03
-1.24E+01	8.85E-04	2.15E-03	3.76E-03	5.65E-03	7.77E-03
-1.25E+01	8.30E-04	2.03E-03	3.57E-03	5.38E-03	7.42E-03
-1.26E+01	7.79E-04	1.92E-03	3.39E-03	5.13E-03	7.09E-03
-1.27E+01	7.30E-04	1.81E-03	3.22E-03	4.88E-03	6.77E-03
-1.28E+01	6.85E-04	1.71E-03	3.05E-03	4.65E-03	6.47E-03
-1.29E+01	6.42E-04	1.62E-03	2.90E-03	4.43E-03	6.18E-03
-1.30E+01	6.02E-04	1.53E-03	2.75E-03	4.22E-03	5.90E-03
-1.31E+01	5.65E-04	1.44E-03	2.61E-03	4.02E-03	5.64E-03
-1.32E+01	5.29E-04	1.37E-03	2.48E-03	3.83E-03	5.39E-03
-1.33E+01	4.96E-04	1.29E-03	2.36E-03	3.65E-03	5.14E-03
-1.34E+01	4.65E-04	1.22E-03	2.24E-03	3.48E-03	4.91E-03
-1.35E+01	4.36E-04	1.15E-03	2.12E-03	3.31E-03	4.69E-03
-1.36E+01	4.09E-04	1.09E-03	2.02E-03	3.16E-03	4.48E-03
-1.37E+01	3.83E-04	1.03E-03	1.91E-03	3.01E-03	4.28E-03
-1.38E+01	3.59E-04	9.71E-04	1.82E-03	2.86E-03	4.09E-03
-1.39E+01	3.37E-04	9.17E-04	1.72E-03	2.73E-03	3.90E-03
-1.40E+01	3.16E-04	8.66E-04	1.64E-03	2.60E-03	3.73E-03
-1.41E+01	2.96E-04	8.18E-04	1.55E-03	2.47E-03	3.56E-03
-1.42E+01	2.78E-04	7.73E-04	1.47E-03	2.36E-03	3.40E-03
-1.43E+01	2.60E-04	7.30E-04	1.40E-03	2.24E-03	3.24E-03
-1.44E+01	2.44E-04	6.90E-04	1.33E-03	2.14E-03	3.10E-03

-1.45E+01	2.28E-04	6.51E-04	1.26E-03	2.03E-03	2.96E-03
-1.46E+01	2.14E-04	6.15E-04	1.20E-03	1.94E-03	2.82E-03
-1.47E+01	2.01E-04	5.81E-04	1.13E-03	1.84E-03	2.70E-03
-1.48E+01	1.88E-04	5.49E-04	1.08E-03	1.76E-03	2.57E-03
-1.49E+01	1.76E-04	5.18E-04	1.02E-03	1.67E-03	2.46E-03
-1.50E+01	1.65E-04	4.89E-04	9.69E-04	1.59E-03	2.35E-03
-1.51E+01	1.55E-04	4.62E-04	9.19E-04	1.52E-03	2.24E-03
-1.52E+01	1.45E-04	4.36E-04	8.72E-04	1.44E-03	2.14E-03
-1.53E+01	1.36E-04	4.12E-04	8.28E-04	1.37E-03	2.04E-03
-1.54E+01	1.27E-04	3.89E-04	7.85E-04	1.31E-03	1.95E-03
-1.55E+01	1.19E-04	3.67E-04	7.45E-04	1.25E-03	1.86E-03
-1.56E+01	1.12E-04	3.47E-04	7.07E-04	1.19E-03	1.77E-03
-1.57E+01	1.05E-04	3.28E-04	6.71E-04	1.13E-03	1.69E-03
-1.58E+01	9.81E-05	3.09E-04	6.36E-04	1.07E-03	1.62E-03
-1.59E+01	9.20E-05	2.92E-04	6.04E-04	1.02E-03	1.54E-03
-1.60E+01	8.61E-05	2.76E-04	5.73E-04	9.73E-04	1.47E-03
-1.61E+01	8.07E-05	2.60E-04	5.43E-04	9.26E-04	1.41E-03
-1.62E+01	7.56E-05	2.46E-04	5.15E-04	8.82E-04	1.34E-03
-1.63E+01	7.08E-05	2.32E-04	4.89E-04	8.39E-04	1.28E-03
-1.64E+01	6.64E-05	2.19E-04	4.64E-04	7.99E-04	1.22E-03
-1.65E+01	6.22E-05	2.07E-04	4.40E-04	7.60E-04	1.17E-03
-1.66E+01	5.82E-05	1.95E-04	4.17E-04	7.24E-04	1.11E-03
-1.67E+01	5.45E-05	1.84E-04	3.96E-04	6.89E-04	1.06E-03
-1.68E+01	5.11E-05	1.74E-04	3.75E-04	6.56E-04	1.01E-03
-1.69E+01	4.79E-05	1.64E-04	3.56E-04	6.24E-04	9.67E-04
-1.70E+01	4.48E-05	1.55E-04	3.38E-04	5.94E-04	9.22E-04
-1.71E+01	4.20E-05	1.46E-04	3.20E-04	5.65E-04	8.80E-04
-1.72E+01	3.93E-05	1.38E-04	3.04E-04	5.38E-04	8.40E-04
-1.73E+01	3.68E-05	1.30E-04	2.88E-04	5.12E-04	8.01E-04
-1.74E+01	3.45E-05	1.23E-04	2.73E-04	4.87E-04	7.65E-04
-1.75E+01	3.23E-05	1.16E-04	2.59E-04	4.63E-04	7.29E-04
-1.76E+01	3.03E-05	1.10E-04	2.46E-04	4.41E-04	6.96E-04
-1.77E+01	2.83E-05	1.03E-04	2.33E-04	4.20E-04	6.64E-04
-1.78E+01	2.65E-05	9.77E-05	2.21E-04	3.99E-04	6.34E-04
-1.79E+01	2.49E-05	9.22E-05	2.10E-04	3.80E-04	6.04E-04
-1.80E+01	2.33E-05	8.70E-05	1.99E-04	3.62E-04	5.77E-04
-1.81E+01	2.18E-05	8.21E-05	1.88E-04	3.44E-04	5.50E-04
-1.82E+01	2.04E-05	7.75E-05	1.79E-04	3.27E-04	5.25E-04
-1.83E+01	1.91E-05	7.31E-05	1.69E-04	3.11E-04	5.01E-04
-1.84E+01	1.79E-05	6.90E-05	1.61E-04	2.96E-04	4.78E-04

-1.85E+01	1.68E-05	6.51E-05	1.52E-04	2.82E-04	4.56E-04
-1.86E+01	1.57E-05	6.15E-05	1.44E-04	2.68E-04	4.35E-04
-1.87E+01	1.47E-05	5.80E-05	1.37E-04	2.55E-04	4.15E-04
-1.88E+01	1.38E-05	5.47E-05	1.30E-04	2.43E-04	3.96E-04
-1.89E+01	1.29E-05	5.16E-05	1.23E-04	2.31E-04	3.77E-04
-1.90E+01	1.21E-05	4.87E-05	1.17E-04	2.20E-04	3.60E-04
-1.91E+01	1.13E-05	4.60E-05	1.11E-04	2.09E-04	3.43E-04
-1.92E+01	1.06E-05	4.34E-05	1.05E-04	1.99E-04	3.27E-04
-1.93E+01	9.90E-06	4.09E-05	9.95E-05	1.89E-04	3.12E-04
-1.94E+01	9.27E-06	3.86E-05	9.43E-05	1.80E-04	2.98E-04
-1.95E+01	8.68E-06	3.64E-05	8.94E-05	1.71E-04	2.84E-04
-1.96E+01	8.13E-06	3.44E-05	8.48E-05	1.63E-04	2.71E-04
-1.97E+01	7.61E-06	3.24E-05	8.04E-05	1.55E-04	2.59E-04
-1.98E+01	7.12E-06	3.06E-05	7.62E-05	1.47E-04	2.47E-04
-1.99E+01	6.67E-06	2.89E-05	7.22E-05	1.40E-04	2.35E-04

Table B2. The Free Molecular Enhancement factor as a function of the coulomb and image potential energy ratios.

$$\eta_f(\psi_E,\psi_I)=\begin{cases}\exp(\psi_E),\ \psi_I=0\\ 2\int_{v=0}^{\infty} v^{*3}\exp\left(-v^{*2}\right) b_{crit}^{*\,2}(v^*,\psi_E,\psi_I)dv^*,\ \psi_I=\alpha|\psi_E|\\ 1+1.2534\psi_I^{0.5},\ \ 0\le\psi_I\le 266,\psi_E=0\end{cases}$$

ψ_E	α=0.2	α=0.4	α=0.6	α=0.8	α=1
0.00E+00	1.00E+00	1.00E+00	1.00E+00	1.00E+00	1.00E+00
-1.00E-01	1.07E+00	1.14E+00	1.20E+00	1.24E+00	1.28E+00
-2.00E-01	1.04E+00	1.14E+00	1.21E+00	1.27E+00	1.33E+00
-3.00E-01	1.00E+00	1.11E+00	1.20E+00	1.27E+00	1.33E+00
-4.00E-01	9.53E-01	1.07E+00	1.17E+00	1.25E+00	1.32E+00
-5.00E-01	9.04E-01	1.03E+00	1.13E+00	1.22E+00	1.30E+00
-6.00E-01	8.55E-01	9.90E-01	1.10E+00	1.19E+00	1.27E+00
-7.00E-01	8.07E-01	9.46E-01	1.06E+00	1.15E+00	1.23E+00
-8.00E-01	7.61E-01	9.02E-01	1.01E+00	1.11E+00	1.19E+00
-9.00E-01	7.17E-01	8.59E-01	9.72E-01	1.07E+00	1.16E+00
-1.00E+00	6.74E-01	8.16E-01	9.30E-01	1.03E+00	1.12E+00
-1.10E+00	6.34E-01	7.75E-01	8.89E-01	9.88E-01	1.08E+00
-1.20E+00	5.95E-01	7.36E-01	8.49E-01	9.48E-01	1.04E+00
-1.30E+00	5.59E-01	6.98E-01	8.10E-01	9.08E-01	9.97E-01
-1.40E+00	5.25E-01	6.61E-01	7.72E-01	8.70E-01	9.58E-01
-1.50E+00	4.92E-01	6.26E-01	7.36E-01	8.33E-01	9.20E-01
-1.60E+00	4.61E-01	5.93E-01	7.01E-01	7.96E-01	8.83E-01
-1.70E+00	4.33E-01	5.61E-01	6.67E-01	7.61E-01	8.47E-01
-1.80E+00	4.05E-01	5.31E-01	6.35E-01	7.27E-01	8.12E-01
-1.90E+00	3.80E-01	5.02E-01	6.04E-01	6.94E-01	7.78E-01
-2.00E+00	3.56E-01	4.74E-01	5.74E-01	6.63E-01	7.45E-01
-2.10E+00	3.33E-01	4.48E-01	5.45E-01	6.33E-01	7.13E-01
-2.20E+00	3.12E-01	4.23E-01	5.18E-01	6.03E-01	6.82E-01
-2.30E+00	2.92E-01	4.00E-01	4.92E-01	5.75E-01	6.53E-01
-2.40E+00	2.74E-01	3.78E-01	4.67E-01	5.49E-01	6.24E-01
-2.50E+00	2.56E-01	3.57E-01	4.44E-01	5.23E-01	5.97E-01
-2.60E+00	2.40E-01	3.37E-01	4.21E-01	4.98E-01	5.70E-01
-2.70E+00	2.24E-01	3.18E-01	4.00E-01	4.75E-01	5.45E-01
-2.80E+00	2.10E-01	3.00E-01	3.79E-01	4.52E-01	5.21E-01
-2.90E+00	1.96E-01	2.83E-01	3.60E-01	4.31E-01	4.98E-01
-3.00E+00	1.84E-01	2.67E-01	3.41E-01	4.10E-01	4.75E-01

-3.10E+00	1.72E-01	2.52E-01	3.24E-01	3.90E-01	4.54E-01
-3.20E+00	1.61E-01	2.38E-01	3.07E-01	3.72E-01	4.33E-01
-3.30E+00	1.50E-01	2.24E-01	2.91E-01	3.54E-01	4.14E-01
-3.40E+00	1.41E-01	2.11E-01	2.76E-01	3.37E-01	3.95E-01
-3.50E+00	1.31E-01	1.99E-01	2.62E-01	3.20E-01	3.77E-01
-3.60E+00	1.23E-01	1.88E-01	2.48E-01	3.05E-01	3.59E-01
-3.70E+00	1.15E-01	1.77E-01	2.35E-01	2.90E-01	3.43E-01
-3.80E+00	1.07E-01	1.67E-01	2.23E-01	2.76E-01	3.27E-01
-3.90E+00	1.00E-01	1.58E-01	2.11E-01	2.62E-01	3.12E-01
-4.00E+00	9.39E-02	1.49E-01	2.00E-01	2.50E-01	2.98E-01
-4.10E+00	8.78E-02	1.40E-01	1.89E-01	2.37E-01	2.84E-01
-4.20E+00	8.21E-02	1.32E-01	1.80E-01	2.26E-01	2.71E-01
-4.30E+00	7.67E-02	1.24E-01	1.70E-01	2.15E-01	2.58E-01
-4.40E+00	7.17E-02	1.17E-01	1.61E-01	2.04E-01	2.46E-01
-4.50E+00	6.70E-02	1.11E-01	1.53E-01	1.94E-01	2.35E-01
-4.60E+00	6.27E-02	1.04E-01	1.45E-01	1.84E-01	2.24E-01
-4.70E+00	5.86E-02	9.82E-02	1.37E-01	1.75E-01	2.13E-01
-4.80E+00	5.47E-02	9.25E-02	1.30E-01	1.67E-01	2.03E-01
-4.90E+00	5.11E-02	8.71E-02	1.23E-01	1.58E-01	1.94E-01
-5.00E+00	4.78E-02	8.21E-02	1.16E-01	1.51E-01	1.85E-01
-5.10E+00	4.47E-02	7.74E-02	1.10E-01	1.43E-01	1.76E-01
-5.20E+00	4.17E-02	7.29E-02	1.04E-01	1.36E-01	1.68E-01
-5.30E+00	3.90E-02	6.87E-02	9.87E-02	1.29E-01	1.60E-01
-5.40E+00	3.65E-02	6.47E-02	9.35E-02	1.23E-01	1.52E-01
-5.50E+00	3.41E-02	6.09E-02	8.85E-02	1.17E-01	1.45E-01
-5.60E+00	3.18E-02	5.74E-02	8.38E-02	1.11E-01	1.38E-01
-5.70E+00	2.97E-02	5.41E-02	7.93E-02	1.05E-01	1.32E-01
-5.80E+00	2.78E-02	5.09E-02	7.51E-02	1.00E-01	1.26E-01
-5.90E+00	2.60E-02	4.80E-02	7.11E-02	9.51E-02	1.20E-01
-6.00E+00	2.43E-02	4.52E-02	6.73E-02	9.03E-02	1.14E-01
-6.10E+00	2.27E-02	4.26E-02	6.37E-02	8.58E-02	1.09E-01
-6.20E+00	2.12E-02	4.01E-02	6.03E-02	8.15E-02	1.03E-01
-6.30E+00	1.98E-02	3.78E-02	5.71E-02	7.74E-02	9.85E-02
-6.40E+00	1.85E-02	3.56E-02	5.40E-02	7.35E-02	9.39E-02
-6.50E+00	1.73E-02	3.35E-02	5.12E-02	6.99E-02	8.94E-02
-6.60E+00	1.61E-02	3.16E-02	4.84E-02	6.64E-02	8.52E-02
-6.70E+00	1.51E-02	2.97E-02	4.58E-02	6.30E-02	8.11E-02
-6.80E+00	1.41E-02	2.80E-02	4.34E-02	5.99E-02	7.73E-02
-6.90E+00	1.32E-02	2.64E-02	4.10E-02	5.69E-02	7.36E-02
-7.00E+00	1.23E-02	2.48E-02	3.88E-02	5.40E-02	7.01E-02

-7.10E+00	1.15E-02	2.34E-02	3.68E-02	5.13E-02	6.67E-02
-7.20E+00	1.07E-02	2.20E-02	3.48E-02	4.87E-02	6.36E-02
-7.30E+00	1.00E-02	2.07E-02	3.29E-02	4.63E-02	6.05E-02
-7.40E+00	9.36E-03	1.95E-02	3.12E-02	4.39E-02	5.76E-02
-7.50E+00	8.75E-03	1.84E-02	2.95E-02	4.17E-02	5.49E-02
-7.60E+00	8.17E-03	1.73E-02	2.79E-02	3.96E-02	5.23E-02
-7.70E+00	7.63E-03	1.63E-02	2.64E-02	3.76E-02	4.98E-02
-7.80E+00	7.13E-03	1.53E-02	2.50E-02	3.57E-02	4.74E-02
-7.90E+00	6.66E-03	1.45E-02	2.36E-02	3.39E-02	4.51E-02
-8.00E+00	6.22E-03	1.36E-02	2.24E-02	3.22E-02	4.30E-02
-8.10E+00	5.81E-03	1.28E-02	2.12E-02	3.06E-02	4.09E-02
-8.20E+00	5.43E-03	1.21E-02	2.00E-02	2.91E-02	3.90E-02
-8.30E+00	5.07E-03	1.14E-02	1.89E-02	2.76E-02	3.71E-02
-8.40E+00	4.74E-03	1.07E-02	1.79E-02	2.62E-02	3.53E-02
-8.50E+00	4.42E-03	1.01E-02	1.70E-02	2.49E-02	3.36E-02
-8.60E+00	4.13E-03	9.48E-03	1.61E-02	2.36E-02	3.20E-02
-8.70E+00	3.86E-03	8.93E-03	1.52E-02	2.24E-02	3.05E-02
-8.80E+00	3.60E-03	8.40E-03	1.44E-02	2.13E-02	2.90E-02
-8.90E+00	3.37E-03	7.91E-03	1.36E-02	2.02E-02	2.76E-02
-9.00E+00	3.14E-03	7.45E-03	1.29E-02	1.92E-02	2.63E-02
-9.10E+00	2.94E-03	7.01E-03	1.22E-02	1.82E-02	2.50E-02
-9.20E+00	2.74E-03	6.60E-03	1.15E-02	1.73E-02	2.38E-02
-9.30E+00	2.56E-03	6.22E-03	1.09E-02	1.64E-02	2.27E-02
-9.40E+00	2.39E-03	5.85E-03	1.03E-02	1.56E-02	2.16E-02
-9.50E+00	2.24E-03	5.51E-03	9.75E-03	1.48E-02	2.06E-02
-9.60E+00	2.09E-03	5.19E-03	9.22E-03	1.41E-02	1.96E-02
-9.70E+00	1.95E-03	4.88E-03	8.72E-03	1.33E-02	1.86E-02
-9.80E+00	1.82E-03	4.60E-03	8.25E-03	1.27E-02	1.77E-02
-9.90E+00	1.70E-03	4.33E-03	7.81E-03	1.20E-02	1.69E-02
-1.00E+01	1.59E-03	4.07E-03	7.39E-03	1.14E-02	1.61E-02
-1.01E+01	1.48E-03	3.84E-03	6.99E-03	1.08E-02	1.53E-02
-1.02E+01	1.39E-03	3.61E-03	6.61E-03	1.03E-02	1.46E-02
-1.03E+01	1.29E-03	3.40E-03	6.25E-03	9.77E-03	1.39E-02
-1.04E+01	1.21E-03	3.20E-03	5.92E-03	9.27E-03	1.32E-02
-1.05E+01	1.13E-03	3.01E-03	5.60E-03	8.80E-03	1.26E-02
-1.06E+01	1.05E-03	2.84E-03	5.29E-03	8.35E-03	1.20E-02
-1.07E+01	9.85E-04	2.67E-03	5.01E-03	7.93E-03	1.14E-02
-1.08E+01	9.20E-04	2.51E-03	4.74E-03	7.53E-03	1.08E-02
-1.09E+01	8.59E-04	2.37E-03	4.48E-03	7.15E-03	1.03E-02
-1.10E+01	8.02E-04	2.23E-03	4.24E-03	6.78E-03	9.81E-03

-1.11E+01	7.49E-04	2.10E-03	4.01E-03	6.44E-03	9.34E-03
-1.12E+01	7.00E-04	1.97E-03	3.79E-03	6.11E-03	8.89E-03
-1.13E+01	6.53E-04	1.86E-03	3.59E-03	5.80E-03	8.46E-03
-1.14E+01	6.10E-04	1.75E-03	3.39E-03	5.51E-03	8.05E-03
-1.15E+01	5.70E-04	1.65E-03	3.21E-03	5.23E-03	7.66E-03
-1.16E+01	5.32E-04	1.55E-03	3.04E-03	4.96E-03	7.29E-03
-1.17E+01	4.97E-04	1.46E-03	2.87E-03	4.71E-03	6.94E-03
-1.18E+01	4.64E-04	1.37E-03	2.72E-03	4.47E-03	6.61E-03
-1.19E+01	4.33E-04	1.29E-03	2.57E-03	4.24E-03	6.29E-03
-1.20E+01	4.05E-04	1.22E-03	2.43E-03	4.03E-03	5.99E-03
-1.21E+01	3.78E-04	1.14E-03	2.30E-03	3.82E-03	5.70E-03
-1.22E+01	3.53E-04	1.08E-03	2.17E-03	3.63E-03	5.42E-03
-1.23E+01	3.30E-04	1.01E-03	2.06E-03	3.44E-03	5.16E-03
-1.24E+01	3.08E-04	9.55E-04	1.95E-03	3.27E-03	4.91E-03
-1.25E+01	2.88E-04	8.99E-04	1.84E-03	3.10E-03	4.67E-03
-1.26E+01	2.69E-04	8.46E-04	1.74E-03	2.94E-03	4.45E-03
-1.27E+01	2.51E-04	7.96E-04	1.65E-03	2.79E-03	4.23E-03
-1.28E+01	2.34E-04	7.49E-04	1.56E-03	2.65E-03	4.03E-03
-1.29E+01	2.19E-04	7.05E-04	1.47E-03	2.52E-03	3.83E-03
-1.30E+01	2.04E-04	6.64E-04	1.39E-03	2.39E-03	3.65E-03
-1.31E+01	1.91E-04	6.25E-04	1.32E-03	2.27E-03	3.47E-03
-1.32E+01	1.78E-04	5.88E-04	1.25E-03	2.15E-03	3.30E-03
-1.33E+01	1.66E-04	5.54E-04	1.18E-03	2.04E-03	3.14E-03
-1.34E+01	1.55E-04	5.21E-04	1.11E-03	1.94E-03	2.99E-03
-1.35E+01	1.45E-04	4.90E-04	1.05E-03	1.84E-03	2.85E-03
-1.36E+01	1.35E-04	4.62E-04	9.97E-04	1.75E-03	2.71E-03
-1.37E+01	1.26E-04	4.35E-04	9.43E-04	1.66E-03	2.58E-03
-1.38E+01	1.18E-04	4.09E-04	8.92E-04	1.57E-03	2.45E-03
-1.39E+01	1.10E-04	3.85E-04	8.43E-04	1.49E-03	2.34E-03
-1.40E+01	1.03E-04	3.62E-04	7.98E-04	1.42E-03	2.22E-03
-1.41E+01	9.62E-05	3.41E-04	7.55E-04	1.34E-03	2.11E-03
-1.42E+01	8.98E-05	3.21E-04	7.14E-04	1.28E-03	2.01E-03
-1.43E+01	8.39E-05	3.02E-04	6.75E-04	1.21E-03	1.92E-03
-1.44E+01	7.83E-05	2.84E-04	6.38E-04	1.15E-03	1.82E-03
-1.45E+01	7.31E-05	2.68E-04	6.04E-04	1.09E-03	1.73E-03
-1.46E+01	6.83E-05	2.52E-04	5.71E-04	1.04E-03	1.65E-03
-1.47E+01	6.38E-05	2.37E-04	5.40E-04	9.83E-04	1.57E-03
-1.48E+01	5.96E-05	2.23E-04	5.11E-04	9.33E-04	1.49E-03
-1.49E+01	5.56E-05	2.10E-04	4.83E-04	8.85E-04	1.42E-03
-1.50E+01	5.19E-05	1.98E-04	4.57E-04	8.40E-04	1.35E-03

-1.51E+01	4.85E-05	1.86E-04	4.32E-04	7.97E-04	1.29E-03
-1.52E+01	4.53E-05	1.75E-04	4.09E-04	7.57E-04	1.23E-03
-1.53E+01	4.23E-05	1.65E-04	3.86E-04	7.18E-04	1.17E-03
-1.54E+01	3.95E-05	1.55E-04	3.65E-04	6.81E-04	1.11E-03
-1.55E+01	3.69E-05	1.46E-04	3.46E-04	6.47E-04	1.06E-03
-1.56E+01	3.44E-05	1.37E-04	3.27E-04	6.14E-04	1.00E-03
-1.57E+01	3.22E-05	1.29E-04	3.09E-04	5.82E-04	9.56E-04
-1.58E+01	3.00E-05	1.22E-04	2.92E-04	5.53E-04	9.10E-04
-1.59E+01	2.80E-05	1.15E-04	2.76E-04	5.24E-04	8.65E-04
-1.60E+01	2.62E-05	1.08E-04	2.61E-04	4.98E-04	8.24E-04
-1.61E+01	2.45E-05	1.01E-04	2.47E-04	4.72E-04	7.84E-04
-1.62E+01	2.28E-05	9.55E-05	2.34E-04	4.48E-04	7.46E-04
-1.63E+01	2.13E-05	8.99E-05	2.21E-04	4.25E-04	7.09E-04
-1.64E+01	1.99E-05	8.46E-05	2.09E-04	4.04E-04	6.75E-04
-1.65E+01	1.86E-05	7.96E-05	1.98E-04	3.83E-04	6.42E-04
-1.66E+01	1.74E-05	7.49E-05	1.87E-04	3.64E-04	6.11E-04
-1.67E+01	1.62E-05	7.05E-05	1.77E-04	3.45E-04	5.82E-04
-1.68E+01	1.51E-05	6.64E-05	1.67E-04	3.27E-04	5.53E-04
-1.69E+01	1.41E-05	6.25E-05	1.58E-04	3.11E-04	5.27E-04
-1.70E+01	1.32E-05	5.88E-05	1.50E-04	2.95E-04	5.01E-04
-1.71E+01	1.23E-05	5.53E-05	1.41E-04	2.80E-04	4.77E-04
-1.72E+01	1.15E-05	5.21E-05	1.34E-04	2.66E-04	4.54E-04
-1.73E+01	1.07E-05	4.90E-05	1.27E-04	2.52E-04	4.32E-04
-1.74E+01	1.00E-05	4.61E-05	1.20E-04	2.39E-04	4.11E-04
-1.75E+01	9.37E-06	4.34E-05	1.13E-04	2.27E-04	3.91E-04
-1.76E+01	8.75E-06	4.08E-05	1.07E-04	2.15E-04	3.72E-04
-1.77E+01	8.17E-06	3.84E-05	1.01E-04	2.04E-04	3.54E-04
-1.78E+01	7.63E-06	3.62E-05	9.57E-05	1.94E-04	3.37E-04
-1.79E+01	7.12E-06	3.40E-05	9.05E-05	1.84E-04	3.20E-04
-1.80E+01	6.65E-06	3.20E-05	8.56E-05	1.75E-04	3.05E-04
-1.81E+01	6.21E-06	3.02E-05	8.09E-05	1.66E-04	2.90E-04
-1.82E+01	5.80E-06	2.84E-05	7.65E-05	1.57E-04	2.76E-04
-1.83E+01	5.42E-06	2.67E-05	7.24E-05	1.49E-04	2.63E-04
-1.84E+01	5.06E-06	2.51E-05	6.85E-05	1.42E-04	2.50E-04
-1.85E+01	4.72E-06	2.37E-05	6.47E-05	1.34E-04	2.38E-04
-1.86E+01	4.41E-06	2.23E-05	6.12E-05	1.27E-04	2.26E-04
-1.87E+01	4.12E-06	2.10E-05	5.79E-05	1.21E-04	2.15E-04
-1.88E+01	3.85E-06	1.97E-05	5.47E-05	1.15E-04	2.05E-04
-1.89E+01	3.59E-06	1.86E-05	5.18E-05	1.09E-04	1.95E-04
-1.90E+01	3.35E-06	1.75E-05	4.90E-05	1.03E-04	1.85E-04

-1.91E+01	3.13E-06	1.64E-05	4.63E-05	9.81E-05	1.76E-04
-1.92E+01	2.92E-06	1.55E-05	4.38E-05	9.31E-05	1.68E-04
-1.93E+01	2.73E-06	1.46E-05	4.14E-05	8.83E-05	1.60E-04
-1.94E+01	2.55E-06	1.37E-05	3.92E-05	8.38E-05	1.52E-04
-1.95E+01	2.38E-06	1.29E-05	3.70E-05	7.95E-05	1.45E-04
-1.96E+01	2.22E-06	1.21E-05	3.50E-05	7.55E-05	1.37E-04
-1.97E+01	2.08E-06	1.14E-05	3.31E-05	7.16E-05	1.31E-04
-1.98E+01	1.94E-06	1.07E-05	3.13E-05	6.80E-05	1.24E-04
-1.99E+01	1.81E-06	1.01E-05	2.96E-05	6.45E-05	1.18E-04

Appendix C: Measured Properties of Ions used in Charge Distribution Calculations described in Chapter 6

Table C1: The masses and electrical mobilities of ions generated with a 10mCi Po-210 alpha particle source from high purity, water free (zero) air and directed in to a parallel-plate differential mobility analyzer (P5 SEADM, Valladolid, Spain) coupled to a time-of-flight mass spectrometer (QSTAR XL, MDS Sciex, Ontario, Canada). The detected relative abundances (Rel. Abd.) of each ion are noted. The measurements were made near atmospheric pressure and a nominal temperature of 300 K.

Mean mass of positive ions = 167.2261 Da

Mean mass of negative ions = 117.7268 Da

Mean mobility of positive ions = 1.68 $cm^2s^{-1}V^{-1}$

Mean mobility of negative ions = 1.98 $cm^2s^{-1}V^{-1}$

Mass (Da)	Mobility ($cm^2s^{-1}V^{-1}$)	Charge	Rel. Abd.
71.1469	2.07	1	0.018642
73.1256	1.91	1	0.010728
74.1236	2.16	1	0.005687
83.1140	1.88	1	0.010680
85.1335	1.81	1	0.006058
85.1683	1.80	1	0.006058
87.1105	1.88	1	0.010333
89.1315	1.87	1	0.005747
99.1190	1.84	1	0.024137
101.1377	1.88	1	0.040085
109.1799	2.00	1	0.017025
113.2203	1.80	1	0.009662
115.1630	1.77	1	0.008321
117.1384	1.80	1	0.015732
123.1323	1.36	1	0.013529
125.1873	1.95	1	0.006334
127.2042	2.00	1	0.017385
129.1858	1.74	1	0.005208
131.1655	1.78	1	0.004358
135.1394	1.78	1	0.013194
141.1914	1.66	1	0.006801

143.2067	1.95	1	0.011841
145.2226	1.62	1	0.006010
151.2160	1.62	1	0.004705
155.2133	1.59	1	0.004693
157.2268	1.61	1	0.004382
159.2105	1.88	1	0.008273
169.2373	1.55	1	0.008058
171.2557	1.59	1	0.008010
177.1723	1.66	1	0.008405
177.2876	1.67	1	0.026328
183.2964	1.64	1	0.004586
185.2431	1.52	1	0.004777
195.3041	1.67	1	0.018342
199.3010	1.33	1	0.008058
201.2452	1.53	1	0.006178
211.3101	1.45	1	0.005376
217.3216	1.43	1	0.004238
219.3404	1.44	1	0.005783
221.3014	1.40	1	0.007483
235.3187	1.30	1	0.013050
242.4097	1.28	1	0.005292
259.3929	1.20	1	0.006669
279.3364	1.11	1	0.004047
285.4590	1.16	1	0.006848
355.2845	1.31	1	0.006501
371.3178	1.31	1	0.024413
372.3266	1.31	1	0.009016
373.3223	1.31	1	0.006489
391.5162	1.11	1	0.006441
71.9822	1.95	-1	0.002139
72.9817	2.27	-1	0.002343
73.9655	2.24	-1	0.008506
74.0042	2.15	-1	0.009881
75.9888	2.24	-1	0.006825
77.9765	2.41	-1	0.013191
79.9127	2.48	-1	0.004991
80.9556	2.41	-1	0.002037
81.9134	2.52	-1	0.005348
86.0377	2.15	-1	0.003158
88.0217	2.10	-1	0.046297

88.0569	2.05	-1	0.009575
89.0239	2.10	-1	0.001935
90.0390	2.13	-1	0.151574
91.0454	2.15	-1	0.005399
92.0467	2.10	-1	0.002699
94.0583	2.15	-1	0.032698
95.0650	2.10	-1	0.002598
100.0399	2.10	-1	0.002088
100.0774	1.80	-1	0.001935
102.0609	2.05	-1	0.007996
102.0988	1.92	-1	0.005144
104.0408	2.10	-1	0.005755
114.0374	2.15	-1	0.005552
116.0933	1.88	-1	0.024855
118.0739	2.02	-1	0.006672
122.0894	1.86	-1	0.003005
130.1165	1.80	-1	0.003463
132.0963	1.84	-1	0.002088
144.1723	2.13	-1	0.006723
158.1837	1.59	-1	0.007793
166.1019	1.63	-1	0.001935
170.1824	1.49	-1	0.001986
172.1994	1.53	-1	0.023989
173.2000	1.53	-1	0.002648
174.1343	1.62	-1	0.002648
182.1436	1.51	-1	0.002088
184.1486	1.54	-1	0.002088
186.1646	1.56	-1	0.006316
188.1761	1.50	-1	0.002750
198.1213	1.50	-1	0.001885
71.1469	2.07	1	0.018642
73.1256	1.91	1	0.010728
74.1236	2.16	1	0.005687
83.1140	1.88	1	0.010680
85.1335	1.81	1	0.006058
85.1683	1.80	1	0.006058
87.1105	1.88	1	0.010333
89.1315	1.87	1	0.005747
99.1190	1.84	1	0.024137
101.1377	1.88	1	0.040085

109.1799	2.00	1	0.017025
113.2203	1.80	1	0.009662
115.1630	1.77	1	0.008321
117.1384	1.80	1	0.015732

Appendix D: Supporting Information for Drag Measurements described in Chapter 7

INFORMATION AVAILABLE

In this section, the information available includes:

- Aerosol Generation Methods
    1. Electrospray Aerosolization
    2. Collision Nebulization
    3. Flame Synthesis
- DMA settings for Mobility and TEM sample Preparation
- Particle and Gas Parameters for friction factor Evaluation

Please note that all parameters not defined here are defined in the main text.

Aerosol Generation:

1) Spherical and cylindrical gold nanoparticles were produced by electrospray aerosolization (Chen & Pui, 1997) of colloidal solutions purchased from Nanopartz Inc. using the TSI 3480® Electrospray Aerosol Generator (fig. D1a). The solutions were custom ordered to limit the amount of dissolved surfactant by proprietary methods of Nanopartz Inc. By such procedures, all the surfactant used in such synthesis procedures (cetyltrimethylammonium bromide) was removed to produce a stable colloidal solution with very little dissolved salts. This is crucial to the production of electrospray droplets that lead to residue particle formation in sizes less than 5 nm approximately and thereby allowing accurate mobility distribution determination of gold nanoparticles. The purchased solutions were diluted in suitable proportions with Ammonium Acetate (Sigma Aldrich) buffer to optimize the concentration of produced particles and electrosprayed without further processing followed by charge reduction using a Po-210 strip to prevent coulombic fission of droplets. Polymicro™ silica capillaries were used for spraying by manually grinding the tip using sand paper and a pottery wheel. The taper of the capillary tip was arrived at by visual inspection using a magnifying glass and was approximately 40°-50°. Capillaries of OD 360 μm was used for all samples, while different IDs were used in order to electrospray particles from about 50 nm to 250 nm in their longest dimension. All of the solutions were assumed to have nearly the same conductivity which was not quantified but approximated to be close to the conductivity of standard 10mM Ammonium Acetate buffer used for dilution, as the solutions were certified by the manufacturer to contain very small amounts of dissolved salts and non-volatile residue. Aerosols were generated in two different gases 1) industrial grade compressed air (Matheson Inc.) with a very small amount of carbon dioxide (<2% of the total flow rate) to avoid a corona discharge from forming between the capillary tip and grounded surface and 2) industrial grade Carbon dioxide (Matheson Inc.). The gases were certified to be 99.9% pure by the manufacturer. Downstream of the electrospray, a tubular furnace

(Lindberg TF5503A-1) with a ceramic tube was operated at a suitable temperature to vaporize any coating of surfactant or organic residue from the surface of the particles without shrinking or sintering them. Electrospray settings such as capillary pressure drop ($ES_{\Delta p}$), voltage applied (ES_v), particle current (ES_i), capillary ID (ES_{ID}) and the furnace temperature used for each sample are tabulated in Table D1.

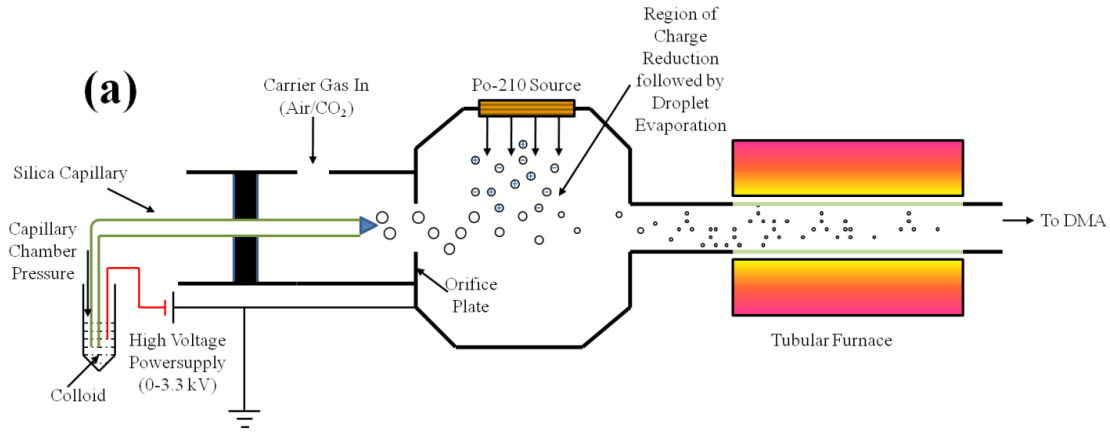

Figure D1(a): Schematic representation of electrospray aerosolization using TSI 3480 followed by conditioning using a tubular furnace.

Table D1: Electrospray settings to generate gold nanoparticles. Abbreviations: $\mathbf{ES_{ID}}$ inner diameter of electrospray capillary, $\mathbf{ES_{\Delta p}}$ applied capillary pressure drop, $\mathbf{ES_v}$ electrospray voltage between capillary tip and the grounded orifice plate, $\mathbf{ES_i}$ electrospray particle current reading from TSI 3480.

Dataset	Electrospray (ES) Settings					Furnace Temp. (°C)	Solution part# (Nanopartz Inc.)
	Gas	ES_{ID} (µm)	$ES_{\Delta p}$ (psid)	ES_v (kV)	ES_i (nA)		
50 nm spheres	Air	100	0.5	2.16	635	300	A11C-50
	CO_2	40	4.0	2.61	330		
70 nm spheres	Air	100	0.5	1.82	326	300	A11C-80
	CO_2	40	2.8	2.85	339		
$\frac{l_p}{d_p}$**=1.8**	Air	25	5.0	2.20	201	500	30-PU-40-650-50
	CO_2	25	5.0	2.55	224		
$\frac{l_p}{d_p}$**=3.8**	Air	40	5.0	2.11	701	150	CA1-2F-10-850-MU
$\frac{l_p}{d_p}$**=9.4**	Air	50	3.2	2.43	950	-	AR12-25-1400-TMU-5
$\frac{l_p}{d_p}$**=14**	Air	60	0.5	2.62	770	-	CA1-2F-10-2000-MU

2) NIST certified 125 nm PSL solution (Duke Scientific 3125A, 125nm ± 3nm, σ = 4.5nm) diluted with De-ionized water (Sigma Aldrich) was aerosolized by passing compressed air (house supply) at 50 psi through a home built stainless steel collision nebulizer (fig. D1b) to create droplets containing 0, 1 or 2 particles each. After evaporation of the droplets with the aid of a diffusion dryer containing silica beads, a Po-210 neutralizer was used to impart a steady state charge distribution to the particles before mobility classification. For the purposes of this study, singly charged doublets of PSL spheres with primary particles of 125 nm diameter were only considered (table 1). It

was observed that in spite of the coating of Platinum that was applied on the TEM grids to prevent evaporation of PSL under high energy electron beams, some evaporation was observed as soon as the beam was switched on – this might have contributed to some shrinkage as is evident from the observed mean diameter for the sample of 116 nm ± 6.7 nm. The images were collected and reported without any correction for this evaporation. Comparison to theory was done purely based on measured size.

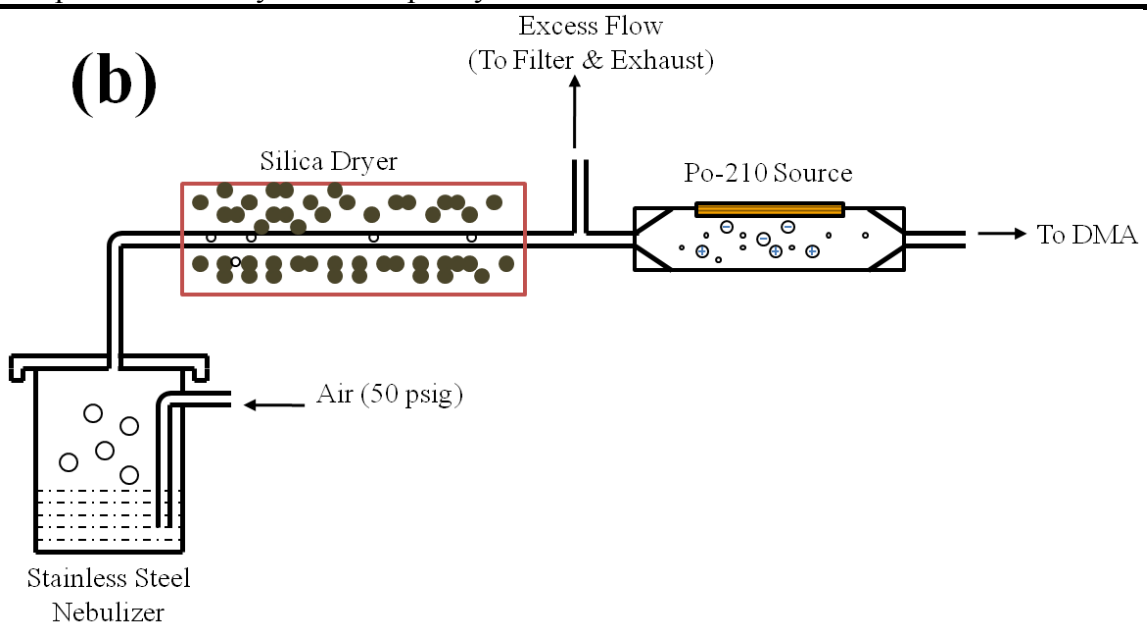

Figure D1(b): Schematic representation of generation of PSL doublets using a collision nebulizer.

3) Lastly, Single Walled Carbon Nanotubes (SWCNT) of high length to diameter ratios (10 to 240) were generated in an inverse diffusion ethylene flame reactor (fig. D1c) as described in detail elsewhere (Unrau *et al.*, 2007b; Unrau & Axelbaum, 2010). Briefly, a co-axial burner with oxygen flowing in the inner most tube, ethylene in the middle tube and a large flow of nitrogen through the outermost tube to shield the flame from external disturbances is used. A stream of nitrogen containing vapors of Ferrocene (Sigma Aldrich) and Tetra-Ethyl-Orthosilicate (TEOS, Sigma Aldrich) was added to the fuel. The flame formed at the interface of the oxygen and the ethylene streams acts as a source of heat for the thermal decomposition of Ferrocene, while TEOS is added to improve the yield of nanotubes, to form vapors of precursor iron atoms which nucleate, grow and oxidize to form iron/iron sub-oxide nanoparticles of size ~ 2 nm. These precursor particles act as nucleation sites for the excess non-combusted ethylene (after many intermediate steps) to grow into single walled carbon nanotubes. Industrial grade nitrogen, oxygen, ethylene from Matheson Inc. was used for all of the flows, which were

controlled using MKS® mass flow controllers of appropriate range, calibrated using a Gilian® Gilibrator flowcell (accuracy 1%) at room temperature. While these experiments were done, the ambient temperature in the lab, which is regulated by Honeywell® thermostats, was approximately 20 – 25° C. In this range, the fluctuation in the calibration relationships was not expected to be huge as was seen in repeated calibrations done on an alternate days showing variations no more than 1%. The particles generated in the flame were sampled for measurement using an Air-Vac® ejector dilutor (AVR062H). Two of these dilutors were used in series to obtain a dilution ratio of 100 – 200 to make sure the size distribution of particles were not modified by coagulation in the sampling lines. The sampled particles were charge neutralized before mobility classification by passing through a neutralizer housing containing a Po-210 strip. Due to multiple charging of SWCNTs, high polydispersity in the lengths (650 nm ± 270 nm) of collected particles was observed even though the diameter distribution was comparatively narrow (7.6 nm ±2.6 nm). The examined particles are not perfectly straight cylinders but fibrous shaped particles with long straight sections with branches. Bending of Nanotubes to form coils or bundles is not uncommon in such synthesis routes (Kulkarni, et al., 2009; Ku, 2010). SWCNT samples of 3 mobility diameters (d_m) are considered as listed in table 7.1.

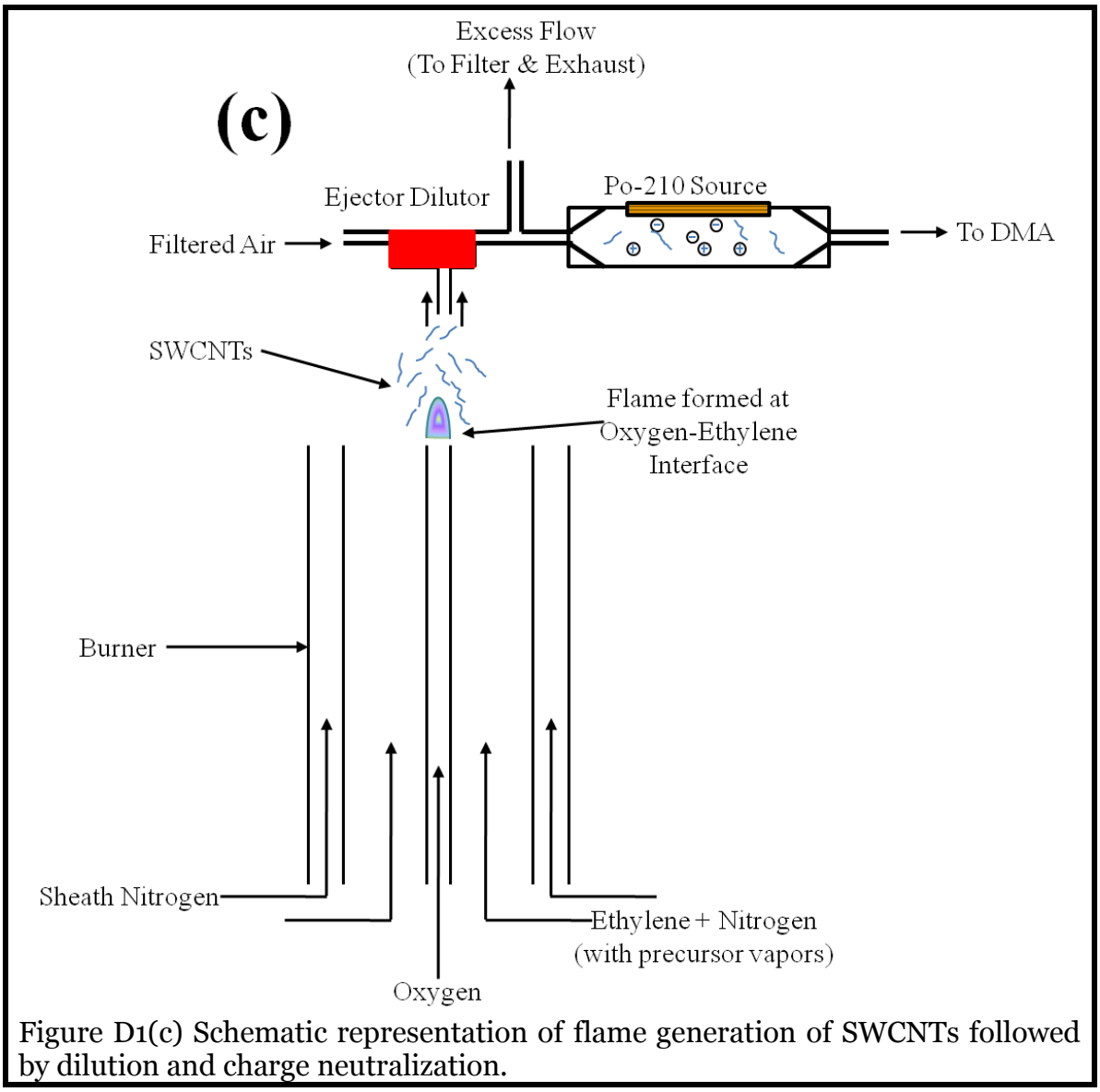

Figure D1(c) Schematic representation of flame generation of SWCNTs followed by dilution and charge neutralization.

Table D2: TEM sampling of mobility classified particles – DMA operating conditions.

Dataset	DMA settings			
	Sheath Gas	**Classification voltage (V)**	**Sheath flow rate (lpm)**	**Sheath flow temperature (^{o}C)**
50 nm spheres	Air	4250	10.1	24.0
	CO_2	4900	11.0	24.3
70 nm spheres	Air	7200	9.1	24.0
	CO_2	7505	9.0	24.9
$\frac{l_p}{d_p}$**=1.8**	Air (singly charged)	6130	10.0	23.0
	Air (doubly charged)	3070	10.0	23.1
	CO_2 (singly charged)	7270	10.1	24.2
	CO_2 (doubly charged)	3660	10.1	23.9
$\frac{l_p}{d_p}$**=3.8**	Air	1630	10.0	23.0
$\frac{l_p}{d_p}$**=9.4**	Air	7400	10.1	25.6
$\frac{l_p}{d_p}$**=14**	Air	6460	10.0	23.0
125 nm PSL Doublets**	Air	3755	10.1	23.1
SWCNTs	Air	3255	7.5	25.0

	(d_m=48.3 nm)			
	Air (d_m=53.9 nm)	3990	7.5	25.2
	Air (d_m=60.3 nm)	4890	7.5	24.9

(** long DMA of classifying length 44.44 cm was used)

Particle Parameters: The sphere has only one relevant length scale, the diameter $\boldsymbol{d_p}$, hence $\boldsymbol{R_s = \frac{d_p}{2}, PA = \frac{\pi d_p^2}{4}}$. For cylinders (diameter $\boldsymbol{d_p}$ and an end-to-end length $\boldsymbol{l_p}$) the following regression fit (Hansen, 2004) as a function of $\boldsymbol{x = \ln\left(\frac{l_p}{d_p}\right)}$ is used to calculate $\boldsymbol{R_s}$:

$$\boldsymbol{R_s = \left(\frac{3}{16} d_p^2 l_p\right)^{1/3} (1.0304 + 0.0193x + 0.06229x^2 + 0.00476x^3 + 0.00166x^4 + 2.66\times10-6x7}$$ (D1a)

The above expression assumes perfectly straight cylinders, while the electrosprayed gold nanorods considered in this work have a curved end cap (see sample images in fig. 7.2). The maximum error associated with this simplification was estimated to be less than 1% by comparing the predictions of equation (D1a) with calculations using the methods of Zhou *et al.* (1994). The total length of the SWCNTs, some of whom were had kinks and branches, was measured and used for R_s calculation, the expression for which assumes perfectly straight cylinders. These approximations were made to tractably compare the measured and predicted drag for these complicated nanoparticles. $\boldsymbol{PA}$ was calculated using Cauchy's theorem for convex shapes (Cauchy, 1908):

$$\boldsymbol{PA = \frac{\pi}{4} d_p l_p}$$ (D1b)

Again, the flame generated SWCNTs had in many instances more than one iron catalyst particles stuck to them, leading to bending of the particles. The area of the iron dots was counted from the TEM images and added to the total surface area for *PA* calculation.

For doublets made up of two point contacting spheres of diameters $\boldsymbol{d_{p1}}$ and $\boldsymbol{d_{p2}}$ ($\boldsymbol{d_{p1} \geq d_{p2}}$), $\boldsymbol{R_s}$ and $\boldsymbol{PA}$ are calculated from the following regression fits:

$$\boldsymbol{R_s(d_{p1}, d_{p2}) = \frac{d_{p1}}{2}\left(0.3794\left(\frac{d_{p2}}{d_{p1}}\right)^2 + 0.0188\frac{d_{p2}}{d_{p1}} + 0.9958\right)} \quad \text{(D1c)}$$

$$\boldsymbol{PA(d_{p1}, d_{p2}) = \frac{d_{p1}^2}{4}\left(3.0727\left(\frac{d_{p2}}{d_{p1}}\right)^2 - 0.4138\frac{d_{p2}}{d_{p1}} + 3.1587\right)} \quad \text{(D1d)}$$

These expressions were developed by fitting polynomials to R_s and PA calculations performed using the methods described in (Gopalakrishnan, et al., 2011).

Gas Parameters: The viscosity of the gas $\boldsymbol{\mu_g}$ is calculated using the empirical Sutherland law of viscosity (Chapman & Cowling, 1970) as a function of the sheath flow temperature $\boldsymbol{T_g}$:

$$\boldsymbol{\mu_g = \mu_{g,o}\left(\frac{T_{g,o}+C_g}{T_g+C_g}\right)\left(\frac{T_g}{T_{g,o}}\right)^{3/2}} \quad \text{(D2a)}$$

($\boldsymbol{\mu_{g,o}}$, $\boldsymbol{T_{g,o}}$, $\boldsymbol{C_g}$ are Sutherland constants for Air or Carbon dioxide) The mean free path of gas molecules $\boldsymbol{\lambda_g}$ calculated as a function of the density $\boldsymbol{\rho_g}$ and mean thermal speed $\boldsymbol{\bar{c}_g}$ (Fuchs & Stechkina, 1962):

$$\boldsymbol{\lambda_g = \frac{\mu_g}{0.499\rho_g\bar{c}_g}} \quad \text{(D2b)}$$

Finally, the slip correction coefficients $\boldsymbol{a_1, a_2, a_3}$ are taken from the recent measurements of Ku & de la Mora (2009) for air and from Rader (1990) for carbon dioxide (table D3).

Table D3**:** Sutherland constants and Slip correction coefficients used for Air and CO_2

Gas	$\boldsymbol{\mu_{g,o}}$ (Pa.s)	$\boldsymbol{T_{g,o}}$ (K)	$\boldsymbol{C_g}$ (K)	$\boldsymbol{a_1}$	$\boldsymbol{a_2}$	$\boldsymbol{a_3}$
Air	$1.83\text{x}10^{-5}$	291.15	120	1.257	0.4	1.1
CO_2	$1.48\text{x}10^{-5}$	293.15	240	1.207	0.45	0.92

Appendix E: Supporting Information for Charging Measurements described in Chapter 8

INFORMATION AVAILABLE

In this section, the information available includes:

- Aerosol Generation Methods using Electrospray Aerosolization
- Ion mobility standards in UHP air and CO_2
- Mass-Mobility Contours of Ions measured in UHP air and CO_2
- Table of Charging Ion Properties in UHP air and CO_2

Please note that all parameters not defined here are defined in the main text.

Table E1: TSI 3480 electrospray settings for generating gold gold nanoparticles and DMA settings for charge fraction measurements. Abbreviations: $\mathbf{ES_{ID}}$ inner diameter of electrospray capillary, $\mathbf{ES_{\Delta p}}$ applied capillary pressure drop, $\mathbf{ES_v}$ electrospray voltage between capillary tip and the grounded orifice plate, $\mathbf{ES_i}$ electrospray particle current reading from TSI 3480.

Dataset	Furnace Temp. (°C)	Gas	Electrospray (ES) Settings				DMA-1 Settings			DMA-2 Settings	
			ES_{ID} (µm)	$ES_{\Delta p}$ (psid)	ES_v (kV)	ES_i (nA)	V_1 (V)	Q_{sh1} (lpm)	T_{g1} (°C)	Q_{sh2} (lpm)	T_{g2} (°C)
50 nm spheres	300	UHP	100	0.75	2.24	420	6667	15.0	25.2	15.1	23.6
		CO_2	40	3.00	2.08	248	7500	15.0	25.5	15.1	26.6
70 nm spheres	300	UHP	100	0.50	2.03	527	7600	9.0	24.4	9.1	24.0
		CO_2	40	3.00	2.50	260	7450	8.0	23.5	8.3	24.0
$\frac{l_p}{d_p}$**=2.2 nanorods**	500	UHP	100	0.75	1.87	430	8500	13.0	23.9	13.0	24.0
		CO_2	40	5.00	2.32	343	7200	10.1	24.7	10.2	24.7

$\frac{l_p}{d_p}$=4.3 nanorods	150	UHP	100	0.25	2.10	540	2650	15.0	24.8	15.1	23.3
		CO_2	50	1.00	1.97	610	3250	15.0	24.4	15.1	23.6
$\frac{l_p}{d_p}$=11.3 nanorods	-	UHP	50	1.00	1.82	580	7400	10.0	23.6	10.1	24.3
$\frac{l_p}{d_p}$=14.9 nanorods	-	UHP	50	1.25	2.16	960	6900	10.0	22.5	10.1	22.9

Table E2: Details of parallel plate DMA calibration for ion mobility measurement

Gas	Reference Ion	Reference Mobility ($m^2s^{-1}V^{-1}$)	Source from Literature	Reference Voltage (volt)	Measured Mass (Da)
UHP Air	$(THABr)THA^+$	$6.53x10^{-5}$	Ude & de la Mora (2005)	3461	900
CO_2	THA^+	$6.64x10^{-5}$	de la Mora *et al.* (2012)	3004	410

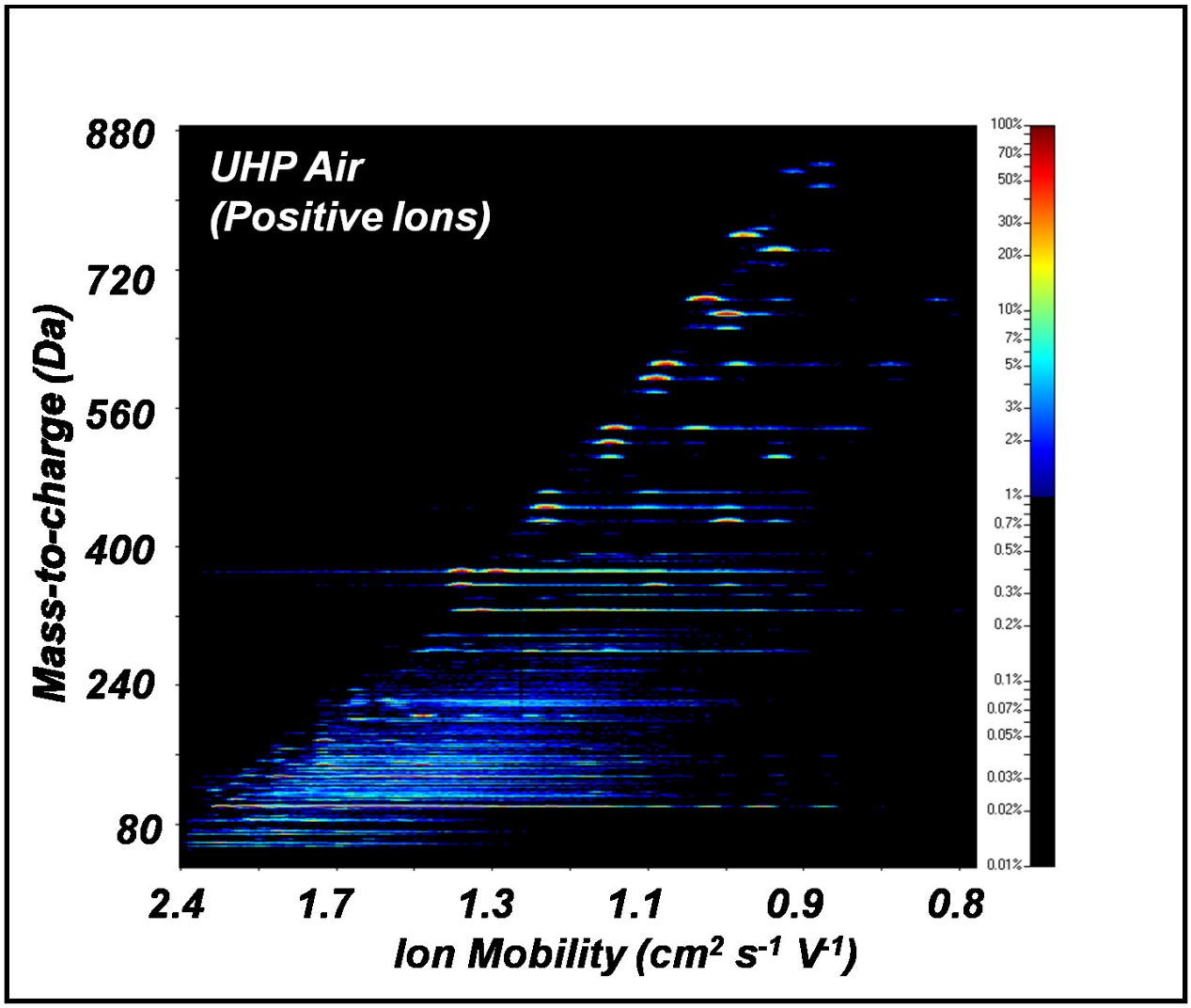

Figure E1 (a): UHP air positive ions

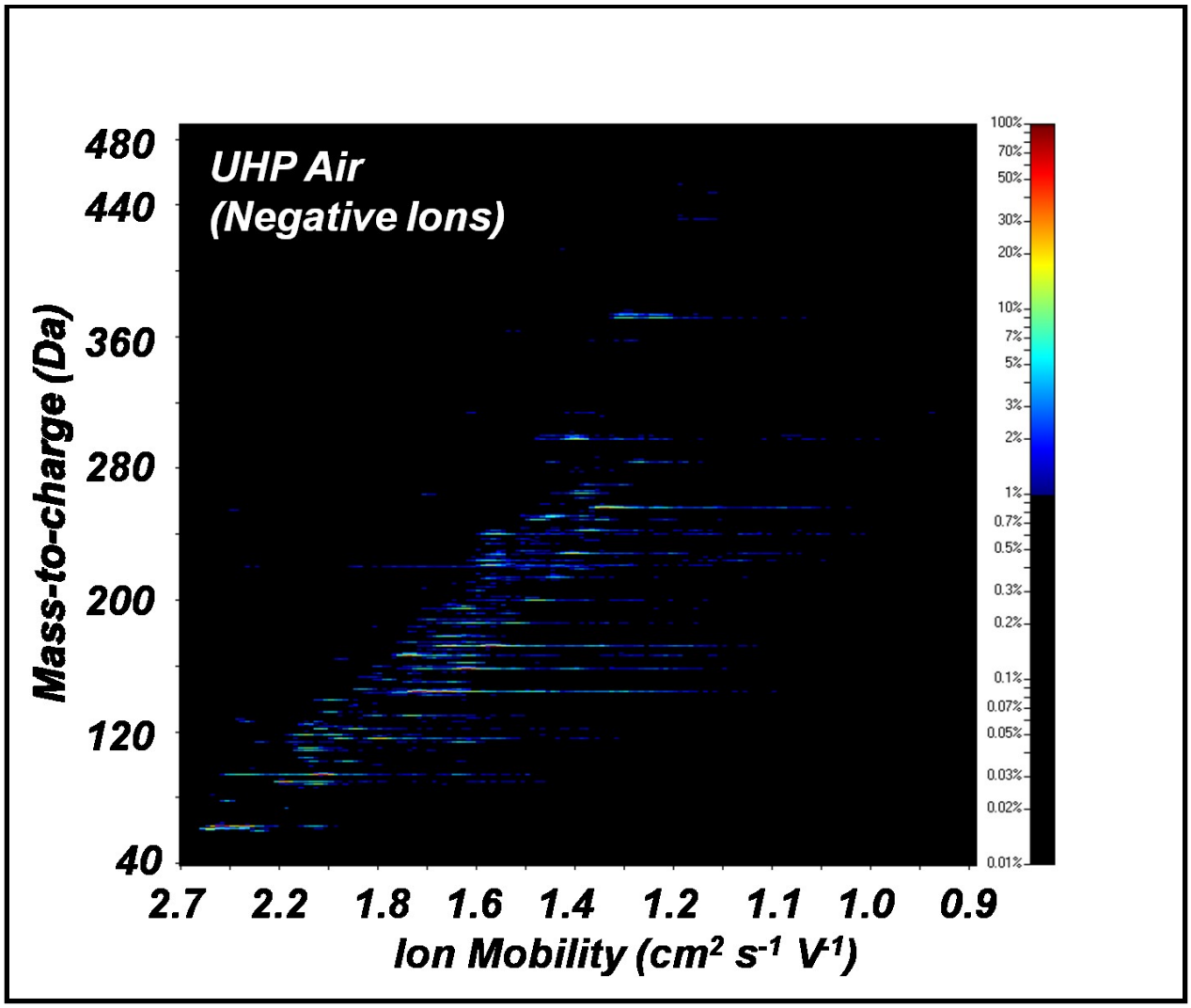

Figure E1 (b) UHP air negative ions

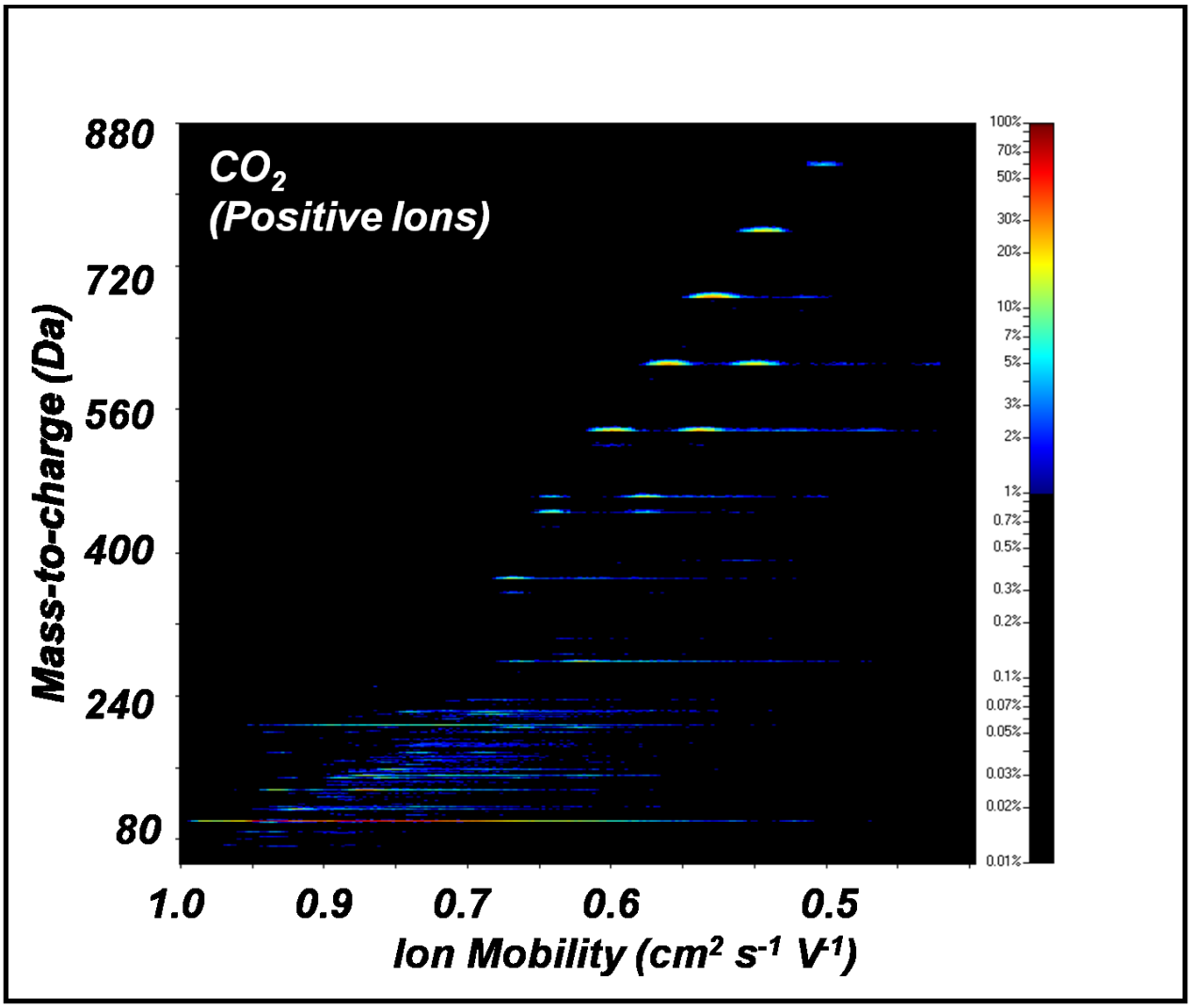

Figure E1 (c) CO_2 positive ions

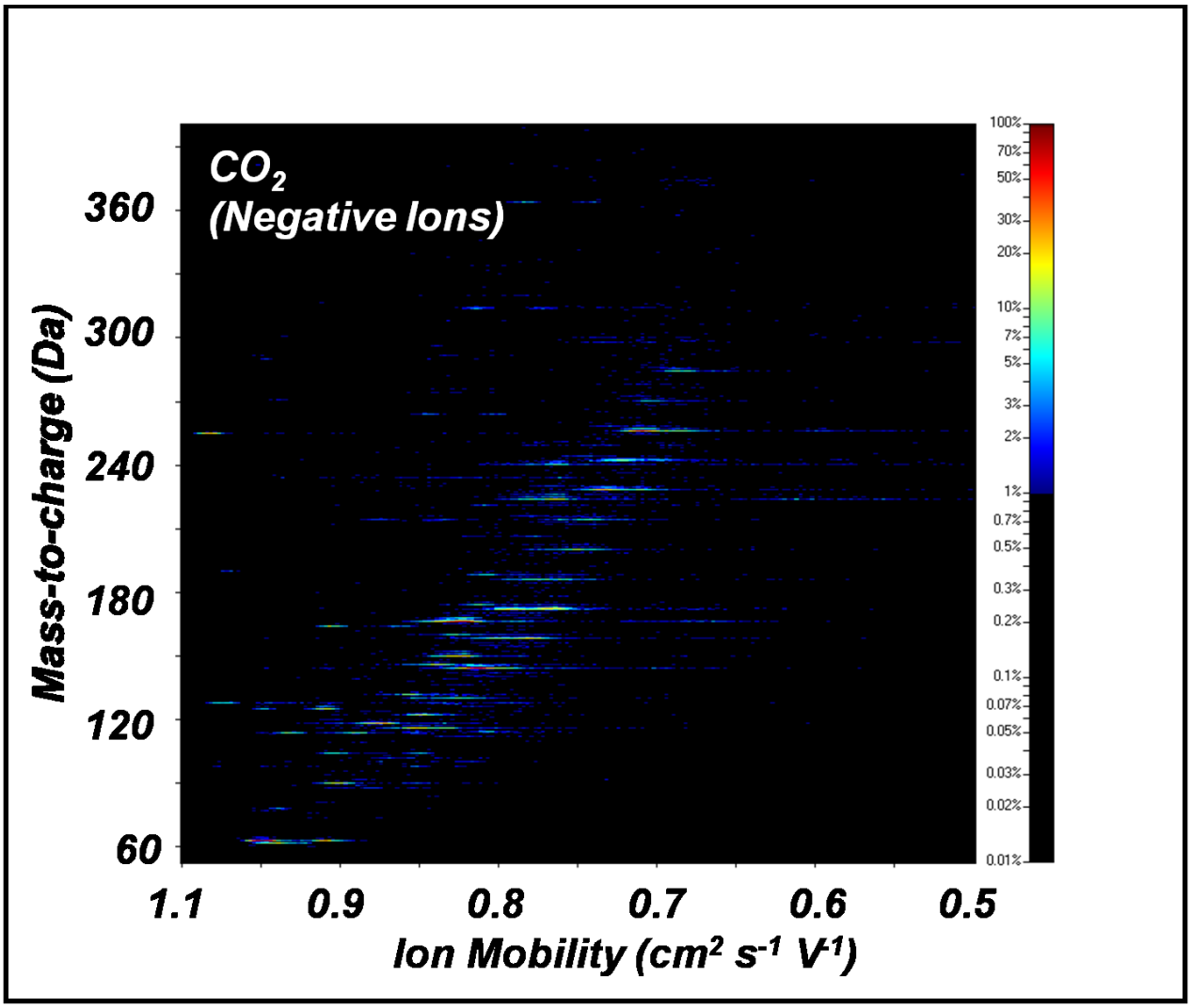

Figure E1 (d) CO_2 negative ions

Table E3 (a) Properties of Ions in UHP air

#	Mol. Wt. (Da)	Mobility ($m^2s^{-1}V^{-1}$)	Charge	Fraction
1	59.0294	2.19E-04	1	0.003604
2	69.0543	1.84E-04	1	0.003211
3	85.0574	1.98E-04	1	0.004036
4	100.0656	2.15E-04	1	0.071261
5	101.0547	2.15E-04	1	0.013684
6	109.0839	2.07E-04	1	0.005317
7	111.0984	1.51E-04	1	0.005746

8	113.1114	1.31E-04	1	0.006662
9	114.0784	1.90E-04	1	0.007696
10	117.0856	1.79E-04	1	0.00732
11	123.0335	1.69E-04	1	0.004984
12	127.109	2.07E-04	1	0.00738
13	135.1001	1.88E-04	1	0.023053
14	136.0206	2.01E-04	1	0.00452
15	143.114	1.71E-04	1	0.00507
16	145.1297	1.69E-04	1	0.006955
17	149.038	1.44E-04	1	0.009187
18	149.1299	1.72E-04	1	0.002253
19	151.1273	1.69E-04	1	0.003832
20	152.1425	1.50E-04	1	0.006368
21	155.1243	1.67E-04	1	0.004426
22	158.1729	1.62E-04	1	0.005391
23	169.1525	1.36E-04	1	0.002646
24	177.0874	1.71E-04	1	0.004363
25	199.2162	1.34E-04	1	0.004119
26	201.1658	1.61E-04	1	0.00451
27	205.1419	1.44E-04	1	0.004058
28	217.1929	1.51E-04	1	0.005362
29	219.206	1.60E-04	1	0.008594
30	223.0801	1.61E-04	1	0.015446
31	279.2244	1.44E-04	1	0.008819
32	327.193	1.31E-04	1	0.019267
33	328.1948	1.31E-04	1	0.004152
34	355.2052	1.35E-04	1	0.016054
35	356.2063	1.35E-04	1	0.006471
36	371.2476	1.35E-04	1	0.032698
37	372.2493	1.35E-04	1	0.013921
38	373.2451	1.35E-04	1	0.010242
39	429.1798	1.20E-04	1	0.010905
40	429.2734	9.62E-05	1	0.003828
41	445.3253	1.20E-04	1	0.02002
42	519.3284	1.10E-04	1	0.00827
43	536.3674	1.10E-04	1	0.010969
44	537.3706	1.10E-04	1	0.00616
45	593.4188	1.04E-04	1	0.007063
46	594.428	1.04E-04	1	0.004577
47	610.46	1.03E-04	1	0.008156

48	611.465	1.03E-04	1	0.005195
49	667.5073	9.62E-05	1	0.008575
50	668.5095	9.62E-05	1	0.006161
51	669.5028	9.62E-05	1	0.005168
52	684.5489	9.83E-05	1	0.009225
53	685.5441	9.83E-05	1	0.007059
54	686.5499	9.83E-05	1	0.005993
55	60.9233	2.53E-04	-1	0.008601
56	62.9333	2.47E-04	-1	0.03287
57	88.071	2.05E-04	-1	0.003189
58	90.0532	2.16E-04	-1	0.011265
59	94.0693	2.03E-04	-1	0.023816
60	102.1063	1.94E-04	-1	0.003447
61	109.0816	2.07E-04	-1	0.004963
62	110.0907	2.07E-04	-1	0.006576
63	116.1459	1.83E-04	-1	0.016852
64	118.0943	2.08E-04	-1	0.010558
65	122.1019	1.91E-04	-1	0.008942
66	130.1678	1.75E-04	-1	0.006981
67	139.1059	1.99E-04	-1	0.003721
68	144.1903	1.72E-04	-1	0.054669
69	145.1964	1.72E-04	-1	0.005436
70	158.2073	1.60E-04	-1	0.025711
71	162.2046	1.61E-04	-1	0.004487
72	166.1212	1.75E-04	-1	0.018408
73	167.1235	1.75E-04	-1	0.00376
74	172.2191	1.55E-04	-1	0.027072
75	173.2247	1.55E-04	-1	0.003264
76	174.1937	1.55E-04	-1	0.00328
77	178.1665	1.65E-04	-1	0.005996
78	186.1851	1.59E-04	-1	0.006178
79	195.1444	1.60E-04	-1	0.006314
80	200.2281	1.46E-04	-1	0.01092
81	214.2269	1.42E-04	-1	0.007251
82	221.1832	1.25E-04	-1	0.015939
83	224.0653	1.26E-04	-1	0.013127
84	228.228	1.13E-04	-1	0.019218
85	240.0733	1.25E-04	-1	0.017201
86	242.2284	1.10E-04	-1	0.010507
87	249.1776	1.18E-04	-1	0.007437

88	251.1413	1.15E-04	-1	0.006746
89	256.2191	1.08E-04	-1	0.030853
90	257.2168	1.08E-04	-1	0.005742
91	265.1269	1.11E-04	-1	0.005654
92	284.1953	1.04E-04	-1	0.0044
93	297.9526	1.12E-04	-1	0.012861
94	299.9371	1.12E-04	-1	0.005758
95	371.8047	1.02E-04	-1	0.010963
96	372.7962	1.02E-04	-1	0.003796
97	373.7817	1.02E-04	-1	0.005273

Table E3 (b) Properties of Ions in CO_2

#	Mol. Wt. (Da)	Mobility ($m^2s^{-1}V^{-1}$)	Charge	Fraction
1	100.0957	9.31E-05	1	0.143314
2	101.1002	9.31E-05	1	0.015893
3	114.1266	9.02E-05	1	0.00711
4	117.1385	9.06E-05	1	0.004128
5	135.157	9.27E-05	1	0.018159
6	149.0885	8.48E-05	1	0.003706
7	149.1667	8.10E-05	1	0.005123
8	152.1797	8.24E-05	1	0.016231
9	155.1524	8.31E-05	1	0.002973
10	158.2061	7.97E-05	1	0.008998
11	177.1275	7.79E-05	1	0.003879
12	199.264	7.20E-05	1	0.003661
13	205.1958	6.97E-05	1	0.004701
14	219.3175	7.17E-05	1	0.003464
15	223.2207	7.88E-05	1	0.00677
16	224.3133	7.58E-05	1	0.003262
17	236.3625	7.12E-05	1	0.001968
18	279.344	7.00E-05	1	0.011657
19	371.3347	7.05E-05	1	0.009054
20	445.4444	6.81E-05	1	0.006039
21	462.4891	6.27E-05	1	0.008853
22	463.4855	6.27E-05	1	0.003473
23	464.4911	6.27E-05	1	0.002423

24	536.5941	6.39E-05	1	0.021894
25	537.5975	6.39E-05	1	0.011215
26	538.5931	6.39E-05	1	0.008003
27	539.5983	6.39E-05	1	0.002511
28	610.6832	6.12E-05	1	0.016219
29	611.6884	6.12E-05	1	0.009945
30	612.6944	6.12E-05	1	0.007886
31	613.6919	6.12E-05	1	0.003332
32	684.6474	5.88E-05	1	0.023966
33	684.7952	5.88E-05	1	0.011334
34	685.6525	5.88E-05	1	0.02803
35	686.6584	5.88E-05	1	0.014406
36	686.7768	5.88E-05	1	0.007823
37	687.6453	5.88E-05	1	0.007723
38	687.7934	5.88E-05	1	0.003794
39	758.8093	5.68E-05	1	0.010981
40	759.8052	5.68E-05	1	0.008659
41	760.7913	5.68E-05	1	0.007438
42	61.9788	9.90E-05	-1	0.005816
43	62.978	0.000101	-1	0.040101
44	90.1137	9.22E-05	-1	0.008739
45	104.1288	9.22E-05	-1	0.004927
46	114.1255	9.75E-05	-1	0.008013
47	116.1863	8.43E-05	-1	0.012738
48	118.1636	8.73E-05	-1	0.016435
49	122.1848	8.36E-05	-1	0.008484
50	125.1504	9.34E-05	-1	0.007262
51	128.0709	0.000105	-1	0.004393
52	130.2234	8.09E-05	-1	0.008477
53	132.2127	8.47E-05	-1	0.005576
54	144.2939	7.90E-05	-1	0.044084
55	145.3004	7.90E-05	-1	0.003828
56	146.2378	7.90E-05	-1	0.00908
57	150.1968	8.03E-05	-1	0.0143
58	151.2005	8.03E-05	-1	0.00222
59	158.3253	7.54E-05	-1	0.012467
60	160.2662	8.09E-05	-1	0.004269
61	164.1883	9.30E-05	-1	0.004726
62	166.2421	8.03E-05	-1	0.047247
63	167.2447	8.03E-05	-1	0.007255

64	168.2454	8.03E-05	-1	0.004261
65	172.3471	7.40E-05	-1	0.014045
66	173.3482	7.35E-05	-1	0.001879
67	174.2877	7.90E-05	-1	0.004416
68	186.3284	7.46E-05	-1	0.00618
69	188.3099	7.81E-05	-1	0.003186
70	200.3821	7.19E-05	-1	0.005367
71	214.3641	7.11E-05	-1	0.008361
72	221.3394	7.87E-05	-1	0.002846
73	224.2113	7.35E-05	-1	0.021183
74	225.2121	7.35E-05	-1	0.005043
75	226.2152	7.35E-05	-1	0.003357
76	228.381	7.01E-05	-1	0.023372
77	229.3854	7.01E-05	-1	0.004006
78	234.3198	7.32E-05	-1	0.004857
79	240.2303	7.35E-05	-1	0.012653
80	242.3627	6.94E-05	-1	0.013627
81	254.9838	0.000109	-1	0.014207
82	256.3993	6.80E-05	-1	0.04079
83	257.4093	6.80E-05	-1	0.007293
84	264.1263	7.81E-05	-1	0.002336
85	270.3744	6.73E-05	-1	0.005004
86	284.4103	6.60E-05	-1	0.00652
87	298.1728	7.04E-05	-1	0.003039
88	364.0061	7.51E-05	-1	0.001732